Environment Environnement
da

Environment Canada Environnement Canada

e de la
tion de
onnement

[illegible]

The Arctic Marine Oilspill Program (AMOP) Remote Sensing Study

Canada

Technology Development
Report EPS 4-EC-83-3

Environmental Impact Control Directorate
March 1983

ENVIRONMENTAL PROTECTION SERVICE REPORT SERIES

Technology Development Reports describe technical apparatus and procedures, and results of laboratory, pilot plant, demonstration or equipment evaluation studies. They provide a central source of information on the development and demonstration activities of the Environmental Protection Service.

Other categories in the EPS series include such groups as Regulations, Codes, and Protocols; Policy and Planning; Economic and Technical Review; Surveillance; Training Manuals; Briefs and Submission to Public Inquiries; and, Environmental Impact and Assessment.

Inquiries pertaining to Environmental Protection Service Reports should be directed to the Environmental Protection Service, Department of the Environment, Ottawa, Ontario, Canada, K1A 1C8.

THE ARCTIC MARINE OILSPILL PROGRAM (AMOP) REMOTE SENSING STUDY

by

R.A. O'Neil
Canada Centre for Remote Sensing
R.A. Neville*, Vince Thomson**
Intera Environmental Consultants Ltd.

for the

Environmental Emergency Branch
Environmental Impact Control Directorate
Environmental Protection Service
Environment Canada

EPS 4-EC-83-3

---

* now with the Canada Centre for Remote Sensing
** now with the National Research Council of Canada

Disponible en français

s'adresser au:

Coordonnateur des publications
Direction générale du contrôle des incidences environnementales
Service de la protection de l'environnement
Environnement Canada
Ottawa (Ontario)
K1A 1C8

et demander:

Programme de lutte contre les
déversements d'hydrocarbures dans
l'Arctique - étude de télédétection

© Minister of Supply and Services Canada - 1983

Cat. No.: En 46-4/83-3E
ISBN: 0-662-12477-4

ABSTRACT

The Arctic Marine Oilspill Program (AMOP) remote sensing project was undertaken in order to evaluate the capability of state-of-the-art sensors to detect oil in ice-infested waters. This report outlines the experiment plan for, and results obtained from, four remote sensing missions (Montreal Island, Scott Inlet, Wallops Island, and the KURDISTAN) involving 12 different sensors.

Oil detection systems presently in use in Canada and abroad are examined. Recommendations are given for an integrated sensor package together with a real-time display system. The recommended sensors include: a side-looking radar (SLR); a UV-IR dual channel line scanner; a laser fluorosensor; a low-light-level television (LLLTV); and annotated photographic cameras. A real-time display system allows operator interaction with the sensors for the presentation of oil spill imagery and analysis. Hard copy can be obtained for presentation to those responsible for oil spill management.

RÉSUMÉ

Le volet télédétection du Programme sur les déversements d'hydrocarbures en milieu marin arctique (AMOP) a été entrepris en vue d'évaluer la capacité des détecteurs les plus perfectionnés à repérer les hydrocarbures dans des eaux encombrées par les glaces. Le présent rapport décrit le plan d'expériences et les résultats de quatre missions (île Montréal, inlet Scott, île Wallops et le KURDISTAN) au cours desquels 12 capteurs ont été utilisés.

On y passe en revue les systèmes de détection des hydrocarbures actuellement en usage au Canada et à l'étranger et on y donne des recommandations concernant un ensemble de capteurs intégré à un système de visualisation en temps réel. Ces capteurs comprennent: le radar à balayage latéral (SLR); le "scanner" ligne à ligne à deux canaux; le fluorodétecteur à laser; la télévision à faible niveau lumineux (LLLTV); et les chambres de prise de vues annotées. La visualisation en temps réel permet la commande des capteurs pour l'obtention et l'analyse d'images des déversements. Il est possible de procurer des copies sur papier aux responsables de l'intervention.

FOREWORD

This project was jointly sponsored by the Arctic Marine Oilspill Program (AMOP), Environmental Protection Service, Environment Canada; and the Canada Centre for Remote Sensing (CCRS), Department of Energy, Mines and Resources.

A major part of the work was performed by research personnel of Intera Environmental Consultants Ltd., Ottawa Branch. The Genesys Group developed much of the new software used. Reports prepared by the Biological Sciences Division of the National Research Council of Canada and the Centre for Cold Ocean Resources Engineering, as part of this remote sensing project, have been published as separate titles by the Environmental Protection Service.

ACKNOWLEDGEMENTS

The authors gratefully thank the following people for their contributions to the analysis of data collected during the AMOP remote sensing project:

L. Buja-Bijunas	CCRS
K. Dagg	The Genesys Group
A.L. Gray	CCRS
R.K. Hawkins	CCRS

We also acknowledge the commendable effort put forth by the personnel at the Canada Centre for Remote Sensing, Data Acquisition Division. The management at CCRS has been very cooperative in providing assistance for the AMOP project and in allocating time on their aircraft for the different airborne missions; in particular, gratitude is extended to N. de Villiers, G. Fitzgerald and J. Granot; to W. McColl and H. Zwick for their advice on optical sensors; to J. Allen, R. Marois, D. Percy and others who participated in the mission flights; to K. Holthusen, W. Laden, shop and technical personnel for the extra effort they put forth in order to complete installation of equipment into the aircraft within the limited time available; to the secretarial staff for the preparation of papers and reports; and, to P. Sharpe, B. Thompson, and B.A.K. Townshend for the drafting of diagrams for reports.

The Data Processing Division at CCRS is to be thanked for and indeed commended on the enormous volume of data which was processed and prepared for presentation; in particular, we express gratitude to H. Edel, R. Graves, M. Jager, K. Langley and I. Press.

We thank the management of Intera Environmental Consultants Ltd.; in particular, M.E. Kirby.

We would like to recognize the efforts of the engineers and pilots of Innotech Aviation Inc., who prepared and flew the aircraft on the different missions, and the personnel of Intera Environmental Consultants Ltd., who made preparations for and who operated equipment on the airborne missions. Also we thank the personnel at the Environmental Research Institute of Michigan, who operated the SAR, processed the data to image film and provided advice for data collection and analysis.

D.M. Rayner of the Biological Sciences Division, National Research Council of Canada, carried out the fluorescence analysis of various target samples.

The authors acknowledge the invitation from C. Rivet at the Environmental Protection Service (EPS), Quebec Regional Office, to participate in the oil spill surveillance at Montreal harbour. We thank Eric Levy of the Bedford Institute of Oceanography (DFO) and Brian MacLean of the Atlantic Geoscience Centre (EMR) for their efforts in sharing with us their surface data on the oil seep at Scott Inlet. We express gratitude for the hospitality accorded the AMOP team by the people of Clyde River and in particular by the Qakigiaq Coop Association during the Scott Inlet mission. We also sincerely thank W. Croswell, NASA Langley Research Center, for the invitation to participate in the test oil spill experiment at Dump Site 106 and appreciate his assistance and those of other personnel at NASA, Wallops Island Flight Center, for their cooperation in the execution of the experiment.

The authors also express their appreciation to M. Fingas, EPS, for his assistance on the myriad tasks and problems that arose during the AMOP project.

This project has been funded in part through the Arctic Marine Oilspill Program of the Environmental Emergencies Branch, Environmental Protection Service, Environment Canada.

TABLE OF CONTENTS

Page

ABSTRACT i

RÉSUMÉ ii

FOREWORD iii

ACKNOWLEDGEMENTS iv

LIST OF FIGURES x

LIST OF TABLES xvii

1 INTRODUCTION 1

1.1 Purpose 1
1.2 Summary of Experiments 1
1.3 Role of Remote Sensing 2
1.3.1 Search 2
1.3.2 Mapping and Tracking 3
1.3.3 Cleanup Support 3

2 EXISTING OIL SPILL REMOTE SENSING CAPABILITIES 4

2.1 State of the Art of Operational Systems 4
2.1.1 Canada 4
2.1.2 International 5
2.1.2.1 U.S. Coast Guard AIREYE System 5
2.1.2.2 Swedish Coast Guard System 6
2.2 Systems Operating in Canada 7

3 RECOMMENDATIONS 8

3.1 Sensors 8
3.1.1 Laser Fluorosensor 8
3.1.2 Dual Channel Line Scanner (DCLS) 9
3.1.3 Side-looking Airborne Radar (SLAR) 9
3.1.4 Low-light-level Television (LLLTV) 10
3.1.5 Photographic Cameras 11
3.2 Analysis/Display System 11
3.2.1 Fluorosensor 12
3.2.2 Dual Channel Line Scanner 13
3.2.3 Low-light-level Television 14
3.2.4 Side-looking Airborne Radar 15
3.2.5 Photographic Cameras 15
3.3 Platforms 15
3.4 Future Research Programs 17

Page

3.4.1 Sensor Development 18
3.4.2 Analytic Techniques 21
3.4.3 Pilot Projects 23

4 PRESENT STUDY: THE AMOP REMOTE SENSING PROJECT 26

4.1 Detectable Effects 26
4.1.1 Suppression of Capillary Waves 26
4.1.1.1 Slick detection 26
4.1.1.2 Sensors 27
4.1.2 Effects on the Surface Reflectance of Visible and Near Visible Light 27
4.1.2.1 Oil on water 27
4.1.2.2 Oil on ice 35
4.1.2.3 Sensors 36
4.1.3 Thermal Effects 36
4.1.3.1 Oil on water 37
4.1.3.2 Oil on ice 41
4.1.3.3 Sensors 41
4.1.4 Fluorescence 41
4.1.4.1 Oil detection 42
4.1.4.2 Techniques 43
4.1.4.3 Sensors 44
4.1.5 Raman Scattering Suppression 45
4.1.5.1 Raman scattering 45
4.1.5.2 Oil detection 45
4.1.6 Microwave Radiation Effects 46
4.1.6.1 Oil detection on water 48
4.1.6.2 Microwave radiometer experiments: oil on water 49
4.1.6.3 Oil detection on ice 52
4.2 Data Collection 52
4.3 Data Reduction 53
4.4 Results and Discussion 53
4.4.1 Microwave Sensors 54
4.4.1.1 Microwave scatterometer 54
4.4.1.2 ERIM SAR 62
4.4.2 Near Ultraviolet, Visible, Near Infrared 64
4.4.2.1 Photography 65
4.4.2.2 Low-light-level television 67
4.4.2.3 MSS 74
4.4.2.4 UVLS 90
4.4.2.5 MEIS 99
4.4.3 Thermal IR 99
4.4.3.1 Wallops Island test oil spills 99
4.4.3.2 Scott Inlet oil seep 111
4.4.3.3 Montreal Island oil spill 111
4.4.3.4 KURDISTAN oil spill 114
4.4.4 Integrated Multispectral Analysis 116
4.4.5 Fluorosensor 125

Page

4.4.5.1 Scott Inlet oil seep 125
4.4.5.2 Wallops Island test oil spill 127
4.5 Conclusions and Recommendations 140
4.5.1 Microwave Sensors 140
4.5.1.1 Oil on water 140
4.5.1.2 Oil on ice 141
4.5.1.3 Recommended sensors 141
4.5.2 Near Ultraviolet, Visible, Near Infrared 143
4.5.2.1 Spectral dependence 143
4.5.2.2 Polarization 144
4.5.2.3 Recommended sensors 144
4.5.3 Thermal IR 145
4.5.3.1 Oil on water 145
4.5.3.2 Oil on ice 146
4.5.3.3 Recommended sensor 146
4.5.4 Fluorescence 146
4.5.4.1 Recommended sensor: CCRS MK III fluorosensor 149
4.5.5 Oil Spill Detection from Satellites 149
4.5.5.1 Optical sensors 149
4.5.5.2 Microwave sensors 150

REFERENCES 151

BIBLIOGRAPHY 155

APPENDIX A SPECIFICATIONS FOR THE SENSORS USED FOR THE AMOP REMOTE SENSING PROJECT 159

APPENDIX B NAVIGATION TRACK RECOVERY 175

APPENDIX C AUTOMATIC DATA ACQUISITION SYSTEMS 179

APPENDIX D PLATFORMS USED FOR THE AMOP REMOTE SENSING PROJECT 185

APPENDIX E FLIGHT OPERATIONS DURING THE AMOP REMOTE SENSING PROJECT 197

APPENDIX F PROCESSING OF THE AMOP REMOTELY SENSED DATA 227

APPENDIX G SCOTT INLET/CLYDE RIVER OIL SIGHTINGS 241

APPENDIX H FIRMS AND AGENCIES WITH OPERATIONAL SYSTEMS APPLICABLE TO THE REMOTE SENSING OF OIL SPILLS 245

APPENDIX I INFORMATION ON DATA AVAILABLE FROM THE AMOP REMOTE SENSING PROJECT 249

APPENDIX J ACRONYMS 253

LIST OF FIGURES

Figure		Page
1	PERPENDICULAR COMPONENT; SPECTRAL RADIANCE OVER THE SEA, CALCULATED FOR CLEAN WATER SURFACE AND CLEAR SKY.	31
2	PERPENDICULAR COMPONENT; SPECTRAL RADIANCE OVER THE SEA, CALCULATED FOR AN OILED SURFACE AND CLEAR SKY.	32
3	PARALLEL COMPONENT; SPECTRAL RADIANCE OVER THE SEA, CALCULATED FOR CLEAN WATER SURFACE AND CLEAR SKY.	32
4	PARALLEL COMPONENT; SPECTRAL RADIANCE OVER THE SEA, CALCULATED FOR AN OILED WATER SURFACE AND CLEAR SKY.	33
5	PERPENDICULAR COMPONENT; SPECTRAL RADIANCE OVER THE SEA, CALCULATED FOR CLEAN WATER SURFACE AND OVERCAST SKY.	33
6	PERPENDICULAR COMPONENT; SPECTRAL RADIANCE OVER THE SEA, CALCULATED FOR OILED WATER SURFACE AND OVERCAST SKY.	34
7	PARALLEL COMPONENT; SPECTRAL RADIANCE OVER THE SEA, CALCULATED FOR CLEAN WATER SURFACE AND OVERCAST SKY.	34
8	PARALLEL COMPONENT; SPECTRAL RADIANCE OVER THE SEA, CALCULATED FOR OILED WATER SURFACE AND OVERCAST SKY.	35
9	TYPICAL OIL FLUORESCENCE SPECTRA.	42
10	FRAUNHOFER LINE DISCRIMINATION.	44
11	MICROWAVE BRIGHTNESS TEMPERATURE AS A FUNCTION OF OIL THICKNESS ON WATER.	50
12	MICROWAVE BRIGHTNESS TEMPERATURE AS A FUNCTION OF LOOK ANGLE FOR DIFFERENT WATER SURFACE ROUGHNESS.	51
13	SENSOR FIELDS OF VIEW AS MOUNTED IN C-GRSA.	55
14	SENSOR FIELDS OF VIEW AS MOUNTED IN C-GRSC.	55

Figure		Page
15	RC-10 AERIAL PHOTOGRAPH, WALLOPS OIL SPILL. C-GRSC Flight Line 3, November 2, 1978.	56
16	SCATTEROMETER, WALLOPS OIL SPILL.	56
17	SCATTEROMETER, WALLOPS OIL SPILL.	57
18	SCATTEROMETER, WALLOPS OIL SPILL.	57
19	SCATTEROMETER, WALLOPS OIL SPILL.	58
20	SCATTEROMETER, WALLOPS OIL SPILL.	59
21	SCATTEROMETER, WALLOPS OIL SPILL.	60
22	SCATTEROMETER, WALLOPS OIL SPILL.	60
23	SCATTEROMETER, WALLOPS OIL SPILL.	61
24	SCATTEROMETER, WALLOPS OIL SPILL.	62
25	ERIM SAR L_{VV} IMAGES AND CORRESPONDING 35 mm PHOTOGRAPHS, SCOTT INLET.	63
26	ERIM SAR X_{HH} AND L_{HH} IMAGES, WALLOPS OIL SPILL.	65
27	LOW-LIGHT-LEVEL TELEVISION, WALLOPS OIL SPILL.	68
28	LOW-LIGHT-LEVEL TELEVISION, WALLOPS OIL SPILL.	69
29	LOW-LIGHT-LEVEL TELEVISION, WALLOPS OIL SPILL.	70
30	LOW-LIGHT-LEVEL TELEVISION, WALLOPS OIL SPILL.	71
31	LOW-LIGHT-LEVEL TELEVISION, WALLOPS OIL SPILL.	72
32	LOW-LIGHT-LEVEL TELEVISION, WALLOPS OIL SPILL.	73
33	MSS 2, WALLOPS OIL SPILL. C-GRSA Flight Line 9, November 2, 1978.	75
34	MSS 3, WALLOPS OIL SPILL. C-GRSA Flight Line 9, November 2, 1978.	75
35	MSS 4, WALLOPS OIL SPILL. C-GRSA Flight Line 9, November 2, 1978.	76

Figure		Page
36	MSS 6, WALLOPS OIL SPILL. C-GRSA Flight Line 9, November 2, 1978.	76
37	MSS 8, WALLOPS OIL SPILL. C-GRSA Flight Line 9, November 2, 1978.	77
38	MSS 9, WALLOPS OIL SPILL. C-GRSA Flight Line 9, November 2, 1978.	77
39	MSS 10, WALLOPS OIL SPILL. C-GRSA Flight Line 9, November 2, 1978.	78
40	MSS 2, WALLOPS OIL SPILL. C-GRSA Flight Line 22, November 3, 1978.	79
41	MSS 3, WALLOPS OIL SPILL. C-GRSA Flight Line 22, November 3, 1978.	79
42	MSS 4, WALLOPS OIL SPILL. C-GRSA Flight Line 22, November 3, 1978.	80
43	MSS 6, WALLOPS OIL SPILL. C-GRSA Flight Line 22, November 3, 1978.	80
44	MSS 8, WALLOPS OIL SPILL. C-GRSA Flight Line 22, November 3, 1978.	81
45	MSS 9, WALLOPS OIL SPILL. C-GRSA Flight Line 22, November 3, 1978.	81
46	MSS 10, WALLOPS OIL SPILL. C-GRSA Flight Line 22, November 3, 1978.	82
47	RC-10 PHOTOGRAPH, WALLOPS OIL SPILL. C-GRSC Flight Line 6, November 2, 1978.	82
48	RC-10 PHOTOGRAPH, WALLOPS OIL SPILL. C-GRSC Flight Line 4B, November 3, 1978.	83
49	DCLS, WALLOPS OIL SPILL. UV and IR colour enhanced images. C-GRSC Flight Line 6, November 2, 1978.	84
50	DCLS, WALLOPS OIL SPILL. UV and IR Colour Enhanced Images. C-GRSC Flight Line 7, November 2, 1978.	85
51	DCLS, THEMATIC COLOUR IMAGE, WALLOPS OIL SPILL. C-GRSC, Flight Line 4B, November 3, 1978	86

Figure		Page
52	MSS IR, SCOTT INLET OIL SEEP. C-GRSA Sortie 9, Flight Line 16, September 19, 1978.	89
53	MSS 3, SCOTT INLET OIL SEEP. C-GRSA Sortie 9, Flight Line 16, September 19, 1978.	89
54	MSS, KURDISTAN OIL SPILL. Composite image of MSS channels 3, 6, 8. C-GRSB Flight Line 2, March 23, 1979.	91
55	MSS IR, KURDISTAN OIL SPILL. C-GRSB Flight Line 2, March 23, 1979.	91
56	DCLS, WALLOPS OIL SPILL. UV and IR images. C-GRSC Flight Line 3, November 2, 1978.	93
57	DCLS, WALLOPS OIL SPILL. UV and IR images. C-GRSC Flight Line 6, November 2, 1978.	94
58	DCLS, WALLOPS OIL SPILL. UV and IR colour enhanced images. C-GRSC Flight Line 3, November 2, 1978.	95
59	DCLS, KURDISTAN OIL SPILL. UV and IR images. C-GRSD Flight Line 4, March 29, 1979.	97
60	DCLS, KURDISTAN OIL SPILL. UV and IR images. C-GRSD Flight Line 15, April 2, 1979.	98
61	RC-10 PHOTOGRAPH, KURDISTAN OIL SPILL. C-GRSD, Flight Line 2, April 2, 1979.	100
62	RC-10 PHOTOGRAPH, KURDISTAN OIL SPILL. C-GRSD, Flight Line 3, April 2, 1979.	100
63	MEIS, WALLOPS OIL SPILL.	101
64	MSS IR, WALLOPS OIL SPILL. Colour enhanced image. C-GRSA Flight Line 9, November 2, 1978.	102
65	MSS IR, WALLOPS OIL SPILL. Colour enhanced image. C-GRSA Flight Line 22, November 3, 1978	103
66	MSS IR, WALLOPS OIL SPILL. C-GRSA Flight Line 9, November 2, 1978.	104

Figure Page

67 MSS IR, WALLOPS OIL SPILL. C-GRSA Flight Line 22, November 3, 1978. 104

68 VINTEN COLOUR PHOTOGRAPH, WALLOPS OIL SPILL. C-GRSA Flight Line 22, November 3, 1978. 107

69 VINTEN COLOUR PHOTOGRAPH, WALLOPS OIL SPILL. C-GRSA Flight Line 17, November 2, 1978. 109

70 LOW-LIGHT-LEVEL TELEVISION, SCOTT INLET. Scan print of oil seep. 112

71 VINTEN COLOUR PHOTOGRAPH, SCOTT INLET OIL SEEP. 112

72 IRLS, MONTREAL HARBOUR. 113

73 DCLS THEMATIC COLOUR IMAGE, WALLOPS OIL SPILL. C-GRSC Flight Line 4A, November 3, 1978. 117

74 DCLS THEMATIC COLOUR IMAGE, WALLOPS OIL SPILL. C-GRSC Flight Line 3, November 2, 1978. 118

75 DCLS AND MSS THEMATIC COLOUR IMAGES, WALLOPS OIL SPILL. Comparison of DCLS, C-GRSC Flight Line 6, AND MSS, C-GRSA Flight Line 2, November 2, 1978. 119

76 DCLS, WALLOPS OIL SPILL. Superposition of UV and IR colour enhanced images. C-GRSC Flight Line 6, November 2, 1978. 120

77 DCLS, WALLOPS OIL SPILL. UV colour enhanced image. C-GRSC Flight Line 6, November 2, 1978. 120

78 DCLS, WALLOPS OIL SPILL. IR colour enhanced image. C-GRSC Flight Line 6, November 2, 1978. 121

79 MSS THEMATIC COLOUR IMAGES, WALLOPS OIL SPILL. C-GRSA Flight Line 2, November 2, 1978. 122

80 MSS THEMATIC COLOUR IMAGE, WALLOPS OIL SPILL. C-GRSA Flight Line 2, November 3, 1978. 124

81 FLUOROSENSOR, SCOTT INLET OIL SEEP. C-GRSA Sortie 9, Flight Line 16, September 19, 1978. 126

82 CORRELATION OF FLUOROSENSOR DATA IN FIGURE 81 WITH MURBAN CRUDE OIL FLUORESCENCE SPECTRUM. 126

Figure		Page
83	MURBAN CRUDE OIL FLUORESCENCE SIGNATURE OBTAINED WITH LABORATORY FLUOROMETER.	128
84	LA ROSA CRUDE OIL FLUORESCENCE SIGNATURE OBTAINED WITH LABORATORY FLUOROMETER.	128
85	FLUOROSENSOR, WALLOPS TEST SPILL. Fluorosensor response to rhodamine dye.	129
86	CORRELATION OF DATA IN FIGURE 85 WITH RHODAMINE WT FLUORESCENCE SPECTRUM.	129
87	CORRELATION OF DATA IN FIGURE 85 WITH MURBAN CRUDE OIL FLUORESCENCE SPECTRUM.	130
88	SAMPLE SPECTRAL SIGNATURES FROM THE WALLOPS ISLAND TEST SPILLS.	130
89	FLUOROSENSOR, WALLOPS OIL SPILL. Fluorosensor response to Murban crude oil.	131
90	CORRELATION OF DATA IN FIGURE 89 WITH A MURBAN CRUDE OIL FLUORESCENCE SPECTRUM.	131
91	FLUOROSENSOR, WALLOPS OIL SPILL. Fluorosensor response to Murban crude oil.	132
92	CORRELATION OF DATA IN FIGURE 91 WITH MURBAN CRUDE OIL, LA ROSA CRUDE OIL AND RHODAMINE WT FLUORESCENCE SPECTRA.	132
93	CORRELATION OF DATA IN FIGURE 91 WITH LIGHT OIL SAMPLE LO_3 FLUORESCENCE SPECTRUM.	133
94	COMPARATIVE DIAGRAM SHOWING LIGHT, CRUDE AND HEAVY OIL FLUORESCENCE EFFICIENCIES.	133
95	FLUOROSENSOR AND MSS IR, WALLOPS OIL SPILL.	135
96	FLUOROSENSOR, WALLOPS OIL SPILL. Fluorosensor response to Murban crude oil.	135
97	CORRELATION OF DATA IN FIGURE 96 WITH A MURBAN CRUDE OIL FLUORESCENCE SPECTRUM.	136
98	FLUOROSENSOR, WALLOPS OIL SPILL. Response shown as a colour enhanced time history.	137

Figure		Page
99	FLUOROSENSOR, WALLOPS OIL SPILL. Fluorosensor response to La Rosa crude oil.	138
100	FLUOROSENSOR, WALLOPS OIL SPILL. Fluorosensor response to La Rosa crude oil.	138
101	CORRELATION OF DATA IN FIGURE 99 WITH LA ROSA CRUDE OIL FLUORESCENCE SPECTRUM.	139
102	CORRELATION OF DATA IN FIGURE 100 WITH LA ROSA CRUDE OIL FLUORESCENCE SPECTRUM.	139
103	SCATTEROMETER, WALLOPS OIL SPILL.	142

LIST OF TABLES

Table		Page
1	MSS AND DCLS MEASURED SPECTRAL RADIANCES.	87
2	TEMPERATURES AND EMITTANCES CALCULATED FROM THERMAL INFRARED DATA FROM MSS AND DCLS.	105
3	TEMPERATURES AND EMITTANCES OF CIAS CLUSTERED ZONES.	108
4	SENSOR PERFORMANCE: OIL ON WATER	147
5	SENSOR PERFORMANCE: OIL ON ICE	147
6	SENSOR PERFORMANCE: OIL IN OPEN PACK ICE	148

1 INTRODUCTION

1.1 Purpose

Arctic oil spills are of major concern, as oil exploration activities increase in the Canadian Arctic. The finding of major oil reserves and ensuing transportation of oil under adverse arctic conditions will increase the probability of oil spill occurence. Faced with potentially serious environmental damage, government agencies and industry must prepare for the difficult task of response. Under adverse weather and sea ice conditions, response operations may be facilitated by quickly locating and tracking the oil. In many cases, this can only be achieved using airborne remote sensing.

The Canada Centre for Remote Sensing (CCRS) has undertaken the development and testing of a remote sensing package capable of detecting oil spills in ice-infested waters, for the Environmental Protection Service (EPS), as part of the Arctic Marine Oilspill Program (AMOP). The study included a literature search of existing technology; experiment planning; data acquisition, processing and analysis; and a formulation of recommendations.

1.2 Summary of Experiments

It was initially proposed that experiments be performed at Scott Inlet, Baffin Island, on the natural seep reported there (Levy, 1977); in Hudson Bay, on an intentional, controlled oil spill on and under landfast ice; and in the Labrador Sea, on an intentional oil spill in moving pack ice. The last two experiments did not materialize, however, for a number of reasons.

Experiments were actually conducted in Montreal Harbour in June, 1978; near Scott Inlet in September, 1978; at Dump Site 106 off the New Jersey coast in November, 1978; and off the Nova Scotia coast in conjunction with the KURDISTAN accident in March and April, 1979. The first, an early experiment over an oil spill in Montreal Harbour, was conducted with a limited sensor complement but yielded information on the detection of oil at night. The Scott Inlet experiment, while it did not involve an oil-in-ice situation as had been hoped for, provided valuable sensor performance data and operational experience under arctic conditions. The flights over Dump Site 106, flown out of the National Aeronautics and Space Administration (NASA) Flight Center at Wallops Island, provided the only data over an intentional oil spill. As this was the only experiment for which the exact spill location was known and for which all the sensors were operated, it provided most of the data accumulated over oil. Consequently, advanced processing and analysis techniques have been concentrated on these data. The KURDISTAN spill gave the CCRS-AMOP team valuable experience in a real search situation and it was the only occasion on which oil was observed in ice. Unfortunately, the prime oil sensor, the laser fluorosensor, was undergoing modifications at the time of the last experiment and was not tested under these conditions.

1.3 Role of Remote Sensing

Drawing on various experiences, realistic assertions may be made regarding the possible role that remote sensing could play in the event of an oil spill. The role is threefold: the search for and location of the region polluted by the oil spill; the mapping and tracking of the slick(s); and the classification by thickness of the oil, in support of the actual cleanup operation.

1.3.1 Search. Classification of oil spills by search complexity yields three general types, listed in order of increasing difficulty:

I- Fixed-source, continuous-flow spills, coupled with continuous surface currents and short spill-to-search delay times, are most easily dealt with. One has only to locate the source and follow the oil.

II- A moving source with a continuously flowing spill or a fixed-source, continuous-flow spill, coupled with discontinuous surface currents and long spill-to-search delay times, makes the task of locating the oil more difficult. This is because the original slick is likely to have been separated into smaller slicks which may move along different paths depending on the current zones they encounter.

III- The potentially most demanding situation involves a single brief spill incident, from either a fixed or a moving source, the degree of difficulty varying with the square of the time delay between spill and search. For given bounds on the surface current velocity there is a limiting delay time for each sensor/aircraft system beyond which that particular combination can no longer search the area, as it is expanding more rapidly than it can be searched (O'Neil et al., 1982).

Other environmental factors that affect sensor operation and search difficulty are sea ice and weather conditions. It is likely that, in the short-term, the prevailing weather conditions will be those that tend to increase the probability of an accident - there will be high sea states, often accompanied by low ceilings, and/or heavy sea ice conditions. Such situations seriously hamper the search for oil.

The situation most often portrayed in oil spill "scenarios" is type I, in which an oil well has blown out or a tanker has run aground, with the source still emitting oil at the time the search is undertaken. Incidents of this type that have occurred in Canada include the ARROW and the NEPCO 140 accidents, but many others, such as the KURDISTAN, have been of type III. In some instances the oil loss may be not be noticed immediately. For example in the spill from the SIR JOHN A. MACDONALD off Cape Parry, NWT, fuel tanks were holed by ice and oil was lost, but the accident went undetected for days. In the latter cases not even the initial spill location was found. For some cases remote sensing is the only viable method to search for the oil.

1.3.2 Mapping and Tracking. Once an oil slick has been located, its mapping and tracking by remote sensing can be routine, provided adequate navigation equipment is available to pinpoint the spill to within the detection radius provided by eye or by the sensors. Periodic overflights would suffice to update a slick's position and areal coverage. On board display equipment can not only produce real time hard copy of oil slick imagery, but maps with aircraft and slick positions traced on them can be produced as well. The imagery from remote sensing techniques coupled with the maps can give the on-scene coordinator a comprehensive overview of the spill.

1.3.3 Cleanup Support. It is important for the on-scene coordinator to be able to direct cleanup resources effectively during oil cleanup on water. Remote sensing can be used to map the location and areal extent of the slick and the relative thickness (and hence volume) of the regions within the slick. The on-scene coordinator can, using this information, direct the cleanup equipment to the thickest part of the slick and to those areas that present the greatest threat to the environment.

2 EXISTING OIL SPILL REMOTE SENSING CAPABILITIES

2.1 State of the Art of Operational Systems

Canada does not yet have a fully integrated oil sensing system, i.e., sensors and real time display installed on board a suitable search aircraft. The Canada Centre for Remote Sensing (CCRS), however, does have a number of first rate sensors. What is lacking is an airborne real time display and analysis system to tie the various detectors together in one cohesive unit. When such a system is assembled, it will be installed in an aircraft which is appropriate for the task at hand. The search requirements would favour an aircraft such as the military CP-140 (Aurora). If the sensor package were to be one-of-a-kind, there would be an additional requirement that the aircraft be able to respond quickly to a spill in any one of the three oceans bounding Canada. This requirement would favour a faster long range jet aircraft such as the Canadair Challenger E.

Internationally, there are two systems worthy of consideration. The United States Coast Guard (USCG) will soon take delivery of six oil spill sensor packages and forty-one Falcon 20 patrol aircraft, each outfitted to accept these systems. The oil sensing package, designated AIREYE (White and Schmidt, 1979), has already undergone development in the form of the prototype AOSS system (Edgerton et al., 1975), and will be fully integrated with a real-time, operator-interactive display system; resulting in a sophisticated fully operational oil sensing system. The Swedish Coast Guard has taken a more economical route and has developed a system using similar sensors with real time displays; this package, however, has only moderately reduced oil detection capability (Backlund, 1979).

There is understandable interest in the use of satellite data for the detection of oil slicks. Some success has been achieved using satellite data collected in the visible, but only under particular sun angle conditions, or for particularly bright oil emulsions. The lack of suitable conditions and the extensive cloud cover which is prevalent in Canada's coastal regions complicate the operational use of satellite-borne optical sensors for oil spill detection.

2.1.1 Canada. The Canada Centre for Remote Sensing (CCRS) owns the best oil spill detection sensors available in Canada. The present report contains the results of analysis of data acquired using these sensors. CCRS employs its sensors for research on numerous projects; however, the sensors are not normally installed together as an oil detection package in an aircraft ready to respond to an emergency situation.

CCRS owns a closed circuit, low-light-level television system, including a video monitor and tape recorder. Fitted with the appropriate optical filters, such a system provides, at modest cost, an oil detection capability giving high oil-water contrast imagery.

CCRS also operates a dual channel line scanner and a multispectral line scanner, which produce excellent imagery of oil spills from the ultraviolet to the thermal infrared portion of the electromagnetic spectrum. Using the laser fluorosensor developed by CCRS and Barringer Research Ltd., oil can be discriminated from other substances on water or ice and classified by types.

CCRS, in collaboration with the Environmental Research Institute of Michigan (ERIM), owns and operates a synthetic aperture radar. This is a four channel research radar which provides high resolution imagery in the X and L microwave bands with both like and cross receive polarizations while transmitting either vertically or horizontally polarized microwaves. The advantage of such an airborne radar unit is that it can provide all-weather detection of oil slicks.

2.1.2 International.

2.1.2.1 U.S. Coast Guard AIREYE system. In the development of an operational oil spill remote sensing system, the U.S. Coast Guard has placed considerable emphasis on the detection of illegal dumping of oil at sea, such as occurs when ships clean tanks or pump out their bilges. As a consequence, the AIREYE system includes sensors specifically designed for the identification of ships, as well as for the detection of oil spills (Edgerton et al., 1975; White and Schmidt, 1979).

The primary sensor in this system is an X-band, real aperture, side-looking airborne radar (SLAR) which permits the detection of slicks over a swath width of 48 to 80 km. This allows quick coverage of large areas. In order to fill in a narrow gap in the SLAR swath directly below the aircraft and to provide spectral information on the slick, an ultraviolet-infrared (UV-IR) line scanner is also used. This scanner has nearly identical performance to that used in the AMOP experiments. These two sensors together comprise the oil detecting part of the system.

To provide identification of a violating vessel, the USCG is developing a pointable, laser illuminated, range gated television system. This television system, since it illuminates the target by means of a laser, will operate day or night. Because it will have the capability to "zoom in" and "lock onto" the target, it will be able to read 30 cm high letters while the aircraft is flying past the ship up to 0.5 km away. In addition, a reconnaissance camera is carried in order to have a photographic record of the oil spills and ships in the area.

The significant aspect of the system, as it applies to operational spill detection, is the computerized control centre. Not only does it contain the controls for the individual sensors, it has a multipurpose television monitor on which the operator can display any of the SLAR, TV, or UV-IR line scanner images, or a computerized map of way points, targets, etc. In addition, because the system is coupled to an inertial navigation system, the position of any target indicated by the operator on the SLAR display is automatically calculated by the computer. The aircraft can then be directed to the proper location for closer inspection of a suspected violator.

The UV-IR line scanner and SLAR imagery, recorded on dry silver film, and the photographic imagery are annotated with time, latitude, and other pertinent parameters. All electronic imagery displayed on the monitor is recorded on videotape for future reference.

2.1.2.2 Swedish Coast Guard system. The Swedish Space Corporation has developed a much less expensive system for the Swedish Coast Guard. The oil detecting sensors are again a UV-IR line scanner and an X band SLAR. Both have been developed as separate systems mounted in two Cessna 337 aircraft (Backlund, 1979). The UV-IR line scanner is similar to that used in the AMOP experiment. The SLAR is a much less powerful unit than that in the USCG system, giving poorer resolution and a swath width reduced to 20 km. However, its performance is adequate for the detection of oil slicks on water. The system is complemented by two annotated 35 mm cameras, one down looking and the other pointable.

The data from each of these sensors are displayed on a TV monitor and recorded on videotape. The displays are fully annotated with pertinent navigation information. The line scanner data are processed in real time giving an enhanced image which can be photographed by a Polaroid camera and can be transmitted down to a ship in near real time by means of a radio link.

2.2 Systems Operating in Canada

There are a number of government agencies and commercial companies which offer remote sensing services in Canada. Of these only a few have systems which would be useful in an oil spill situation. These agencies/companies and the types of equipment they operate are listed in Appendix H. CCRS, whose systems are outlined in this report, has been heavily involved in the remote sensing of oil spills. The Department of National Defence (DND), Atmospheric Environment Service (AES) and the Canadian Coast Guard (CCG) have been involved in oil spill searches; the majority of these search operations have employed only visual observations as the means of oil detection.

3 RECOMMENDATIONS

3.1 Sensors

3.1.1 Laser Fluorosensor. Positive identification of oil on water, ice, or land, requires a sensor which makes measurements that are specific enough to allow discrimination between substances having similar appearances. The laser fluorosensor is the only known operational remote sensing instrument with the required special capabilities necessary for the remote detection of oil on ice and in ice-infested water; a task that is considerably more difficult than the detection of oil on open water. In ice, the diversity of naturally occurring surface conditions with the resultant variability of spectral signatures over the wide spectral range from the ultraviolet to the thermal infrared, make universal detection of oil virtually impossible by any other means. The fluorosensor measures the presence of oil, not the effect of the oil on the substrate, and hence is unhampered by variable backgrounds. Although it was not possible during the course of this project to test the fluorosensor on oil-in-ice, successful operation under these conditions can be predicted on the basis of its inherent mode of operation and its success over oil on water. The only restrictive condition applying to its use is that the oil must be present at or near the surface of the ice; or in water in sufficient concentrations to be detectable. It is expected that any surface concentration sufficient to represent a significant environmental threat will be within this detectable range. For these reasons the laser fluorosensor must be considered the prime sensor for the detection of oil spills in Canadian waters.

The present fluorosensor is a profiling instrument with a limited field of view, which restricts its areal coverage. This could be a serious limitation under circumstances where the fluorosensor is the only sensor capable of detecting even a recognizable anomaly. A programme should be undertaken to develop an imaging fluorosensor based on the technology presently available in the form of the existing instrument. It is suggested that a MEIS-like instrument offers an attractive means of imaging a fluorescent target (see Appendix A). This detector coupled to a UV laser with sufficiently high power and repetition rate may achieve the desired result. In lieu of an imaging fluorescence detector, the present fluorosensor used in conjunction with a dual channel line scanner, as described below, offers a good imaging, oil-detection sensor combination.

3.1.2 Dual Channel Line Scanner (DCLS). Under many variable circumstances, oil has been detected on the water's surface using a UV-IR dual channel line scanner. Information collected during the course of the present study indicates that, with the appropriate real time processing of the data from the two channels, a dual channel UV-IR line scanner can discriminate oil slicks from most other natural slicks. In addition, properly processed dual channel data will yield a map of an oil slick classified as to relative oil thickness. The IR channel alone can be used at night to detect and map oil slicks, although the thinnest parts of the slick cannot be detected with the IR channel. It is highly recommended, therefore, that the dual channel line scanner be included in the oil sensing package.

The dual channel scanner used in the experiments as part of this study was a Daedalus 1230 line scanner with the UV channel covering the spectral range 300-370 nm and the IR channel 8.5-12.5 µm. Data collected with a multispectral scanner indicate that one can also use the visible part of the spectrum up to 500 nm. Large atmospheric backscatter in the UV makes it desirable to replace the UV filter on the detector with a filter which passes the longer wavelength UV and violet-blue portion of the visible spectrum. It is preferable that this be a simple in-flight operation. A digital recording system for scanner data will assist in the simultaneous registration, processing and interpretation of the two channels of imagery.

The KURDISTAN accident presented the opportunity to test the dual channel line scanner in an "oil-in-ice" situation. The DCLS provided imagery in which oil was visible in both the UV and the thermal IR. It is granted that these observations were made under a particular set of circumstances with a single heavy oil type, but they represent the only reported instance of the remote detection of oil-in-ice. Results may vary under different ice conditions or for a different oil type. In addition, the signature of the oil relative to the ice is similar to that of sand or silt on ice. Thus one can expect, at most, the detection of an anomaly which will require further investigation either with a fluorosensor or with an in situ surface sample.

3.1.3 Side-looking Airborne Radar (SLAR). For a quick coverage of large areas, a side-looking radar is the best instrument to use. It has been proven by the USCG to be extremely useful in detecting small oil slicks resulting from intentional discharges in open water. Extension of its use into arctic waters, however, is somewhat doubtful. The presence of heavy ice cover (or even open pack) is almost certain to obscure the presence of oil in the radar imagery. Frazil or slush ice produces slicks that cannot be distinguished from oil slicks in radar imagery. During the Scott Inlet experiment, many slicks were observed in fair weather in the vicinity of grounded icebergs. Whatever the real cause of the slicks, they were not oil slicks, and yet they appeared as oil slick-like areas in the radar imagery. The false alarm rate in arctic waters is expected to be so high that the side-looking radar is rendered virtually useless for the detection of oil under these conditions. Nevertheless, the open water and all weather capabilities afforded by a SLAR are without equal. As such, it is recommended for inclusion in the oil detection package.

There are two commercially available SLAR's designed or modified for optimal slick detection. One is the Motorola AN/APS-94D radar as upgrated for use by the USCG. This unit will have a peak power of 200 kW to give both good resolution and slick detecting range of 24-40 km. This radar looks both to the left and right and the resultant imagery covers an 80 km swath, with a relatively small gap directly beneath the aircraft. The other radar is the L.M. Ericsson SLAR which, with only 10 kW peak power, has poorer resolution and an oil detection range of 15-20 km, but at a cost approximately one-tenth that of the Motorola radar. The type of radar chosen depends ultimately on the emphasis to be placed on search activities in open water and on other search roles if the radar is to be multipurpose.

3.1.4 Low-light-level Television (LLLTV). The RCA TC1030H filtered as tested in the AMOP experiments coupled to a television monitor and 2.5 cm videotape recorder offers a low cost yet highly effective oil detecting system. It is more discriminating than the SLAR in that it can differentiate oil slicks from wind slicks, wake scars, etc. However, it does lack the capability of the DCLS to classify different areas within a slick as to oil thickness. It can be operated in twilight, but not in darkness, as can the IRLS. Neither can it discriminate foam, slush ice, and brash ice from oil in water; all appear bright against a dark background.

The high contrast imaging of oil slicks was accomplished in the experiments by using a Corning 7-51 spectral filter and a Polaroid HNP'B polarizing filter aligned to pass horizontally polarized light, and by viewing the surface at or near Brewster's angle (53° for water). It may be possible to differentiate oil from foam, slush ice, etc., by devising a filter holding mechanism that switches quickly between horizontal and vertical polarizations synchronously with the 30 Hz picture repetition rate. If one chooses the appropriate filter densities, the oil will appear as a flashing target, the foam, slush, etc., as a constant one.

An additional modification to the system that would allow 360° viewing is the implementation of a pointable, remotely controlled gimbal mount. This would facilitate the mapping of an oil spill over a wider swath than is now possible with non-microwave sensors.

As a fixed, mounted system, the LLLTV provides a high contrast image which, because of its dynamic quality, permits the operator to follow the target across the field of view of the camera. This fact allows the operator to discriminate against temporary phenomena such as white caps. The LLLTV system, as tested in the AMOP experiments, is recommended as a highly cost effective addition to any oil spill detection package. As a pointable system, the LLLTV becomes even more powerful, although considerably more costly, and is also recommended in a more sophisticated search and mapping system.

3.1.5 **Photographic Cameras.** A system of cameras with full annotation is necessary in order to have good documentary photographs of an oil spill. Also a high resolution photograph provides the detail that is often necessary for high altitude detection of small targets, such as localized areas of oil pollution along a shoreline. While a 70 mm format camera is lighter and less expensive, a 23 cm format aerial survey camera is preferable.

The recommended camera complement would have:

1. a nadir looking camera with wide angle lens and true colour film;
2. a forward looking camera with black and white film and suitably filtered for UV detection (Wratten 18A); and
3. a hand held 35 mm format camera with true colour film for documentary use.

All cameras should have full annotation.

3.2 Analysis/Display System

The efficient application of remote sensing to the problem of searching for, mapping and tracking of, and the cleanup of oil spills demands that the on-scene coordinator have access to analyzed imagery in near real time. This is best accomplished by an on-board computer which is coupled to all the sensors and navigational systems. This computer would be programmed to process and provide the necessary integration of the data from each sensor. The operators/analysts should be able to interact with the system to produce, in near real time, and in hard copy form, imagery that has been analyzed and annotated, and maps indicating the location, extent and relative thickness of the oil. This can be accomplished using the recommended sensors coupled to television monitors and a sufficiently capable computer programmed to perform the processing and analysis as outlined below. An important component of such a system is the operator; he should be knowledgeable and experienced in both the data acquisition and in the analysis of data acquired over oil spills.

The fluorosensor, DCLS, LLLTV, and SLAR data should all be displayed on monitors simultaneously, the fluorosensor and DCLS in colour, the SLAR and LLLTV in black and white. In addition to the sensor imagery, the following annotation should be displayed on each monitor: date and/or mission identification number, time, latitude, altitude, heading and track angle. The system should be capable of recording all the data either directly from the sensors or as video imagery onto video tape recorders. In addition it should have the capability of producing hard copy of selected portions of colour imagery for two sensors simultaneously.

In order to avoid the tedious and time consuming task of transforming flight line and oil sighting coordinates from the imagery to a map, there should be an automatic track and target plotter included in the system. Such a plotter would trace, in real time on a standard map, both the aircraft track and an outline of the perimeter of the oil slick, or of a particular thickness zone within the slick. The latter operation would require that the map plotter and sensor displays be of an interactive type whereby an operator/analyst could indicate a position on the display and have the corresponding point plotted on the map. In addition to a computer this process would require an inertial navigation system and accurate altimeter, since aircraft attitude, altitude and position would be involved in the calculations.

The individual sensors produce data which, for oil detection, require specialized processing. The recommendation as to the precise process to which each data set is to be subjected is the result of a considerable amount of analysis which was performed as a part of this project.

3.2.1 Fluorosensor. The fluorosensor output consists of data from 16 spectral channels. The shape of the spectrum of the fluorescence radiation from a target is indicative of the target composition. Thus, if one compares the shapes of the measured spectra to those from known targets one can identify a fluorescent substance. This comparison can be done by calculating correlation coefficients, a procedure that has been shown in this project to give good results (see Appendix F). Calculation of correlation coefficients should be carried out by the on-board computer. An effective method for displaying the fluorosensor data involves colour coding the intensities registered in the 16 channels and displaying these as segments in vertical arrays on the monitor (see Appendix F). This can also be done for the correlation coefficients, with each column corresponding to a sample target, (e.g., heavy oil, light oil, phytoplankton), against which the current data is being compared. This will give the analyst/operator a readily visible alarm when a fluorescent target is detected and also indicate the identity of that target.

3.2.2 Dual Channel Line Scanner. As has been pointed out previously the UV-IR data properly processed will give a nearly positive identification of oil on water. The physical basis for the procedure is the spectral difference in the UV and IR radiance received from oil as compared to water. Methods have been worked out which permit the mapping and classification of an oil layer by thickness ranging from a thin, sheen producing film to an optically thick layer (see Appendix F). This process has been developed for post-flight analysis but could be implemented by the on-board computer.

In order to initiate the process, the system would be normalized over water with the particular sensor parameters of the current mission. An image of water would be recorded and the set of UV-IR intensity pairs representative of water would be determined. Then, on the basis of data that have already been analyzed, the system would establish a correspondence between certain regions in the UV-IR intensity space and the oil layer thickness. Each pair of UV-IR data values that is subsequently collected would be classified in real time as water or as a certain thickness of oil, and the corresponding pixel in the image would be colour coded accordingly. The operator can then trace out, via the interactive display, the various thickness contours on the map plotter.

One phenomenon that is often apparent, especially in the UV (or visible) scanner imagery, is a variation of intensity with across track angle. Usually this is observed as an increase in intensity toward the edges of the swath and is caused by either a higher sky radiance in that direction or by increased path radiance since the light path is longer at the edges of the swath. This change in intensity would be misinterpreted by the processor as a thin film of oil. To rectify this problem an across track normalization of the scanner data should be done at the same time as the water signature normalization. This would be repeated for every flight line but would produce an image that has uniform intensity over the water. An increase in intensity would then be properly interpreted as oil.

Further experience with oil-in-ice might permit the same type of encoding as with oil on water; although the background conditions in this case are much more variable, anomalous features would probably be apparent in the display. If the fluorosensor data were integrated with the line scanner data, these anomalies in the ice could be identified if they were in fact oil. One could colour code the centre pixel(s) in the scanner display according to the fluorescence detected by the fluorosensor. The centre pixels would provide positive identification of the visible feature in the UV-IR data because they are directly comparable with the line scanner data and correspond to the fluorosensor footprint. This system, of course, would also permit identification of oil on water.

The aspect ratio of the scanner image depends on the scan frequency and the aircraft altitude and speed. The scan frequency is generally not continuously variable and the aircraft altitudes and speed are determined by weather conditions or desired swath widths, so it is often not possible to achieve the proper image aspect ratio without some correction process. This can be done in real time simply by repeating or deleting lines from the monitor image. Another geometric distortion, termed S-bend distortion, arises in mechanically scanned imagery because the across track scan is made at constant angular velocity; hence, the instantaneous footprint travels at a variable velocity. Procedures for correcting this distortion are available and are even included as part of the instrument package with some scanners.

3.2.3 Low-light-level Television. If the LLLTV were mounted on an operator controlled gimbal system in an appropriate location on the aircraft, it would permit 360° viewing. The increased effective swath width would be limited only by altitude and visiblity conditions. This would allow the perimeter of a large oil slick to be scanned while the aircraft makes one pass over the centre of the slick. An interactive display would enhance the utility of this instrument, as it would permit the operator to transfer a trace of the perimeter of the oil slick via the computer to the plotter and onto a standard map in real time.

When the television is used as an off-nadir looking camera the picture it presents is distorted geometrically, as compared to a line scanner or nadir directed camera. This difference in perspective can prevent the operator/analyst from making a quick comparison of the television image and the line scanner image even when there is overlap in the field of view. The same problem would arise if the television were pointed to one side in order to view the area covered by the SLAR. This problem can be solved easily by applying a geometric correction directly to the television monitor image.

3.2.4 Side-looking Airborne Radar. As indicated previously the SLAR is extremely useful as a wide swath, quick survey, but non-specific slick detection instrument. The image normally requires correction for intensity variation in range, i.e., across track.

The resultant imagery can then be compared directly with the other imagery from LLLTV etc. and also with standard maps. The SLAR monitor should be an interactive type so that the operator/analyst can transfer pertinent targets from the display to the map plotter in real time.

3.2.5 Photographic Cameras. Photographic camera information should be available to the operator/analyst in order to know what photographic documentation is available on a given flight line. The annotation from the cameras, including frame numbers, should be displayed on the real time monitor so that complete information about photographic records is available.

3.3 Platforms

The following discussion is limited to aircraft since a satellite borne package implementing all the capabilities of the recommended sensor package is not expected to be developed before 1990. Satellite operations using optical sensors are also plagued by cloud cover, which is often prevalent in Canada's coastal and arctic regions and, especially, at the time and location of shipping accidents. In any event, satellites used for oil pollution experiments must always be supported by aircraft carrying a sophisticated sensor package.

The main thrust of the present study is to determine the oil detection capabilities of the various sensors, and once determined, to recommend an integrated package that best applies these to the desired end. The recommendations, therefore, concentrate on the sensor, processing and displays systems. The aircraft recommendations are best made by experts in that field. Outlined here are simply the weight and electrical power requirements imposed by the detection package and the major considerations in making the choice of aircraft.

The weight and power consumption of the individual sensors, with supporting instrumentation, but without the real time processors, are contained in Appendix A. The total weight and power requirements of the package including the processing and display systems are estimated to be 1 150 kg and 8 kW. Operation of the system would require approximately four persons which, with the pilot, copilot and possible engineer, bring the weight up to 1 850 kg. Once these requirements have been met, the major concerns are quick response and long range, with special emphasis on the latter for northern flights.

An analysis of aircraft requirements for an oil spill search was made for the KURDISTAN report (O'Neil et al., 1982). It was pointed out there that the search area expands as the square of the time between the spill and the arrival on the scene. Therefore, it is important to have an aircraft that can be mobilized quickly and can reach the target in a minimum time. This requires that the sensor package be either fitted permanently in the aircraft or that it be capable of being installed with little delay. It also requires an aircraft with a fast cruising speed, especially if it is to be shared with other tasks. The initial response should not be impeded by poor weather conditions between the aircraft's main base and the target area; this requires an aircraft that can operate at or above 5 500 m.

The range requirements are affected by the on target speed, the transit speed, and the distance from the target to the nearest usable air base. The effective "on target speed", averaged over a complete search and refueling cycle should be maximized. That is, maximize:

$$v_{eff} = \frac{v_s T_{search}}{T_{total}} \tag{1}$$

where:
v_{eff} = effective speed
v_s = search speed
T_{search} = search endurance time
T_{total} = total time

$$T_{total} = T_{search} + 2T_{transit} + T_{refuel}, \tag{2}$$

where:
T_{refuel} = refueling time
$T_{transit}$ = transit time (one way)

$$T_{transit} = \frac{D_{transit}}{v_t} \tag{3}$$

where: $D_{transit}$ = transit distance

v_t = transit speed

$$T_{search} = \frac{1}{r_s}(F - 2r_t \cdot T_{transit}) \tag{4}$$

where: r_s = fuel consumption rate at search speed and altitude

r_t = fuel consumption rate at transit speed and altitude

F = total usable fuel load, allowing for sufficient fuel to reach an alternate.

Combining expressions (1) through (4) one obtains:

$$v_{eff} = \frac{\frac{v_s}{r_s}\left(F - 2r_t \frac{D_{transit}}{v_t}\right)}{\frac{F}{r_s} + 2\left(\frac{r_s - r_t}{r_s}\right)\frac{D_{transit}}{v_t} + T_{refuel}} \tag{5}$$

The refueling time T_{refuel} and local transit distance $D_{transit}$ must be estimated, the former depending upon the aircraft in question and the refueling facilities available; the latter depending upon the spacing of airstrips suitable for the particular aircraft in the region to be covered. For operations in the Canadian arctic, one requires an aircraft either with a very long range, or with short take off and landing capabilities on gravel airstrips, because there are very few paved runways.

3.4 Future Research Programs

In the present study, it was shown what results can be expected from the various remote sensing systems when they are brought to bear, more or less independently, on an oil slick. To do this, the state-of-the-art was assessed and an approach was synthesized from the information available in the literature; from identified Canadian requirements seen in the context of the Arctic Marine Oilspill Program; and from the tentative ideas of experts in the field of remote sensing. The findings of other investigations have been verified and clarified in many cases. The state-of-the-art has itself been advanced in several areas but most notably in proving the laser fluorosensor. The analytical techniques applied to the reduction and enhancement of the data have been extended particularly in the methods for handling imagery from line scanners. As a result it has been possible to recommend the most useful and cost effective sensor package for the Canadian situation.

It was not possible to carry out as thorough a study as had been hoped in this program, of the remote sensing techniques applicable to the detection of oil in ice-infested waters. There has been insufficient research on the topic to support conclusions valid over the wide variety of conditions encountered in the arctic. More experience is needed in the remote sensing of oil in ice-infested waters to prove sensors; develop analytic techniques; and to determine conditions under which successful remote sensing missions can be performed.

Whatever research programs are carried out, there will be a need for test oil spills which can be used for remote sensing. During the first tests of a sensor system under a given set of conditions, care must be taken that adequate surface measurements are made to verify the specific parameters being sensed. As experience is gained with the sensor, the need for surface measurements diminishes and the data from one sensor can provide certain information essential to the interpretation of data from another. The ultimate goal remains: to develop an integrated remote sensing package in which the data from the various systems contributes to the overall consistent interpretation of what is happening on and in the sea.

3.4.1 Sensor Development. The sensors used in the present study were often flexible research systems in no way optimized for oil pollution surveillance. Several of the sensors were prototypes which could only demonstrate the principles involved in the detection of oil or determine the feasibility of the technique. In general, the future development of individual sensor systems must concentrate on reducing the amount of data to be acquired (that is, tailoring the sensor for the mission, and making the data available in real time in an easily interpreted form).

Undoubtedly, the users will demand the best possible signal-to-noise ratio in the data; however, many trade-offs will be made in sensor performance before the optimum operational system is realized.

Looking ahead to the time when such systems will be used in routine missions, operator interactions with the sensors will be simplified and, as in any sensor improvement exercise, the designer will be attempting to reduce the complexity of the hardware, improving the reliability and maintainability, while minimizing the weight, volume and power consumption.

The laser fluorosensor, though demonstrated to have adequate performance, is still a rather new instrument and could benefit from further optimization for its role in the detection of oil.

Future research and development on fluorosensor techniques should include the replacement of the nitrogen laser (337 nm) by an eximer laser (220-308 nm) and the change from a profiling to an imaging sensor. The use of the shorter wavelengths would improve the sensitivity to thin oil films tenfold (Rayner, 1979); it would also allow the use of the "structure" present in fluorescence spectra in the range 300-400 nm for more precise discrimination of oil types. The advantages of an imaging fluorosensor, although partially provided by the fluorosensor-DCLS combination, are obvious: wider swath width, quicker and more complete coverage of a given area, and the presentation of an image whose geometrical features can aid in interpretation.

The laser fluorosensor is the only sensor which can probe the water column; thus, a fluorosensor should be able to detect dissolved fractions of the oil and sunken masses of oil lying, neutrally bouyant, just below the surface even though an oil slick is not apparent. Studies should be undertaken to assess the potential of the laser fluorosensor against such targets: a derivative of the present system could be built to further exploit this capability.

The fluorosensor may also be useful in monitoring the distribution and effectiveness of aerially applied dispersants. Any new application of the laser fluorosensor or any change in the spectroscopic characteristics of the laser fluorosensor (number and width of receiver channels, excitation wavelength) should be supported by a laboratory program. As the fluorosensor is flown over a wider variety of targets, the laboratory backup will help explain the response of the sensor to each new set of conditions.

In the immediate future, a significant effort should be made to develop an effective real time display for the dual channel line scanner incorporating the enhancement algorithms demonstrated as part of the current project.

Pushbroom scanners such as the MEIS system flown during the Scott Inlet and Wallops Island missions are under active development. These sensors have no moving parts (an important consideration in airborne and satellite applications) and can be much more sensitive than the MSS. An additional benefit of the pushbroom scanner is the ease with which the most useful spectral bands may be selected. With a good understanding of the spectral characteristics of oil on the sea, it may be possible to exploit this sensitivity to create a highly selective oil imaging sensor.

Side-looking radars have undergone a great deal of development by the military. As a result, the capability and sophistication of this sensor exceeds the requirements for oil pollution detection roles. It is necessary to determine the optimum tradeoff between cost and performance before a suitable side-looking radar system can be built. Not only must the radar be able to detect and map oil slicks but it must be integrated with the rest of the airborne oil pollution package to produce annotated imagery in real time. With such a data product, search patterns can be modified in flight to investigate anomalies, and large-scale maps of the pollution target can be made available almost immediately for use by the on-scene coordinator. In future experiments involving oil spills, in open water, an attempt should be made to cover many more wind and sea conditions including different look directions relative to the wind. During small test oil spills, care must also be taken for all microwave sensors that the size of the slick exceeds the footprint or pixel dimensions of the sensors.

If it is decided that it is important to measure oil film thicknesses in the range of 0.1 to 10 mm, then a passive microwave radiometer should be developed. As suggested in Section 4.5.1 a profiling system integrated with the thermal infrared channel of a line scanner could be a cost effective approach. The response of a microware radiometer to emulsified oil has not been reported.

The passive television system was shown to be a very inexpensive sensor for the mapping of oil slicks in daylight; it is however, unsuitable for reading the names on ships. An airborne surveillance system tasked with identifying vessels under unfavourable lighting conditions (haze, light snow or rain) must be equipped with an active gated television system (AGTV). Such systems are costly because they contain very complex electro-mechanical subsystems for pointing the camera, and complex electro-optical subsystems containing the pulsed laser illuminator and the range gated receiver.

Although photography is a well developed technology it is still necessary to find a reliable camera system which operates well at low temperatures. The precise image format chosen is dependent on the desired resolution, the weight of the overall camera system, and ease with which the camera can be modified to annotate the image at the time of exposure. Compact flash systems suitable for nighttime aerial photography should be investigated as they become available.

Before any airborne oil pollution surveillance system becomes operational, a significant effort must be made to integrate data from all the sensors in the aircraft. The data should be presented to the sensor operators so that a fairly accurate assessment of the situation can be made while in the air. In the simplest case, overlays of one sensor's data on another's can be displayed; however, as experience is gained and confidence develops in the processing algorithms, a single display could contain a synthesis of all the data collected.

Accurate navigation data are required to annotate displays. It is important, therefore, that the aircraft be equipped with a sophisticated method for updating and correcting navigation data prior to the annotation of sensor data. During sorties in which a regular search is being carried out, real time plotting of the flight lines flown would be valuable. The navigation data handling system would also provide updated way points (positions at which course changes are to be made) to the pilots, thereby ensuring that the entire area is covered to the satisfaction of the mission manager.

Provision to down link the remotely sensed data should also be considered. A down link would be useful during countermeasures operations in which it is necessary, for example, to provide the on-scene coordinator with the current location of the thickest regions of the slick relative to the skimmers and recovery vessels. The distance over which the link is to operate and the speed at which the imagery (or other data) is transmitted are important tradeoffs in the design of a system. If the interpreter, with assistance from a sophisticated display system, can reduce the data to a contour map of relative oil thickness with the location of ships, buoys, and coastal features plotted, the complexity of the down link is significantly reduced.

A system for producing a permanent record of the imagery integrated with data from other resources should be included as part of the airborne system. If required, the airborne system could be complemented by a more sophisticated ground system deployable to the operational base of the aircraft which could carry out the more complex manipulations of the data yielding high quality imagery as a final product. The on-scene coordinator will undoubtedly demand the imagery for a rapid situation assessment. The legal requirements associated with the prosecution of illegal dumping incidents can be documented only with hard copies of imagery and maps.

3.4.2 Analytic Techniques. To present, the data from sensors have been reduced and interpreted more or less independently from those provided by other sensors. This is because of the mixture of profiling and imaging sensors, differences in fields of view and the inability to handle large quantities of data in real time. Oil spills have seldom been observed with several sensors simultaneously; thus, there have been few realistic data with which to develop suitable manipulative techniques.

Computer technology now makes it possible to consider processing these data in real time on board the aircraft and presenting it to an interpreter. The major emphasis, however, must be in the development of algorithms and analytical techniques which manipulate the data prior to their display. The overall goal is to integrate the data originating from the various sensors and to provide both qualitative and quantitative imagery (perhaps in the form of annotated and contoured maps) to the mission manager and ultimately to the on-scene coordinator.

The laser fluorosensor, as the single sensor capable of identifying and classifying oil, will play a key role in the interpretation of imagery from other sensors. In the simplest form of integration, the time history of the fluorescence return in a characteristic fluorescence channel could be used as an overlay on the imagery from the LLLTV or MSS. A more sophisticated overlay would use the correlation techniques as a means of identifying oil. A study in progress indicates that the correlation technique should be able to classify the oil correctly better than 80% of the time. This promises to provide the means whereby the centre pixels of an image may be identified as being water, heavy residual, light refined, or crude oil. The correlation algorithm can be incorporated into the fluorosensor data processor (FDF-80) which acquires and displays the data in real time on board the aircraft. Other facets of the correlation technique need to be explored; of these, the most important is the ability of the technique to discriminate against other substances which may occur as part of the normal ocean background. While it may be assumed that the technique will be satisfactory, it is difficult to prove. Sample collection and laboratory analysis is a feasible technique for discrete oil samples; however, for the water conditions and areas which should be investigated, an airborne pilot project as suggested in Section 3.4.3 may be the only way to obtain sufficient data.

The interpretation of imagery from the UV/IRLS was found to be much easier when data from the two channels were handled simultaneously. In the simplest case, the contrast stretched imagery from the IR and UV channels would be overlaid. A more sophisticated procedure might include a clustering type of analysis which could provide qualitative thickness estimates. In any imagery there should be as little ambiguity as possible between oil and other features in the scene. Ideally any system should display an image with as little human intervention as possible. In all, it is a non-trivial problem to develop the necessary algorithms (or ascertain acceptable shortcuts) which will work in a real time airborne environment. As mentioned above, the integration of imagery from the UV/IRLS with data from other imaging and profiling sensors will be necessary to create the required displays; the algorithms for such an integration do not exist.

In an operational airborne oil pollution system a side-looking radar (SLR) system will always be used as an anomaly detector searching a wide swath to either side of the aircraft. The efficiency of a sensor operating in such a mode will be improved as the false alarm rate decreases. Using the radar backscatter signatures and the geometric shape of the anomaly, an experienced operator should be able to discriminate fairly well between ships, icebergs, land targets, wind and current induced features and oil slicks. There are no other sensors which cover the same area as the radar; thus the operator will be required to call upon his own experience, his knowledge of the radar performance against the potential targets under the prevailing conditions, and auxillary data bases. Auxillary data bases could be map overlays of coastlines; shipping lanes; iceberg probabilities; ocean currents; and estimated vessel positions from the Vessel Traffic Management Centres.

Before a remote sensing system could be operational, and particularly before the data were to be presented routinely in courts of law, a set of interpretation keys would have to be developed. These keys would lay out the steps for the interpretation of the data from each sensor, but more importantly, how to arrive at a consistent interpretation of the data from the entire sensor package considered as a whole. The keys would be matched to the performance of the individual sensors, reflecting their capabilities and limitations under the wide variety of conditions that might be encountered. Before an interpretation key becomes widely used, it would have to reflect the experience of many oil pollution surveillance missions and an understanding of the legal arguments it might be called upon to support.

3.4.3 Pilot Projects. In most parts of the world it is extremely difficult to lay out test oil spills because of concern for the potential environmental hazards. For certain types of research one can make use of small confined spills; however, for remote sensing experiments large unconfined spills are a more realistic test of the sensor and the interpretation. Without realistic test targets, proving of an oil pollution surveillance system will take place slowly. This will postpone the day when such detection and tracking systems may be used with confidence in an operational role. It would seem that the only way to obtain sufficient expertise in the remote sensing of oil spills is to carry out some sort of operational pilot study, in which a large number of accidental oil spills are observed under a wide variety of sea and atmospheric conditions.

The objective of a pilot project would be threefold:

- to provide sufficient data that the performance of the sensors and interpretation techniques can be verified and improved using realistic conditions;
- to determine the magnitude of the accidental oil spill problem and the cost effectiveness of remote sensing techniques by carrying out frequent routine surveillance of a large area; and
- to accustom users (such as the on-scene coordinator) to the use of remotely sensed data for the detection and management of oil spills, thereby introducing remote sensing techniques to routine operations.

It is proposed that a suitable aircraft be equipped with the recommended sensor package (SLR, UV/IRLS, LLLTV, laser fluorosensor, cameras, real time displays, navigation and data recording equipment) and flown in a series of routine patrols. Ideally the patrol would be flown daily throughout several seasons to obtain adequate experience under a wide variety of conditions. In this way the aircraft, the sensors, data reduction and the analysis would be tested in an operational environment. This is to say that the aircraft would be tasked by the Canadian Coast Guard; any spills, shipping, or other targets of interest would be reported to their operational headquarters. Few data would be examined in detail other than the anomalies, thus the data reduction and interpretation would proceed in nearly real time. A small fraction of the data with targets of special interest or unusual conditions could, nevertheless, be set aside for additional analysis.

This datum set would be used either as examples for compilation of interpretation keys or as sources of additional information on sensor performance. Information from each sortie would be accumulated for use in the study of the cost effectiveness of the individual sensors and the overall system. Were an aircraft engaged in such a pilot study, it would also be able to respond to oil spill emergencies with the optimum sensor package. The remote sensing mission should proceed smoothly because the aircraft, as one information source among the many accessible to the on-scene coordinator, would be partially integrated into Coast Guard operations. In particular tasking procedures would be set up for the aircraft (air traffic clearances, fuel, etc.), communications with the on-scene coordinator would be established, and a satisfactory means of presenting him with timely reports and situation maps would be available.

An operational facility could participate in international test oil spills to compare the system as implemented with systems developed by other nations. Not only would the participants familiarize themselves with the actual data acquired on the various systems (data are exchanged for the prosecution of vessels found discharging oil) but new sensors, operating and analytical techniques would be compared directly under the same conditions.

Many of the systems used for oil pollution surveillance are similar or identical to those used in other ocean surveillance missions. Having an aircraft configured to carry out an oil pollution surveillance pilot project would provide an excellent opportunity to demonstrate the use of advanced remote sensing techniques in such roles as search and rescue, fisheries and coastal surveillance, vessel traffic management and ice patrol. Special systems could be added if necessary, allowing the overall package to perform even more effectively in the specific role.

4 PRESENT STUDY: THE AMOP REMOTE SENSING PROJECT

4.1 Detectable Effects

4.1.1 Suppression of Capillary Waves. An oil film on the water's surface calms the water thereby producing a 'slick'. The calming is caused by two mechanisms (Pronk, 1975; van Kuilenburg, 1975): the formation of capillary waves is suppressed by the oil film which acts as a membrane between wind and water; and the propagation of larger waves (up to 10 m wavelengths) is mechanically damped by thicker oil layers (in the mm range). Since the long waves gain their energy from the wind via the capillary waves, and because the oil slick prevents the formation of the latter by reducing the wind to water coupling, even a thin film can halt the development of long waves. The damping action of externally formed waves which propagate into the slick results from the dissipation of mechanical energy within the thicker oil layers. The rate at which this dissipation occurs is proportional to the viscosity of the oil and to the thickness of the layer.

Slicks, however, result from causes other than the presence of oil; internal waves, freshwater "streams" on the seawater surface, ships wake "scars", frazil or grease ice, are only a few.

4.1.1.1 Slick detection. Slicks are visible to light sensors; however, the contrast resulting simply from the wave suppression is generally low and variable, depending on the lighting conditions. There is one situation in which a slick appears as a high contrast feature in the visible. If the slick is viewed within the sun's glitter pattern at an angle such that the sun is reflected by the high wave slopes of the capillary waves but not by the lesser wave slopes within the slick regions, the slick will appear dark against a bright background. This technique is used in slick detection with satellite borne sensors (Deutsch et al., 1977). Such a method, however, can be used only within certain narrow time frames and with clear skies.

It is in the application of microwave sensors that this effect is important. Passive microwave radiometers can observe a small reduction in the apparent brightness temperature caused by the wave suppression; however, the primary interest is the reduction of backscatter to active microwave devices. The electromagnetic energy emitted as microwaves by radar and microwave scatterometers is reflected from the water's surface. If the water's surface appears rough on a scale determined by the wavelength of the electromagnetic wave, a portion of this reflected energy will be returned to the sensor, appearing, in radar nomenclature, as "sea clutter". When the sea surface is smooth, as in a slick, there is little return and such an area will appear dark in the resultant imagery. The fact that the presence of the oil film affects primarily the short wavelength capillary waves, as opposed to longer wavelengths, is a determining factor in the relative performance of the different microwave wavelengths. What appears rough, and hence bright, to a high frequency (short wavelength) sensor may appear smooth, and hence dark, to a lower frequency (longer wavelength) device.

4.1.1.2 **Sensors.** The active microwave instruments involved in the present study are the CCRS-Ryan scatterometer and the ERIM synthetic aperture radar (SAR); both are installed on the CCRS Convair 580 (C-GRSC) (see Appendix A).

The scatterometer is a Ku band (13.3 GHz) profiling instrument that measures microwave scattering cross sections as a function of incidence angle across the range of +60° to -60°. It operates in either horizontal (H) or vertical (V) polarization transmit mode; both like and cross polarizations are received simultaneously for each transmit mode. The SAR operates in both X(9.350 GHz) and L(1.315 GHz) bands with H or V transmit polorization and both like and cross receive modes. It has a slant range of 5.6 km which, for the depression angles used over the test oil spills in the Wallops Island mission, gives a ground range or swath width of approximately 8 km.

4.1.2 Effects on the Surface Reflectance of Visible and Near Visible Light.

4.1.2.1 **Oil on water.** An oil layer increases the surface reflectance in the ultraviolet, visible, and near infrared spectral region. This is a direct result of the greater indices of refraction for oils as compared to that of water. This difference is greater in the ultraviolet region than in the visible; thus, it would appear that one need only view the target in the ultraviolet region to obtain the highest contrast image. Although this is the case in certain circumstances, the general situation is complicated by a number of factors.

In addition to the surface reflected light, the total radiance received by a sensor in this spectral region consists of a volume reflected component, which is light scattered from within the volume of the water, and a path radiance component scattered by the intervening atmosphere into the field of view of the sensor. The component carrying the most information as to the oil's presence is the surface reflected radiation; the other components often act to mask this information. In determining how best to accentuate the surface reflected component, and thereby enhance the oil to water contrast, it is necessary to know the nature of each component and the processes involved in its production. The properties of interest in this exercise are the relative magnitudes of the three components, their spectral characteristics, and their polarization properties. The factors involved in their formation are: the actual physical processes involved, reflection, absorption, or scattering; the medium, air, water, or oil; and the source of the radiation, sun, sky or clouds. Important also in determining the final apparent oil to water contrast is the performance of the sensor used to make the observation. In the following discussion, the situation existing for water will be outlined first and then the effect of the oil's presence on the received radiation will be presented.

The spectral nature of the water surface reflected light is generally the same as that of the source; thus, the spectrum of this component will be high at the blue end of the spectrum for clear skies and flatter for overcast skies. The volume reflected radiation will have a spectrum that peaks in the blue or green, the absorptance of water being least in the blue for pure water, shifting towards the green as phytoplankton and 'gelbstoff' concentrations increase. Silt content causes an increase in the overall magnitude of the volume reflected component and can produce a spectral shift towards the red if concentrations are high enough. The spectral nature of this component is not significantly affected by cloud cover because it consists of scattered sun and sky light. Path radiance for clear air is concentrated at the short wavelength end of the spectrum since it obeys the Rayleigh λ^{-4} (λ = wavelength) scattering law. Aerosol content will increase the magnitude and produce a flatter spectrum. Since the source of this component is global radiation, i.e. sun and sky light, its spectrum does not depend significantly on cloud conditions.

The polarization properties are important because the differences between the various radiation components allow enhancement of one over the other by means of a linear polarizer. Radiation reflected from a smooth, flat, water surface at 53° from the vertical (Brewster's angle for water) is 100% linearly polarized perpendicular to the plane of incidence and parallel to the water's surface. This perpendicularly polarized component is also referred to as the horizontal component. As the angle of incidence deviates from 53°, the degree of polarization falls off to 80% at 65° and 41°. Under most naturally occurring conditions the water's surface is not flat but has waves on it. These reduce the polarization but not usually to less than 92% when looking at 53°.

At the same time, the radiation from a clear sky is in general polarized, the degree and direction of the polarization depending on the viewing direction relative to the sun. If, as is normally done to avoid sun glitter, the sensor's azimuth angle is adjusted so that it is pointing away from the sun, then, the clear sky radiation will be horizontally polarized. The degree of polarization varies with sun elevation and sensor viewing angle and is, in general, diminished by increased aerosol concentration. If the sensor viewing angle is chosen to be 53° from vertical and the sun's elevation is between 20° and 70°, as it would be for most operations at Canadian latitudes, then the degree of horizontal polarization can vary from 20 to 50%. The scattering process gives rise to the clear sky radiance, and the surface reflection contributes to the horizontal polarization of the surface reflected component of the total radiation. In contrast to the clear sky case, the light scattered by an overcast sky will not be polarized to any significant degree.

The water volume reflected radiation, for viewing at an angle of 53° from the vertical and away from the sun with sun elevations between 20° and 70°, is usually polarized in the orthogonal direction, i.e., parallel to the plane of incidence and hence with a vertical component. The electric vector in this case is not strictly vertical; in fact it makes an angle of 37° with respect to the 'vertical' component. The degree of polarization again depends on water clarity but could not be expected to exceed 12%.

The path radiance, which results from the same process as sky radiance, is likewise horizontally polarized. However, because the angle between the viewing direction and that of the sun's radiation is smaller for the above angles, the resulting scattered light is less polarized, being usually less than 10%.

Thus, one can accentuate the surface reflected component by placing a horizontally aligned polarizer before the detector and operating at, or near, the Brewster angle. This would eliminate very little (no more than 5%) of the surface component while blocking up to 56% of the volume component and at least 45% of the path radiance. In addition to the polarization sensitive absorption, there is a non-discriminating absorption by film polarizers; this, of course, reduces the intensity of all three radiation components proportionally.

The optical effects of the presence of oil on water depend on its complex index of refraction. From it one can calculate, using Fresnel's equations, the reflection coefficient as a function of angle and the oil's absorptive properties. There is generally a greater variation in these properties for oil than for water in the visible and near visible regions of the spectrum. Both the reflectivity and absorptivity of oil are higher than for water and both increase markedly in the near UV (Horvath et al., 1970; Rayner, 1979). The surface reflected component from oil, therefore, will be larger than from water and the difference increases with shorter wavelengths. Calculations based on measurements made on representative crude oils (Horvath et al., 1970) indicate that oil's surface reflectance is higher than water's by factors of 2.1 at 400 nm and 1.6 at 1200 nm. At the same time an oil layer on the water surface will absorb radiation emerging from the water volume and will do so preferentially at the shorter wavelengths. Whether the volume component will be decreased or increased will depend, however, on the scattering properties of the oil versus that of the water. Highly emulsified oil contains many scattering centres and because of this appears brighter than water. This effect combined with the preferential absorption of the blue light gives rise to the 'chocolate mousse' colour that is commonly observed.

The addition of the oil layer onto the water's surface will not have a substantial effect on the polarization properties of the surface and volume reflected radiation. The Brewster angle is larger (55 to 57°) depending on wavelength because the index of refraction for oil is greater than for water. The angular range over which the degree of polarization is greater than 80% is 44-68°, giving a large overlap with the corresponding range for water. Any effect on the polarization of the volume reflected radiance will probably be small and variable, depending on the emulsification state and absorptivity of the oil.

The key to the enhancement of the oil to water contrast is the selection of the appropriate spectral region(s) and polarization mode. The foregoing discussion indicates that the surface reflected component to background ratio can be increased by a factor of two by employing a horizontally aligned linear polarizer. The choice of spectral region depends on the detector capabilities in addition to the oil and water reflectance properties. If the detector is sufficiently sensitive in the near UV, then, filtering it to detect only this region will accentuate the surface contrast. High altitude observations, however, will suffer from high path radiance at these short wavelengths; in this case a somewhat longer wavelength may be preferable. In the red region of the spectrum, although the surface contrast will be lower, both the path radiance and the volume reflection will be much smaller. A clear sky, however, has low radiance values at these longer wavelengths and the corresponding sensor sensitivity must, therefore, be high. An overcast sky, having a flatter spectrum, will increase the sky (cloud) radiance available in the red region.

The preceding enhancement procedure would be used to accentuate the surface reflected radiation. One can, however, detect the presence of the oil, if the layer is sufficiently thick, by observing its effect on the volume reflectance. The resulting signature would be highly variable, darker than water for a highly absorptive, non-emulsified oil, brighter than water for an emulsified oil. For such an observation, one would either rotate the polarizer through 90° to exclude the surface component, or remove it altogether to permit both polarizations through. The choice of spectral range would depend on the absorptivity and emulsification state of the oil.

The relative magnitudes of the three radiance components calculated for a particular set of conditions are plotted as a function of wavelength in Figures 1 through 8. The calculations, based on data contained in Millard and Arvesen (1971), Henderson (1970), Horvath et al. (1970), Cox and Munk (1954) and Neville and Gower (1977), assume a sun elevation of 20°, a 45° look angle, an altitude of 300 m and a wind speed of 3.3 m/s, and are made for combinations of clear or overcast sky, parallel or perpendicular polarizations, and an oil or water surface. In these calculations the oil layer is assumed to be very thin, affecting only the surface reflectance.

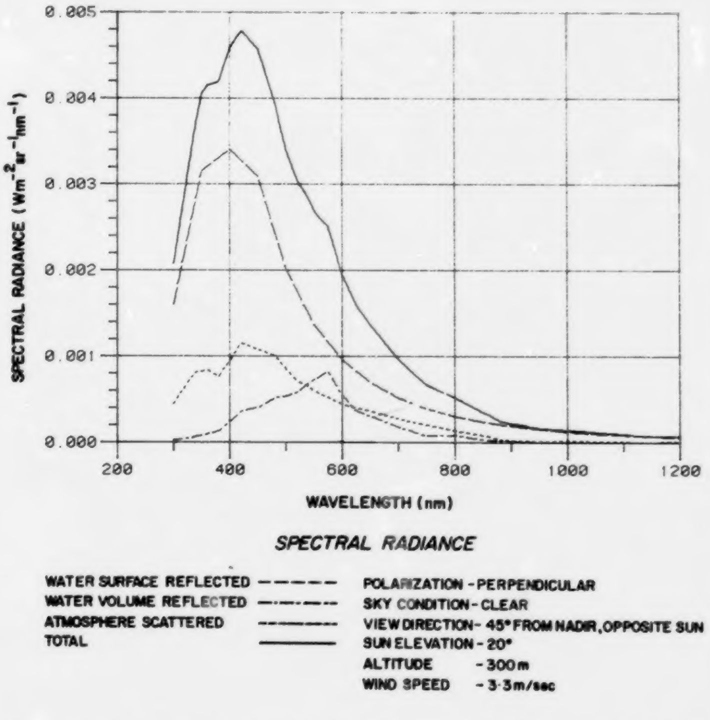

FIGURE 1 PERPENDICULAR COMPONENT; SPECTRAL RADIANCE OVER THE SEA, CALCULATED FOR CLEAN WATER SURFACE AND CLEAR SKY.

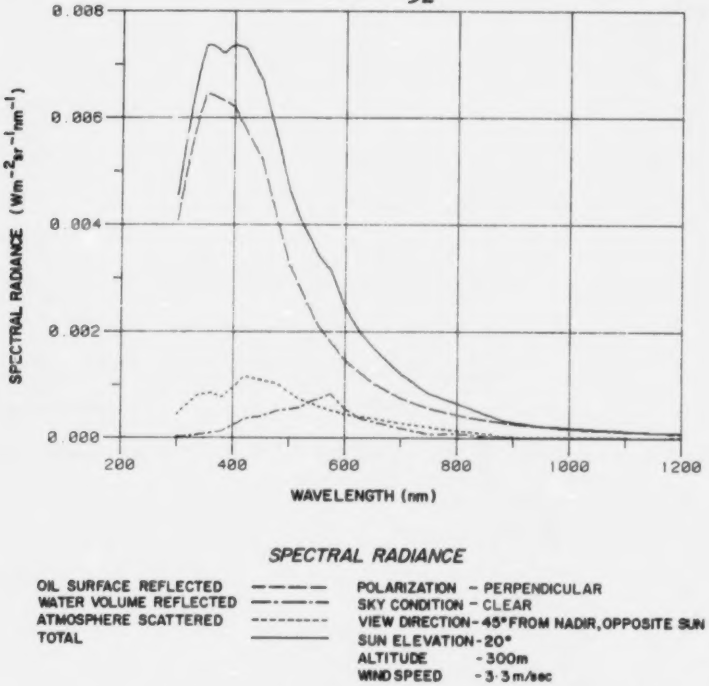

FIGURE 2 PERPENDICULAR COMPONENT; SPECTRAL RADIANCE OVER THE SEA, CALCULATED FOR AN OILED SURFACE AND CLEAR SKY.

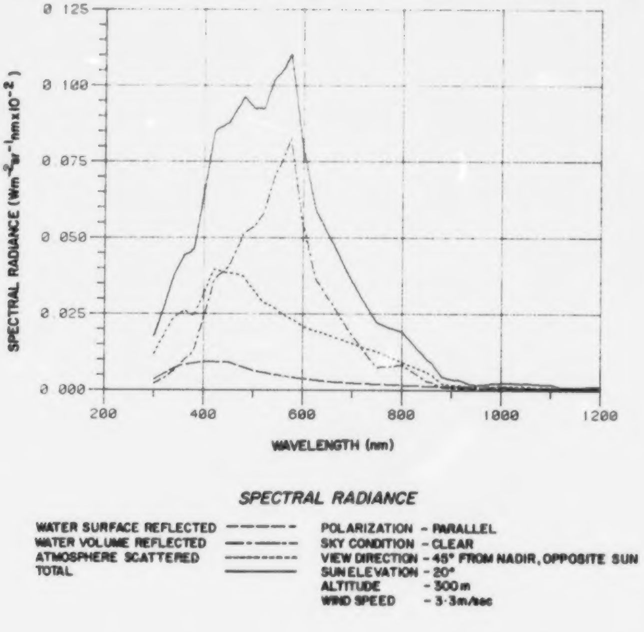

FIGURE 3 PARALLEL COMPONENT; SPECTRAL RADIANCE OVER THE SEA, CALCULATED FOR CLEAN WATER SURFACE AND CLEAR SKY.

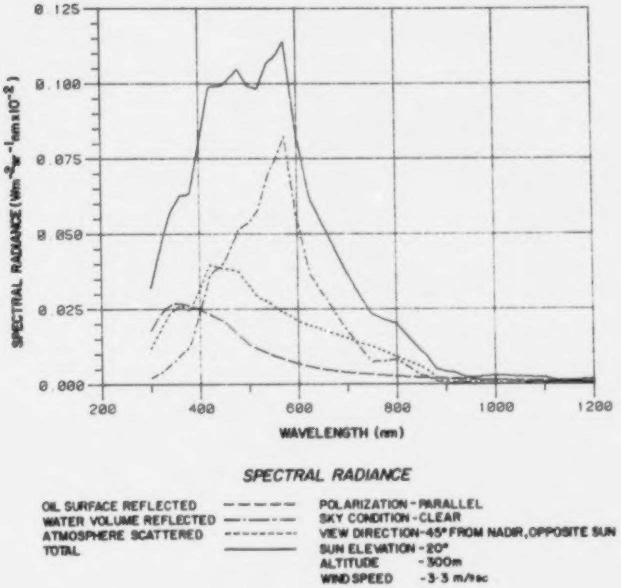

FIGURE 4 PARALLEL COMPONENT; SPECTRAL RADIANCE OVER THE SEA, CALCULATED FOR AN OILED WATER SURFACE AND CLEAR SKY.

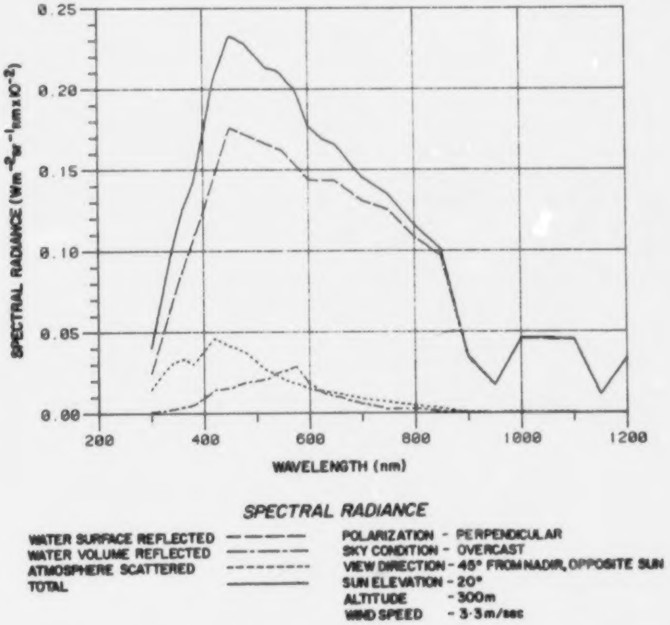

FIGURE 5 PERPENDICULAR COMPONENT; SPECTRAL RADIANCE OVER THE SEA, CALCULATED FOR CLEAN WATER SURFACE AND OVERCAST SKY.

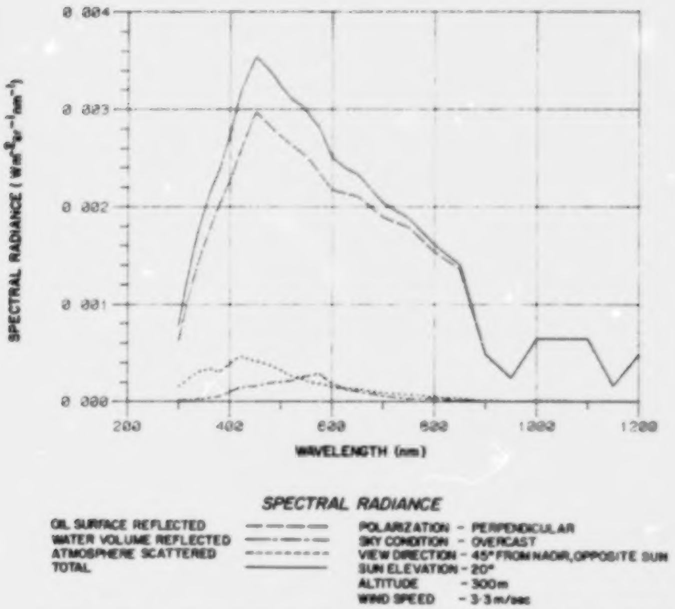

FIGURE 6 PERPENDICULAR COMPONENT; SPECTRAL RADIANCE OVER THE SEA, CALCULATED FOR OILED WATER SURFACE AND OVERCAST SKY.

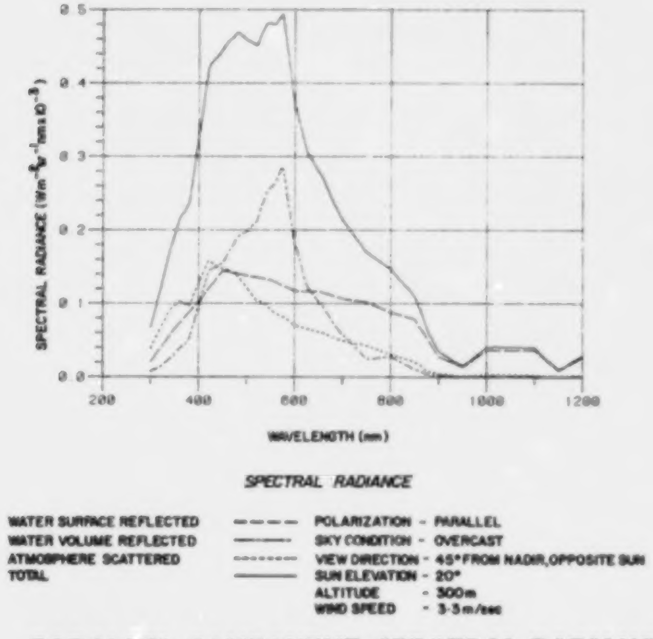

FIGURE 7 PARALLEL COMPONENT; SPECTRAL RADIANCE OVER THE SEA, CALCULATED FOR CLEAN WATER SURFACE AND OVERCAST SKY.

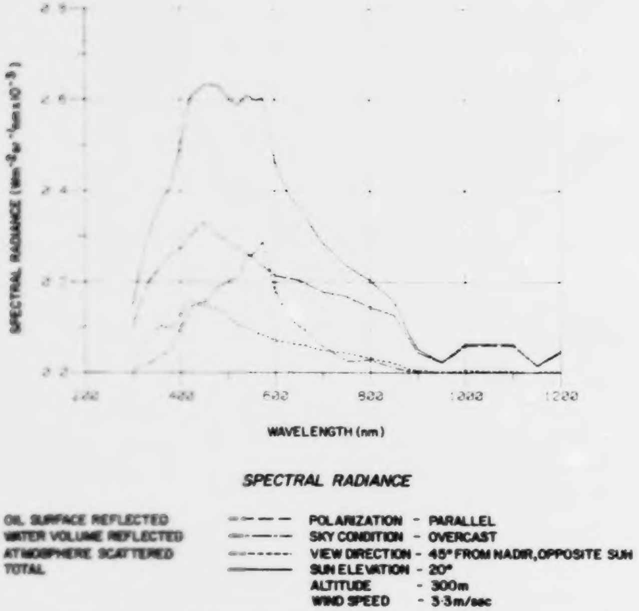

FIGURE 8 PARALLEL COMPONENT; SPECTRAL RADIANCE OVER THE SEA, CALCULATED FOR OILED WATER SURFACE AND OVERCAST SKY.

4.1.2.2 **Oil on ice.** The appearance of oil on ice will depend both on the ice conditions and on the properties of the oil. It is not possible to predict what effect the oil will have without knowing the ice conditions and properties of the oil because of the wide range in both these sets of variables.

If the oil is on or mixed into the upper surface of ice of a type that normally appears bright in the visible, then one can expect the oil to look dark; the degree depending on the absorptivity and the thickness of the oil. Since oil is more absorptive in the ultraviolet, this effect should be most pronounced in that spectral region. However, water and ice mixtures will also appear dark. Some other spectral range must be used to differentiate the oil-ice and water-ice mixture.

If the oil is on the surface of melt pools on top of the ice, the net effect of the oil will depend on the depth of the water, the reflectivity of the water-ice interface, and the absorptivity and thickness of the oil layer. One can expect the oil to increase the surface reflectance, but it is doubtful that this increase is sufficient to be observable against a large and variable background of subsurface ice. One can expect a highly absorbing oil to decrease the volume reflected component. Again, however, the variable nature of the background may mask this effect. In general, while the oil can be expected to produce a visible feature in the imagery, it is unlikely that measurements in the UV-visible-near IR range alone will serve to distinguish the oil from the already highly varying water-ice background.

4.1.2.3 **Sensors.** A number of sensors were operated in the near UV-visible-near IR spectral region. These include a UV line scanner (the UV channel of the DCLS), a multiple detector electro-optical imaging scanner (MEIS), a multispectral scanner (MSS), a low-light-level television (LLLTV), a four channel photometer (MPPH), a 500 channel spectrometer (OMA), 70 mm Vinten cameras and a Wild Heerbrugg RC-10 camera (see Appendix A). The mechanical scanners, DCLS-UV and MSS, together image the wavelength range from 300 to 1100 nm providing calibrated radiance measurements in a number of spectral bands. These scanners were not fitted with polarizers, because of the nature of the operation. Neither were MPPH and OMA, both profiling instruments which, in addition to measuring the radiance from the sea surface, make downwelling radiance measurements from which reflectances can be calculated. The LLLTV and MEIS were fitted with polarizers and spectral filters chosen to accentuate the oil on water. The LLLTV was filtered with a Corning 7-51 spectral filter and a Polaroid HNP'B polarizer. The former passes light in the ranges 310-420 nm and 700-1100 nm (see Appendix A). The polarizer, active over the range 240-740 nm, is special in that its useful range extends into the UV. The MEIS, a two channel instrument, was fitted with HNP'B polarizers, one passing the horizontal mode, the other the orthogonal polarization. Two types of spectral filters were used, one a Corning 7-54, which is similar to the 7-51 but with narrower pass bands, the other a Corning 2-64 which passes wavelengths longer than 650 nm. A nadir looking Vinten camera was used with Kodak Aerocolour negative film (type 2445); a forward looking (at 45°) Vinten camera was used with a UV lens and filter (Wratten 18A), and Kodak Double X Aerographic film (type 2405). The latter combination was chosen to exploit the higher contrast available in the UV. The nadir directed RC-10 camera was used with Kodak Aerocolour negative film (type 2445), on one occasion with Kodak Aerochrome positive infrared film (type 2443) primarily to provide photographic documentation of the target area.

4.1.3 **Thermal Effects.** A thermal infrared sensor measures thermal radiation, which is electromagnetic radiation in the wavelength range 4 to 20 µm. The intensity of the thermal radiation emitted by a target depends on the physical temperature, and on the emittance of the surface of the object.

The radiation process is described by Planck's law:

$$N_\lambda = 2c^2h\lambda^{-5}(e^{hc/\lambda kT}-1)^{-1} \quad (6)$$

where: N_λ = spectral radiance emitted by a perfect radiator (black body) ($W\ m^{-2}\ sr^{-1}\ m^{-1}$)
c = speed of light ($m\ s^{-1}$)
h = Planck's constant ($j\ s$)
λ = wavelength (m)
k = Boltzman constant ($j\ deg^{-1}$)
T = temperature (deg Kelvin)

The spectral emittance of a given target can be defined as:

$$E(\lambda) = \frac{N_\lambda\ (\text{target})}{N_\lambda\ (\text{black body})} \quad (7)$$

and as such is the efficiency of the target as a thermal radiator. For temperatures near 290 K, the radiation from a perfect emitter peaks near 10 μm. Infrared sensors used for airborne observation of terrestial targets generally restrict their sensitive ranges to the atmospheric windows at 4.5 - 5.1 μm and 8 - 14 μm; outside these windows, what is received by the thermal detector is a combination of target and atmospheric path radiance.

4.1.3.1 Oil on water. For the experiments conducted as part of this project, the IR range 8.5 to 12.5 μm was employed for the detection of oil on water. In this range the emissivity of water is very high and is reported to have a maximum of 0.993 at 10.9 μm with an average of 0.988 over the range 8.5 to 12.5 μm (Wolfe, 1965). Oil has an emissivity that is slightly less than water in this spectral range. Munday et al. (1971), Horvath et al. (1971), and Buettner and Kern (1965) place it at 0.94, 0.96 and 0.97 respectively. Because of the lower emissivity, the oil will radiate less than water at the same physical temperature; it, therefore, will appear cooler than the water. For emissivities of 0.95 to 0.99 and temperatures in the range 275 to 295 K, a radiance measurement at 10.5 μm will give apparent temperatures that decrease by 0.6 K for a 0.01 decrease in emissivity. This would lead one to expect the oil to appear as much as 3 K cooler than the water. One would not expect, however, that this full temperature reduction would be achieved for thin oil films but would be approached gradually as the oil layer became sufficiently thick to be effectively opaque at the wavelengths in question;

otherwise, the observed radiation would be that emitted by the subsurface water and transmitted by the oil to the air above, and hence would be subject to the water's emissivity, not the oil's. For a number of crude oils, measured by Horvath et al. (1970) to have attenuation coefficients near 0.005 μm^{-1} in the wavelength range 8.5 to 12.5 μm, a 320 μm thick layer of oil would be required in order that the resultant thermal radiation originate 80% from the oil and 20% from the underlying water.

In addition to this emissivity effect on the apparent temperature, oil can have an effect on the physical, or real, temperature of the sea surface. This effect may arise from a number of causes; some of them tending to produce an increase, others a decrease, in the surface temperature. The temperature of freshly spilled oil may retain the source temperature for a short period of time. Very volatile components in the oil can produce evaporative cooling in excess of the normal cooling occurring at the water-air interface (Horvath et al., 1971). If these constituents have all evaporated or if the oil was of a heavier type initially, then the presence of an oil film is likely to reduce evaporation, and hence cause a warming of the surface relative to the water-air surface. Oil, which is a poor heat conductor, can impede the flow of heat across the air-water boundary, thereby causing a warming or cooling of the surface depending on whether the air is warmer or cooler than the water. For optically thick layers of oil, the most probable effect under sunlit conditions will be a warming of the surface resulting from the solar heating of the oil. The point at which this becomes the dominant effect depends on the intensity of the solar irradiance, the thickness of the oil layer, and the absorptivity of the oil in the visible region. Attenuation coefficients for crude oils have been measured in the visible region by Horvath et al. (1970): the values at 500 nm vary from $0.7 \times 10^{-3}\ \mu m^{-1}$ for a light crude (API gravity = 44.7°) to $200 \times 10^{-3}\ \mu m^{-1}$ for a heavy crude (API gravity = 18.5°). One could expect solar heating to have an appreciable effect for oil layers absorbing 80% or more of the incident solar irradiation; such oil layers would have thicknesses of 2300 to 8 μm for the range of attenuation coefficients given above. Absorption of solar irradiation by an oil layer has been measured to produce real temperature increases up to 10 K under natural conditions.

The surface emittance of an oil film on water may depend on factors other than the bulk oil emissivity alone. The thermal radiation that emanates from a clean water surface is emitted from the upper water layer of a thickness depending on the absorptivity of the water at the measured wavelength; for wavelengths in the 8.5 to 10.5 μm range, 80% of the radiation is emitted by the top 30 μm of water; for wavelengths in the 10.5 to 12.5 μm range this thickness is 7 μm (based on extinction coefficients listed in Wolfe (1965)). Part of this radiation is ultimately reflected at the water-air surface in accordance with Fresnel's equations, giving an emittance of 0.988 for an index of refraction of 1.25. When an oil film is added on top of the water there are now two reflecting surfaces, a water-oil surface and an oil-air surface. As the index of refraction for oil (1.43 for $\lambda = 10.5$ μm) is greater than for water (1.25) and for air (1.0), the internally reflected component of the upwelling thermal radiation will be increased, and the emitted component decreased. This will result in a reduced surface emittance. An extension of McMahon's calculation (McMahon, 1950) yields the following expression for the emittance $E(\lambda)$ normal to the surface:

$$E(\lambda) = \frac{\left(1 - R_2(\lambda)\right)\left(1 - R_1(\lambda)T^2(\lambda)\right)}{1 - R_1(\lambda)R_2(\lambda)T^2(\lambda)} \tag{8}$$

where:
$R_1(\lambda)$ = the reflectance at the water-oil surface
$R_2(\lambda)$ = the reflectance at the oil-air surface
$T(\lambda)$ = the transmittance proper of the oil layer, and is given by:

$$T(\lambda) = e^{-k(\lambda)d} \tag{9}$$

where:
$k(\lambda)$ = the absorption coefficient for the oil
d = the oil film thickness

When the reflectances R_1 and R_2, calculated from Fresnel's equations using the indices of refraction, and the transmittance T, calculated using the value $k = 0.005$ μm^{-1} (Horvath et al., 1970), are substituted into Equation 8, one obtains $E(\lambda) = 0.963$. This would give an apparent temperature reduction of approximately 1.5 K.

This expression (Equation 8), however, is not applicable to thin films of thickness of the order of a wavelength (10 μm) or less. For such thin films, the radiation retains its coherence as it is multiply reflected between the two surfaces. Constructive or destructive interference results, giving an emittance that is larger or smaller than that given by Equation 8. The derivation of Equation 8 is valid only for the incoherent case for which interference is assumed not to occur. An appropriate expression for the coherent case has been derived, but is too complicated to reproduce here. The net result is that for films approaching zero thickness, the emittance approaches the clean water value. As the thickness is increased the emittance value oscillates about the value given by Equation 8. The amplitude of the oscillation is initially equal to the difference between the water emittance and the value obtained from Equation 8, and decays with increasing thickness at a rate governed by the transmittance as in Equation 9. The bulk oil emissivity value is approached for thick (>500 μm) layers; however, long before these thicknesses are reached, the radiation coherence will have been degraded to the point where Equation 8 will apply. That is, the incoherent result will be approached more rapidly than indicated by the purely coherent expression. The film thicknesses resulting in emittance minima are given by:

$$d = (2m+1)\frac{\lambda}{4n} \tag{10}$$

where: d = film thickness

λ = radiation wavelength (10.5 μm)

n = index of refraction for the film material ($n_{oil} = 1.43$)

m = an integer ≥ 0.

Equation 10 is valid for normal incidence; for other angles the expression on the right side includes the cosine of the incidence angle (internal to the oil film) in the denominator. The first minimum, reached at a thickness of 1.83 μm as calculated from Equation (10), gives an emittance of 0.940 which would result in an apparent temperature reduction of approximately 3.0 K.

To summarize, there are three processes contributing to a reduced surface emittance: interference, increased reflectance, and reduced bulk oil emissivity. The first two are expected to dominate for the thin film regions (<10 μm); the second for intermediate thicknesses (10 to 150 μm); and the third for thick layers (>150 μm). At some thickness, depending on solar irradiance, visible light absorption by the oil, thermal conductivity of the oil, air temperature at the surface, etc., solar heating will increase the physical temperature by an amount that just offsets the apparent temperature reduction caused by emittance effects. This should not cause any problem, however, as the occurrence of an oil layer of precisely the right uniform thickness over the large areas involved is extremely improbable and such an area will be delineated by the thinner and thicker regions to either side. The thinner regions, down to approximately 2 μm, will appear cooler than water; the thicker regions, where solar heating dominates, will appear warmer than water.

4.1.3.2 Oil on ice. As for oil on water the observed temperature of the oil depends on both the physical temperature of the oil and its emittance relative to the background emittance, in this case, that of the ice.

Again if the solar irradiance is sufficient, the oil will heat up, appearing warmer than the ice background. The emittance of ice, in the IR range under investigation (8.5 to 12.5 μm), is again high. Laboratory measurements on a clean, freshly prepared ice surface indicate that its emittance is approximately 0.99 for the range 8.5 to 10.5 μm but drops sharply above 10.5 μm to a value below that measured for oils (Poulin, 1973). This implies that if oil is to be detected in a water-ice mixture by emittance effects alone, i.e., for low solar irradiance, then one should restrict the detector's range to 8.5 to 10.5 μm. Under these conditions, assuming the physical temperature of the oil-ice-water mixture is uniform, the oil will appear colder than its surroundings.

The difficulty confronting the thermal detection of oil in ice, or oil in a mixture of ice and water, is the potentially large variability in the physical temperatures of the ice or ice and water. For air temperatures below freezing, the temperature of the ice depends on factors such as ice thickness, exposure to wind, snow cover depth, etc. For mixtures of ice and water there will be considerable variability in the water temperature caused by cold interfacial regions and cold streams of meltwater on the surface of the ice. In addition, the ice can be warmer, as well as colder, than the water if its salinity is lower.

4.1.3.3 Sensors. Two IR detectors were flown during this project; one in the dual channel line scanner (DCLS); the other in the multispectral scanner (MSS). Both were filtered to detect the IR band 8.5 to 12.5 μm for the oil on water experiments. The IR detector in the DCLS was restricted to the 8.5 to 10.5 μm band for the oil-in-ice overflights of the KURDISTAN mission. The detailed specifications for these detectors are found in Appendix A.

4.1.4 Fluorescence. Fluorescence is a radiation stimulated luminescence which continues for approximately 10^{-8} seconds after the stimulating radiation ceases. When a molecule absorbs a quantum of light of the proper energy, the molecule is raised from its ground state to an excited state. It can de-excite by reemitting a photon of the same energy as it absorbed (resonance), by emitting an infrared photon, or by undergoing radiationless losses of vibrational energy. The latter two processes leave the molecule in a somewhat less energetic but still excited state. From this state the molecule may: i) undergo radiationless loss of electronic energy through collisions or other interactions; ii) emit an ultraviolet or visible light photon in dropping from an excited singlet state to the ground state (fluorescence); or iii) undergo a transition to a metastable triplet state and some time later return to its ground state usually by the emission of an ultraviolet or visible light photon (phosphorescence).

4.1.4.1 **Oil detection.** Few molecules exhibit fluorescence; however, of those which do, an important group are the aromatic hydrocarbons. It is this class of molecules which exhibits fluorescence in oils. There are two properties of the fluorescence radiation which can be measured in order to characterize the source of the fluorescence: spectral character and decay rate of the emitted radiation. Typical oil fluorescence spectra are shown in Figure 9. Oils can be distinguished from other fluorescent substances in the water, such as phytoplankton, by comparing fluorescence spectra alone. Additionally, oils of different types (light, heavy, etc.), can be differentiated spectrally. Laboratory studies have indicated that a combination of spectral and time decay analysis on the emitted fluorescence radiation can yield quite specific identification of oils (Rayner and Szabo, 1976).

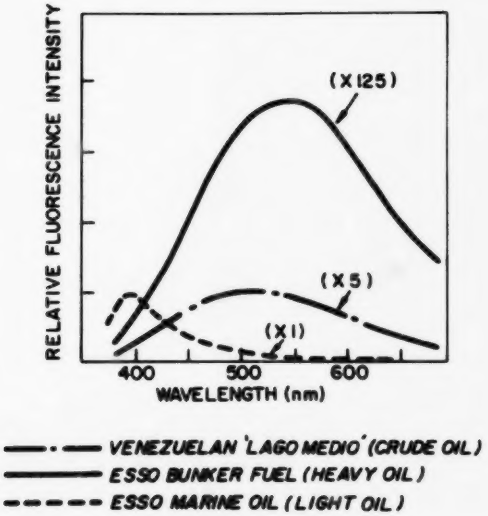

FIGURE 9 TYPICAL OIL FLUORESCENCE SPECTRA. The fluorescence conversion efficiencies on peak emission wavelengths may be compared.

Because of the specificity of the fluorescence radiation emitted by oils, techniques which separate this radiation from the reflected solar radiation can detect and distinguish oils from other targets in almost any background environment, whether it be water, ice, or soil. Such methods must, therefore, be considered to have the best prospect of successfully detecting oil in an arctic environment.

4.1.4.2 **Techniques.** There are basically two techniques for separating the fluorescence radiation emitted by the fluorescent substance from the reflected solar radiation. One is an active technique in which an artificial light source is used; the other is a passive technique in which only solar illumination is required.

Active. The active method involves the illumination of the target with a well defined pulse of light, as from a pulsed laser, and the detection of the resultant fluorescence radiation emitted by the target. The background reflected solar radiation can be measured separately and subtracted to give the net fluorescence radiation. Both spectral and temporal analyses can be applied to give specific identification of targets. This technique has an additional advantage in that measurements can be made regardless of solar illumination conditions. This is an important feature if arctic operations are to be undertaken.

Passive. The passive method, referred to as 'Fraunhofer line discrimination', involves the measurement and comparison of the depths of the Fraunhofer lines in the target reflected radiance with those in the incident solar radiance (Watson and Hemphill, 1976; Watson et al., 1977). The Fraunhofer lines, dark lines in the solar spectrum caused by absorption in the outer cooler regions of the sun or in the earth's atmosphere, will be filled in by fluorescence from an observed fluorescent target (see Figure 10). The degree of infilling present in the target reflected radiance, as compared with the solar radiance, will be proportional to the fluorescence conversion efficiency of the target. This technique is limited by the number of appropriate Fraunhofer lines available, and by the need for adequate solar illumination. The latter constraint is quite stringent as the Fraunhofer lines are very narrow; hence, the wavelength band over which a detector can integrate radiation is correspondingly narrow. Of course, time decay analysis cannot be applied to this technique.

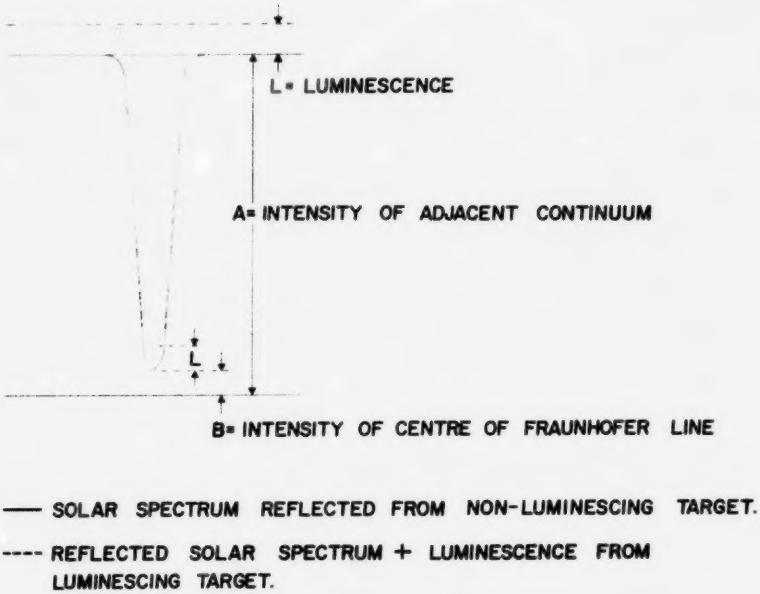
L = LUMINESCENCE
A = INTENSITY OF ADJACENT CONTINUUM
L
B = INTENSITY OF CENTRE OF FRAUNHOFER LINE
—— SOLAR SPECTRUM REFLECTED FROM NON-LUMINESCING TARGET.
---- REFLECTED SOLAR SPECTRUM + LUMINESCENCE FROM LUMINESCING TARGET.

FIGURE 10 FRAUNHOFER LINE DISCRIMINATION

4.1.4.3 Sensors. Two fluorescence detecting sensors were used in the experiments undertaken as part of this project: the laser fluorosensor, an active sensor, and the optical multichannel analyzer (OMA), a passive sensor.

The laser fluorosensor. The laser fluorosensor is an active device which emits ultraviolet radiation at 337 nm from a nitrogen gas laser and is range gated in order to assist it in the detection of any resulting fluorescence (see Appendix A). The laser induced fluorescence is gathered by a telescope, dispersed by a concave holographic grating, optically amplified by proximity focused microchannel plate intensifiers and measured by photodiodes as found in Appendix A (O'Neil et al., 1980). The fluorosensor is able to detect weak fluorescence signals in daylight because of its range gating capability which selects a short operating time coincident with the return of the induced fluorescence signal. This ensures that the number of fluorescence photons is greater than the number of background photons. The background can be subtracted automatically from the detected fluorescence signal, since the background is measured separately by activating the detector between laser pulses.

The fluorosensor detects a fluorescence return in 16 spectral channels covering the range of 377 to 689 nm (for sensor specifications see Appendix A). The fluorosensor does not presently measure decay times, but provisions have been made for inclusion of this feature in the future should it be deemed necessary for a particular application.

The optical multichannel analyzer (OMA). The OMA, with a high dispersion grating capable of resolving the Fraunhofer lines and a highly sensitive modified SIT-TV tube as a detector, was used to gather data on the Wallops Island oil spill mission.

4.1.5 Raman Scattering Suppression.

4.1.5.1 Raman scattering. When molecules are irradiated by a light source, a portion of the radiation is scattered; most of the radiation which is scattered has the original frequency (Rayleigh scattering), but some of the light is found at other frequencies (Raman scattering). The difference in the frequencies between the incident and scattered light is characteristic of the molecule irradiated and corresponds to excitation of certain vibrational and rotational states. When an incident photon interacts with a molecule in any of its stable states, the energy of the molecule is momentarily raised. If the resulting state is not a stable allowed state, the molecule immediately de-excites to a lower energy state and the corresponding amount of energy is emitted (scattered). If the molecule returns to the original state, Rayleigh scattering occurs; if the molecule returns to another energy state, Raman scattering results. If upon excitation, the resulting state of the molecule is stable, the photon will be absorbed; as discussed in Section 4.1.4, the molecule can subsequently de-excite by the emission of resonance, fluorescence, or phosphorescence radiation.

4.1.5.2 Oil detection. Seawater, containing phytoplankton and other naturally occurring substances, can exhibit all of the aforementioned processes if irradiated by light in the appropriate wavelength range. If the incident irradiation is broad band, such as for sunlight, covering the near UV, visible and IR, it is difficult to differentiate the Raman scattered radiation from the Rayleigh scattered radiation; although the Raman spectrum is shifted toward the longer wavelength, it overlaps the unshifted Rayleigh spectrum. The Raman scattering will contribute to Fraunhofer line infilling, as will fluorescence and phosphorescence. Thus, it is difficult to separate out the Raman scattered radiation if the incident illumination is solar irradiation. If, however, the incident irradiation is monochromatic, as from a laser, the Raman scattered radiation from the water appears in a narrow spectral band (width ~8 nm) shifted from the incident wavelength by an amount characteristic of the water molecule. A sufficiently thick surface layer of some substance, such as oil, that absorbs the incident radiation before it penetrates to the water, consequently suppresses the Raman scattered radiation from the water. This suppression can, therefore, be used as an indication of the presence of some foreign absorptive material on the water's surface.

The laser fluorosensor can in fact be used in this mode. The water Raman scattered radiation resulting from the laser irradiation at 337 nm appears at 381 nm. The first channel of the fluorosensor spectrometer, centred at 381 nm with a width of 8 nm has been designed to detect this Raman scattered light. Some oils, in particular the lighter types, fluoresce at these short wavelengths; as a result, a layer of such oil, while suppressing the water Raman scattered radiation, will replace it, in part at least, with fluorescence radiation. The heavy oils fluoresce less readily at these shorter wavelengths and can be detected more consistently by their suppression of the water Raman scattering. This effect can of course be caused by surface substances other than oil. The oil can be detected by this method, but its identification as oil depends on its fluorescence radiation.

4.1.6 Microwave Radiation Effects. Microwave radiation is continuously emitted and reflected from the earth's surface; this microwave emission arises from the same process as does the thermal radiation discussed in Section 4.1.3. The microwave region of the electromagnetic spectrum is in the frequency range of 1 to 300 GHz (wavelengths of 30 to 0.1 cm). The instruments designed to measure this radiation, microwave radiometers, express the measurement as a brightness temperature, T_b; this temperature is exactly equivalent to the 'apparent temperature' of thermal IR terminology. Radiometers are usually designed to measure either vertical or horizontal polarizations, and thus give T_b^v or T_b^h. (Vertical and horizontal polarizations are defined such that the electric vectors lie in planes perpendicular and parallel to the earth's surface respectively.)

For a natural surface, such as the sea surface, the brightness temperature depends on the look angle and polarization. In addition, because the atmosphere absorbs radiation emitted by the surface and emits its own radiation, depending on the temperature of the atmosphere, any remote measurement of a target depends on the altitude of the detector. More explicitly, the brightness temperature measured at an incidence angle, "Θ", from an altitude, "h", can be expressed (Troy and Hollinger, 1977):

$$T_b^i(\theta,h) = \tau(0,h)\left\{ \left[1 - \frac{1}{4\pi}\int_\mu \gamma_i(\theta,\theta')d\Omega'\right] T + \frac{1}{4\pi}\int_\mu \gamma_i(\theta,\theta')\, T_s(\theta')d\Omega' \right\} \quad (11)$$

$$+ \int_0^h T_a(h') \frac{\partial \tau(h', h)}{\partial h'} dh'$$

where: i = $\begin{cases} \text{v-for vertical polarization} \\ \text{h-for horizontal polarization} \end{cases}$

T = physical temperature of the target surface

T_s = brightness temperature of the sky

$T_a(h')$ = physical temperature of the atmosphere at height h'

$\gamma_i(\theta, \theta')$ = surface scattering coefficient for polarizaiton i

$\tau(h', h)$ = transmittance through the layer of atmosphere from height h' to height h

$\int_\mu d\Omega'$ = integral over the upper hemisphere

The scattering coefficient depends on the incident (θ') and scatter (θ) angle, and may depend on the azimuth angles as it would, for example, for a sea surface with parallel wavefronts on it. The integral of $\gamma_i(\theta,\theta')$ over the upper hemisphere can be considered to be an average reflectance, $r_i(\theta)$, the average being taken over the incident directions.

$$r_i(\theta) = \frac{1}{4\pi} \int_\mu \gamma_i(\theta, \theta') \quad d\Omega' \quad (12)$$

For a specular reflector, e.g. a smooth surface, the integral of $\gamma_i(\theta,\theta')T_s(\theta')$ can be written:

$$r_i(\theta)\,T_s(\pi-\theta) = \frac{1}{4\pi}\int_{\mu} \gamma_i(\theta,\theta')\,T_s(\theta')\,d\Omega' \qquad (13)$$

Since the emittance $\epsilon_i(\theta)$ satisfies:

$$\epsilon_i(\theta) = 1-r_i(\theta) \qquad (14)$$

Equation (11) can be simplified to:

$$T_b^i(\theta,h) = \tau(0,h)\,\big(\epsilon_i(\theta)\,T + r_i(\theta)\,T_s(\pi-\theta)\big) + \int_0^h T_a(h')\,\frac{\partial\tau(h',h)}{\partial h'}\,dh' \qquad (15)$$

where the emitted, reflected, and atmospheric terms appear in an explicit fashion. Since the scattering coefficients, and hence the emittance and reflectance, differ for the two polarizations, the brightness temperature will also differ. For the sea surface, T_b^v is greater than T_b^h for non-nadir look angles; this difference reaches a maximum for $60° < \theta < 70°$ for a wavelength of 1.55 cm and a flat sea surface (Edgerton and Trexler, 1969).

4.1.6.1 Oil detection on water. In the microwave region of the electromagnetic spectrum, water has an emissivity of approximately 0.4; therefore, it appears cold. Oil has an emissivity of approximately 0.8 and consequently its brightness temperature is closer to its actual physical temperature. An oil film on water behaves as a matching layer at the air-water interface because oil has a dielectric constant between that of air and water. Reflection is minimized and emission will be a maximum when the film has an effective thickness (i.e., thickness times index of refraction) equal to an odd multiple of a quarter wavelength of the observed microwave energy.* Therefore, as an oil film thickness on the water increases, the brightness temperature, measured at a given microwave energy and radiometer look angle, increases at first to a maximum and, then, oscillates between maxima and minima (see Figure 11). Thus, two or more oil thicknesses can have the same brightness temperature. The detection of oil due to this higher emittance is the primary effect for observation by a microwave radiometer.

---

* This is analogous to the interference phenomenon referred to in the discussion on the emittance of an oil film covered water surface. In the thermal IR case the quarter wave thickness gave a minimum (Equation 10) since the index of refraction of the oil was greater than that of either the water or the air. In the microwave case it produced a maximum because the index of refraction of the oil was intermediate between that of the water and the air.

A second effect by which a microwave radiometer observes an oil slick is the damping of water waves by the oil. The horizontal component of the microwave brightness temperature is increased with increased water surface roughness; the vertical component is changed very little (see Figure 12). Oil slicks on water, because they reduce the water surface roughness, reduce the emittance, and hence the brightness temperature. When observing an oil slick on water with a microwave radiometer in the horizontal polarization mode, the increased brightness temperature of the rough water is reduced in the area of the oil slick. This effect is independent of oil film thickness.

These two effects, the slick induced depression of the emittance resulting from the decreased surface roughness, and the oil layer induced increase in the emittance resulting from the better matching at the sea-air interface, oppose each other. The former effect, a function of sea surface roughness and hence wind speed, has been calculated (Hollinger, 1974) to give an approximate brightness temperature reduction of 5 K for a 20 knot wind; a reduction of approximately 6 K has been measured (Edgerton and Hinds, 1971a) for a sea state of 2. In contrast the latter effect can result in brightness temperature increases of 0 to 120 K, depending on the oil layer thickness and the frequency, or wavelength, at which the microwave measurement is made. Thus, the sea surface roughness suppression effect will dominate for thin oil films, the surface emission matching effect for thicker oil layers.

4.1.6.2 Microwave radiometer experiments: oil on water. Many studies have been performed with both profiling and imaging microwave radiometers on the detection and mapping of oil slicks (Edgerton et al., 1969, 1971a, 1971b, 1975; Hollinger, 1974; Troy and Hollinger, 1977; Parashar et al., 1979). The best developed instrument seems to be the dual frequency passive microwave imager developed and tested by the Naval Research Laboratory, Washington D.C. (Troy and Hollinger, 1977). Two frequencies are used in this instrument in order to eliminate the ambiguity arising from 'alias' oil thickness measurements such as occur when observations are performed with a single frequency. This imaging system can detect oil thickness down to a 50 μm limit, and is especially

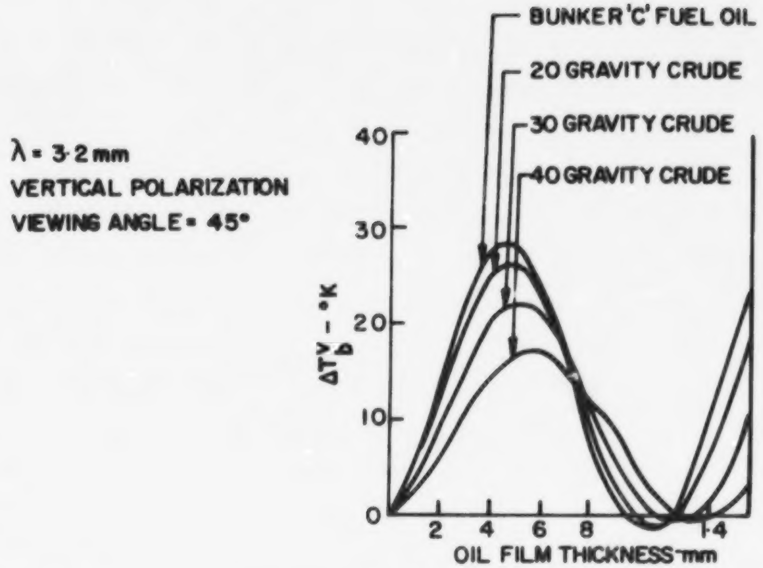

VERTICAL BRIGHTNESS TEMPERATURE INCREASE, ΔT_b^v, VERSUS OIL FILM THICKNESS AT 3·2 mm WAVELENGTH FOR SMOOTH WATER SURFACES

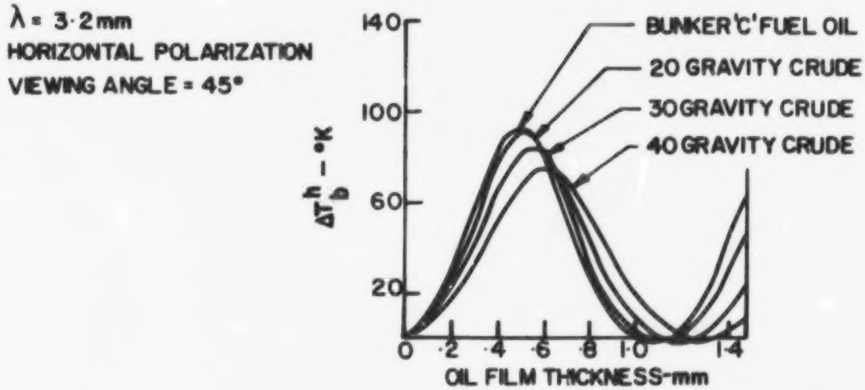

HORIZONTAL BRIGHTNESS TEMPERATURE INCREASE, ΔT_b^h, VERSUS OIL FILM THICKNESS AT 3·2 mm WAVELENGTH FOR SMOOTH WATER SURFACES

(EDGERTON, 1971b)

FIGURE 11 MICROWAVE BRIGHTNESS TEMPERATURE AS A FUNCTION OF OIL THICKNESS ON WATER.

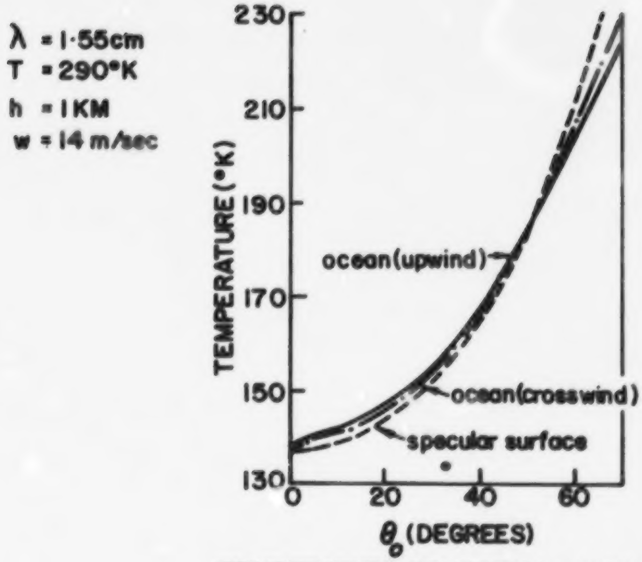

TEMPERATURE OF VERTICALLY POLARIZED RADIATION AS A FUNCTION OF ANGLE

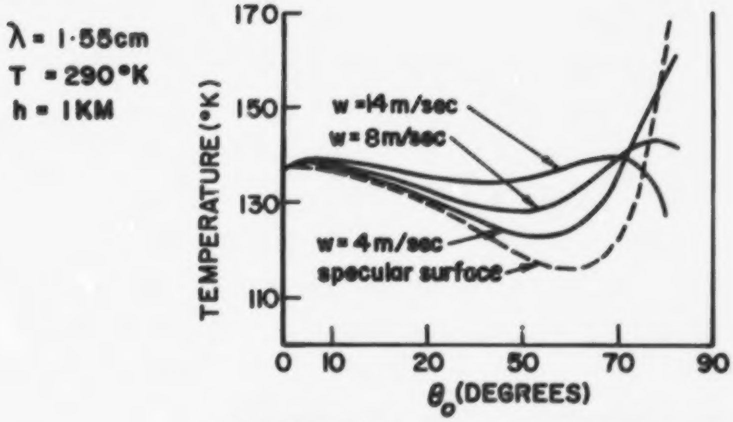

TEMPERATURE OF HORIZONTALLY POLARIZED RADIATION AS A FUNCTION OF ANGLE (UPWIND CASE)

OCEAN SURFACE APPARENT TEMPERATURE
(EDGERTON 1969)

FIGURE 12 MICROWAVE BRIGHTNESS TEMPERATURE AS A FUNCTION OF LOOK ANGLE FOR DIFFERENT WATER SURFACE ROUGHNESS.

good for oil volume prediction. It was the NRL instrument that was flown by NASA on the Wallops Island oil spill experiments described in this report.

4.1.6.3 Oil detection on ice. The emissivity of sea ice varies from 0.95 for first-year ice to 0.75 for multiyear in the 5 to 49 GHz frequency region (Parashar et al., 1979). Since the emissivity of water is approximately 0.4, sea ice will have a high brightness temperature compared to water. The difference in brightness temperature between first-year ice and seawater can be up to 150 K, depending on the frequency (Edgerton and Poe, 1972); multiyear ice or weathered ice can have a brightness temperature somewhere in between, approximately 50 to 75 K lower than first-year ice. Because oil has an emissivity of approximately 0.8 it is very difficult to distinguish oil from multiyear ice; this problem could occur either for oil on multiyear ice or for oil in a mixed field of first-year and multiyear ice.

Snow has dielectic properties at microwave frequencies similar to oil and like oil, snow acts as a matching layer between ice and air (Lapp, 1975). Therefore, discrimination of oil from thin snow layers on ice is difficult.

In waters with some ice cover, discrimination of oil from ice is also difficult. Since passive microwave detectors, depending on frequency, usually have large 'footprints', ice, in open pack ice conditions, may only fill a fraction of a detector's field of view and, while showing an increase in brightness temperature, this increase is not as large as if the detector were viewing only ice; without complementary data, this effect would be indistinguishable from that produced by the presence of oil on water.

There are insufficient remotely sensed microwave radiometer data for oil on different ice types to arrive at a firm conclusion as to its utility. While oil might appear as an anomalous feature in microwave radiometer imager, it is fairly certain that the oil will be indistinguishable from naturally occurring features, except when it is on first-year ice.

4.2 Data Collection

The AMOP remote sensing project operations consisted of four missions and test flights. The four missions were: Montreal Island, Scott Inlet, Wallops Island, and the KURDISTAN. Each mission was performed under a different set of operational circumstances; and each provided for the remote detection of oil spills under a different set of environmental conditions.

Technical descriptions of the sensors used may be found in Appendix A. A brief description of the aircraft track recovery system which was especially important during the Scott Inlet and KURDISTAN missions may be found in Appendix B. With the exception of the cameras and the SAR, which record on photographic film, the data collected during this project were recorded on magnetic tape using the systems described in Appendix C. Appendix E contains a summary of the purpose, logistics and execution of each of the four missions.

4.3 Data Reduction

Throughout the processing and analysis of the data collected during the AMOP remote sensing project, examples of data from each sensor were chosen which showed the capability of an individual sensor for detecting oil in ice-infested waters and which contrasted the relative capabilities of the sensors. During the four AMOP remote sensing missions, an accumulated total of 114.5 hours of data was collected by the various sensors, excluding human observers. This does not take into account the fact that sensors such as MSS are multiple detectors nor does it include the approximately 87 hours of data recorded for each of the inertial navigation system and the time code generator. The processing and display of this huge volume of data is discussed in Appendix F.

4.4 Results and Discussion

The enormous quantity of data collected during the four separate missions precludes analysis and presentation here of the complete set of results. Instead, examples from each mission have been selected, processed and analyzed in detail, and they are presented in this report. The Wallops Island mission over the two test oil spills provided the most comprehensive set of data. For this reason the advanced processing techniques were developed using this data set. The majority of the sensor performance comparisons are done on the Wallops Island results as this was the only mission on which all the sensors were operated together over oil. The other three missions provided data collected under special circumstances. The Montreal Island mission gave thermal IR oil spill imagery under day and night conditions and provided an opportunity to test the LLLTV system under these same conditions. The Scott Inlet mission, although it did not involve an oil-on-ice situation as had been hoped for, did provide oil slick results obtained under Arctic lighting and operating conditions. The information gained on the mission will be important for future development of a remote sensing package to be operated in the

Arctic. The KURDISTAN incident provided an opportunity to apply some of the techniques developed in the earlier missions to a realistic oil spill situation. It also provided the only imagery of oil-in-ice.

The results and analyses are organized into the following sections: microwave; near ultraviolet, visible, and near infrared; thermal infrared; integrated multispectral analysis; fluorescence. Each section is in turn divided into subsections, first by sensor or analysis technique and then by missions. The relative fields of view of each of the sensors on the aircraft C-GRSA and C-GRSC are compared in Figures 13 and 14.

4.4.1 Microwave Sensors.

4.4.1.1 Microwave scatterometer.

Scott Inlet oil seep. The microwave scatterometer was operated at Scott Inlet; however, no oil was overflown during scatterometer data collection. Gray et al. (1979) have used the data set obtained at Scott Inlet with the microwave scatterometer for analysis on icebergs.

Wallops Island test oil spills. The microwave scatterometer was flown over the two test spills on November 2 and 3, 1978, on ten flight lines; of these, only three flight lines resulted in data suitable for analysis. They were flight lines 3(V), 6(H) on November 2 and 4B(H) on November 3, where scatterometer transmit polarization is indicated in brackets. Shown in Figure 15 is a photograph taken by an RC10 aerial survey camera; on the photograph is indicated the projection of the scatterometer forebeam. The scene shown is that of flight line 3 on November 2. The corresponding backscatter cross section observed by the scatterometer is plotted in Figure 16. The data have been suitably shifted so that each footprint is shown at the time at which it crossed the nadir regardless of the look angle used. A densigram containing the complete scattering history is shown in Figure 17. In both diagrams the locations of the ship and oil spill are indicated. A summary of the data is contained in a plot of backscatter depression versus incidence angle which is shown in Figure 18. Similarly the scatterometer information for flight line 6 on November 2, 1978 is displayed in Figures 19-21 and for flight line 4B on November 3, 1978 in Figures 22-24. As indicated in Figure 23, a ship is present in the aft beam backscatter and not in the fore beam; this is due to the drift of the aircraft when passing over the oil spill, i.e., a difference in the aircraft track and aircraft heading (see Figure 15).

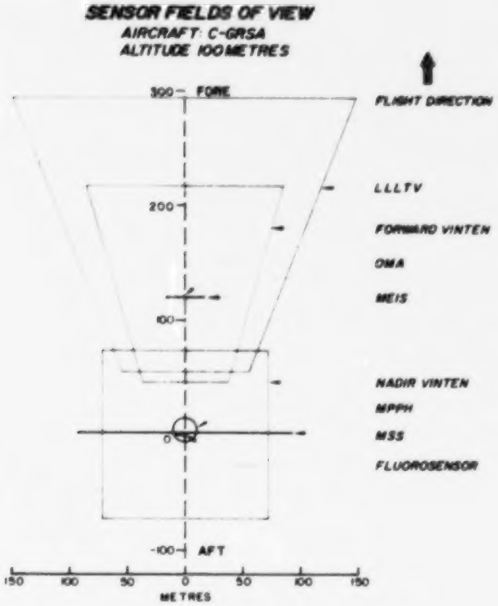
SENSOR FIELDS OF VIEW
AIRCRAFT: C-GRSA
ALTITUDE 100 METRES
300 FORE
FLIGHT DIRECTION
LLLTV
200
FORWARD VINTEN
OMA
MEIS
100
NADIR VINTEN
MPPH
MSS
0
FLUOROSENSOR
-100 AFT
150
100
50
0
50
100
150
METRES

FIGURE 13 SENSOR FIELDS OF VIEW AS MOUNTED IN C-GRSA.

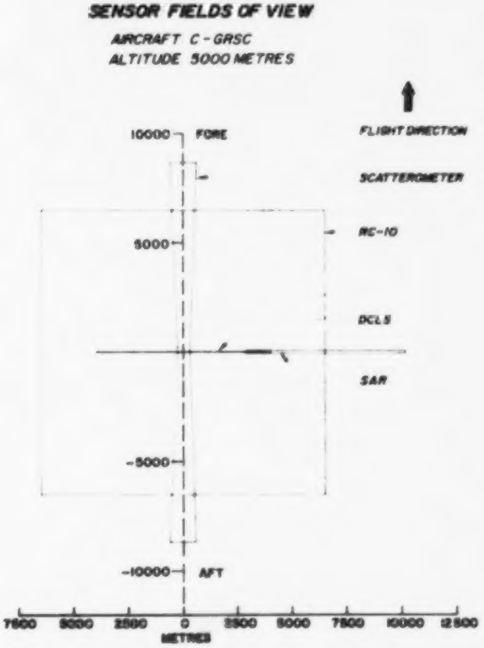
SENSOR FIELDS OF VIEW
AIRCRAFT C-GRSC
ALTITUDE 5000 METRES
10000 FORE
FLIGHT DIRECTION
SCATTEROMETER
RC-10
5000
DCLS
SAR
-5000
-10000 AFT
7500
5000
2500
0
2500
5000
7500
10000
12500
METRES

FIGURE 14 SENSOR FIELDS OF VIEW AS MOUNTED IN C-GRSC.

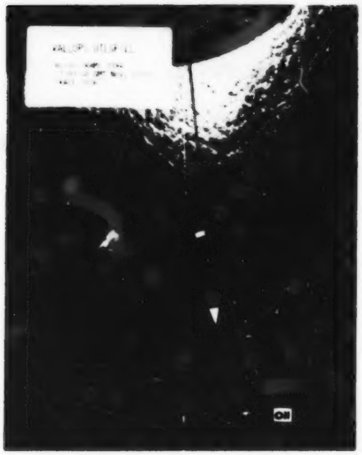

AERIAL PHOTOGRAPH OF C-GRSC
FLIGHT LINE 3, NOVEMBER 2,1978

White Line – Aircraft Track
Dotted Line – Projection of Scatterometer Forebeam (Aircraft Heading)
White Square – Scatterometer Footprint at Nadir and 60°

FIGURE 15 RC-10 AERIAL PHOTOGRAPH, WALLOPS OIL SPILL. C-GRSC Flight Line 3, November 2, 1978. Indicated are the sensor look direction; the aircraft track direction; and the microwave scatterometer footprint.

13.3 GHz SCATTEROMETER
VV POLARIZATION
WALLOPS ISLAND
C- GRSC
FLIGHT LINE 3
NOVEMBER 2,1978

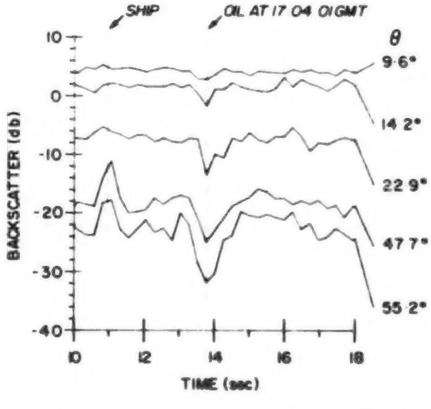

FIGURE 16 SCATTEROMETER, WALLOPS OIL SPILL. Microwave backscatter as a function of time for several incidence angles. C-GRSC Flight Line 3, November 2, 1978.

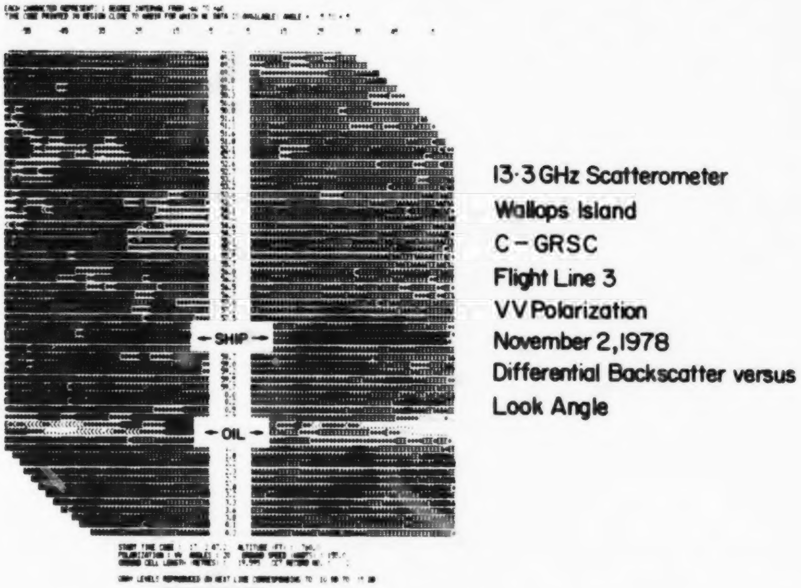

FIGURE 17 SCATTEROMETER, WALLOPS OIL SPILL. Densigram showing microwave backscatter depression for several incidence angles. C-GRSC Flight Line 3, November 2, 1978.

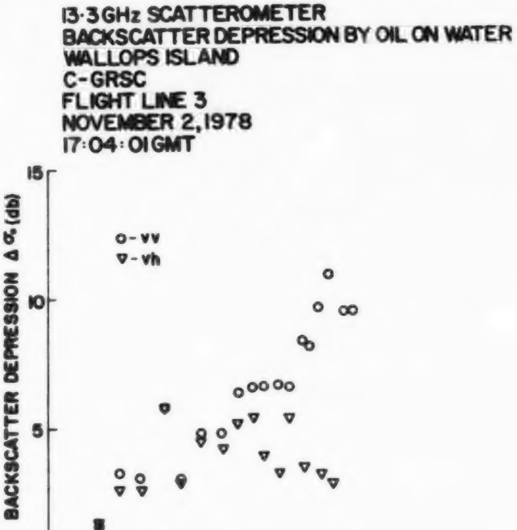

FIGURE 18 SCATTEROMETER, WALLOPS OIL SPILL. Microwave backscatter depression as a function of incidence angles. C-GRSC Flight Line 3, November 2, 1978.

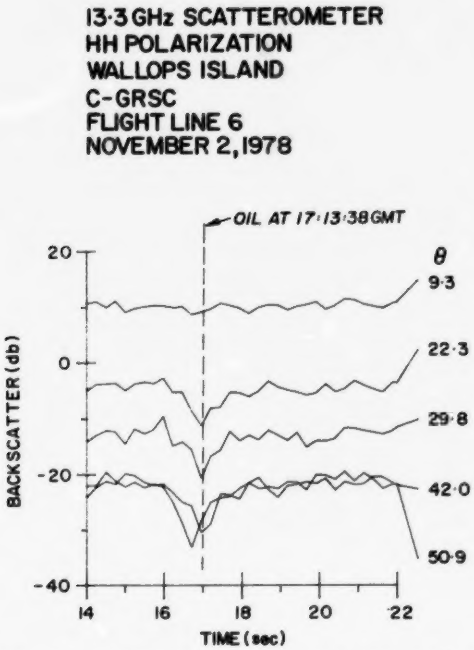

FIGURE 19 SCATTEROMETER, WALLOPS OIL SPILL. Microwave backscatter as a function of time for several incidence angles. C-GRSC Flight Line 3, November 2, 1978.

Polarization does not seem to be a significant factor in the results. The departure of cross from like polarized data in Figure 18 (VV, VH combinations) is inconsistent with the results in Figures 21 and 24 (HH, HV combinations). Reciprocity implies that the VH and HV results should be similar; the origin of the difference apparent in these results has not been determined to date.

In the diagrams of backscatter versus time (Figures 16,19,22) the data show a trend of higher oil to sea contrast as the incidence angle increases. The falloff shown in total sea return as the incidence angle increases is the normal dependence (Krishen, 1971).

The results summarized in Figures 18, 21, and 24 indicate:

i) suppression by oil of the ocean backscatter cross section is negligible for incidence angles less than 10°, increases to approximately 7 to 12 db for incidence angles between 30° to 55°, and falls to 5 to 7 db for an incidence angle of 60°.

ii) the combination of horizontally polarized transmit and receive radiation (HH) leads to comparable suppression of radar cross section when compared to VV data for incidence angles less than 60°.

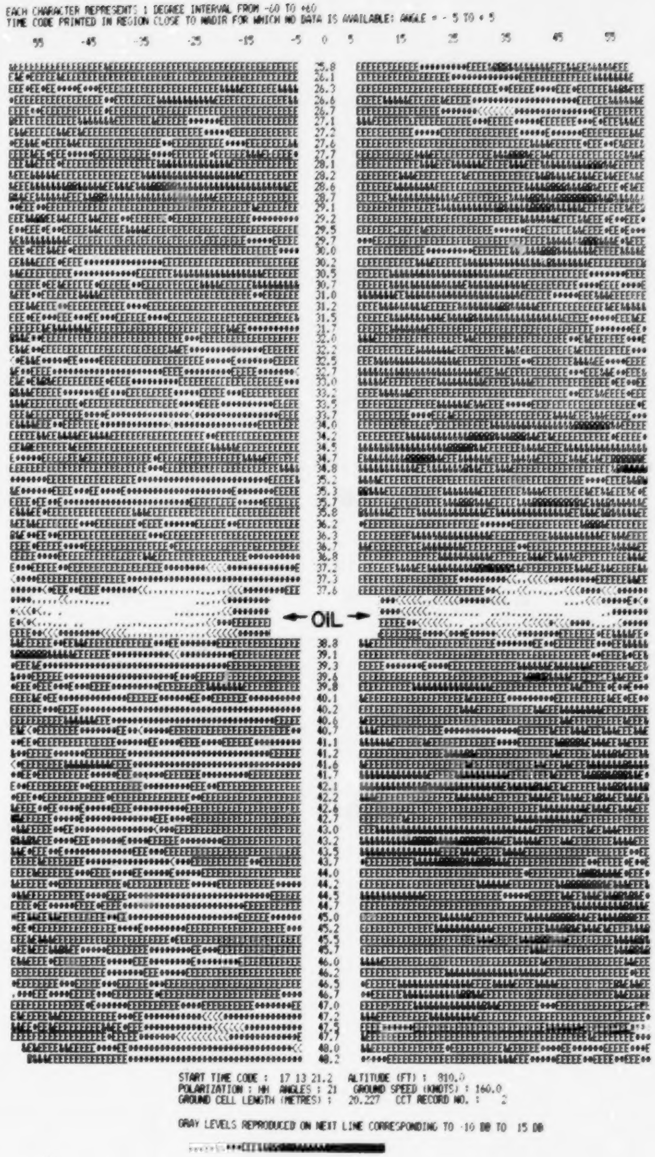

EACH CHARACTER REPRESENTS 1 DEGREE INTERVAL FROM -60 TO +60
TIME CODE PRINTED IN REGION CLOSE TO NADIR FOR WHICH NO DATA IS AVAILABLE: ANGLE = - 5 TO + 5

START TIME CODE : 17 13 21.2 ALTITUDE (FT) : 810.0
POLARIZATION : HH ANGLES : 21 GROUND SPEED (KNOTS) : 160.0
GROUND CELL LENGTH (METRES) : 20.227 CCT RECORD NO. : 2

GRAY LEVELS REPRODUCED ON NEXT LINE CORRESPONDING TO -10 DB TO 15 DB

13·3 GHz Microwave Scatterometer

Wallops Island

C-GRSC

Flight Line 6

HH Polarization

November 2, 1978

17:13:38 GMT

Differential Backscatter versus Look Angle

FIGURE 20 SCATTEROMETER, WALLOPS OIL SPILL. Densigram showing microwave backscatter depression for several incidence angles. C-GRSC Flight Line 6, November 2, 1978.

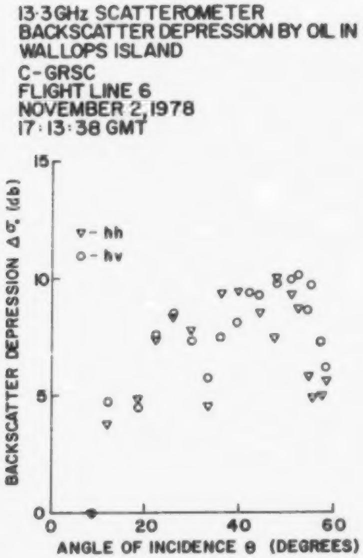

FIGURE 21 SCATTEROMETER, WALLOPS OIL SPILL. Microwave backscatter depression as a function of incidence angle. C-GRSC Flight Line 6, November 2, 1978.

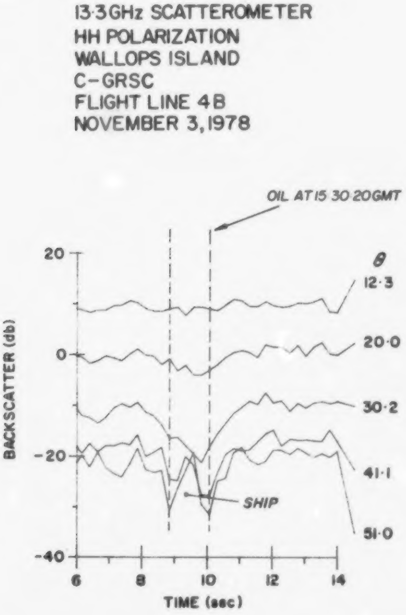

FIGURE 22 SCATTEROMETER, WALLOPS OIL SPILL. Microwave backscatter as a function of time for several incidence angles. C-GRSC Flight Line 4B, November 3, 1978.

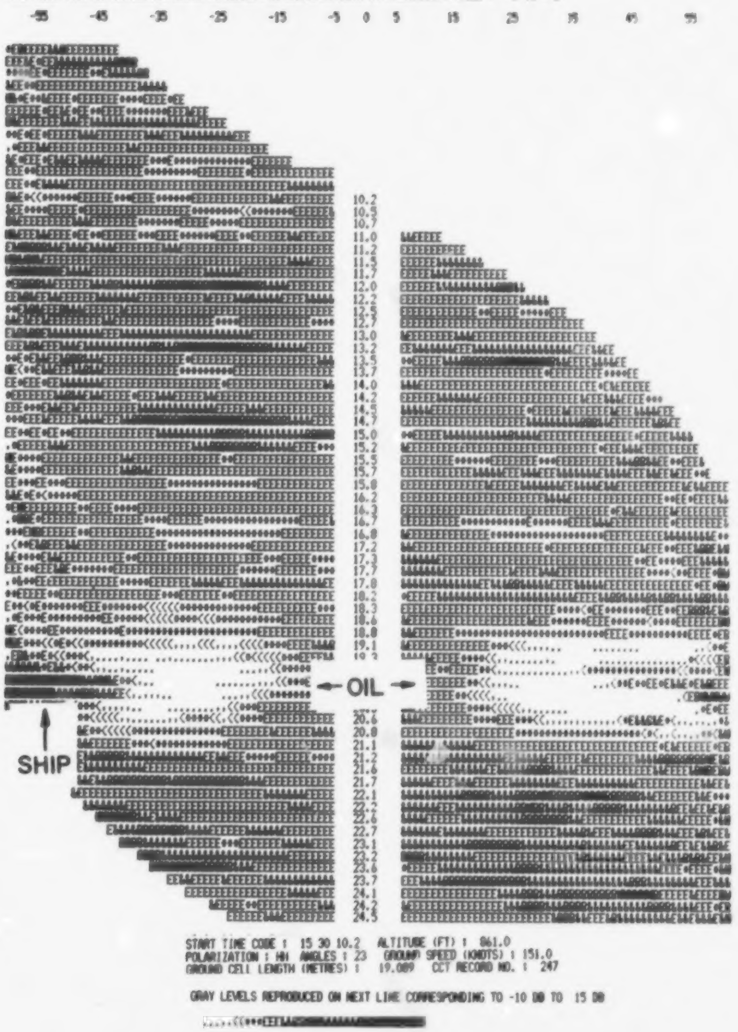

EACH CHARACTER REPRESENTS 1 DEGREE INTERVAL FROM -60 TO +60
TIME CODE PRINTED IN REGION CLOSE TO NADIR FOR WHICH NO DATA IS AVAILABLE: ANGLE = - 5 TO + 5

START TIME CODE : 15 30 10.2 ALTITUDE (FT) : 861.0
POLARIZATION : HH ANGLES : 23 GROUND SPEED (KNOTS) : 151.0
GROUND CELL LENGTH (METRES) : 19.089 CCT RECORD NO. : 247

GRAY LEVELS REPRODUCED ON NEXT LINE CORRESPONDING TO -10 DB TO 15 DB

13·3 GHz Scatterometer
Wallops Island
C – GRSC
Flight Line 4B
HH Polarization
November 3, 1978
Differential Backscatter versus
Look Angle

FIGURE 23 SCATTEROMETER, WALLOPS OIL SPILL. Densigram showing microwave backscatter depression for several incidence angles. C-GRSC Flight Line 4B, November 3, 1978.

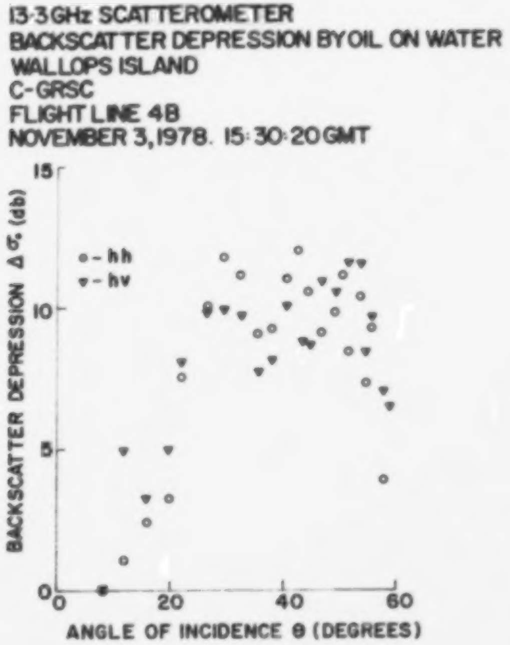

FIGURE 24 SCATTEROMETER, WALLOPS OIL SPILL. Microwave backscatter depression as a function of incidence angle. C-GRSC Flight Line 4B, November 3, 1978.

iii) neither cross polarized component of the backscatter radiation shows larger backscatter suppression than the like-polarized components.

4.4.1.2 ERIM SAR.

Scott Inlet oil seep. The ERIM SAR was operated on 5 sorties in C-GRSC at Scott Inlet. On these sorties no oil was detected by the SAR or any other sensor on C-GRSC: nor was oil observed by the personnel of C-GRSC operating on the same days. The X-band imagery gathered by the SAR was poor as a result of equipment malfunctions. Representative data from L band are shown in Figure 25. These SAR images are for VV polarization with a depression angle of 12° at image centre.

The SAR imagery in Figure 25 (frames 50 and 51) was collected on September 11, 1978 over a time span of approximately 4 minutes. The items of interest are the slick like features in Frame 51. There is no apparent sea clutter in Frame 50, only icebergs and bergy bits, while Frame 51 is covered by sea clutter and slick like features. It is obvious that these naturally occurring features will cause great problems in radar return

ERIM SAR Lvv (Frame 50)
Scott Inlet
C - GRSC
Flight Line 5
September 11, 1978
16:43:03 GMT (Image Centre)
12° Depression Angle at middle of the Image.
Altitude 610m, Swath Width 5.6 km

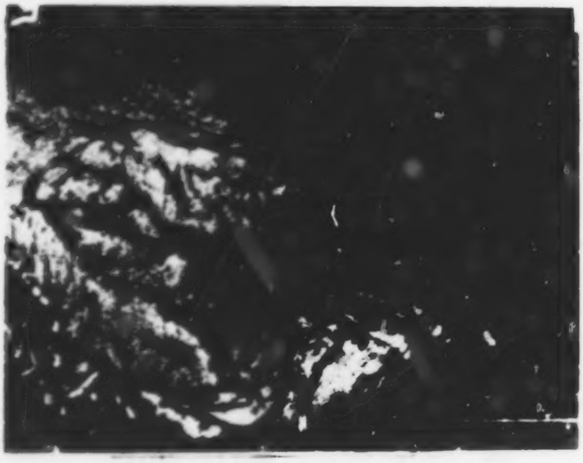

ERIM SAR Lvv (Frame 51)
Scott Inlet
C - GRSC
Flight Line 5
September 11, 1978
16:44:53 GMT (Image Centre)

FIGURE 25 ERIM SAR L_{VV} IMAGES, SCOTT INLET.
C-GRSC Flight Line 5, September 11, 1978.

interpretation during any search for oil slicks. These sea features were very common in the eastern Arctic during the Scott Inlet mission.

Many authors have used the datum set recorded with the ERIM SAR on the Scott Inlet mission for analysis on sea ice and icebergs (Gray et al., 1979; Lowry et al., 1979; Kirby and Lowry, 1979).

Wallops Island test oil spills. The two test spills of November 2 and 3, 1978 were imaged by the SAR in both X and L bands with horizontal transmit polarization and the antenna in the steep (43°) depression mode. The SAR imaged the slick on nine of the flight lines flown at an altitude of 5.5 km. Contrast between the oil slick and surrounding ocean was good in the X_{HH} images (Figure 26), not so good in the L_{HH} images and poor in both X_{HV} and L_{HV} images. Oil slick to ocean contrast did not exhibit any apparent change with different look directions relative to the wind direction. This may be because the oil slicks were imaged at relatively large depression angles (33° to 49°).

A confusing factor in the identification of oil slicks in SAR imagery is the occurrence of a darkened area in the neighbourhood of a bright target, e.g., a ship; this is referred to as small signal suppression and is common in the SAR detection of strong signals. (Subsequent to the acquisition of this imagery, the ERIM SAR has been modified so that this problem has been almost totally eliminated.) Examples are seen in Figure 26, where a ship is stationed to either side of the slick; the effects of small signal suppression are observed near the ships in the image. These darkened areas near the ships might be mistaken for oil slicks; however, an experienced observer can distinguish between the two phenomena by differences in the spatial patterns. Also seen on the right side of the image (Figure 26) is a tugboat pulling a barge with a large wake behind.

4.4.2 Near Ultraviolet, Visible, Near Infrared. Presented in this section is the imagery and analysis of data collected by those sensors operating in the near ultraviolet, visible, and near infrared regions of the electromagnetic spectrum. This includes the photography provided by the Wild Heerbrugg RC10 camera in the visible and near IR, and by the Vinten camera in the visible and near UV; the LLLTV imagery; the multispectral scanner imagery in the visible and near IR; the UV imagery obtained with the dual channel scanner; and the MEIS imagery obtained in selected regions in the visible.

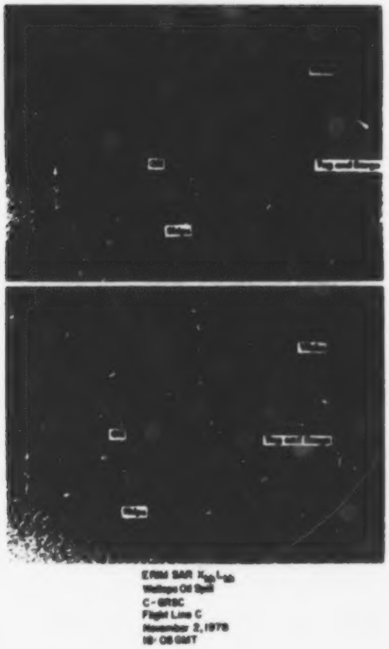

FIGURE 26 ERIM SAR X_{HH} AND L_{HH} IMAGES, WALLOPS OIL SPILL. C-GRSC Flight Line C, November 2, 1978.

4.4.2.1 Photography.

Film types. Since many experiments and studies had been performed (Munday, 1971; Wobber, 1971; Thomson and McColl, 1972; de Villiers, 1973; Thomson et al., 1974; Axelsson, 1975) prior to the outset of the AMOP remote sensing project, experimentation with different film types was not planned. Results obtained by the above investigators indicated that two types of photography would be adequate for the present study: colour and ultraviolet.

The Kodak type 2445 Aerocolour negative film used produced generally good photographs when illumination was sufficient. The colour photographs revealed good detail in the slick regions, discriminated between thin and thick areas, and provided good visual records for the different oil spill missions. Although thin areas of the oil slick could be discerned in the colour photography, the water/oil contrast was not very high.

Kodak type 2405 Double-X Aerographic film was used in conjunction with a Wratten 18A filter on the camera in order to produce ultraviolet photographs. The ultraviolet photographs provided better water/oil contrast than did the colour photography; however, they provided little, if any, discrimination between thin and thick slick areas (see Appendix F). The use of ultraviolet photography was intended to exploit the high oil to water contrast in the surface reflected radiance. Expectations were borne out by the results (see Appendix F). Although a camera malfunction on the Scott Inlet mission prevented acquisition of UV photography of the oil slick in the Arctic, doubts concerning the availability of adequate UV illumination at low (20°) sun elevations were apparently unfounded judging from UV photography of the sea surface. (The Vinten UV camera was operated at f/2 and 1/500 s for all missions.)

Colour photography was obtained during the KURDISTAN incident for oil-in-ice conditions. Good contrast was obtained with type 2445 Aerocolour negative film; differentiation of oil-ice mixtures from water-ice mixtures was possible, but difficult under some lighting conditions. Kodak type 2443 Aerochrome infrared film using a "minus blue" filter was also tried over oil-in-ice. The contrast obtained between oil and ice was good to average; however, the discrimination of oil-ice mixtures from water-ice mixtures was poor to negligible, making oil identification impossible. For this reason the use of colour infrared film with this filter is not recommended for detection of oil-ice and water-ice mixtures (O'Neil et al., 1982). Results from this study and previous studies surveyed indicate that both colour photography and ultraviolet photography can provide imagery adequate for the detection of oil on water. Axelsson (1975) found that near-IR photography yielded better contrast than ultraviolet photography on cloudy days. Near-IR photography of oil on water was not obtained as part of this study; however, other observers involved with the KURDISTAN spill used near-IR photography for this purpose with very poor results. For oil on or in ice, both UV and colour photography can be expected to delineate the oil. The UV should provide higher contrast but at the sacrifice of the spectral information present in the colour photography. In the more variable oil-water-ice mixture it is doubtful that, even together, the UV and colour photography would be sufficient.

Cameras. Two types of cameras were used during this project: a Wild Heerbrugg RC10, a 23 cm format survey camera and a Vinten 70 mm format camera (see Appendix A).

The RC10 cameras were used with type 2445 Aerocolour negative and type 2443 Aerochrome infrared film; they performed well and produced excellent quality photography. The only drawback in using this type of camera is the excess weight.

The Vinten cameras were used for both colour and ultraviolet photography; they also produced very good quality photographs. However, their reliability, particularly in cold weather, was poor. If a 70 mm format is desired, Vinten cameras are not recommended, especially not during cold climate conditions.

4.4.2.2 Low-light-level television.

Montreal Island oil spill. The low-light-level television was flown on the Montreal Island mission June 30-July 1, 1978. For this mission the camera was not yet fitted with the Corning 7-51 filter and HNP'B polarizer; the camera was also nadir looking. The imagery displayed in real time was good during twilight conditions but poor during night conditions. No data are presented here since a 1/2" low resolution video recorder was used on this flight, and the resultant reproduced imagery is not representative of the quality of the video data presented by the television system in real time.

The video imagery observed over Montreal Island harbour appeared to have sufficient dynamic range and sensitivity in order to detect oil on water at night. Oil was not detected, however, because the presence of one harbour or ship's light in the camera's field of view caused the automatic gain control and the automatic iris to reduce the sensitivity drastically. When there were no lights in the field of view, the television camera produced a good picture with some detail visible in the water; unfortunately, those night scenes containing oil also included artificial light sources.

In order to use a low-light-level television in a situation in which harbour or ships' lights will be in the field of view, the addition of an automatic iris/eclipser control system to the video camera is recommended.

Scott Inlet oil seep. The low-light-level television system, filtered, proved to be the most sensitive sensor for detecting oil on the Scott Inlet mission. All the other optical sensors had difficulty detecting oil and producing good imagery because of the small amount of sunlight available in September at 71°N. The low light level coupled with the thin, scattered character of the oil slick at Scott Inlet made oil detection difficult for most sensors; the low-light-level television, on the other hand, produced good imagery, and detected oil on 9 flight lines. (The production of scan prints is discussed in Appendix F.4.)

With the low-light-level television system there are some difficulties in distinguishing oil from foam and whitecaps on very rough waters; however, experienced operators, by using spatial patterns and persistence times, can usually interpret the video imagery satisfactorily.

Wallops Island test oil spills. The low-light-level television system produced excellent imagery over the two test oil spills at Wallops. The television system was not only used for oil detection but also served as a tactical display for the pilots of the aircraft C-GRSA. The high contrast television image enabled the pilots to get a good view of the oil spill with discrimination against wind slicks and other anomalies in the area.

As described in Section 4.1.2, the contrast of oil on water is optimized at Brewster's angle. A series of images demonstrating the variation of contrast with viewing angle is shown in Figure 27. The contrast is good at 17:11:36 GMT (approximately Brewster's angle); fair at 17:11:20 and 17:11:45 GMT; and poor at 17:11:49 GMT. The dark object in the centre of the slick is the ANNANDALE. This sequence of images was recorded at an altitude of 1100 metres.

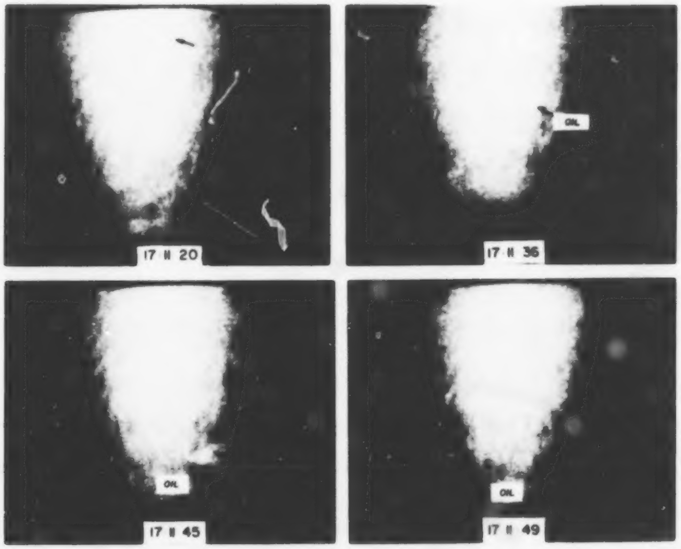

Low Light Level Television
Wallops Oil Spill
C - GRSA
Flight Line 2
November 2, 1978
17 11 20 - 49 GMT

Contrast Wax and Wane as Oil Spill
passes through Brewster's Angle

FIGURE 27 LOW-LIGHT-LEVEL TELEVISION, WALLOPS OIL SPILL. A sequence of four frames showing contrast wax and wane as an oil spill passes through Brewster's angle in the field of view of the television camera. C-GRSA Flight Line 2, November 2, 1978.

Another example of an image which depicts an oil spill at lower altitude (150 m) is shown in Figure 28. The photograph of a television monitor loses the dynamic quality present in video imagery, with the result that the imagery effectiveness is reduced from that of the original television picture. Scan prints of the oil spills, Figures 29-32, retain the content of the oil spill image, demonstrating the high contrast attainable with this system, but still lack the dynamic quality. It is this dynamic quality, present in the original video image, that is one of the main advantages of a television system; this effect is, however, difficult to reproduce in a static representation.

KURDISTAN oil spill. The low-light-level television system was flown on five sorties in the search for oil during the KURDISTAN incident. When the television system was flown over oil on water, the system detected oil with good contrast, producing images similar to those depicted here for Scott Inlet and Wallops Island missions. On March 23, 1978, sortie 5, when the television system imaged both oil and ice on the water; it was very difficult to distinguish small pieces of floating ice from small patches of oil. Larger ice floes could be distinguished by their spatial form or location with respect to land.

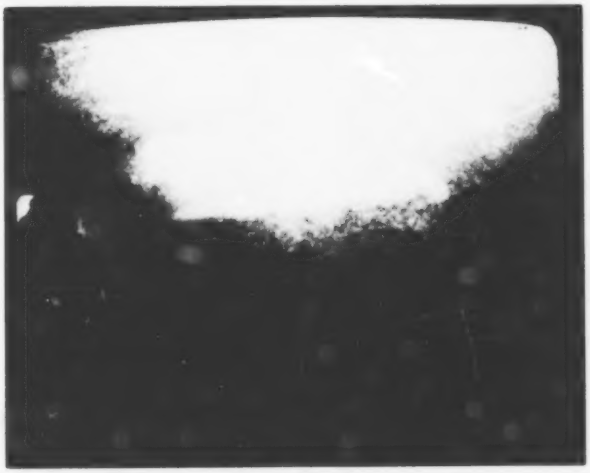

Low Light Level Television
Wallops Oil Spill
C-GRSA
Flight Line 6
November 2, 1978
17:30:58 GMT

FIGURE 28 LOW-LIGHT-LEVEL TELEVISION, WALLOPS OIL SPILL. Photograph of a TV monitor showing oil slick. C-GRSA Flight Line 6, November 2, 1978.

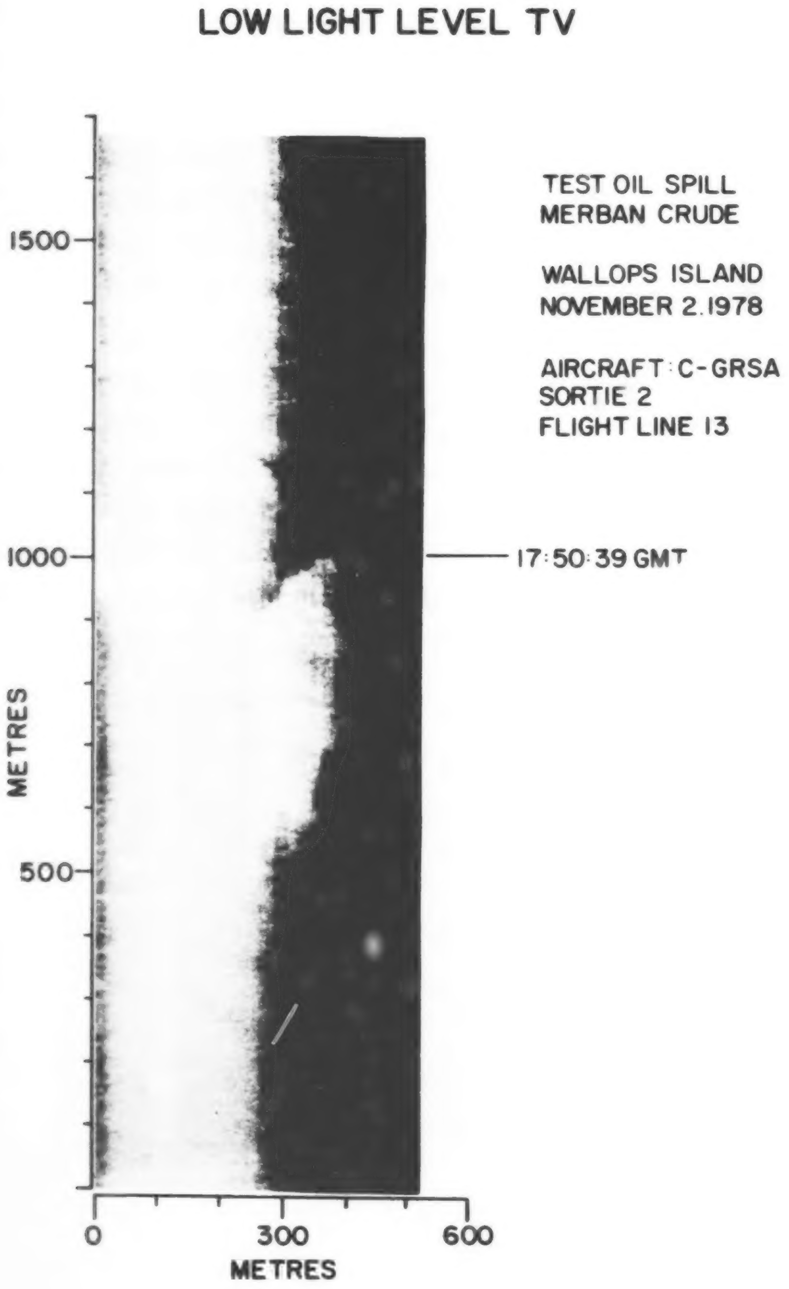
LOW LIGHT LEVEL TV
TEST OIL SPILL
MERBAN CRUDE
WALLOPS ISLAND
NOVEMBER 2.1978
AIRCRAFT: C-GRSA
SORTIE 2
FLIGHT LINE 13
17:50:39 GMT
1500
1000
500
METRES
0
300
600
METRES

FIGURE 29 LOW-LIGHT-LEVEL TELEVISION, WALLOPS OIL SPILL. Scan print of Murban crude oil spill. C-GRSA Flight Line 13, November 2, 1978.

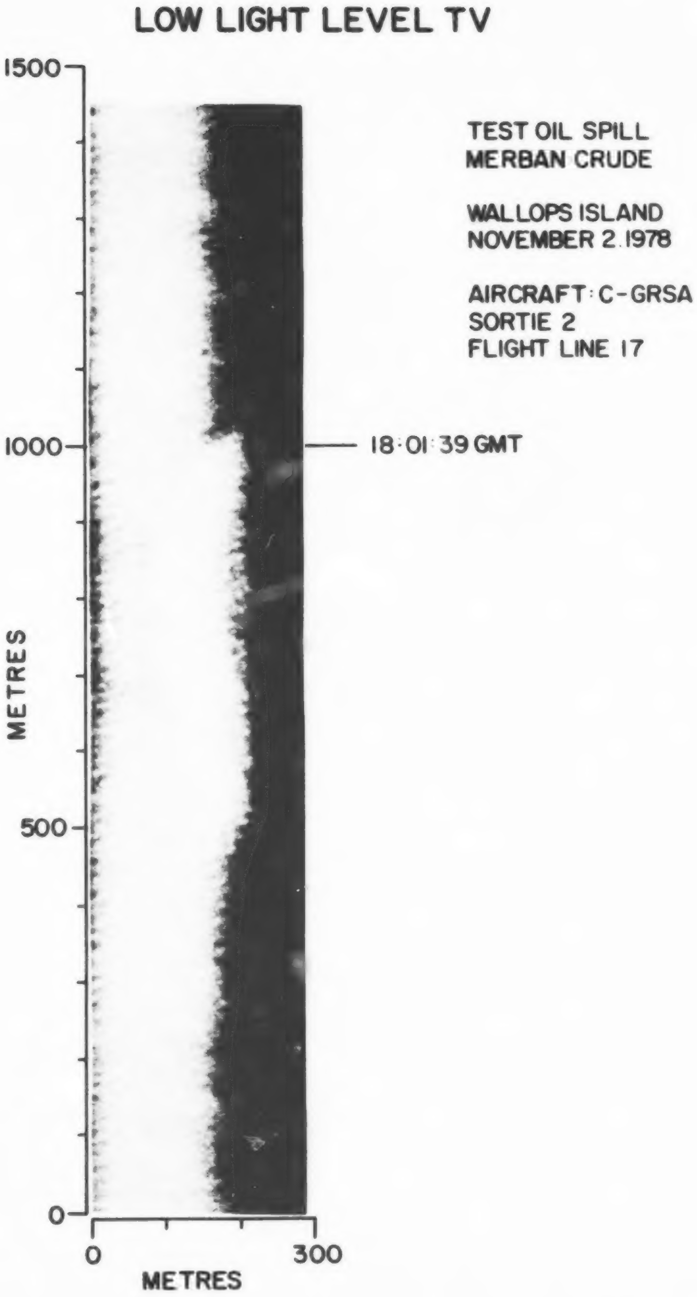
LOW LIGHT LEVEL TV
1500
1000
500
0
METRES
0
300
METRES
TEST OIL SPILL
MERBAN CRUDE
WALLOPS ISLAND
NOVEMBER 2 1978
AIRCRAFT: C-GRSA
SORTIE 2
FLIGHT LINE 17
18:01:39 GMT

FIGURE 30 LOW-LIGHT-LEVEL TELEVISION, WALLOPS OIL SPILL. Scan print of Murban crude oil spill. C-GRSA Flight Line 17, November 2, 1978.

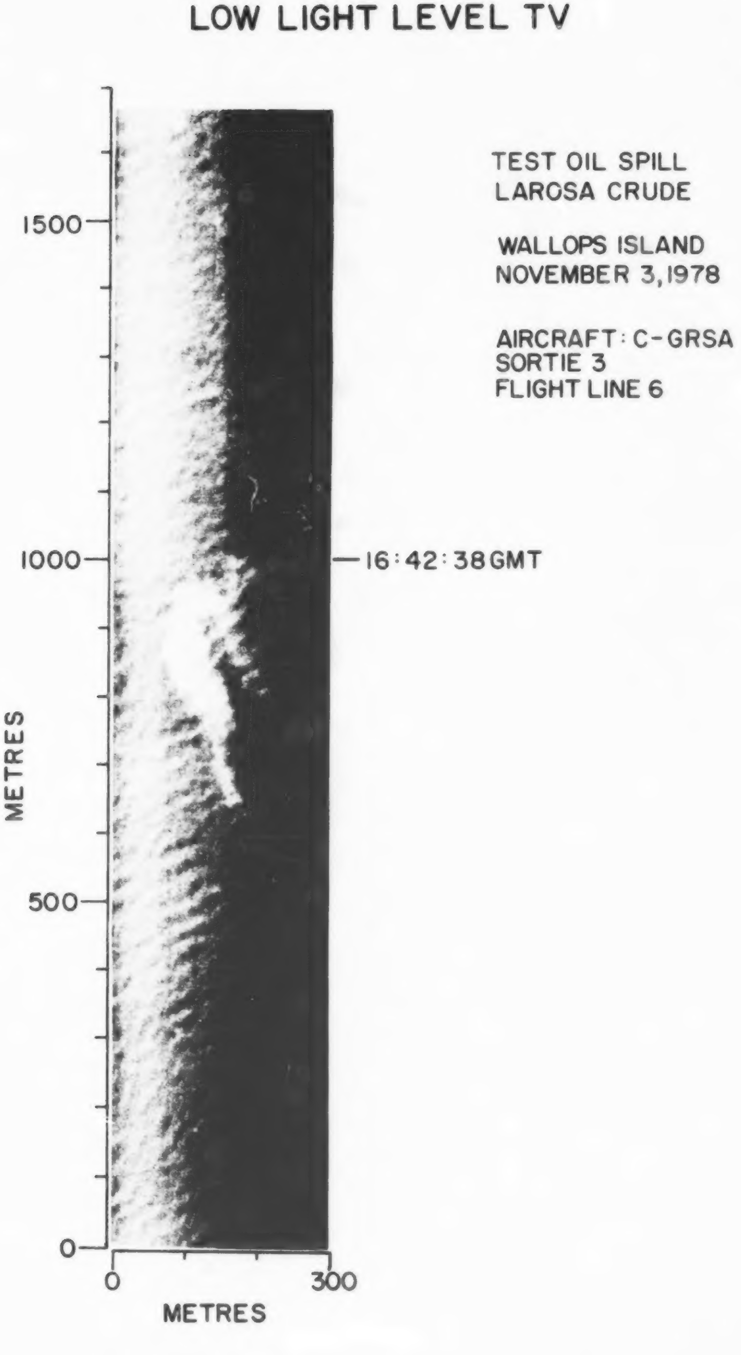
LOW LIGHT LEVEL TV
TEST OIL SPILL
LAROSA CRUDE
WALLOPS ISLAND
NOVEMBER 3, 1978
AIRCRAFT: C-GRSA
SORTIE 3
FLIGHT LINE 6
16:42:38 GMT
1500
1000
500
0
METRES
0
300
METRES

FIGURE 31 LOW-LIGHT-LEVEL TELEVISION, WALLOPS OIL SPILL. Scan print of La Rosa crude oil spill. C-GRSA Flight Line 6, November 3, 1978.

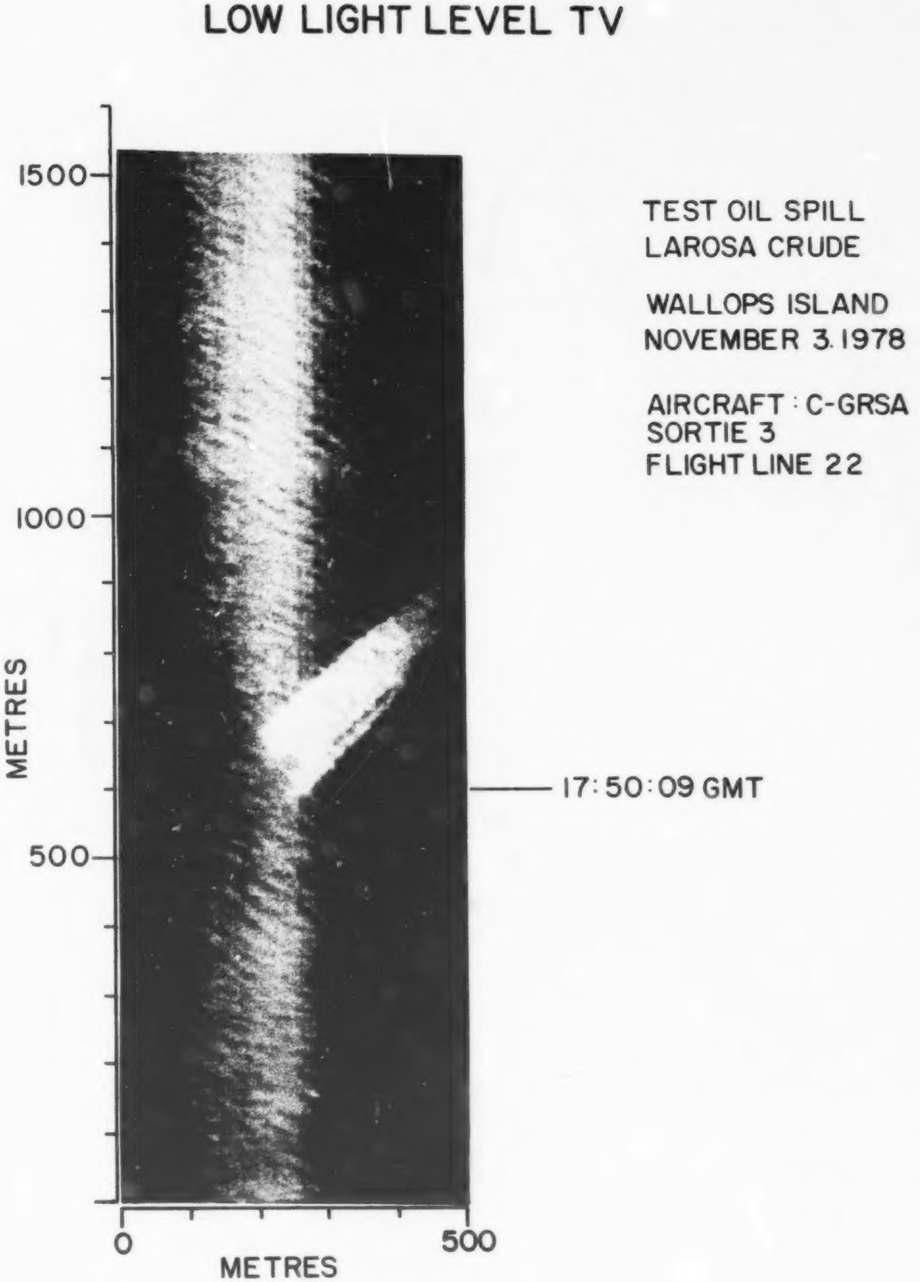
LOW LIGHT LEVEL TV
1500
1000
500
METRES
0
500
METRES
TEST OIL SPILL
LAROSA CRUDE
WALLOPS ISLAND
NOVEMBER 3.1978
AIRCRAFT : C-GRSA
SORTIE 3
FLIGHT LINE 22
17:50:09 GMT

FIGURE 32 LOW-LIGHT-LEVEL TELEVISION, WALLOPS OIL SPILL. Scan print of La Rosa crude oil spill. C-GRSA Flight Line 22, November 3, 1978.

The low-light-level television system was not flown over the oil-in-ice present on March 29 and April 2, 1978. Consequently, no conclusions can be drawn on the performance of the low-light-level television in this case. Nevertheless, the good contrast available in the UV implies that the low-light-level television would easily detect the dark oil against the bright ice; however, it is doubtful that oil-in-ice could be distinguished from water-ice mixtures.

4.4.2.3 **MSS.** MSS data were acquired on three missions: Wallops Island, Scott Inlet and the KURDISTAN spill. The majority of the good oil spill imagery was obtained on the Wallops Island mission and, hence, the main analysis effort has been expended on these data.

Wallops Island test oil spills. Imagery was obtained over two test oil spills: the first, on November 2, 1978 was Murban crude, a relatively light crude oil; the second, on November 3, 1978 was the relatively heavy La Rosa crude. These two oils, primarily because of their different emulsification properties, exhibited quite different spectral reflectance characteristics. This can be seen by comparing the two series of images, one of Flight Line 9 on November 2, the other of Flight Line 22 on November 3. In each series there is one image for each of seven visible and near IR bands. The corresponding thermal IR images are also presented and discussed. The contrast has been enhanced by grey level slicing and colour coding (see Appendix F). That is, for each image only those digital levels in the recorded data that correspond to the radiance levels reflected from the oil have been selected from the total of 256. In the printing process only the pixels with these digital levels have been "turned on". If there are two or more radiance levels corresponding to distinct regions within the oil slick these are coded with different colours. In the text this series is shown in black and white with the thin slick regions appearing grey and the thick, white, when the two regions can be distinguished. The straight horizontal, or cross track, lines visible in some of the imagery are the result of electromagnetic interference from the firing of the Vinten cameras.

The images of the Murban crude oil, Flight Line 9 of November 2, 1978, show that the whole oil slick, including the thin slick area, is detected in bands 2 through 8 (see Figures 33 to 39). Band 9 sees thicker oil layers quite well, but the thin areas only very faintly (see Figure 38). Band 10 detects only the thick regions (see Figure 39). Bands 6 and 8 distinguish the thick regions from the thin, the thick giving higher radiance levels (see Figures 36 and 37). It is apparent in the imagery that the lower bands with shorter

MSS 2

Grey Tone Colour Enhanced

Wallops Oil Spill

C-GRSA

Flight Line 9

November 2, 1978

FIGURE 33 MSS 2, WALLOPS OIL SPILL. C-GRSA Flight Line 9, November 2, 1978.

MSS 3

Grey Tone Colour Enhanced

Wallops Oil Spill

C-GRSA

Flight Line 9

November 2, 1978

FIGURE 34 MSS 3, WALLOPS OIL SPILL. C-GRSA Flight Line 9, November 2, 1978.

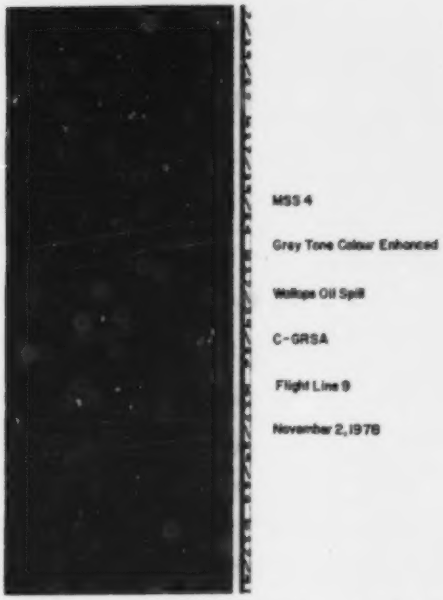
MSS 4
Grey Tone Colour Enhanced
Wallops Oil Spill
C-GRSA
Flight Line 9
November 2, 1978

FIGURE 35 MSS 4, WALLOPS OIL SPILL. C-GRSA Flight Line 9, November 2, 1978.

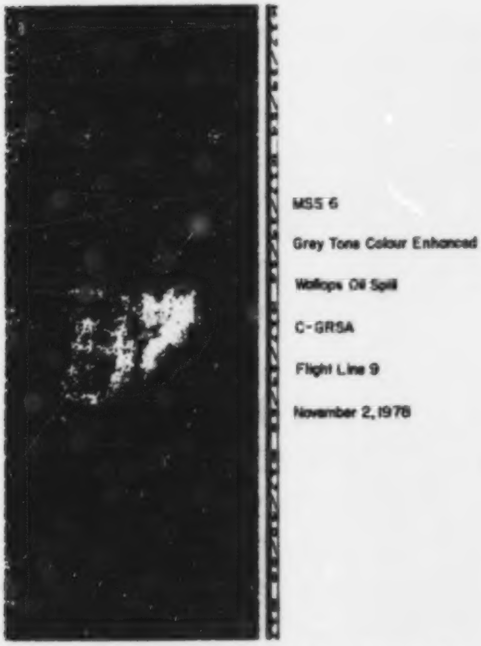
MSS 6
Grey Tone Colour Enhanced
Wallops Oil Spill
C-GRSA
Flight Line 9
November 2, 1978

FIGURE 36 MSS 6, WALLOPS OIL SPILL. C-GRSA Flight Line 9, November 2, 1978.

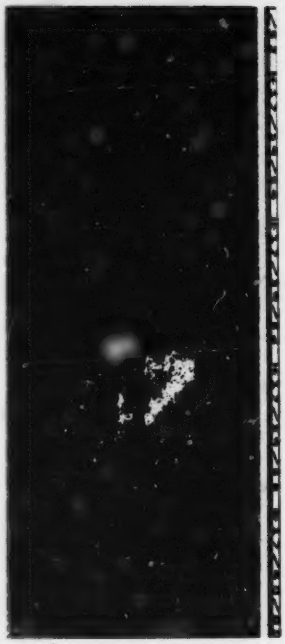
MSS 8
Grey Tone Colour Enhanced
Wallops Oil Spill
C-GRSA
Flight Line 9
November 2, 1978

FIGURE 37 MSS 8, WALLOPS OIL SPILL. C-GRSA Flight Line 9, November 2, 1978.

MSS 9
Grey Tone Colour Enhanced
Wallops Oil Spill
C-GRSA
Flight Line 9
November 2, 1978

FIGURE 38 MSS 9, WALLOPS OIL SPILL. C-GRSA Flight Line 9, November 2, 1978.

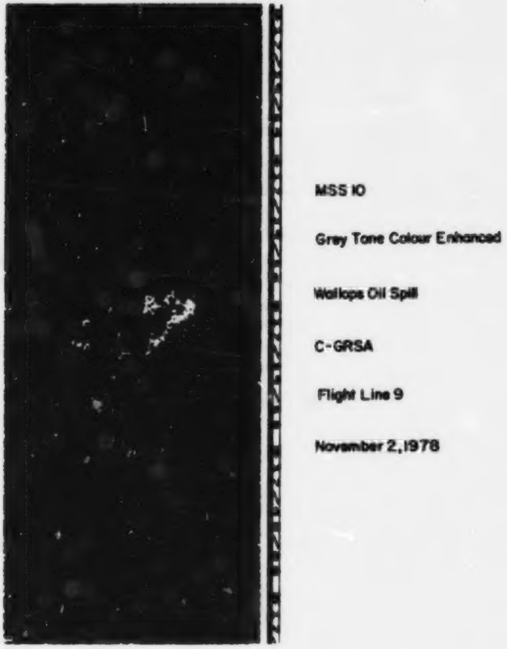

FIGURE 39 MSS 10, WALLOPS OIL SPILL. C-GRSA Flight Line 9, November 2, 1978.

wavelengths detect the thin oil layers; the higher bands with longer wavelengths, the thicker layers. One must conclude from the imagery that, for the light Murban crude, MSS bands 3 - 8 provide the best oil slick detection, with bands 6 and 8 distinguishing the thick from the thin regions.

The La Rosa crude imagery of Flight Line 22, November 3, 1978, exhibits a somewhat different spectral response (see Figures 40 to 46). The thin parts of the slick are detected in MSS bands 2 through 9 and marginally in band 10. In contrast to the Murban crude, the thick oil regions, coded white in the imagery, are detected as areas where the radiance is less than that for water in bands 3 and 4. The longer wavelength bands 6 - 10 do not distinguish the thick oil as bright regions as they do for Murban crude. The reason for this different behaviour is indicated in the RC10 photographs of the two oil spills (see Figures 47 and 48). The thick regions of the Murban crude appear bright and those of the La Rosa crude appear dark. It has been substantiated from on-site observations (private communication, J.C. Johnson, JBF Scientific, 1979) that the lighter

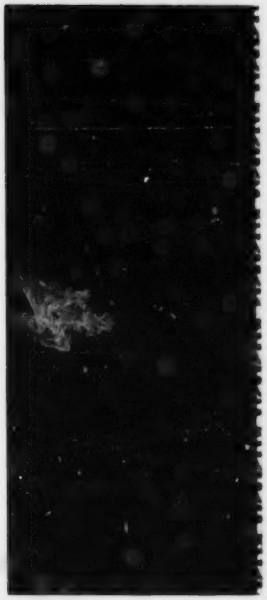

MSS 2
Grey Tone Colour Enhanced
Wallops Oil Spill
C-GRSA
Flight Line 22
November 3, 1978

FIGURE 40 MSS 2, WALLOPS OIL SPILL. C-GRSA Flight Line 22, November 3, 1978.

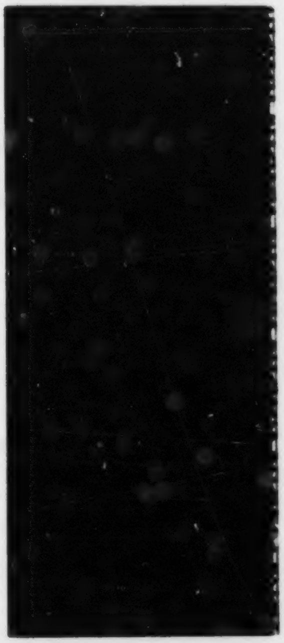

MSS 3
Grey Tone Colour Enhanced
Wallops Oil Spill
C-GRSA
Flight Line 22
November 3, 1978

FIGURE 41 MSS 3, WALLOPS OIL SPILL. C-GRSA Flight Line 22, November 3, 1978.

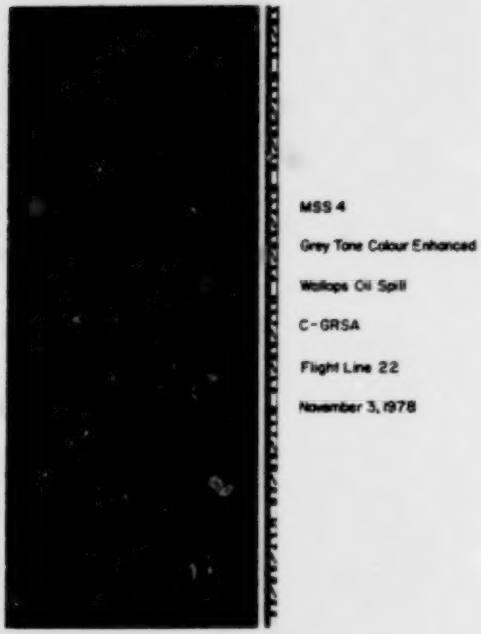
MSS 4
Grey Tone Colour Enhanced
Wallops Oil Spill
C-GRSA
Flight Line 22
November 3, 1978

FIGURE 42 MSS 4, WALLOPS OIL SPILL. C-GRSA Flight Line 22, November 3, 1978.

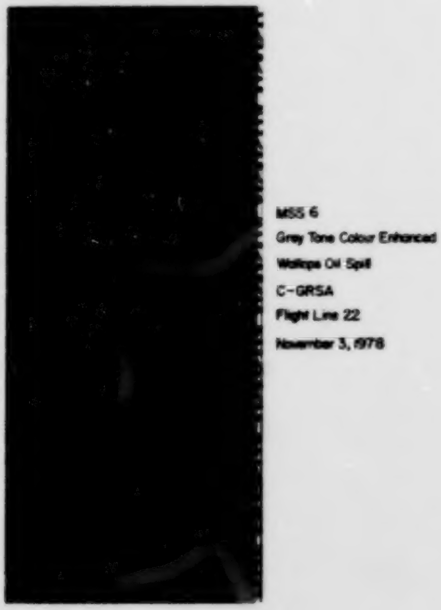
MSS 6
Grey Tone Colour Enhanced
Wallops Oil Spill
C-GRSA
Flight Line 22
November 3, 1978

FIGURE 43 MSS 6, WALLOPS OIL SPILL. C-GRSA Flight Line 22, November 3, 1978.

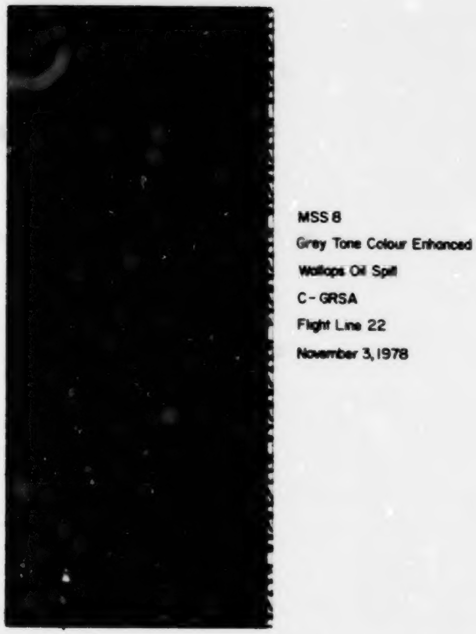
MSS 8
Grey Tone Colour Enhanced
Wallops Oil Spill
C-GRSA
Flight Line 22
November 3, 1978

FIGURE 44 MSS 8, WALLOPS OIL SPILL. C-GRSA Flight Line 22, November 3, 1978.

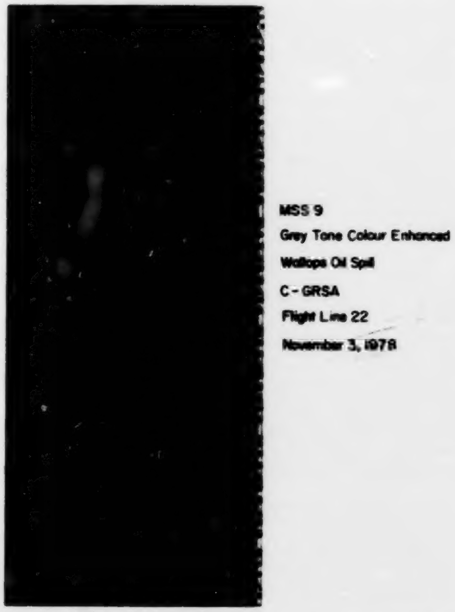
MSS 9
Grey Tone Colour Enhanced
Wallops Oil Spill
C-GRSA
Flight Line 22
November 3, 1978

FIGURE 45 MSS 9, WALLOPS OIL SPILL. C-GRSA Flight Line 22, November 3, 1978.

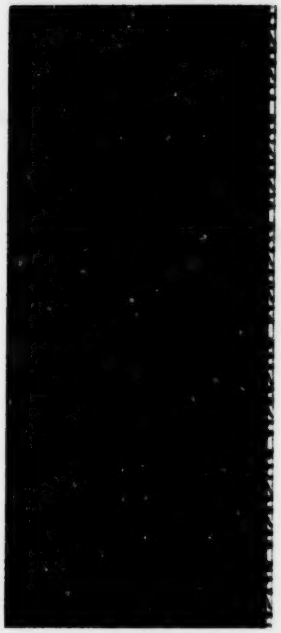

MSS 10
Grey Tone Colour Enhanced
Wallops Oil Spill
C-GRSA
Flight Line 22
November 3, 1978

FIGURE 46 MSS 10, WALLOPS OIL SPILL. C-GRSA Flight Line 22, November 3, 1978.

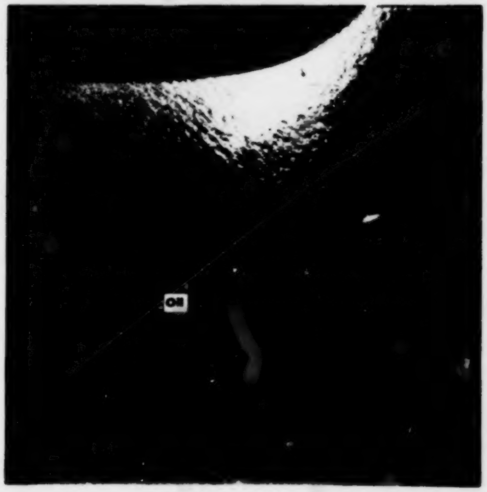

RC10 23cm Format Camera
2445 Aerocolour Negative Film
Wallops Oil Spill
C-GRSC
Flight Line 6
November 2, 1978
17 13 38 GMT

FIGURE 47 RC-10 PHOTOGRAPH, WALLOPS OIL SPILL. C-GRSC Flight Line 6, November 2, 1978.

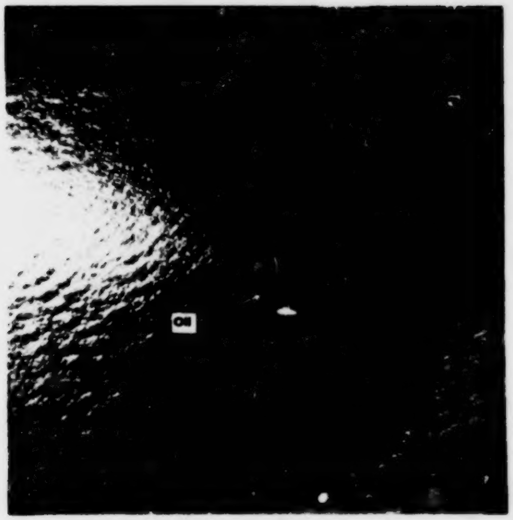

RC 10 23cm Format Camera
2445 Aerocolour Negative Film
Wallops Oil Spill
C-GRSC
Flight Line 4B
November 3, 1978
15 30 19 GMT

FIGURE 48 RC-10 PHOTOGRAPH, WALLOPS OIL SPILL. C-GRSC Flight Line 4B, November 3, 1978.

weight Murban crude has become emulsified during the dumping procedure, whereas the heavier La Rosa crude has not. The large number of oil in water, or water in oil, droplets present in the emulsified oil produces a high concentration of light scatterers. This results in a larger volume scattered component from the emulsified oil than from the unemulsified oil. The thin films, for both types of oil, are visible as regions of increased radiance because of the greater surface reflectance for oil. At the same time, because of the oil's increased absorptivity, especially for the shorter wavelengths, the thick oil layers reduce the radiation that is volume reflected by the water beneath the oil. This would normally act to reduce the total radiance detected by the sensor in the shorter wavelength bands; such is the case for the La Rosa crude. If, however, the oil is emulsified, the increased radiance resulting from volume scattering within the oil can be sufficient both to compensate for the reduction caused by absorption in the shorter wavelength bands, and to produce a significantly higher reflectance in the long wavelength bands. This, of course, is the case for the Murban crude.

Appearing in the MSS imagery, particularly in bands 8-10, are striations aligned at approximately 80° relative to the cross track direction. These are caused by electromagnetic interference picked up by the sensor. The problem becomes most serious in bands 9 and 10 where the water radiance levels fall below the sensitivity limits of the sensor; this, coupled with the added electromagnetic interference, prevents the calculation of meaningful radiance and contrast values for these two bands.

The variation in oil-water contrast as a function of MSS band, or spectral wavelength, as indicated in this imagery may in fact differ from the true contrast in absolute radiance terms. The reason is that the contrast apparent in this imagery is a result of the convolution of the true contrast with two additional functions, the sensor response and the data processing. This is evident from the DCLS UV image of the Murban oil spill displayed in Figure 49; the apparent contrast in this image is markedly better than in the MSS band 2 image of Figure 33. This improvement is due in part to the higher true contrast in the UV, and in part to the better detector performance.

DCLS UV(left) IR(right)
Colour Enhanced Images
Wallops Oil Spill
C-GRSC
Flight Line 6
November 2, 1978

FIGURE 49 DCLS, WALLOPS OIL SPILL. UV and IR colour enhanced images. C-GRSC Flight Line 6, November 2, 1978.

To determine the true contrast K, the absolute radiances of the oil (N_o) and the water (N_w) must be calculated. The contrast is then found from the defining equation.

$$K = \frac{N_o - N_w}{N_o + N_w} \tag{17}$$

These calculations have been performed for the two MSS flight lines of the Wallops Island mission imaged in Figures 33 to 38 and the three DCLS flight lines of Figures 49, 50 and 51; the results are listed in Table 1. The calculated contrasts for the thin oil film regions for both oil types are seen to follow the same wavelength dependence: higher at 17% in the UV, dipping to a minimum of 6% in the 500-600 nm range, and increasing slightly to 9% at 725 nm. The thick oil contrasts are remarkably similar for the two oils for the 325-425 nm region, decreasing from 9% at 325 nm to 5% at 425 nm. They then diverge markedly for the remaining range; the emulsified oil increasing steeply with wavelength from a minimum of 4% at 475 nm to 34% at 725 nm and the non-emulsified oil decreasing to negative values between 450 and 600 nm, with a minimum of -3% at 525 nm increasing to 9% at 725 nm.

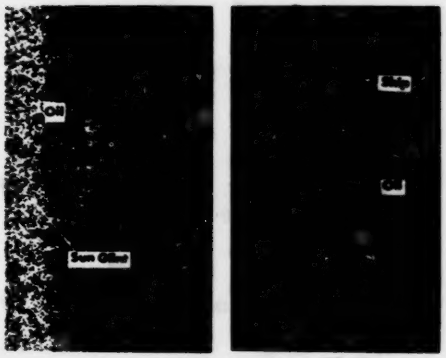

DCLS UV(left) IR(right)
Wallops Oil Spill
C-GRSC
Flight Line 7
Aircraft Altitude 5·5 km
November 2, 1978
17:39:00 GMT

Images are not geometrically correct, they should be reduced 4·5x in the along track direction

FIGURE 50 DCLS, WALLOPS OIL SPILL. UV and IR colour enchanced images. C-GRSC Flight Line 7, November 2, 1978. Altitude 5.5 km, 17:39:00 GMT. Images are not geometrically correct, they should be reduced 4.5 x in the along track direction.

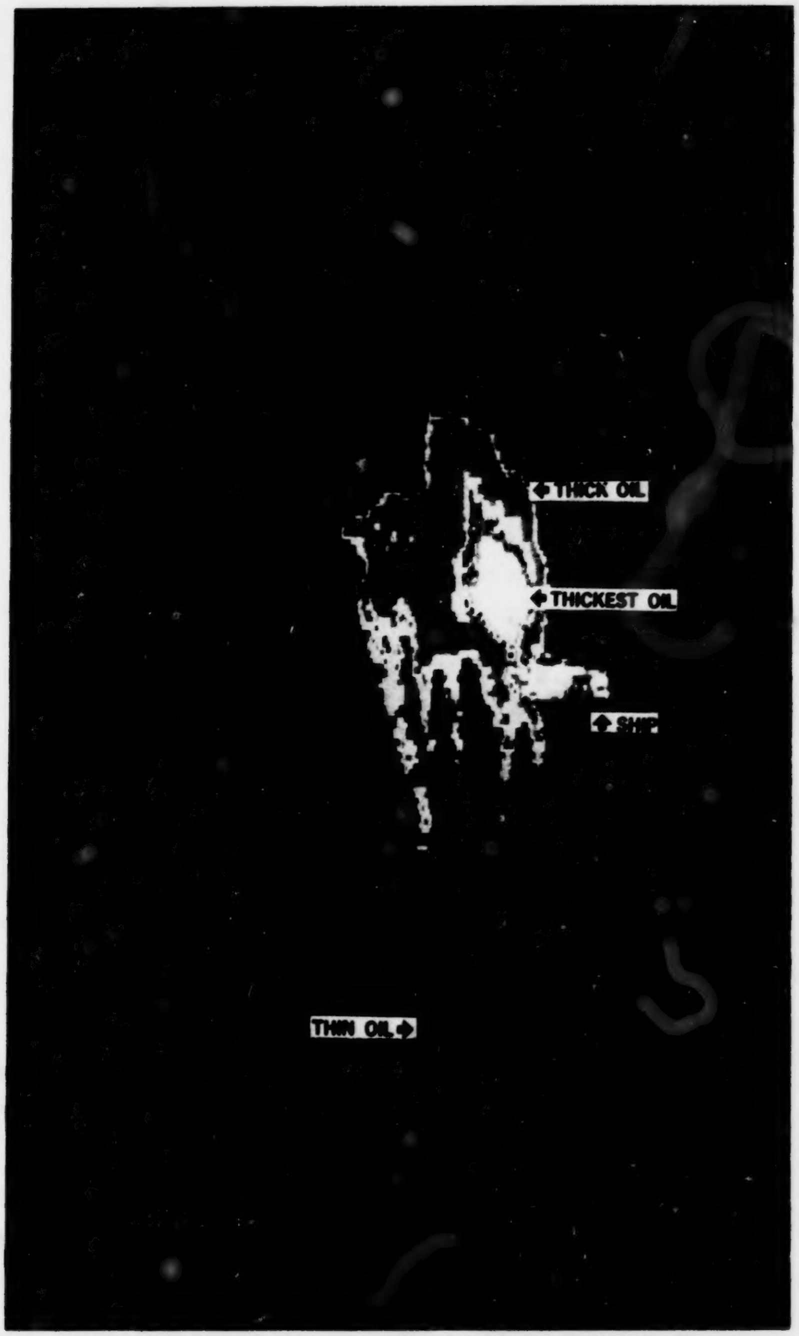
THICK OIL
THICKEST OIL
SHIP
THIN OIL

DCLS Thematic Colour Image

UV IR

Wallops Oil Spill

C-GRSC

Flight Line 4B

November 3, 1978

15:31:06 GMT

FIGURE 51 DCLS THEMATIC COLOUR IMAGE, WALLOPS OIL SPILL. C-GRSC Flight Line 4B, November 3, 1978.

TABLE 1 MSS AND DCLS MEASURED SPECTRAL RADIANCES

Wallops Island Mission		UV 300 - 370 (nm)		2 415-450 (nm)	3 445-495 (nm)	4 500-550 (nm)	6 590-645 (nm)	8 680-780 (nm)
Murban Crude Nov. 2, 1978		DCLS/C-GRSC Flight Line 6 17:13:38 Altitude 250 m Solar El. 34.6°	DCLS/C-GRSC Flight Line 7 17:40:27 Altitude 5 500 m Solar El. 33.3°	MSS/C-GRSA Flight Line 9 17:39:57 Altitude 300 m Solar El. 33.4°				
Radiance	Thin Oil	1.02 ± 0.05	3.06 ±0.15	3.5 ± 0.2	4.9 ± 0.3	4.2 ± 0.4	2.1 ± 0.6	0.8 ± 0.3
W x 10^{-3} / m^2·sr·nm	Water	0.72 ± 0.04	3.02 ±0.15	2.9 ± 0.2	4.2 ± 0.3	3.9 ± 0.4	1.8 ± 0.6	0.7 ± 0.3
Contrast		0.169 ± 0.003	0.0069 ±0.001	0.087 ± 0.009	0.069 ± 0.003	0.044 ± 0.003	0.076 ± 0.006	0.074 ± 0.008
Radiance	Thick Oil	0.87 ± 0.04		3.2 ± 0.2	4.6 ± 0.3	4.7 ± 0.5	3.3 ± 0.6	1.4 ± 0.3
W x 10^{-3} / m^2·sr·nm	Water	0.72 ± 0.04		2.9 ± 0.2	4.2 ± 0.3	3.9 ± 0.4	1.8 ± 0.6	0.7 ± 0.3
Contrast		0.095 ± 0.004		0.051 ± 0.01	0.044 ± 0.004	0.093 ± 0.003	0.291 ± 0.01	0.338 ± 0.015
La Rosa Crude Nov. 3, 1978		DCLS/C-GRSC Flight Line 4B 15:30:20 Altitude 270 m Solar El. 32.8°		MSS/C-GRSA Flight Line 22 17:50:17 Altitude 320 m Solar El. 32.4°				
Radiance	Thin Oil	1.03 ± 0.05		4.6 ± 0.3	5.8 ± 0.4	5.1 ± 0.5	2.4 ± 0.6	1.0 ± 0.3
W x 10^{-3} / m^2·sr·nm	Water	0.72 ± 0.04		3.7 ± 0.3	5.0 ± 0.4	4.4 ± 0.5	2.2 ± 0.6	0.8 ± 0.3
Contrast		0.177 ± 0.003		0.103 ± 0.007	0.071 ± 0.003	0.073 ± 0.003	0.051 ± 0.004	0.101 ± 0.006
Radiance	Thick Oil	0.88 ± 0.04		3.9 ± 0.2	4.6 ± 0.3	4.1 ± 0.4	2.2 ± 0.6	1.0 ± 0.3
W x 10^{-3} / m^2·sr·nm	Water	0.72 ± 0.04		3.6 ± 0.2	4.8 ± 0.3	4.4 ± 0.4	2.2 ± 0.6	0.8 ± 0.3
Contrast		0.103 ± 0.003		0.048 ± 0.006	-0.025 ± 0.003	-0.034 ± 0.003	-0.002 ± 0.004	0.092 ± 0.005

Neither the imagery nor the calculations of Table 1 have been corrected for atmospheric path radiance; thus the radiances used to calculate the contrasts include the path radiance contributed by approximately 300 m of atmosphere. The atmospheric component acts to reduce the observed oil-water contrast and does so more strongly at the shorter wavelengths because the atmosphere scatters light preferentially at these wavelengths. The contrasts at the sea surface will therefore be greater than those listed in Table 1, with the improvement being greatest at the shorter wavelength, UV-blue, end of the spectrum. Conversely, the contrasts will degrade with increasing flight altitudes, with the optimum contrast wavelength shifting from the UV, for thin oil films, towards the longer wavelengths. The degree to which this takes place will depend, not only on altitude, but also on atmosphere type.

In the foregoing discussion, thin and thick oil layers have been referred to without stating what the actual thicknesses are. Surface measurements of oil thickness were not attempted in this experiment. However, laboratory studies on oil film visibility (Horstein, 1972; Fingas et al., 1979) and on light extinction in oils (Horvath et al., 1970) indicates that one could expect increased surface reflectance to dominate in the 50 to 1 000 nm thickness range and absorption of volume reflected light to have a noticeable effect for thicknesses of 1-2 μm and greater. The point at which the oil absorbs more volume reflected radiance than it is adding by increased surface reflectance depends, of course, on the type of oil involved, and specifically on the oil's light extinction properties. Laboratory measurements made at a wavelength of 500 nm give an extinction coefficient for the Murban crude of 0.026 μm^{-1}, for the La Rosa crude, 0.19 μm^{-1} (Hoge and Swift, 1980); thus, 63% of the incident irradiance at 500 nm is absorbed by a 38 μm thick layer of Murban crude, a 5.3 μm layer of La Rosa crude.

Scott Inlet oil seep. Oil was detectable in the MSS data only on Flight Lines 7 and 16 of Sortie 9, and on Flight Line 10 of Sortie 10 because of the limited sky radiance available in the Arctic, and as a result of the low solar elevations. The solar elevations on these flight lines ranged from 14.7° to 19.4°, the latter occurring on Flight Line 16 of Sortie 9. The oil slick was visible only in MSS band 3. Figure 52 is the thermal IR counterpart of Figure 53, which contains an image of MSS band 3 for Flight Line 16 of Sortie 9. As for the Wallops data, the image has been level sliced and colour coded to improve the contrast. The bright band down the left edge of the image is caused by the presence of a brighter light source, probably the sun, in that direction. The oil is the

MSS IR
Scott Inlet Oil Seep
71°23'N 70°10'W
C-GRSA
Sortie 9
Flight Line 16
September 19, 1978

FIGURE 52 MSS IR, SCOTT INLET OIL SEEP. C-GRSA Sortie 9, Flight Line 16, September 19, 1978.

Water
Oil
Sun Glint
Oil

MSS 3
Scott Inlet Oil Seep
C-GRSA Sortie 9 Flight Line 16
September 19, 1978
71°23'N 70°10'W

FIGURE 53 MSS 3, SCOTT INLET OIL SEEP. C-GRSA Sortie 9, Flight Line 16, September 19, 1978.

S-shaped feature that extends across the image. The straight horizontal, or cross track, lines are caused by electromagnetic interference produced by the Vinten camera firings.

It is noted that, although the MSS sensitivity is not maximum in this channel, it is the only visible or near IR band that is capable of detecting the oil under these low light conditions. As the available light level was at or below the MSS sensitivity limit, a blue sky would favour oil detection by the shorter wavelength bands. While the sky was mostly clear on Sortie 9, it was completely overcast on Sortie 10. It must be concluded, therefore, that the oil-water radiance contrast is greatest at these shorter wavelengths. It is assumed that the higher noise level of MSS band 2 prevented it from detecting the oil.

KURDISTAN oil spill. The KURDISTAN oil spill provided an opportunity to apply some of the knowledge gained in the analysis of the Wallops Island oil spill. The KURDISTAN spill consisted of Bunker "C" oil, a very heavy residual oil that under normal circumstances would not be emulsified easily. However, high sea states existed at times between the time of the spill on March 15 and when the MSS imagery of the oil was obtained on March 23. Visual observations indicated that, in addition to large areas of thin, sheen-producing, oil slick, there were smaller patches of mousse surrounded by dark regions, interpreted to be caused by submerged layers of thick oil. This information coupled with the results obtained from the Wallops Island spill suggested that the MSS imagery be printed as a three colour superposition of MSS channels 3, 6 and 8 with channel 3 printed in blue, 6 in green, and 8 in red. The result is an image in which the thin oil appears blue, the mousse white, and the water dark green; intermediate shades of blue represent corresponding surface oil thicknesses. An MSS image was obtained from an altitude of approximately 2 500 m and is reproduced here in black and white (see Figure 54). The corresponding IR image is in Figure 55.

4.4.2.4 **UVLS.** Ultraviolet line scanner imagery in the spectral range 300-370 nm was obtained with the dual channel line scanner on two missions, the Wallops Island oil spill and the KURDISTAN oil spill. The former mission provided UV imagery of an oil on water spill, whereas the latter resulted in oil-in-ice imagery.

Wallops Island test oil spills. The DCLS was mounted in C-GRSC and MSS in C-GRSA, therefore, the UV imagery does not generally coincide in time with the MSS imagery. There are, however, two instances on the November 2 sortie over the Murban crude when they do. Flight Line 2 of C-GRSA at 1 000 m altitude coincides with Flight

OIL
MSS CHANNELS 3,6,8
Kurdistan Oil Spill
C-GRSB
Flight Line 2
March 23,1979

FIGURE 54 MSS, KURDISTAN OIL SPILL. Composite image of MSS channels 3, 6, 8. C-GRSB Flight Line 2, March 23, 1979.

OIL
MSS IR
Kurdistan Oil Spill
C-GRSB
Flight Line 2
March 23,1979

FIGURE 55 MSS IR, KURDISTAN OIL SPILL. C-GRSB Flight Line 2, March 23, 1979.

Line 6 of C-GRSC at 250 m; Flight Line 9 of C-GRSA at 300 m coincides with Flight Line 7 of C-GRSC at 5 500 m. Comparison of the performance of the two scanners on the first of these coincidences is made in Section 4.4.4. The UV imagery obtained on Flight Lines 6 and 7, separated by only 25 minutes, allows a comparison of the low and high altitude performance of the UV scanner. Included in this report are the low altitude black and white, unenhanced UV images of Flight Lines 3 and 6 on November 2, (Figures 56 and 57), the corresponding level sliced, colour enhanced images (Figures 58, and 49), and the high altitude image of Flight Line 7 (see Figure 50).

Comparison of the UV image in Figures 57 and 49 with the MSS series (Figures 33 to 39) shows that, although the MSS images occur some 26 minutes later, the same general pattern is apparent. The oil-water contrast in the UV image is vastly superior to that in the MSS 3 image and, for the thin regions of the oil, is superior to the contrast apparent in any of the MSS channels. Part of this can be attributed to the better sensitivity of the UV detector and part to the improved oil-water radiance contrasts in the UV (see Table 1).

Also to be noted in these UV images (Figures 58, 49, 56, 57) is the variation in radiance levels within the slick area. The thick oil region, even though it is emulsified, appears darker than the thin slick areas. This trend is just noticeable in the MSS bands 2 and 3, but is readily visible in the UV. The implication is that at these short wavelengths (300-450 nm) the absorption of the subsurface reflected radiance has a greater effect on the total reflected radiance than has the increased scattering in the emulsified oil. Although separate UV images of the La Rosa spill on November 3 are not included in this report, the same effect is present; the thin oil is bright in the UV, the thick dark, but not darker than the water, as is the case for MSS 3 and 4 (see Table 1). This implies that although the oil absorbs the upwelling radiation at these wavelengths, the UV upwelling volume scattered component is initially smaller than in the blue, and hence is less significant than the surface reflected component.

Comparison of these UV images with the corresponding IR images shows that the IR detects oil mainly within the thicker oil region i.e., the region where the UV radiance is lower and might, therefore, be mistaken for water in some instances (see Sections 4.4.3 and 4.4.4).

The high altitude (5 500 m) image obtained on Flight Line 7 of C-GRSC on November 2 is shown in Figure 50. As compared with the MSS Flight Line 9 series which is taken at very nearly the same time, the oil slick appears longer in the UV image. This

DCLS UV(left) IR(right)

Wallops Oil Spill

C-GRSC

Flight Line 3

November 2, 1978

FIGURE 56 DCLS, WALLOPS OIL SPILL. UV and IR images. C-GRSC Flight Line 3, November 2, 1978.

DCLS UV(left) IR(right)
Wallops Oil Spill
C-GRSC
Flight Line 6
November 2, 1978

FIGURE 57 DCLS, WALLOPS OIL SPILL. UV and IR images. C-GRSC Flight Line 6, November 2, 1978.

DCLS UV(left) IR(right)

Colour Enhanced Images

Wallops Oil Spill

C-GRSC

Flight Line 3

November 2,1978

FIGURE 58 DCLS, WALLOPS OIL SPILL. UV and IR colour enhanced images. C-GRSC Flight Line 3, November 2, 1978.

is because the aspect ratio has not been corrected for the latter case; the length should be reduced by a factor of 4.5. Also evident is a bright band along the left edge of the image. This is caused by the increased path radiance (atmospheric scattered solar radiance) resulting from the longer path at the edges of the scanner swath; the corresponding band down the other side of the image is not visible in Figure 50 as this figure shows only part of the total swath. The importance of this high altitude image is that, in comparison with the low altitude image (Figure 49), the contrast has been degraded, both by ozone absorption and scattering of the original sea surface target radiance, as well as the atmospheric path radiance. This problem has been aggravated additionally by the fact that the spill was imaged at approximately 29° from the nadir; the path length through the atmosphere was therefore 6 300 m. The oil and water radiances, including the atmospheric contribution, have been calculated to be 3-4 times the low altitude values (see Table 1). The contrast, at 0.69%, has been degraded by a factor of 25 as compared to the 250 m altitude pass, Flight Line 6. It is possible, therefore, that at slightly longer wavelengths the net oil to water contrasts would be superior to the UV contrast, since both the atmospheric scattering and the ozone absorption decrease with increasing wavelength. However, to realize any improvement in the contrast, the detector must have a sensitivity that is comparable to that of the UV detector.

KURDISTAN oil spill. The KURDISTAN oil spill provided the opportunity to gather the only oil-in-ice line scanner imagery obtained during the course of this project. In fact, no other such imagery was located in the literature search conducted as part of this project.

Examples of the imagery obtained with the UV line scanner of oil-in-ice are shown in Figures 59 and 60. The oil mixed into the pack ice appears as dark streamers against a white background. Water and land, however, also appear dark. It is only by correlating the UV and IR images that the oil can be distinguished from water and land. It is noted that the oil to ice contrast is apparently greater in the UV imagery than in photography (see Figures 61 and 62). Although this increased contrast is in agreement with the known fact that the oil is much more absorptive in the UV, a definitive statement must await a quantitative analysis on multispectral data, since the apparent contrast in these images is dependent upon the photographic processing involved in their production.

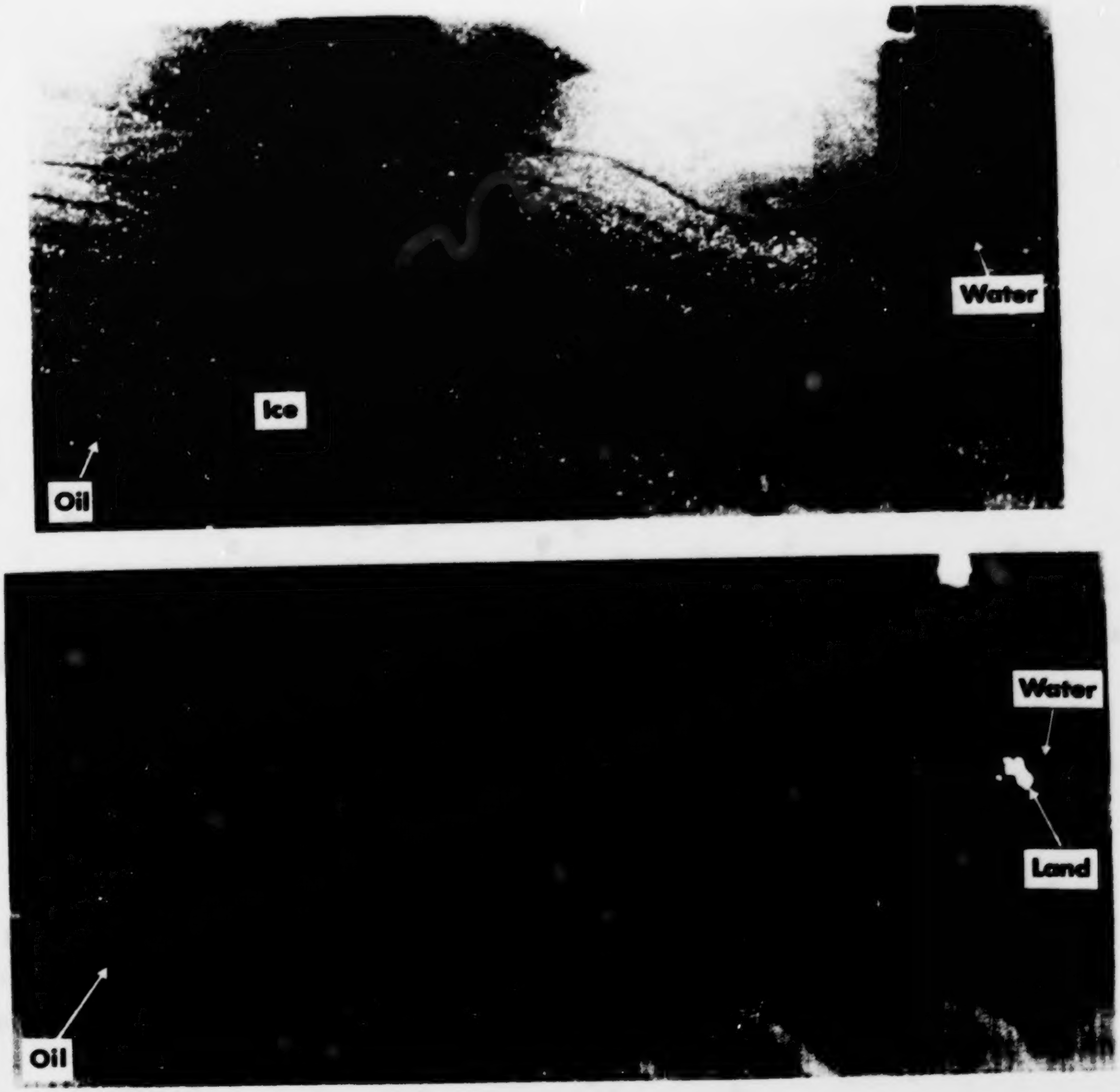
Water
Ice
Oil
Water
Land
Oil

DCLS: UV(top) IR (bottom)
Oil in Ice: Cape Breton
45°55·7'N 59°48·1'W
Scene: 3·4 km by 6·4 km
March 29, 1979
15:23:00 GMT

FIGURE 59 DCLS, KURDISTAN OIL SPILL. UV and IR images. C-GRSD Flight Line 4, March 29, 1979.

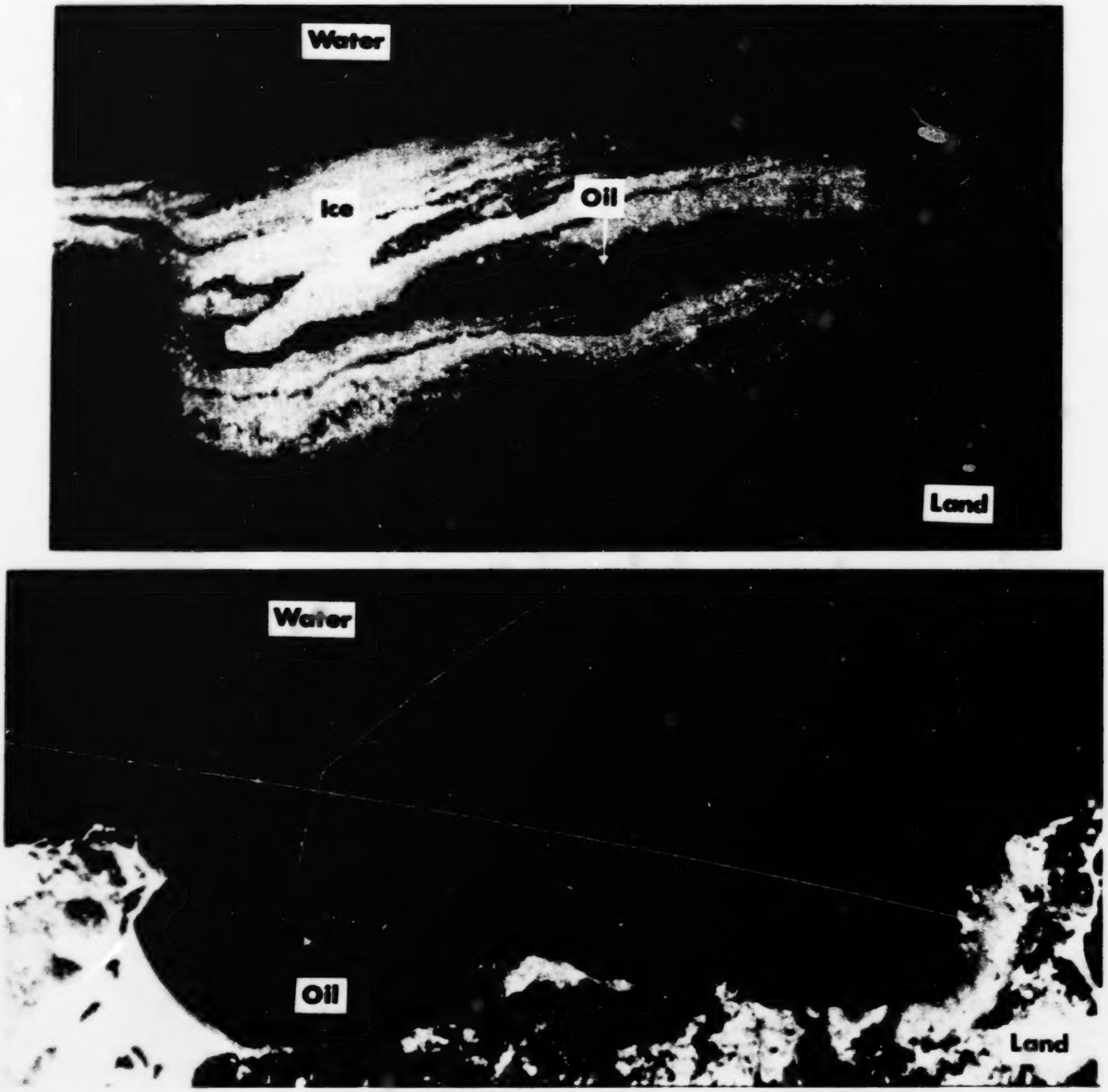
Water
Ice
Oil
Land
Water
Oil
Land

DCLS: UV(top) IR(bottom)
Oil in Ice: Gabarus Bay
45° 49·5'N 60° 09·5'W
Scene: 2·3km by 4·6km
April 2, 1979
19:29:15 GMT

FIGURE 60 DCLS, KURDISTAN OIL SPILL. UV and IR images. C-GRSD Flight Line 15, April 2, 1979.

It must be borne in mind that ice and ice-water mixtures present an extremely variable background against which oil is to be detected. The ice type encountered on this mission is only one of many, and hence the results obtained here generally cannot be extrapolated to other ice situations.

4.4.2.5 MEIS. Two MEIS images are shown in Figure 63, the data for which were collected at an altitude of 600 m over the La Rosa crude oil. One was obtained through a Corning 7-54 filter, which transmits in the near UV and in the far red - near infrared; the other was obtained through a Corning 2-64 filter, which transmits wavelengths of 650 nm and beyond. No definitive conclusions as to which spectral band is better can be drawn from a comparison of the images since the one channel (with the 7-54 filter) has had a radiometric calibration applied to correct for differences in responsivity of the different elements in the diode array detector, whereas the other channel has not. However, the 7-54 filter appears to give better contrast. The images are included here as an example of the output from the type of scanner that may eventually replace the mechanically scanned MSS and DCLS. At the present time, however, MEIS remains strictly a developmental prototype instrument.

4.4.3 Thermal IR. Thermal IR (8.5 - 12.5 μm) imagery was obtained with the IR channel of the MSS on the Scott Inlet, Wallops Island, and KURDISTAN missions, and with the IR channel of the DCLS on the Montreal Island, Wallops Island, and KURDISTAN missions.

4.4.3.1 Wallops Island test oil spills. The Wallops Island mission provided the best IR imagery and hence the major analysis effort was expanded on these data. Sample imagery collected with the MSS IR on two C-GRSA flight lines, one, Flight Line 9 on November 2, over the Murban crude spill, the other, Flight Line 22 on November 3, over the La Rosa crude spill, is presented in Figures 64, 65, 66 and 67. DCLS IR imagery of the Murban crude spill obtained on three C-GRSC flight lines, two, Flight Lines 3 and 6, at low altitude and one, Flight Line 7, at high altitude, is shown in Figures 58, 49, 56, 57 and 50. Figures 66, 67, 56 and 57 contain the same images as Figures 64, 65, 58 and 49 respectively; the former group are black and white unenhanced images, the latter are level sliced and colour coded for contrast enhancement. The oscillating line running the length of Figures 64 and 66 is caused by electromagnetic interference produced by the fluorosensor.

In the black and white imagery (Figures 66, 67, 56 and 57), brightness is indicative of the intensity of thermal radiation detected by the sensor. Most of the oil

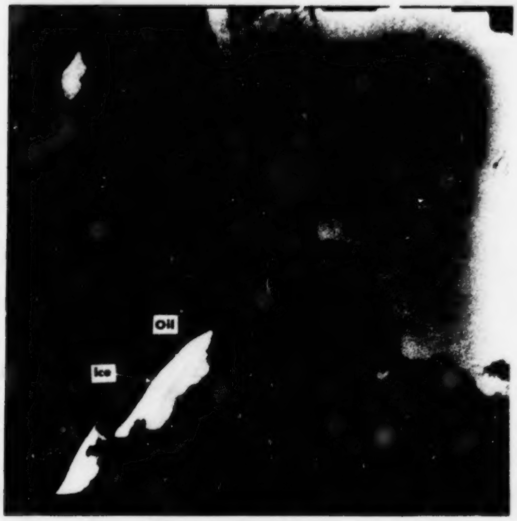

RC 10 23cm Format Camera
2445 Aerocolour Negative Film
Kurdistan Oil Spill
C-GRSD
Flight Line 2
April 2, 1979
16:16:43 GMT

FIGURE 61 RC-10 PHOTOGRAPH, KURDISTAN OIL SPILL. C-GRSD, Flight Line 2, April 2, 1979.

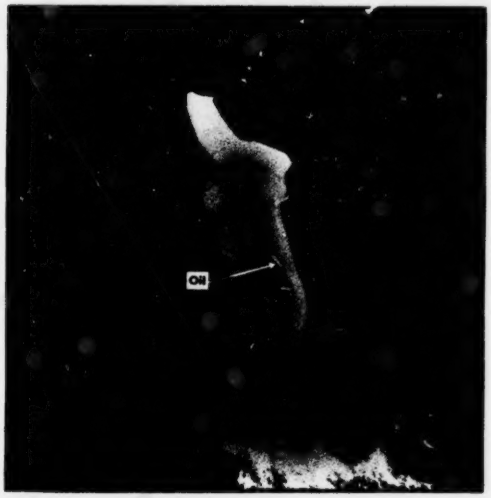

RC 10 23cm Format Camera
2445 Aerocolour Negative Film
Kurdistan Oil Spill
C-GRSD
Flight Line 3,
April 2, 1979
16:20:42 GMT

FIGURE 62 RC-10 PHOTOGRAPH, KURDISTAN OIL SPILL. C-GRSD, Flight Line 3, April 2, 1979.

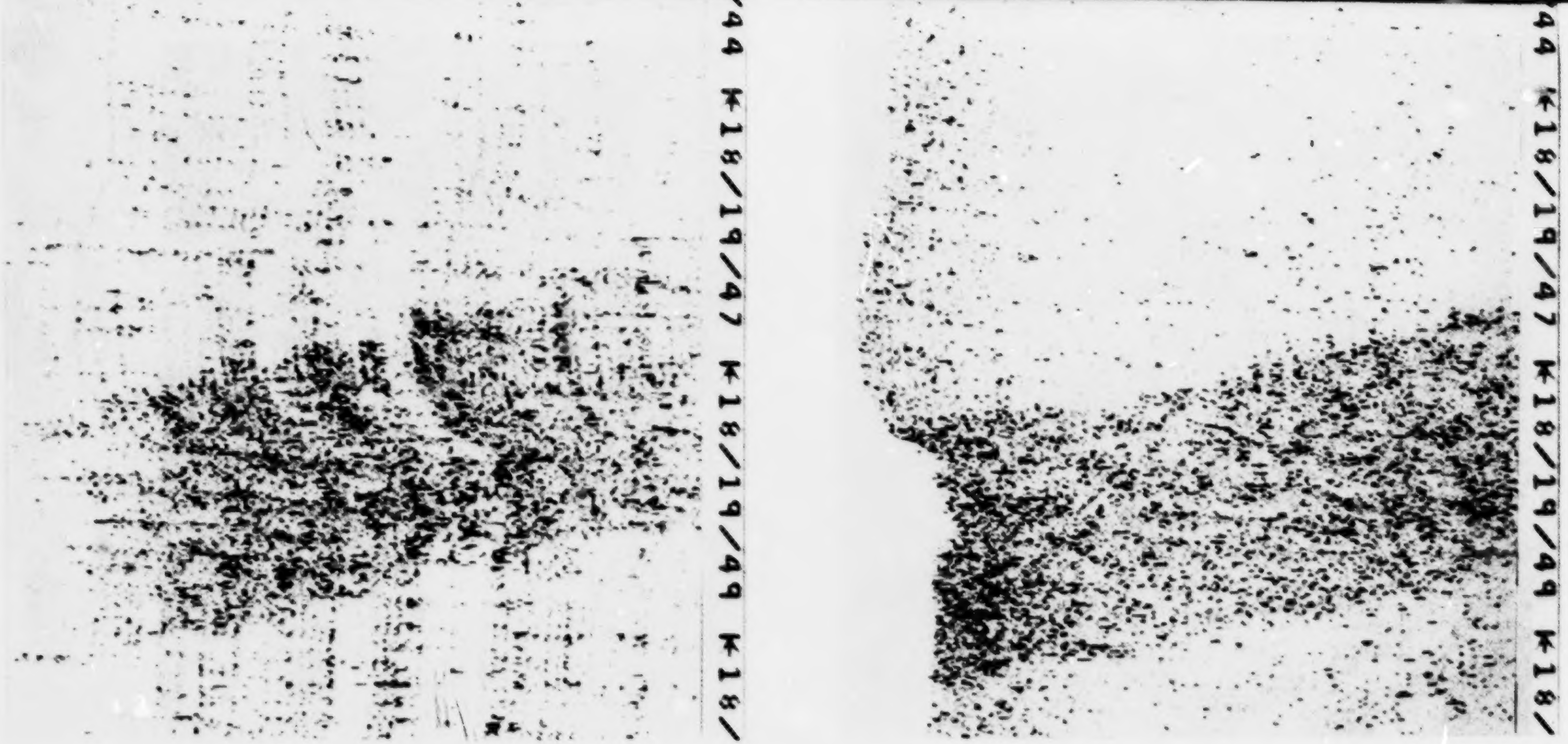
44 ⊬18/19/47 ⊬18/19/49 ⊬18/
44 ⊬18/19/47 ⊬18/19/49 ⊬18/

MEIS
Channel 1: Corning 2-64 Filter
Grey Tone Colour Enhanced
Wallops Oil Spill
C-GRSA
Flight Line 29
November 3, 1978

MEIS
Channel 2: Corning 7-54 Filter
Grey Tone Colour Enhanced
Wallops Oil Spill
C-GRSA
Flight Line 29
November 3, 1978

FIGURE 63 MEIS, WALLOPS OIL SPILL. Colour enhanced images of two channels. C-GRSA Flight Line 29, November 3, 1978.

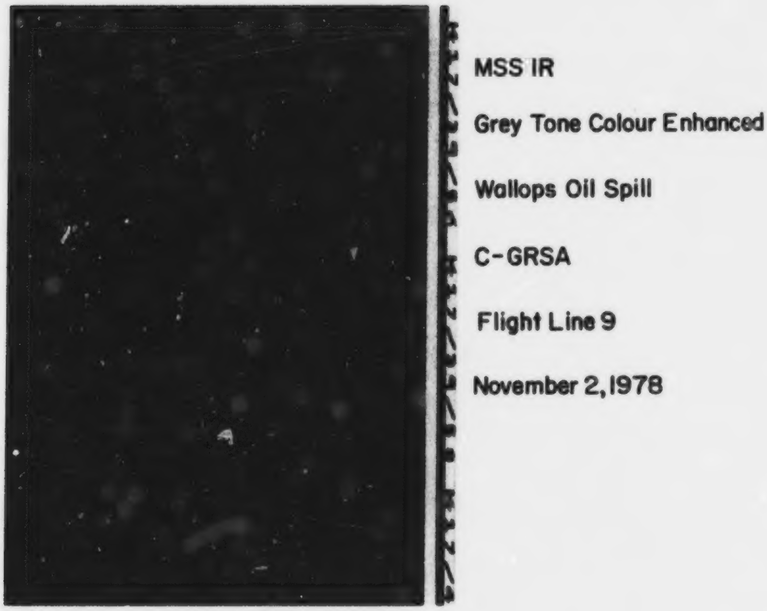

FIGURE 64 MSS IR, WALLOPS OIL SPILL. Colour enhanced image. C-GRSA Flight Line 9, November 2, 1978.

slick, as seen by the IR detectors, appears darker, and hence colder, than the water. In the interior of the dark region is a smaller area that is brighter, therefore warmer, than the water.

In the colour imagery (Figures 64 and 65) these apparent temperature differences are quantified. Each temperature range detected within the oil slick is represented by a different colour (see Table 2). The colours are chosen so that the outermost edge of the slick, as perceived by the IR detectors, is red, the next interior band orange, and the next orange-yellow. The innermost and hottest spot is printed white, with the next warmest region yellow. Two of these colour bands, white and orange-yellow are missing from Figure 65. The temperature range of the water is left black. In Table 2 the colours are listed in order of ascending temperature: orange-yellow, orange, red, black, yellow and white. In the region between the hot centre of the slick and the areas that appear colder than the water, the temperature undergoes an inversion. This band within the oil slick appears to be the same temperature as the water and appears black, therefore, in the colour imagery.

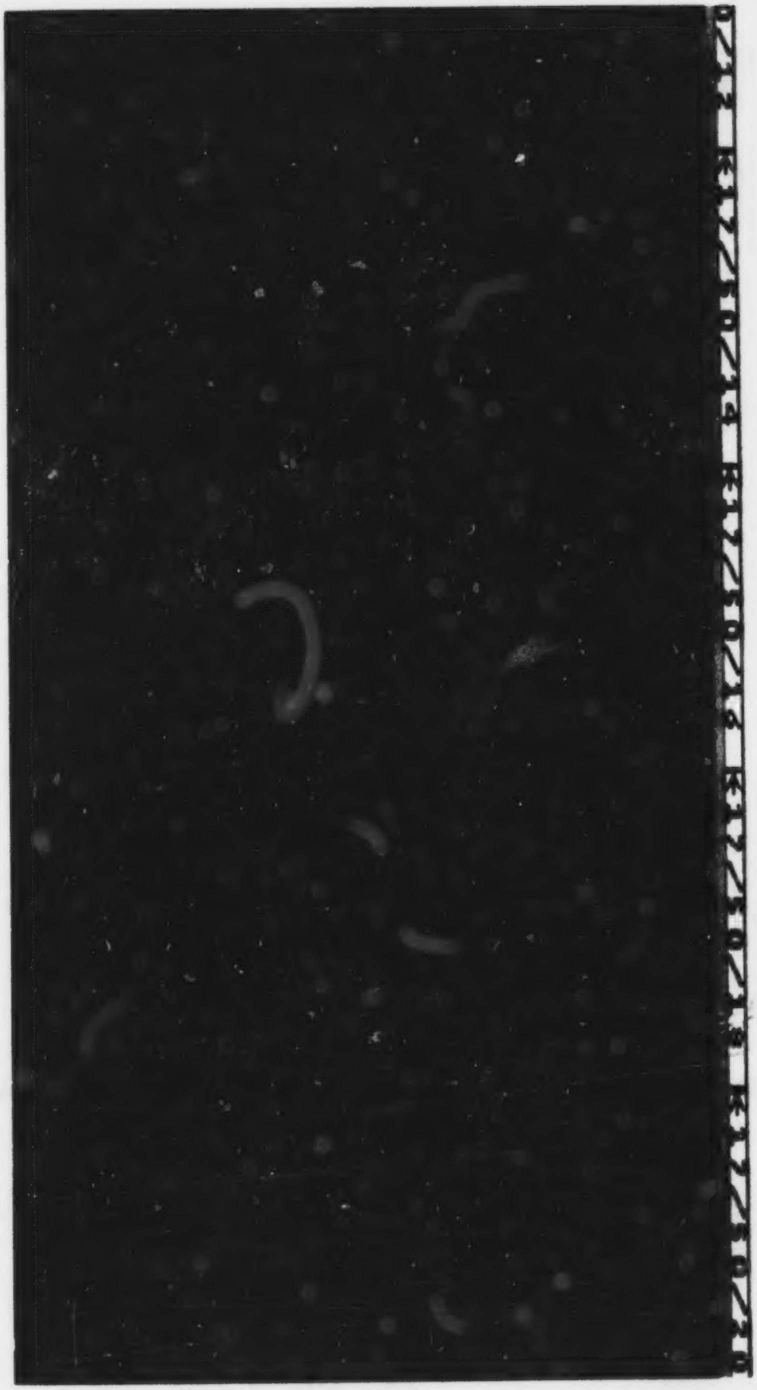

MSS IR

Grey Tone Colour Enhanced

Wallops Oil Spill

C-GRSA

Flight Line 22

November 3,1978

FIGURE 65 MSS IR, WALLOPS OIL SPILL. Colour enhanced image. C-GRSA Flight Line 22, November 3, 1978.

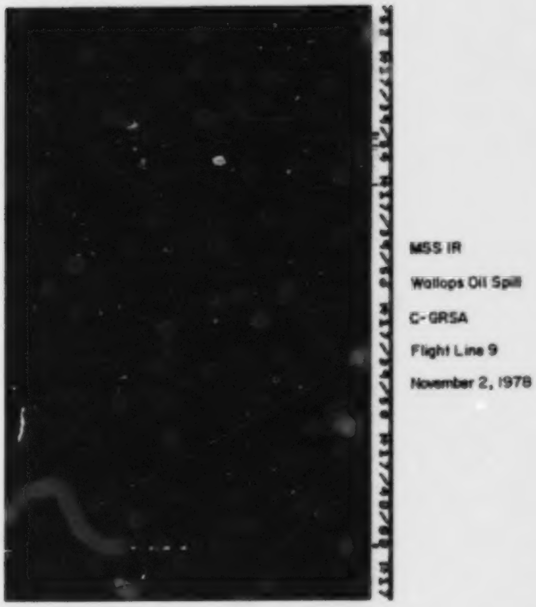
MSS IR
Wallops Oil Spill
C-GRSA
Flight Line 9
November 2, 1978

FIGURE 66 MSS IR, WALLOPS OIL SPILL. C-GRSA Flight Line 9, November 2, 1978.

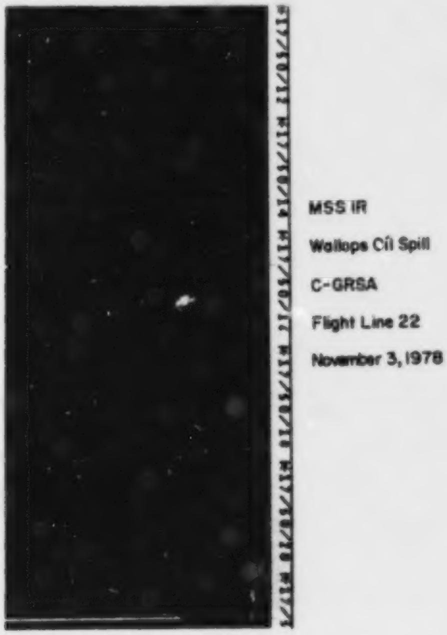
MSS IR
Wallops Oil Spill
C-GRSA
Flight Line 22
November 3, 1978

FIGURE 67 MSS IR, WALLOPS OIL SPILL. C-GRSA Flight Line 22, November 3, 1978.

TABLE 2 TEMPERATURES AND EMITTANCES CALCULATED FROM THERMAL INFRARED DATA FROM MSS AND DCLS

Sensor	Mission/Sortie/Flight Line	Imagery Colour Code	Target	Apparent Temp. (K)	Emittance	Physical Temp. (K)
MSS	Wallops Island	orange-yellow	oil	285.8	0.954	288.6[b]
	November 2, 1978	orange	oil	286.4	0.965	288.6[b]
	Sortie 2	red	oil	287.1	0.975	288.6[b]
	Flight Line 9	black	water	287.9	0.988[a]	288.6
		yellow	oil	288.6	0.971[c]	290.3
		white	oil	289.1	0.971[c]	290.9
MSS	Wallops Island	orange-yellow	oil	286.1	0.959	288.6[b]
	November 2, 1978	orange	oil	286.7	0.969	288.6[b]
	Sortie 2	red	oil	287.4	0.980	288.6[b]
	Flight Line 13	black	water	287.8	0.988[a]	288.6
		yellow	oil	288.8	0.971[c]	290.6
		white	oil	289.8	0.971[c]	291.9
MSS	Wallops Island	orange	oil	285.6	0.950	288.7[b]
	November 3, 1978	red	oil	286.9	0.970	288.7[b]
	Sortie 3	black	water	288.0	0.988[a]	288.7
	Flight Line 22	yellow	oil	289.2	0.970[c]	291.3
MSS	Scott Inlet		oil	272.5	0.972	274.1[b]
	September 19, 1978		water	273.4	0.988[a]	274.1
	Sortie 9					
	Flight Line 16					
DCLS	Wallops Island	orange-yellow	oil	285.4	0.934	289.5[b]
	November 2, 1978	orange	oil	286.5	0.952	289.5[b]
	Sortie 1	red	oil	287.6	0.970	289.5[b]
	Flight Line 3	black	water	288.8	0.988[a]	289.5
		yellow	oil	289.8	0.964[c]	292.0
		white	oil	290.6	0.964[c]	292.9
		green	ship	292.6		
DCLS	Wallops Island	orange	oil	285.6	0.937	289.5[b]
	November 2, 1978	red	oil	287.3	0.964	289.5[b]
	Sortie 1	black	water	288.8	0.988[a]	289.5
	Flight Line 6	yellow	oil	289.8	0.964[c]	292.0
		white	oil	290.6	0.964[c]	292.9
		green	ship	292.6		
DCLS	Wallops Island	orange	oil	289.4	0.956	292.2[b]
	November 2, 1978	red	oil	290.2	0.969	292.2[b]
	Sortie 1	black	water	291.4	0.988[a]	292.2
	Flight Line 7					

[a] obtained from Wolfe (1965).

[b] assumed to be the same temperature as the water.

[c] calculated from the minimum observed film emittance and the coherent theory of oil film emittance.

Comparison of the IR image in Figure 65 with the corresponding series in the visible shows that the oil spill region that is detected in the IR coincides closely with that region interior to the slick that appears dark in channels 4, 3 and 2 (Figures 42, 35 and 40) and also in the Vinten photograph (see Figure 68). These regions have been interpreted as oil films sufficiently thick to absorb a significant portion of the upwelling volume reflected light at the shorter wavelengths. The thickness at which this transition occurs in the visible has been estimated to be in the order of 1-2 μm (Horstein, 1972; Fingas et al., 1979). Indeed, based upon the measured value of 0.19 μm^{-1} for the extinction coefficient at a wavelength of 500 nm for the La Rosa crude, it may be calculated that a 2 μm thick layer of this oil absorbs 32% of the upwelling visible radiance. The implication is that the minimum thickness detectable in the IR is of the order of 2 μm. An emittance reduction at such small thicknesses can be explained consistently only by the coherent theory of thin film emittance discussed in Section 4.1.3. This 2 μm minimum detectable thickness observed here is consistent with the 1.83 μm thickness predicted by Equation 10 as the thickness at which the oil film (n_{oil} 1.43) reaches the first emittance minimum. The emittance value of 0.942 calculated from the observed data for the La Rosa crude (Table 3) would be consistent with a bulk emissivity value of 0.969. This sets a maximum value for the emissivity of this oil, since the observed value of 0.942 for the emittance is an average over a fairly large area; it is highly improbable that a uniform film thickness could be maintained over such a large surface. Hence the 0.942 value is probably greater than the minimum that a 1.83 μm thick film of La Rosa crude oil would suggest. Correspondingly, the calculated value of 0.969 for the bulk emissivity of the La Rosa oil is to be considered an upper bound.

A similar comparison of the IR imagery in Figure 64 with the visible imagery of Flight Line 9 leads to a similar conclusion. The IR detected oil spill region covers the areas of emulsified oil that are apparent in MSS channels 6-10 and includes an additional region in the central part of the spill (see Figures 36 to 39). It is possible that films of unemulsified oil are present in this region; however, the corresponding photography does not provide conclusive evidence on this point (Figure 69).

The imagery in Figures 58 and 49 shows that the regions in the oil spill that appear less bright in the UV coincide with those that are detected by the IR. This indicates that the UV best detects the thin oil; IR the thick. The oil films that increase the surface reflectance in the UV, while not seriously impeding the volume reflectance, appear bright in the UV. As the oil becomes thicker and more opaque in the UV, the

Thin Oil
Thick Oil

Vinten 70mm Camera
2445 Aerocolour Negative Film
Wallops Oil Spill
C-GRSA
Flight Line 22
November 3,1978
17:50:17 GMT

FIGURE 68 VINTEN COLOUR PHOTOGRAPH (printed here in black and white) WALLOPS OIL SPILL. C-GRSA Flight Line 22, November 3, 1978.

increased surface reflectance is partially offset by the decreased volume reflectance resulting from absorption in the oil. At this latter thickness, however, the oil becomes detectable in the IR. This fact can be used advantageously in determining the relative thickness of the oil in the different regions within the slick (see Section 4.4.4). Again there is the question as to what thickness is required to produce a decrease in the UV radiance. As the extinction coefficients for oils are considerably higher in the UV than in the visible ($0.9\ \mu m^{-1}$ at a wavelength of 337 nm for the La Rosa crude (Hoge and Swift, 1980)), one might expect this thickness to be less than 2 μm estimated for the visible; indeed, 36% of the upwelling volume reflected radiance is absorbed by only 0.5 μm of La Rosa crude.

Within oil spill regions detected in the IR, there are significant variations in the apparent temperature which are associated undoubtedly with thickness variations in the oil layer. A number of potential processes involved in determining the apparent surface temperature have been discussed (see Section 4.1.3). It is assumed that transient effects, such as would result from different oil source temperatures, or increased evaporative cooling by the volatile components, cannot be responsible for the observed temperature features. The persistence of the observed effects throughout the course of

TABLE 3 TEMPERATURES AND EMITTANCES OF CIAS CLUSTERED ZONES

Sensor	Mission/Sortie/Flight Line	Imagery Colour Code	Target	Apparent Temp. (K)	Emittance	Physical Temp. (K)
DCLS-IR	Wallops Island	red	oil	286.4	0.950	289.4[b]
	November 2, 1978	rose	oil	287.2	0.963	289.4[b]
	Sortie 1	pink	oil	288.1	0.978	289.4[b]
	Flight Line 3	black	water	288.7	0.988[a]	289.4
	(Figure 74)	blue	thin oil	288.7	0.988	289.4[b]
		yellow	oil	289.9	0.970[c]	291.8
		white	ship	292.3		
DCLS-IR	Wallops Island	red	oil	286.4	0.951	289.5[b]
	November 2, 1978	rose	oil	287.5	0.967	289.5[b]
	Sortie 1	pink	oil	288.5	0.984	289.5[b]
	Flight Line 6	black	water	288.7	0.988[a]	289.5
	(Figure 75)	blue	thin oil	288.7	0.988	289.5[b]
		yellow	oil	290.1	0.970[c]	292.0
		white	ship			
DCLS-IR	Wallops Island	red	oil	286.2	0.945	289.7[b]
	November 3, 1978	rose	oil	287.0	0.957	289.7[b]
	Sortie 2	pink	oil	288.0	0.973	289.7[b]
	Flight Line 4A	black	water	288.9	0.988[a]	289.7
	(Figure 73)	blue	thin oil	288.9	0.988	289.7[b]
		orange	oil	290.0	0.969[c]	291.9
		yellow	oil	291.4	0.969[c]	293.3
		white	oil, ship	292.8	0.969[c]	294.8
DCLS-IR	Wallops Island	red	oil	286.2	0.942	289.8[b]
	November 3, 1978	rose	oil	287.0	0.955	289.8[b]
	Sortie 2	pink	oil	288.0	0.972	289.8[b]
	Flight Line 4B	black	water	289.0	0.988[a]	289.8
	(Figure 51)	blue	thin oil	289.0	0.988	289.8[b]
		orange	oil	290.5	0.969[c]	292.4
		yellow	oil	292.0	0.969[c]	294.0
		white	oil, ship	293.3	0.969[c]	295.3

[a] obtained from Wolfe (1965).

[b] assumed to be the same temperature as the water.

[c] calculated from the minimum observed film emittance and the coherent theory of oil film emittance.

Thick Oil
Thin Oil

Vinten 70mm Camera
2445 Aerocolour Negative Film
Wallops Oil Spill
C-GRSA
Flight Line 17
November 2, 1978
18:01:41 GMT

FIGURE 69 VINTEN COLOUR PHOTOGRAPH (printed here in black and white) WALLOPS OIL SPILL. C-GRSA Flight Line 17, November 2, 1978.

the observation period, which extended up to three hours after the spill, indicates that a steady state had been reached. It is concluded that any apparent temperature difference induced by the oil must be due to emittance effects; a reduced thermal conductivity; a reduced vaporization rate; or an increased solar irradiance absorptivity. Only emittance effects can, in this instance, be responsible for an apparent temperature reduction. Since the air temperature was greater than the water temperature, the reduced thermal conductivity would give a temperature increase and the reduced vaporization rate or increased solar irradiance absorptivity can account only for temperature increases. The coherent theory of thin film emittance can be invoked to explain the fact that the IR appears to detect thicknesses of approximately 2 μm. As the oil increases in thickness the surface emittance of the slick will approach the bulk oil emissivity value. The rate at which this will occur depends on the IR absorption coefficient of the oil. At the same time the proportion of the solar irradiance absorbed by the oil, and hence the degree of solar heating, also increases. In addition, heat loss from the oil to the water decreases as the oil layer becomes thicker. At some point the solar heating effect dominates the surface emittance effect, and the oil appears hot in the IR imagery. Such regions appear whiter than the water in the black and white imagery (Figures 66 and 67) and are colour coded white and bright yellow in the colour enhanced imagery (see Figures 64 and 65). Over 90% of the 500 nm solar irradiance is absorbed by 13 µm of La Rosa crude, 96 µm of Murban. Although surface measurements of oil thickness were not made during this experiment, calculations based on microwave radiometer data (private communication with W.A. Croswell, NASA Langley Research Center, 1979) indicate that the oil slick thickness did not exceed 500 µm. For the observed oils under the prevailing environmental conditions, the thickness at which this transition from colder than water to warmer than water temperature occurs is somewhat less than 500 µm.

In addition to these readily visible features in the unenhanced IR imagery, there are some subtle variations in apparent temperature in the very thin film (<1 µm) region of the slick (see Figure 67). These effects are visible in most of the IR imagery and do not appear to correlate with any particular oil type or time since spill. Over most of the area that appears bright in the UV and lower MSS channels (2, 3, 4) the oil slick appears very slightly warmer than the surrounding water. In contrast, at the very edge of the slick, as perceived by MSS channels 2, 3 and 4, there is a slightly cooler than water fringe. The warm area over the extensive thin film region can be explained by either the reduced conductivity, reduced vaporization rate, or both. The cool fringe at the very edge of the slick may be caused by increased evaporation of the lighter oil components. It is postulated that when the oil film becomes a mono-molecular film, as it will near the edge of the slick, the oil is more easily vaporized than it is in a thicker film. This would occur if the oil to water intermolecular bonding is less than the oil to oil bonding.

The high altitude (5 500 m) IR and UV images obtained on Flight Line 7 of C-GRSC on November 2 are shown in Figure 50. In the IR image, the whole detectable part of the slick appears cooler than the surrounding water (see Table 2). The MSS IR image collected at the same time indicates that the centre portion of the slick appears approximately 3 K warmer than the surrounding cooler oil (see Figure 64). This warm region, as measured in the low altitude image, is calculated to be approximately 3 pixels wide in the high altitude image. As this central warm feature is not apparent in the high altitude imagery, it is assumed that the response of the detector to such a low contrast target is not quick enough to detect a target of this size.

A comparison of the calculated temperatures in Table 2 for the DCLS Flight Lines 6 and 7 of November 2, shows a water temperature increase of 2.7 K with the altitude increase of 5 250 m. This is of course an error and is due to the fact that the detector black bodies used for internal calibration have cooled as they have been exposed to the colder air at the high altitudes. The normal readjustment and recording of the blackbody temperatures were omitted in this instance. The differential in the apparent temperature between the major body of the oil and the water is effectively the same on both flight lines. The maximum apparent temperature differential is greater on the low altitude pass because the oil slick presents a larger (angular) target at this altitude and consequently the different apparent temperature regions are better resolved.

4.4.3.2 Scott Inlet oil seep. Thermal imagery of the oil from the Arctic seep is limited to three MSS IR flight lines, 7, 16 and 20 of Sortie 9 of September 19, 1978. One of these images, obtained on Flight Line 16 appears in Figure 52. The Arctic data were degraded by a periodic drift problem associated with IR scanner which resulted in the cross track banding apparent in Figure 52. In addition, there are cross track interference lines caused by the Vinten camera firings. Also 'visible' in the IR imagery are the many thermal features present in the iceberg-infested waters. These undoubtedly result from the melting of the ice and the mixing of the water as it flows past the grounded icebergs. Cold features were often present in the IR imagery but no corroborative features were apparent in the visible MSS channels, Vinten photography, or LLLTV imagery. It was concluded, therefore, that such cold features were cold surface currents, often appearing as rivers on the sea surface.

The curved feature visible in Figure 52 is the oil on the water's surface. This feature coincides with the lower half of the S-shaped feature in the MSS channel 3 image of Figure 53 and the LLLTV image in Figure 70. That this was indeed oil is confirmed by the fluorosensor response, coinciding in time with the crossing of the centre part of this S-shaped slick, and by visual observations. Part of this slick appears in the Vinten photograph shown in Figure 71.

4.4.3.3 Montreal Island oil spill. IR imagery of an oil spill in Montreal harbour was obtained under two different sets of solar illumination conditions. The first image datum was collected in the early evening with a solar elevation of 4.3°; the second was collected at night when the sun was 19.8° below the horizon (see Figure 72). These are primarily black and white images, where white is hot, black cold, with a small range of intensity levels, corresponding to a small range of apparent temperature levels, accented in yellow. The colour enhanced levels are slightly cooler than the water temperature, with the bright yellow cooler than the orange-yellow.

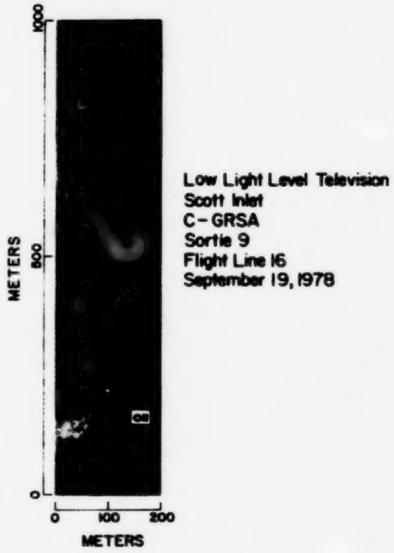
1000
500
0
METERS
Oil
0
100
200
METERS
Low Light Level Television
Scott Inlet
C-GRSA
Sortie 9
Flight Line 16
September 19, 1978

FIGURE 70 LOW-LIGHT-LEVEL TELEVISION, SCOTT INLET. Scan print of the oil seep. C-GRSA Sortie 9, Flight Line 16, September 19, 1978.

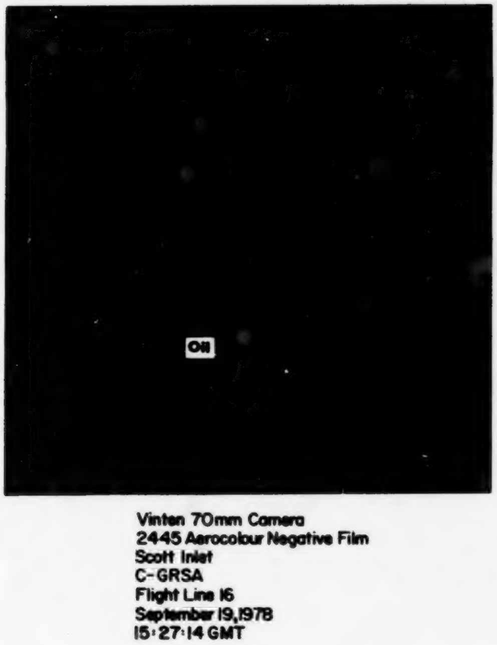
Oil
Vinten 70mm Camera
2445 Aerocolour Negative Film
Scott Inlet
C-GRSA
Flight Line 16
September 19, 1978
15:27:14 GMT

FIGURE 71 VINTEN COLOUR PHOTOGRAPH, (printed here in black and white) SCOTT INLET OIL SEEP. C-GRSA Sortie 9, Flight Line 16, September 19, 1978.

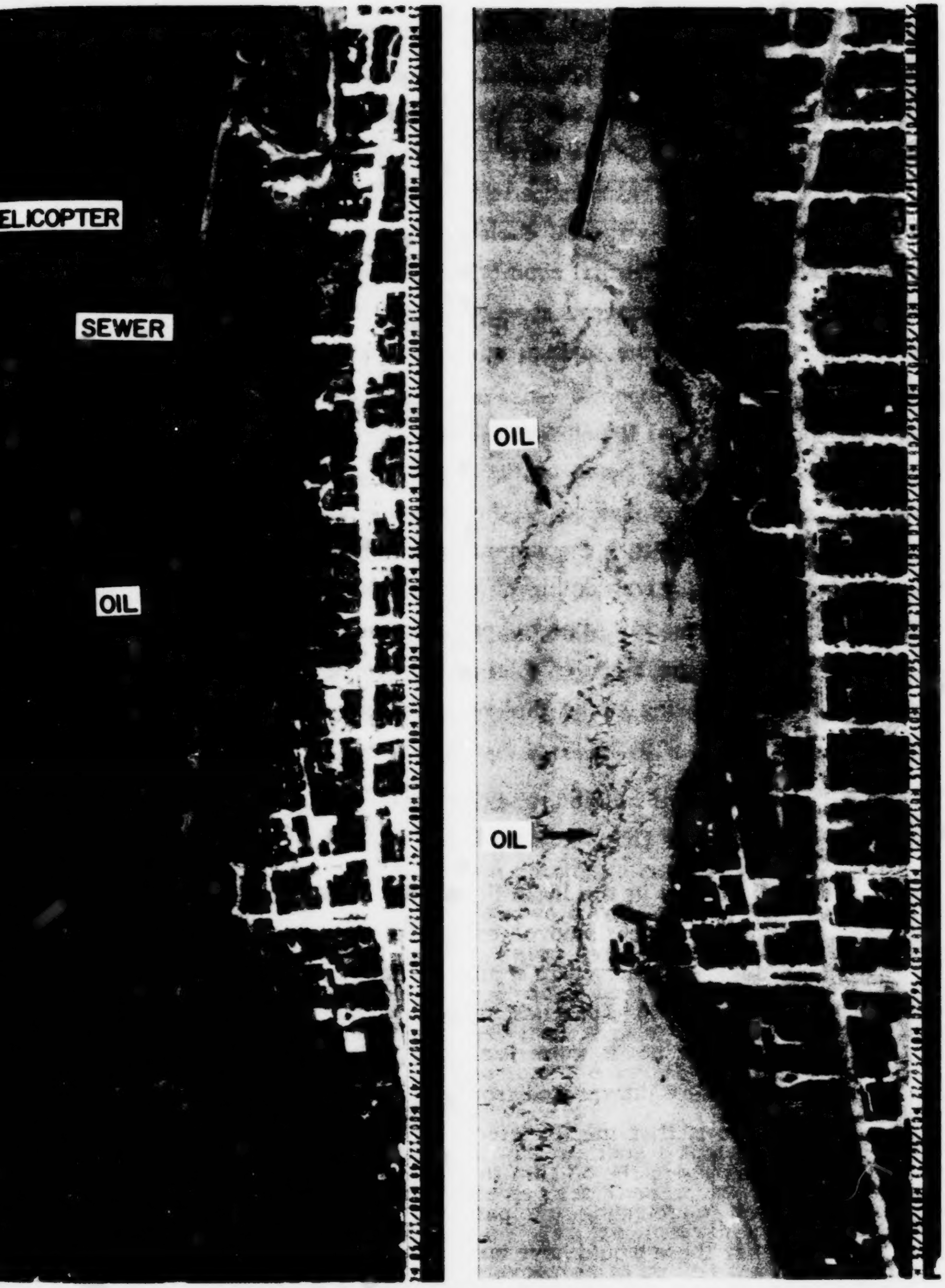
ELICOPTER
SEWER
OIL
OIL
OIL

IRLS Montreal Harbour

Colour Enhanced Images

Flight Line 5 (Left)

Flight Line II (Right)

June 30 - July I, 1978

FIGURE 72 IRLS, MONTREAL HARBOUR. Flight Lines 5 AND 11, June 30 to July 1, 1978.

In the daylight image, the water is colder than the land along the shore; at night the water is warmer; the streets show up hot in both images. The oil is entering the water via a subsurface sewer outlet located just downstream from the pier as indicated in Figure 72. The sewer outfall is warmer than the water and in the daytime image appears as a white (hot) area. The white spot just opposite the end of the pier and further offshore is a Coast Guard helicopter. As the oil cools down, its apparent temperature passes through that of the water and as thermal equilibrium between the oil and water is reached, the oil, as in the other IR imagery, appears cooler than the water. The explanation is that the oil film lowers the surface emittance and hence the apparent temperature (see Section 4.1.3).

There are other regions in the imagery that have the same apparent temperature as the oil (encoded yellow). Some of these occur on land and present no interpretive problem. There are, however, regions in the water, especially near the shore and in shallow regions, that appear cooler than the water. In the night scene, this reduced temperature can be attributed to radiative cooling of the shallow water at night; it is noted that some of the areas that appear cool at night appear warm in the daylight image. There are other shallow areas that appear cooler than the water in both images; these may be attributable to vegetation growing in the shallow water areas or to wet sand or mud areas.

4.4.3.4 KURDISTAN oil spill. On this mission, imagery of oil on water was obtained with the MSS IR and of oil-in-ice with the DCLS IR scanner.

Oil on water. The oil imaged in the IR in Figure 55, and in the three visible and near IR MSS channels in Figure 54, consisted of extensive regions of thin oil film surrounding smaller regions of thick oil, part of it emulsified and part of it submerged. The oil appears in Figure 55 as dark strips and patches; these coincide approximately with the brighter regions of Figure 54, but cover more area than the brightest patches of Figure 54. As these brightest areas were interpreted from Figure 54 to be the emulsified oil, the conclusion to be drawn here is that the IR detects more than just the emulsified oil. These must, therefore, be areas where the oil film thicknesses are at least 2 μm.

Submerged pools of oil surrounding the patches of mousse were observed visually; however, it is unlikely that these would have an effect on the emittance. Eighty percent of the IR radiation in the 8.5 to 10.5 μm band penetrating the surface is emitted by the top 30 μm of water, and in the 10.5 to 12.5 μm band the corresponding depth is 7 μm (Wolfe, 1965).

Although the solar elevation was sufficient (32°) on this flight line that one would expect solar heating of the absorptive oil, only isolated warm spots in the oil appear in the imagery. Observers on board the aircraft have reported that the heavy clumps of 'chocolate mousse' were riding quite low in the water and were periodically awash in the waves. This could, of course, explain why the thick oil did not appear warm here.

Oil-in-ice. Figures 59 and 60 include imagery of oil-in-ice obtained in the thermal IR wavelength range 8.5 to 10.5 μm as well as in the UV. In these images the ice and water exhibit very nearly the same temperature with land appearing much warmer. The water and ice can be differentiated in the UV, the ice being the brighter. The oil in the ice appears warmer than the ice (or water) but not as warm as the land. These warm oil 'streamers' apparent in the IR coincide with the dark 'streamers' seen in the UV. Note also the dark (cold) margin in the water along the ice pack edge; this is caused by the strip of cold meltwater at the edge of the pack. Although both oil and water-ice mixtures appear dark in the UV; the oil appears bright in the IR, the water-ice mixture dark.

Assuming that the pack ice in these images is sea ice and that it is at least as cold as the water, one must conclude from Figure 60, where the ice and water appear to be the same temperature, that the emittance of the ice is equal to or greater than that of the water in the wavelenght range 8.5 to 10.5 μm. In other imagery not included in this report, the ice in some places appears colder than the water, in others warmer. The former case can be explained by a physically colder ice surface. The latter phenomenon can be explained in one or both of two ways: the ice, with perhaps a snow cover, could have a higher emittance than the water, even though the emissivity of water is very close to unity; or the ice or its snow cover could be physically warmer than the water, assuming the salinity of the surface is less than that of the surrounding seawater. The results obtained here, therefore, indicate that the emissivity of this particular type of ice is at least as high as that of water.

Based on analyses of the Wallops Island data we have concluded that the emissivity of the La Rosa crude is less than or equal to 0.97, averaged across the wavelength range 8.5 to 12.5 μm. The oil involved in the KURDISTAN accident was Bunker "C"; its emissivity can be expected to be less than that of the La Rosa crude. In spite of the fact that measures were taken to limit the detection range to the 8.5 to

10.5 µm wavelength band, where the ice has an emissivity equal to or greater than the water and the oil has an emissivity less than the water, the oil appears brighter, hence warmer, than the ice. It is concluded that the oil is physically warmer than the ice, being heated by the sun which had an elevation of 30° to 46°.

4.4.4 Integrated Multispectral Analysis. The CCRS Image Analysis System contains a number of classification programs which permit automatic classification of targets imaged in up to four separate spectral channels. The migrating means model was selected as the most effective method of combining the information contained in 2-4 images of the same scene in order to produce a single image that retains most, if not all, of the original information. The DCLS imagery, in the UV and thermal IR, is ideally suited to this technique. As was noted in Section 4.4.3, the UV contains information on the very thin (<2 µm) oil films; whereas, the IR contains information on the thicker (>2 µm) oil films, including the much thicker layers (up to 500 µm as encountered on the Wallops mission). The two channels are complementary; consequently, they contribute almost totally independent sets of information.

Application of the migrating means model to the UV-IR pair of images of Flight Line 4A, November 3, produced the image in Figure 73. The thin slick region colour coded blue is the area that has the higher intensity in the UV; the thicker region represented by three shades of red is the cooler than water IR region; the thickest region coded yellow and white, is the hot area. Corresponding thematic classifications are performed on the data from three other flight lines: 3 and 6 of November 2, 4B of November 3. The resultant images appear in Figures 74, 75 and 51 respectively. The classification with the corresponding temperatures and emittances is given in Table 3 for Flight Lines 3 and 6, November 2, and 4A and 4B, November 3. The ship, ANNANDALE, is visible in these images as a hot target. Its trail of very thin oil is also visible. In the image from November 3, Flight Line 4B (Figure 51), the blue band along the left edge of the swath is the result of sun glitter in the UV band; on that side of the swath the scanner was looking almost directly into the centre of the sun's glitter pattern. There are also a number of 'horizontal', cross-track, bands visible in these images; these are produced by slight fluctuations in the UV or IR detector signals.

An almost equivalent result has been achieved in Figure 76 by a different route. The UV and IR images from Flight Line 6 of November 2 were individually colour enhanced on the MAD (Figures 77 and 78) negative transparencies produced from the

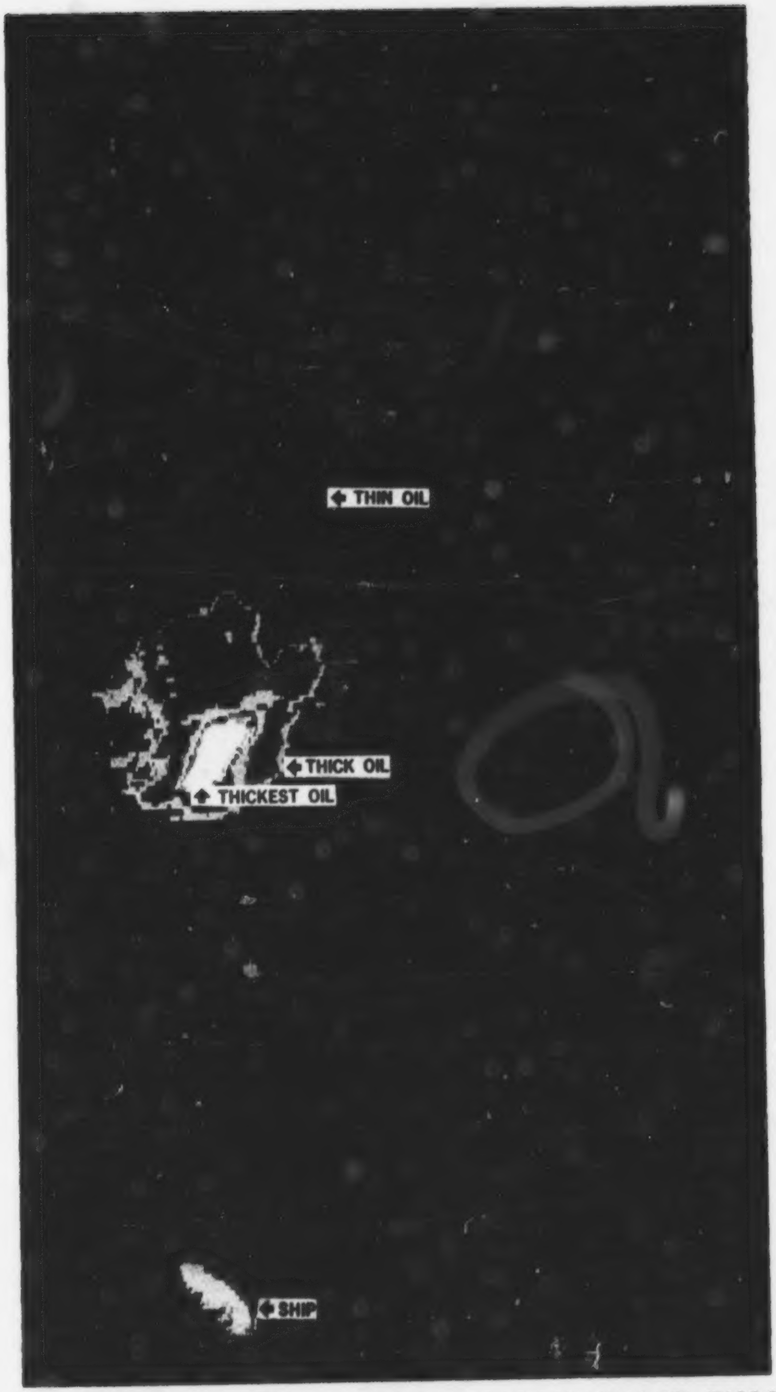
THIN OIL
THICK OIL
THICKEST OIL
SHIP

DCLS Thematic Colour Image

UV IR

Wallops Oil Spill

C-GRSC

Flight Line 4A

November 3,1978

15:27:33 GMT

FIGURE 73 DCLS THEMATIC COLOUR IMAGE, WALLOPS OIL SPILL. C-GRSC Flight Line 4A, November 3, 1978.

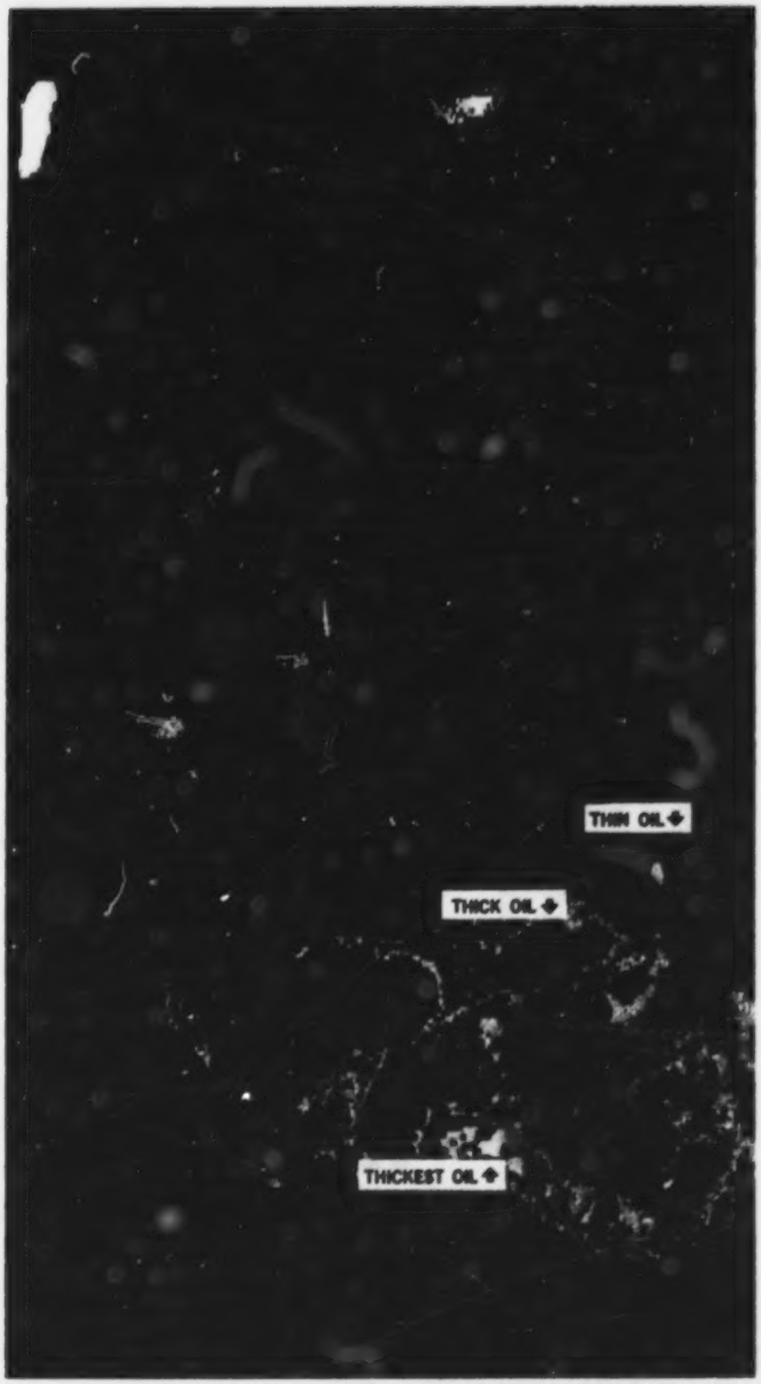
THIN OIL
THICK OIL
THICKEST OIL

DCLS Thematic Colour Image
UV IR
Wallops Oil Spill
C-GRSC
Flight Line 3
November 2, 1978
17:04:01 GMT

FIGURE 74 DCLS THEMATIC COLOUR IMAGE, WALLOPS OIL SPILL. C-GRSC Flight Line 3, November 2, 1978.

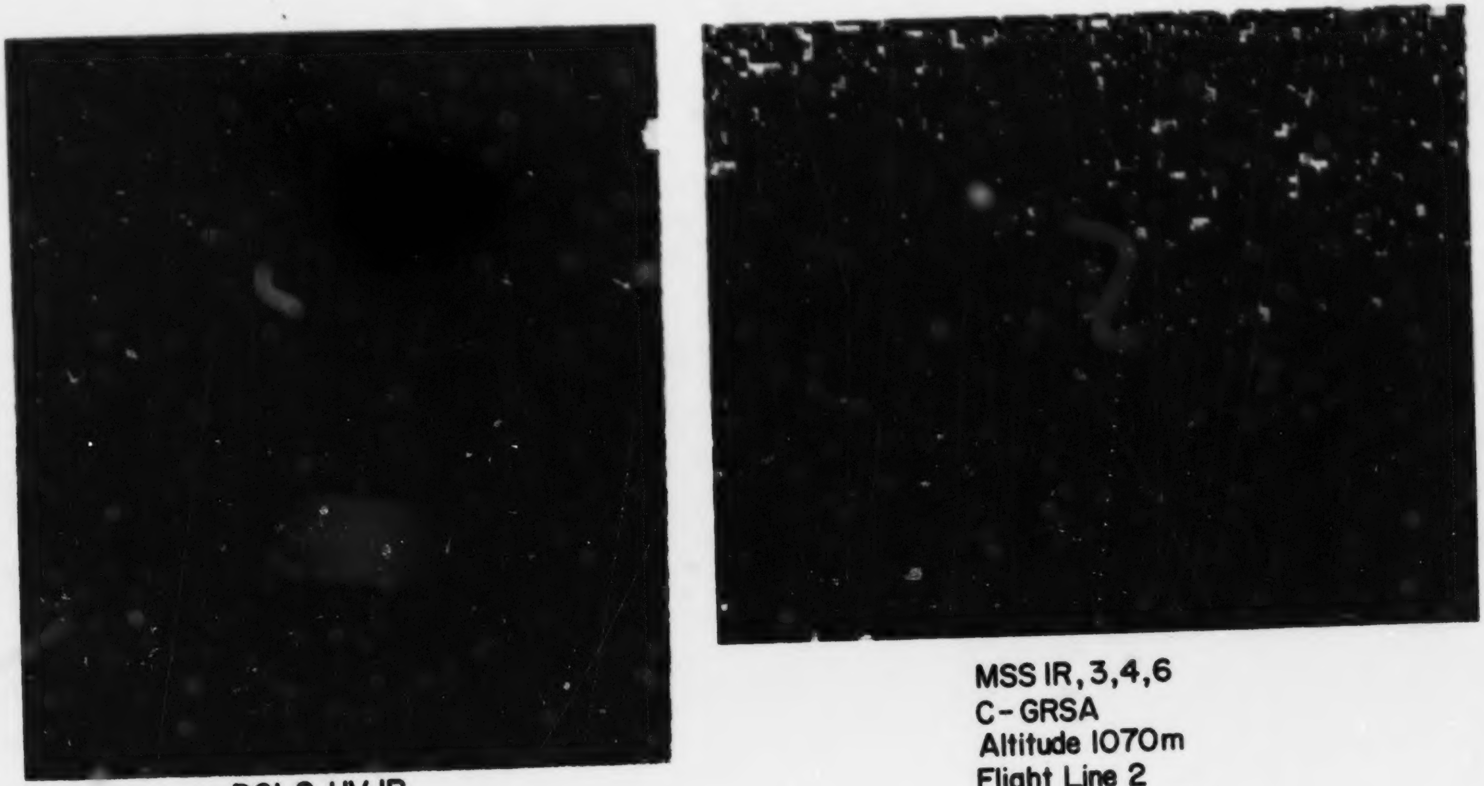

DCLS UV IR
C-GRSC
Altitude 247m
Flight Line 6
November 2, 1978
17:13:41 GMT

MSS IR, 3,4,6
C-GRSA
Altitude 1070m
Flight Line 2
November 2, 1978
17:14:30 GMT

MSS Image Has Been Magnified 5x To Be Comparable To The DCLS Image

FIGURE 75 DCLS AND MSS THEMATIC COLOUR IMAGE, WALLOPS OIL SPILL. Comparison of DCLS, C-GRSC Flight Line 6, and MSS, C-GRSA Flight Line 2, November 2, 1978.

FIGURE 76 DCLS, WALLOPS OIL SPILL. Superposition of UV and IR colour enhanced images. C-GRSC Flight Line 6, November 2, 1978.

FIGURE 77 DCLS, WALLOPS OIL SPILL. UV colour enhanced image. C-GRSC Flight Line 6, November 2, 1978.

CSFR output, and a print made by overlaying the two negatives. Although this is a more tedious operation, it demonstrates that the CIAS image in Figure 75 contains the combined information sets of the separate UV and IR images in Figure 49. A similar equivalence holds for the Flight Line 3 images in Figures 74 and 58.

FIGURE 78 DCLS, WALLOPS OIL SPILL. IR colour enhanced image.
C-GRSC Flight Line 6, November 2, 1978.

The same CIAS technique was applied to the MSS data to try to ascertain which combination of spectral channels produces the best classification. It is noted here that, because there were only two channels of DCLS data, the full 256 level digitized data could be used; however, with the four channels of MSS data, the number of digital units was cut to 64 to allow completion of the migration process in a reasonable time.

Three different combinations of the images collected on Flight Line 2, November 2, in four MSS channels are presented in Figure 79. The colouration along the right side of these images is the result of sun glitter. It is quite obvious that even though channels 6 and 8 contain information on the thick regions of the emulsified oil (see the series of Flight Line 9 images), it is not equivalent to that available in the IR. There appears to be little difference between the MSS 3, 6, 8, IR and MSS 3, 4, 6, IR combinations. Part of the reason for this wide disparity between the MSS 3, 4, 6, 8 combination and the others is undoubtedly the greater contrast apparent in the IR digital

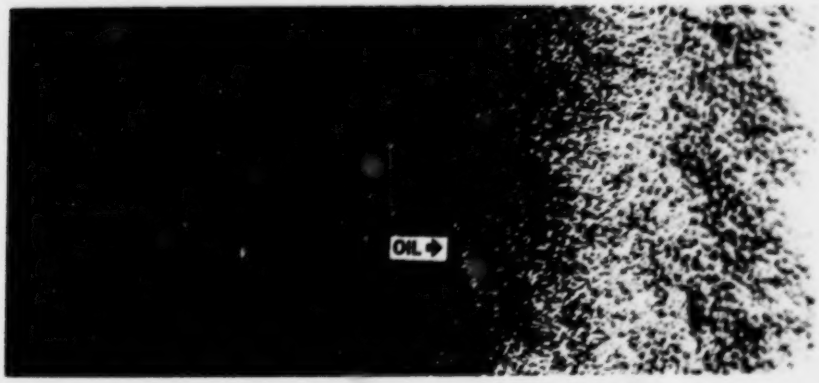

MSS 3 MSS 4 MSS 6 MSS 8

MSS Thematic
Colour Images

Wallops Oil Spill

C-GRSA

Flight Line 2

November 2, 1978

17:14:32 GMT

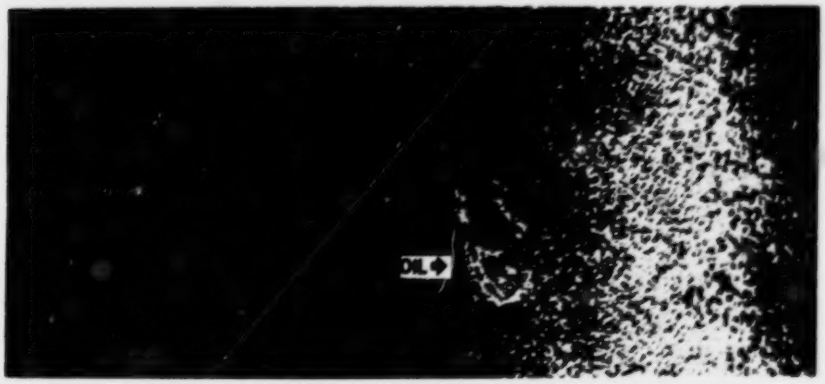

MSS 3 MSS 6 MSS 8 MSS IR

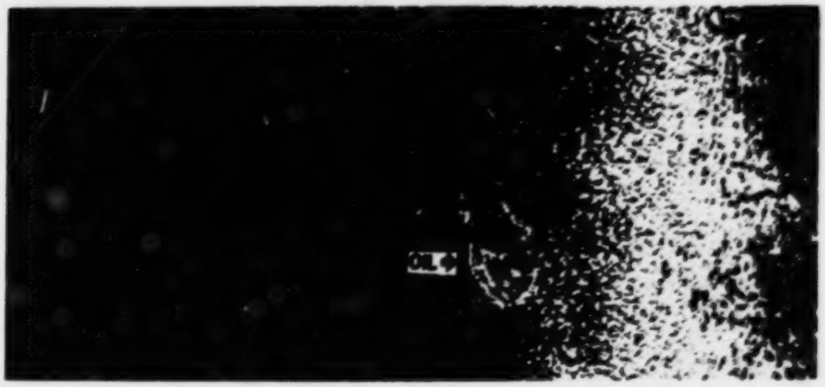

MSS 3 MSS 4 MSS 6 MSS IR

FIGURE 79 MSS THEMATIC COLOUR IMAGES, WALLOPS OIL SPILL. C-GRSA Flight Line 2, November 2, 1978.

data as compared with the MSS 8 digital data. If the signal-to-noise level were sufficient, the MSS 8 contrast, as it appears in the digital data, could be artificially improved by off-setting the zero radiance level (to 'negative' values on the digital scale) and stretching the remaining range across the full 64 intensity levels. On another type of oil, however, such as the La Rosa crude, the thick film information is not present in the MSS 8 imagery (see Figure 44); and a contrast stretch would not improve the situation. The thermal IR is, therefore, one of the prime spectral bands for oil detection, at least for oil on water detection.

The same process was applied to the data from Flight Line 2, November 3, giving combinations MSS 3, 4, 6, IR; MSS 3, IR; and MSS 3, 6, 8, IR (see Figure 80). It is perhaps somewhat surprising that the combination MSS 3, IR performs almost as well as MSS 3, 4, 6, IR; it is certainly surprising that MSS 3, IR performs better than MSS 3, 6, 8, IR. This latter result implies that, although information has been added in the two images from bands 6 and 8, the combination with the existing information in MSS 3, IR nullifies part of this latter set. It may be that more of the 8 available clusters were used in classifying extraneous targets, such as sun glitter or electromagnetic interference, both of which are more prominent in the longer wavelength channels.

The DCLS Flight Line 6, November 2, coincides in time with the MSS Flight Line 2, so the MSS 3, 4, 6, IR combination has been enlarged to the same scale as the UV-IR image and both displayed in Figure 75. There are two factors that prevent a fair comparison of these two images: the MSS image was acquired at an altitude of 1 050 m while the DCLS was at 250 m; the MSS look direction on one limb of its scan was only 21° from the sun, while the DCLS look direction was 83° from the sun. As a result of the reduced spatial resolution in the higher altitude MSS imagery, the fine thermal structure in the slick was lost. The hot region, depicted in the DCLS image, has been averaged in the MSS image together with the surrounding cooler (lower apparent temperature) region to give a region with an apparent temperature equal to that of the water. The proximity of the solar glitter pattern degrades the thin film information since both sun glitter and thin oil film increase the radiance in the visible bands. Additionally, judging from the relative signal-to-noise levels in the UV and MSS 3 channels, as evidenced in Figures 49 and 34 (see Appendix A), one would expect the DCLS to yield superior results.

A determination of the optimum short wavelength band would require flying a number (possibly four would be sufficient) of detectors identical to that in the UV line scanner filtered to permit detection in different spectral bands, e.g. 300 - 370, 370 - 420,

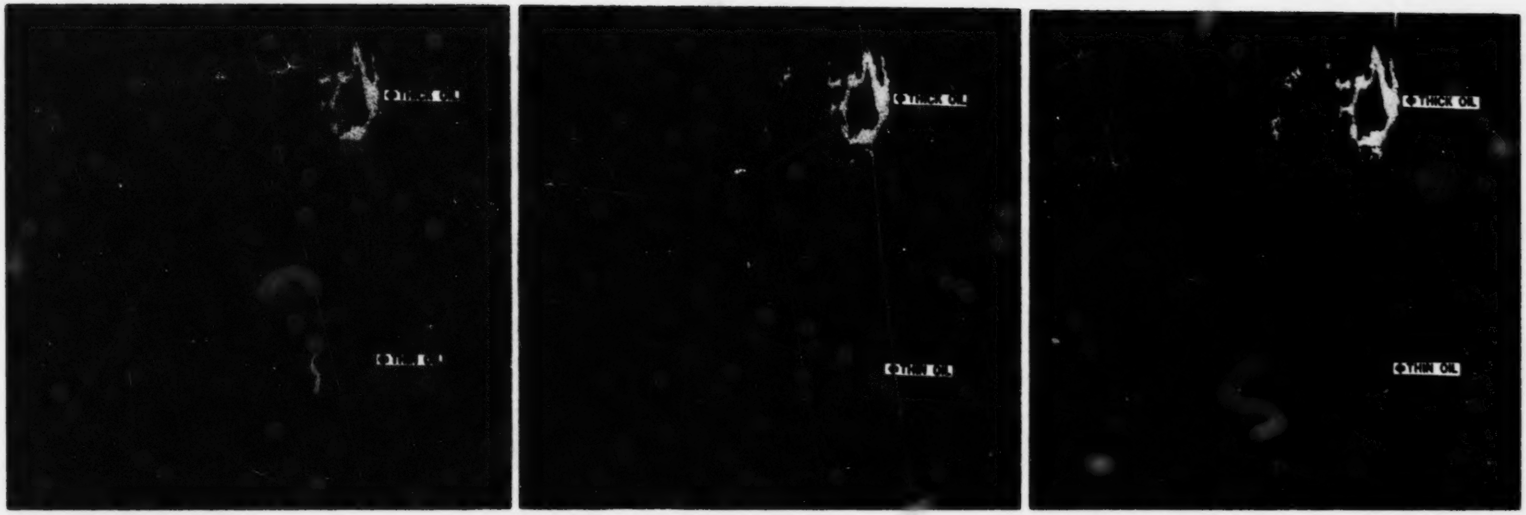
THICK OIL
THIN OIL
THICK OIL
THIN OIL
THICK OIL
THIN OIL

MSS Thematic Colour Image
MSS 3, MSS 6, MSS 8, MSS IR
Wallops Oil Spill
C-GRSA
Flight Line 2
November 3, 1978 16:27:51 GMT

MSS Thematic Colour Image
MSS 3, MSS 4, MSS 6, MSS IR
Wallops Oil Spill
C-GRSA
Flight Line 2
November 3, 1978 16:27:51 GMT

MSS Thematic Colour Image
MSS 3, MSS IR
Wallops Oil Spill
C-GRSA
Flight Line 2
November 3, 1978 16:27:51 GMT

FIGURE 80 MSS THEMATIC COLOUR IMAGE, WALLOPS OIL SPILL. C-GRSA Flight Line 2, November 3, 1978.

420 - 470, and 470 - 520 nm. The experiment should involve flying at various altitudes from 150 m to 6 000 m to compare net oil to water contrasts as more atmospheric path radiance is added.

4.4.5 Fluorosensor.

4.4.5.1 Scott Inlet oil seep. On the Scott Inlet mission, the CCRS MkIII fluorosensor was flown operationally for the first time. The oil seep at Scott Inlet was overflown on September 19, 1978 on Sorties 9 and 10 (see Appendix G). The fluorosensor detected oil on only one Flight Line: Sortie 9, Flight Line 16 and 15:27:15 GMT. The 16 channel fluorosensor response is shown in Figure 81, and that response correlated to a Murban crude oil sample spectrum is shown in Figure 82. Only in the correlation coefficient diagram is the presence of oil indicated, and this is quite small. Comparing Figures 53 and 52 of the MSS channels 3 and thermal IR respectively, it is apparent that at 15:27:15 GMT, there is oil, sufficiently thick to be observable in the IR, at the nadir position, and thus in the fluorosensor's field of view. Of the seven flight lines on Sortie 9 and five flight lines on Sortie 10, on which oil was observed, only Flight Lines 7, 16 and 20 on Sortie 9 had oil targets which were sufficiently thick to be detectable in the thermal IR. The IR can only detect oil films down to 2 μm thick, and the thickness of most of the oil slicks observed near Scott Inlet were less than this. Comparison of visual observations with the results of other investigators (Horstein, 1972; Fingas et al., 1979) indicate that most of these films were less than 0.8 μm in thickness.

The fluorosensor will detect oil films that are approximately an order of magnitude thinner than that observable by a thermal IR detector. However, several electronic problems in the fluorosensor circuitry and a possible optical misalignment on the Scott Inlet mission contributed to a lower overall sensitivity in the operation of the fluorosensor. The degraded sensitivity coupled with the thinness of most of the oil slicks observed in the Scott Inlet region would account for the fact that the fluorosensor observed oil on only one flight line.

It is noted here that while no in situ measurements were made at the time of the oil sighting, the personnel aboard the C.S.S. HUDSON observed oil upwelling in the same area five days later on September 24, 1978, and were able to obtain samples of the oil (MacLean and Falconer, 1979). Photographs taken from the ships show an oil slick

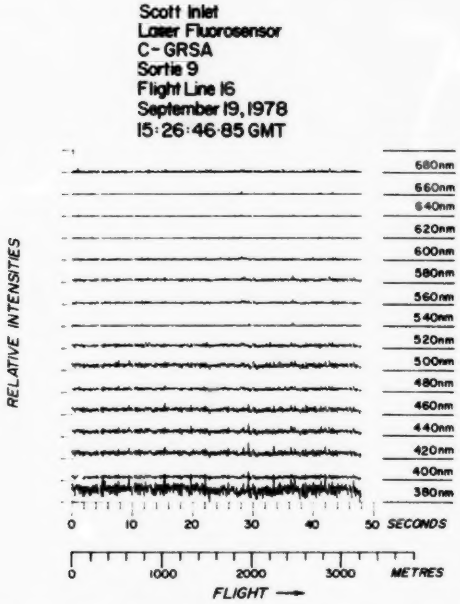

FIGURE 81 FLUOROSENSOR, SCOTT INLET OIL SEEP. C-GRSA Sortie 9, Flight Line 16, September 19, 1978.

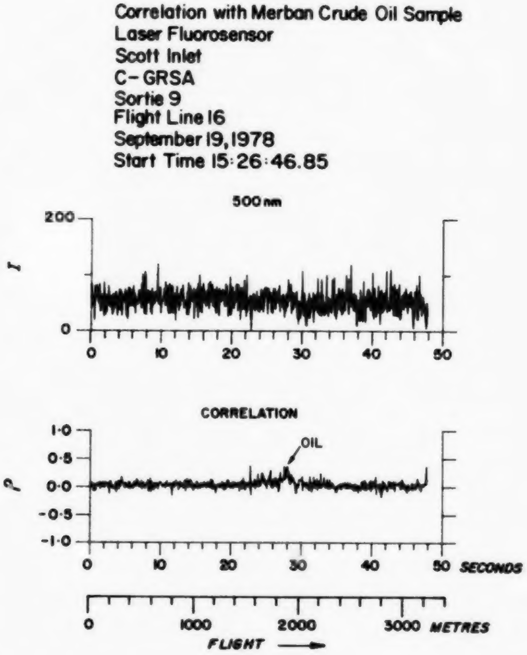

FIGURE 82 CORRELATION OF FLUOROSENSOR DATA IN FIGURE 81 WITH MURBAN CRUDE OIL FLUORESCENCE SPECTRUM.

similar in appearance to that shown in reference Levy (1977). The locations of these oil sightings are plotted in this report (see Appendix E).

4.4.5.2 **Wallops Island test oil spill.** The only other mission on which the fluorosensor was used to collect data was at Wallops Island. In the interim period the fluorosensor was realigned and the majority of the electronic problems were remedied to give improved sensitivity.

In addition to the airborne data collected with the fluorosensor, laboratory measurements were made of the fluorescence conversion efficiencies of the two test oils, Murban and La Rosa crude. These are compared in Figures 83 and 84 with conversion efficiencies calculated from the fluorosensor data. The good correspondence between the two spectra is noted.

November 1, 1978: Rhodamine WT. Prior to the oil spill tests, a trial sortie was performed in which Rhodamine WT dye was used as a target. The fluorosensor was flown on this sortie; a typical response by the fluorosensor to Rhodamine WT is shown in Figure 85 for Flight Line 6. In Figures 86 and 87 are diagrams of correlations, one with Rhodamine WT (Figure 86) and one with Murban crude (Figure 87). The Murban crude test shows no correlation. The fluorescence conversion efficiencies given at 337 nm excitation for Murban crude, La Rosa crude and Rhodamine WT are shown in Figure 88 (the three target materials on the Wallops Island mission). The Rhodamine WT spectrum is significantly different from the crude oil spectra.

The largest concentration of Rhodamine WT measured on the sortie was 13 ppb (private communication, Frank Hoge, NASA Wallops 1979).

November 2, 1978: Murban crude oil. The oil was detected on many passes over the spill on November 2, 1978. The fluorosensor response on Flight Line 12 is shown in Figure 89; the correlation of the fluorosensor response to Murban crude is given in Figure 90. The oil slick occurs at approximately 19 seconds into the flight line. Another feature occurs at 23 seconds; it is the GEO. B. KELEZ, a research vessel standing to the side of the spill. It should be noted that while something on the ship caused a fluorescence return, the correlation with Murban crude oil (Figure 90) discriminates against it.

The fluorosensor response on Flight Line 17 is shown in Figure 91; correlations of the response to several samples are shown in Figures 92 and 93. While the fluorosensor spectra correlate poorly to the light oil sample and the Rhodamine WT sample, they

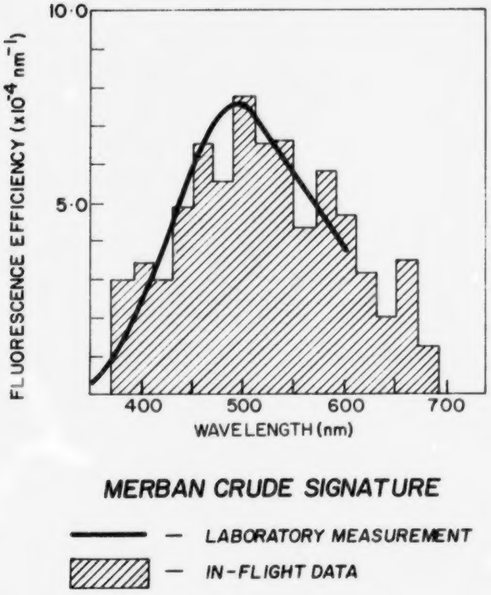

FIGURE 83 MURBAN CRUDE OIL FLUORESCENCE SIGNATURE OBTAINED WITH LABORATORY FLUOROMETER.

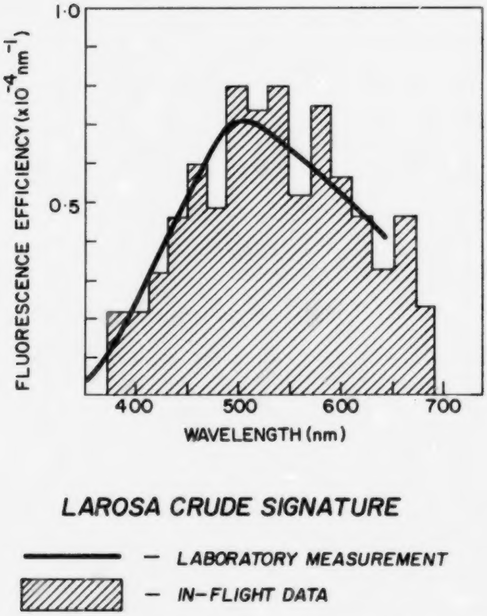

FIGURE 84 LA ROSA CRUDE OIL FLUORESCENCE SIGNATURE OBTAINED WITH LABORATORY FLUOROMETER.

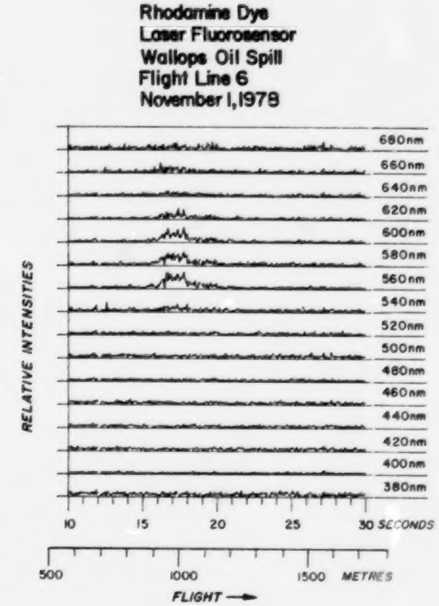

FIGURE 85 FLUOROSENSOR, WALLOPS TEST SPILL. Fluorosensor response to rhodamine dye. C-GRSA Flight Line 6, November 1, 1978.

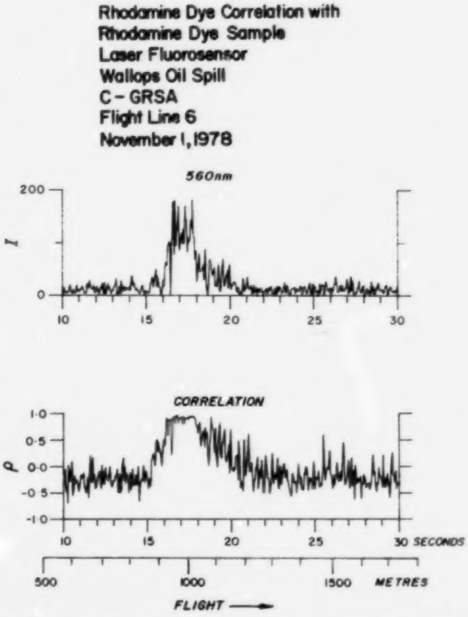

FIGURE 86 CORRELATION OF DATA IN FIGURE 85 WITH RHODAMINE WT FLUORESCENCE SPECTRUM.

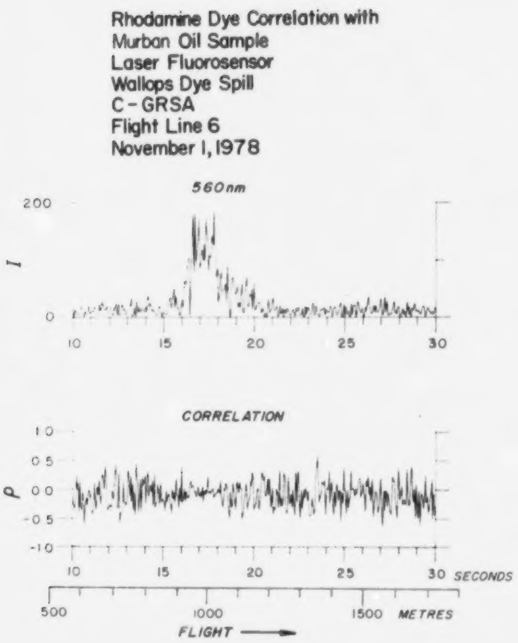

FIGURE 87 CORRELATION OF DATA IN FIGURE 85 WITH MURBAN CRUDE OIL FLUORESCENCE SPECTRUM.

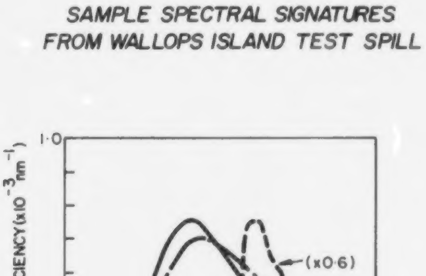

FIGURE 88 SAMPLE SPECTRAL SIGNATURES (Murban crude oil, La Rosa crude oil, Rhodamine WT) FROM THE WALLOPS ISLAND TEST SPILLS.

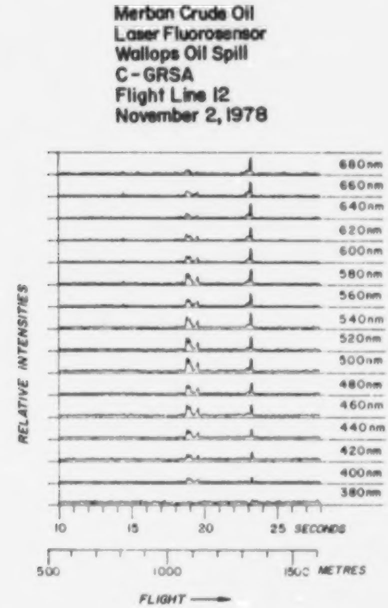

FIGURE 89 FLUOROSENSOR, WALLOPS OIL SPILL. Fluorosensor response to Murban crude oil. C-GRSA Flight Line 12, November 2, 1978.

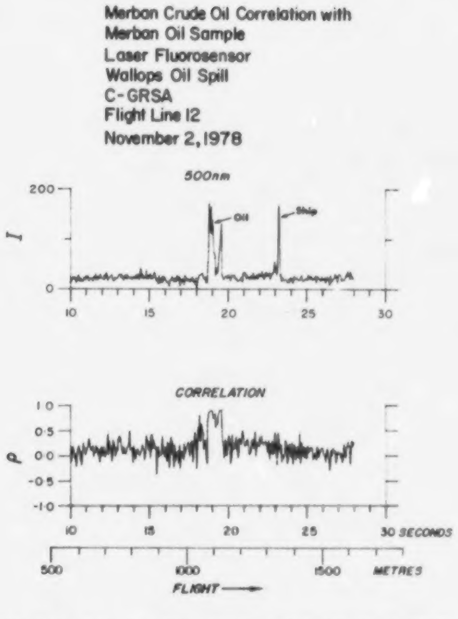

FIGURE 90 CORRELATION OF DATA IN FIGURE 89 WITH A MURBAN CRUDE OIL FLUORESCENCE SPECTRUM.

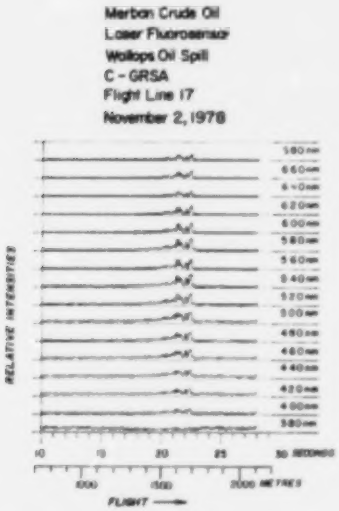

FIGURE 91 FLUOROSENSOR, WALLOPS OIL SPILL. Fluorosensor response to Murban crude oil. C-GRSA Flight Line 17, November 2, 1978.

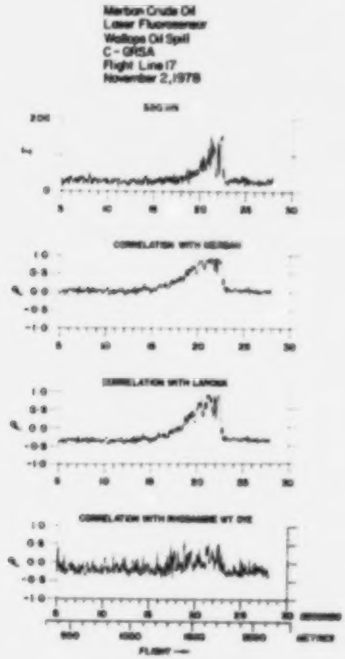

FIGURE 92 CORRELATION OF DATA IN FIGURE 91 WITH A MURBAN CRUDE OIL, LA ROSA CRUDE OIL AND RHODAMINE WT FLUORESCENCE SPECTRA.

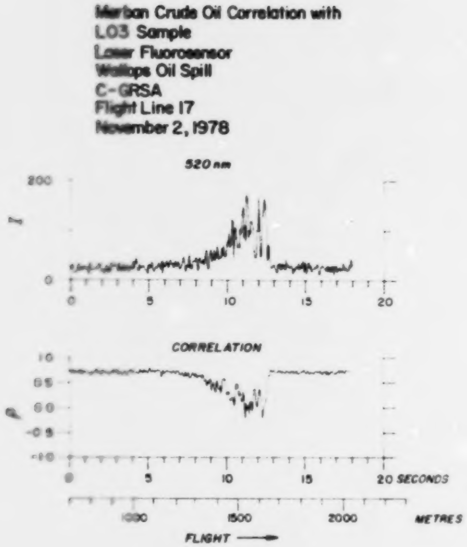

FIGURE 93 CORRELATION OF DATA IN FIGURE 91 WITH LIGHT OIL SAMPLE LO3 FLUORESCENCE SPECTRUM.

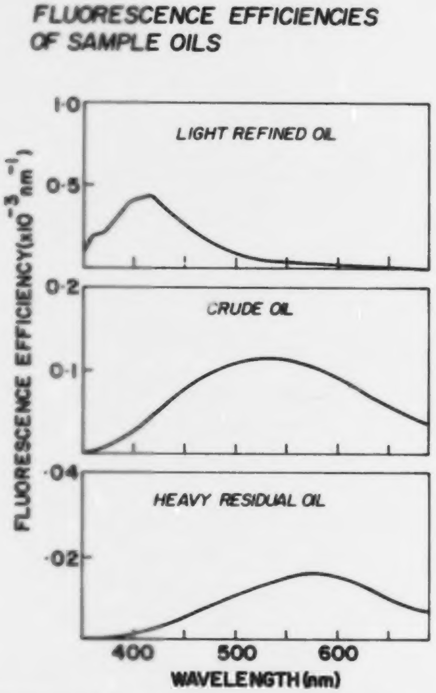

FIGURE 94 COMPARATIVE DIAGRAM SHOWING LIGHT, CRUDE AND HEAVY OIL FLUORESCENCE EFFICIENCIES.

correlate well, and equally so, to the two crude samples. Shown in Figure 94 are the fluorescence conversion efficiencies (given at 337 nm excitation) for a light oil, a crude oil and a heavy residual oil. It is evident that the fluorosensor, with its data processed via the correlation technique, can distinguish between oil types, i.e. oils with significantly different fluorescence spectra, but cannot discriminate between oils with similar fluorescence spectra.

The fluorosensor track for Flight Line 13 is plotted on the MSS thermal IR image in Figure 95. The fluorosensor response is given in Figure 96; its correlation to Murban crude oil in Figure 97. The interval 'A' along the flight track in Figure 95 is the distance over which fluorescence return from oil is discernible in Figure 96; the interval 'B' is that over which the correlation processed data (Figure 97) indicate the presence of oil. From this comparison of the fluorosensor and IR data one can estimate the oil thickness detection threshold for the fluorosensor. The minimum thickness detectable in the IR is approximately 2 μm. Since the interval 'A' completely overlaps the dark (2 μm thick) region in the IR image (Figure 95) it is concluded that the fluorosensor has a shot-to-shot thickness detection threshold of approximately 2 μm for this particular type of oil. This compares well with the detection limit of 1 μm calculated by Rayner (1979) for a fluorescence detection system using a 337 nm excitation wavelength. The application of the correlation technique improves the fluorosensor's performance even beyond this limit. If the oil film thickness in Figure 95 is approximated by an exponential interpolation between the 2 μm thermal IR edge and the 50 nm visible (MSS 3) edge, it is found that the interval 'B' extends out to a point where the oil thickness is estimated to be 0.3 μm. This is considered to be a reasonable estimate, as it compares well with the expected improvement resulting from the correlation procedure. This procedure involves the average of five consecutive fluorosensor spectra before the 16-channel Pearson correlation coefficient is calculated; both steps together should improve the signal-to-noise ratio by approximately ten-fold.

Shown in Figure 98 are colour coded fluorosensor responses of Flight Lines 13 and 17 from November 2. Compared with the 16-channel plots of Figures 96 and 91, presentation of the fluorosensor data in this format makes the data more readily interpretable.

November 3, 1978: La Rosa crude oil. The fluorosensor response to the La Rosa crude oil spill was much less intense than to the Murban oil spill on November 2.

COMPARISON OF DATA FROM MSS AND FLUOROSENSOR

SOLID LINE – PATH OF FLUOROSENSOR
A – REGION WHERE RAW DATA INDICATED OIL
B – EXTENDED REGION WHERE CORRELATION ANALYSIS INDICATED OIL

FIGURE 95 FLUOROSENSOR AND MSS IR, WALLOPS OIL SPILL. Comparison of fluorosensor oil detection to MSS IR oil detection capabilities. C-GRSA Flight Line 13, November 2, 1978.

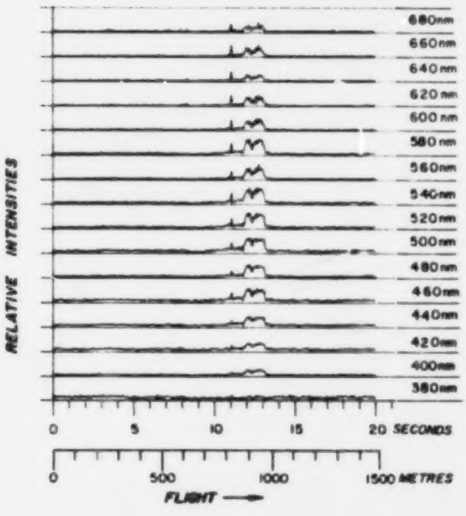

Merban Crude Oil
Laser Fluorosensor
Wallops Oil Spill
C-GRSA
Flight Line 13
November 2, 1978

FIGURE 96 FLUOROSENSOR, WALLOPS OIL SPILL. Fluorosensor response to Murban crude oil. C-GRSA Flight Line 13, November 2, 1978.

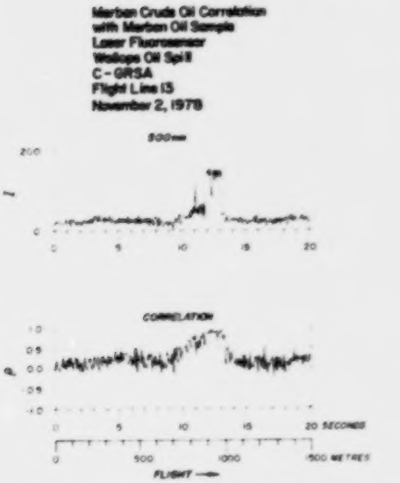

FIGURE 97 CORRELATION OF DATA IN FIGURE 96 WITH A MURBAN CRUDE OIL FLUORESCENCE SPECTRUM.

This is due to the fact that the fluorescence conversion efficiency of the La Rosa crude is one-tenth that of the Murban crude (Figure 88). Data from Flight Line 6 are shown in Figure 99; those from Flight Line 23, in Figure 100. The correlation to La Rosa crude is given in Figures 101 and 102 respectively. While the fluorescence of the target is apparent in the response on Flight Line 6 (Figure 99), it is not for Flight Line 23 (Figure 100); however, the detectability enhancement provided by the correlation process permits the detection of oil in both cases.

A particularly interesting feature present in both Figures 99 and 100 is the negative deflection of the signal in channel one (381 nm) at the times when oil is detected (at 16 seconds in Figure 99; 20 seconds in Figure 100). This is a result of the suppression of the Raman scattered radiation from the water by the surface oil layer (see Section 4.1.5). That this suppression is much more prominent for the La Rosa crude than for the Murban (compare Figures 89, 91 and 96 with Figures 99 and 100) is the result of two factors, both stemming from the decreased conversion efficiency of the La Rosa crude. To compensate for the weak fluorescence radiation from the La Rosa crude, the fluorosensor spectrometer gain is substantially higher than for the Murban crude, thereby accentuating any variation in the water Raman radiation. At the low gain setting for the Murban crude the Raman signal may in fact be masked by the system noise. The other factor is that the Murban oil, a more efficient fluorescence radiator, may be emitting sufficient radiation in this first spectral band to compensate for the lost Raman scattered radiation (see Section 4.1.5). It is evident that for the heavier, less fluorescent oil types

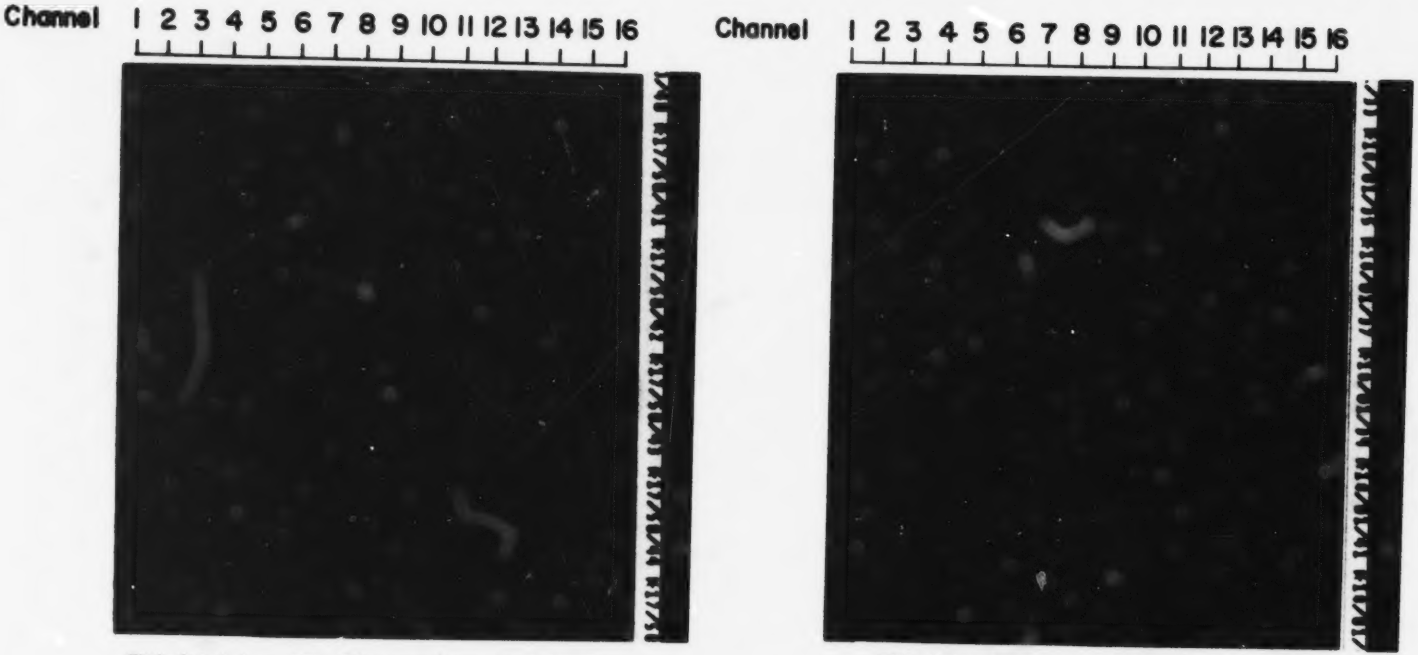

Flight Line 13, November 2, 1978

Flight Line 17, November 2, 1978

Fluorescence Intensity Blue → White

FIGURE 98 FLUOROSENSOR, WALLOPS OIL SPILL. Response shown as a colour enhanced time history. C-GRSA Flight Lines 13 and 17, November 2, 1978.

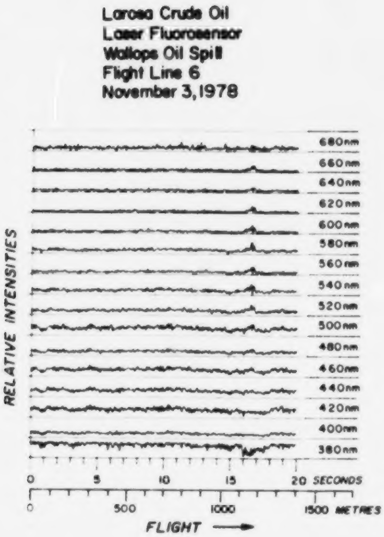

FIGURE 99 FLUOROSENSOR, WALLOPS OIL SPILL. Fluorosensor response to La Rosa crude oil. C-GRSA Flight Line 6, November 3, 1978.

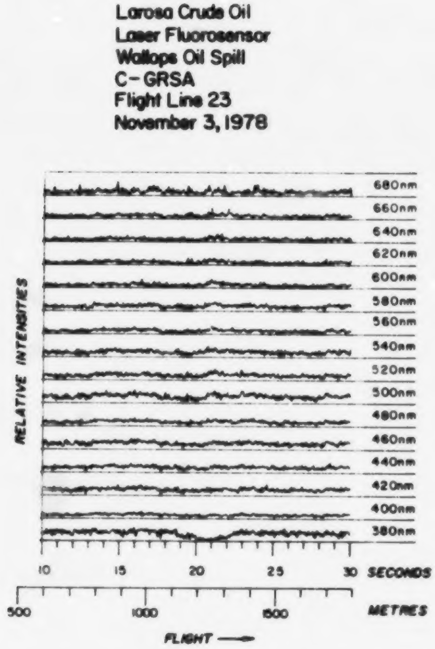

FIGURE 100 FLUOROSENSOR, WALLOPS OIL SPILL. Fluorosensor response to La Rosa crude oil. C-GRSA Flight Line 23, November 3, 1978.

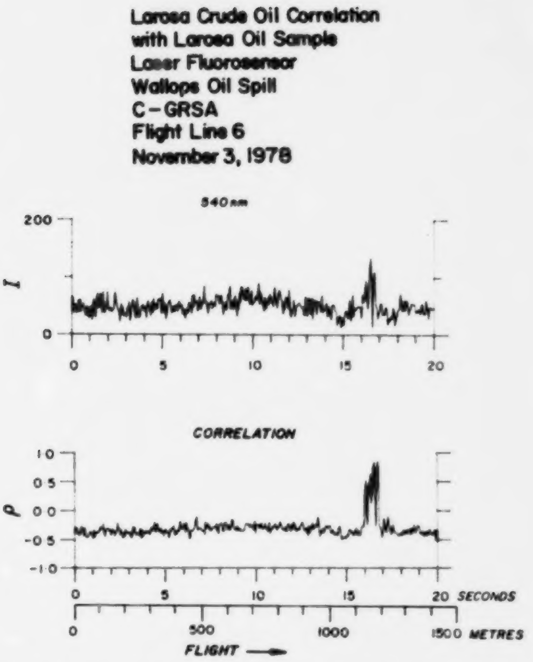

FIGURE 101 CORRELATION OF DATA IN FIGURE 99 WITH LA ROSA CRUDE OIL FLUORESCENCE SPECTRUM.

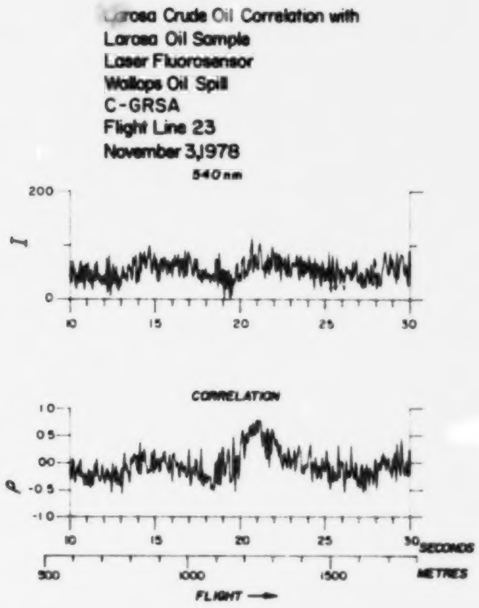

FIGURE 102 CORRELATION OF DATA IN FIGURE 100 WITH LA ROSA CRUDE OIL FLUORESCENCE SPECTRUM.

the application of the water Raman suppression will prove valuable in the detection of oil slicks.

4.5 Conclusions and Recommendations

This section is divided into subsections on the microwave region, the near ultraviolet, visible, near infrared region, the thermal IR region, and on fluorescence methods. Each subsection includes conclusions pertaining to the physical processes involved in the detection of oil; recommendation of sensors; the suggestion of modifications to the sensors and future research; and development that should be undertaken. The expected performance of the recommended sensor package for oil on water, oil on ice and oil in open pack ice is summarized and the detection of oil from satellites is discussed briefly.

4.5.1 Microwave Sensors. Two microwave sensors, both active devices, the ERIM SAR and the CCRS-Ryan scatterometer, were used in this project. Conclusions and recommendations pertaining only to active microwave sensors can be drawn from the results; however, comments are made concerning results of other investigations of the use of microwave radiometers for oil detection.

4.5.1.1 Oil on water.

Frequency. The SAR, a dual frequency radar, produced coincident X and L band imagery from which it was concluded that X band is superior to L band for oil slick detection.

Incidence angle. The implication of the scatterometer results is that any active microwave sensor, SLAR, SAR or scatterometer, should be operated such that the target area falls at an incidence angle in the range of 30 - 55°, i.e. a depression angle range 35 - 60°.

Polarization. The scatterometer results indicate that for the range of incidence angles covered (0-60°) VV and HH polarization combinations see equal depressions in the radar backscatter cross section from an oil slick as compared to a clean sea surface. However, for incidence angles greater than 30° the backscatter cross section, σ_θ, for the sea surface is greater for VV polarization (Skolnik, 1969). The cross polarization combinations do not exhibit higher contrasts and give much reduced cross sections. It is concluded that for radars operating at incidence angles less than 30°, as from a satellite, either VV or HH could be used; for incidence angles greater than 30°, as would be used for airborne operations, VV polarization may be preferable. Coloured densigrams for Flight Line 3 on November 2 and Flight Line 4B on November 3 are shown in Figure 103. The suppression of backscatter cross section is more readily apparent in this form of presentation than other forms presented in this report.

Recommendations for future experiments. In future experiments involving oil spills on open water, an attempt should be made to cover many more wind/sea state conditions, including different look directions relative to the wind direction. In the experiment reported here the diameter of the slick was only a few scatterometer footprints at the time of the scatterometer overflights; large oil slicks are needed for microwave sensors in order to improve the measurement statistics.

4.5.1.2 Oil on ice. Although radar tests of oil on ice or oil in open pack ice were not performed, it is extremely doubtful that a SAR or SLAR would prove very useful. First, oil on ice would offer almost no contrast, oil being relatively transparent, as compared to sea ice. Secondly, backscatter from water is so much lower than that from ice that the reduction of the backscatter resulting from a slick would be offset by even small unresolved pieces of ice in the oil slick. Barring this occurrence, the arctic SAR data indicate that there are many naturally occurring slicks in ice-infested regions which would be confused with oil slicks.

4.5.1.3 Recommended sensors. Two active microwave sensors, the ERIM SAR and the CCRS-Ryan scatterometer, were used in this project. The scatterometer is strictly a research instrument, providing calibrated backscatter cross sections as a function of look angle. The SAR, while providing high resolution radar imagery for various polarization combinations, is a more versatile and complex instrument than is required for an oil detection package. Hence, a simpler SLAR unit operating in the VV polarization mode and giving real time imagery is recommended for an airborne oil detection package. Although the SLAR unit cannot differentiate between slicks of different origins, and is not expected to be very useful for arctic oil detection, its near all weather capability and wide swath widths, giving rapid coverage of a search area, make it an important sensor for oil spill detection.

Microwave radiometers were not tested by the AMOP remote sensing team. However, reports (Hollinger, 1974; Troy and Hollinger, 1977) on the US NRL dual frequency imaging microwave radiometer indicate that it can be used to measure oil

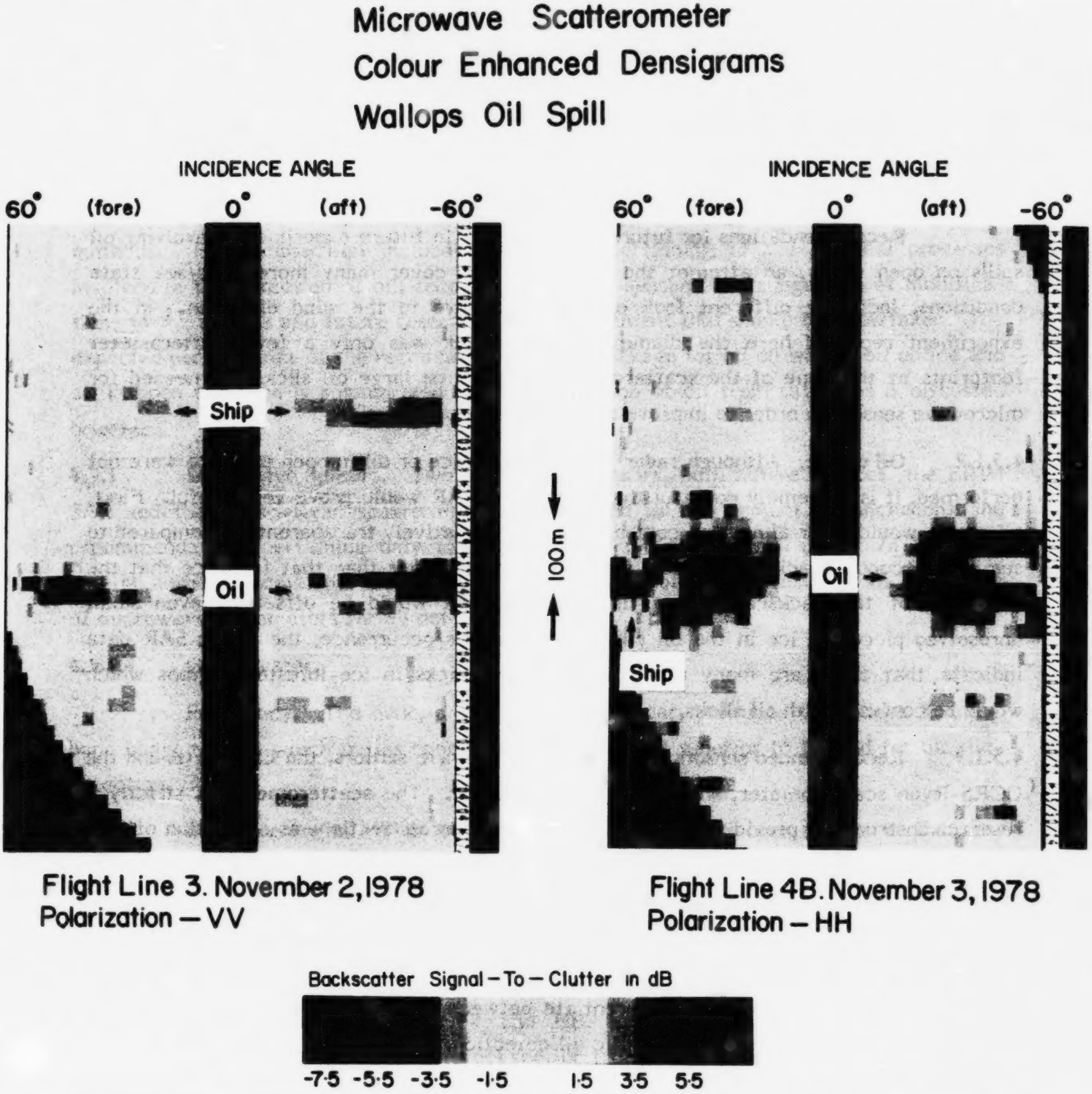

FIGURE 103 SCATTEROMETER, WALLOPS OIL SPILL. Colour enhanced densigram showing microwave scatterometer backscatter suppression for various incidence angles as a time history for VV and HH polarization. C-GRSC, Flight Line 3, November 2, 1978, and Flight Line 4B, November 3, 1978.

thicknesses down to 50 μm, providing that certain parameters, such as sea salinity and temperature and dielectric properties of the oil, are known.

If it is determined that the measurement of spill volumes is of high priority, then, as a possible alternative to the imaging microwave radiometer, it is recommended a study be undertaken to investigate the incorporation of a dual frequency profiling microwave radiometer with the dual channel line scanner. The 'absolute' thickness measured by the microwave radiometer could be used to calibrate the relative thickness measure given by the thermal IR.

Although it has not been sufficiently tested for the detection of oil on ice and in ice-infested waters, the microwave radiometer is not expected to prove satisfactory for this purpose; the reasons for this conclusion are the similar dielectric properties (in this frequency range) of snow, some ice types, some water-ice mixtures, and oil.

4.5.2 Near Ultraviolet, Visible, Near Infrared.

4.5.2.1 Spectral dependence. The presence of oil films on the water's surface increases the surface reflectance; the difference between the clean water reflectance and the oil film on water reflectance increases with decreasing radiation wavelength from 1 100 to 300 nm. Oil films of sufficient thickness to be optically thick absorb the component that is usually reflected from the water's volume. Extinction coefficient measurements reported in the literature (Horvath et al., 1970; Rayner, 1979) indicate that oil is increasingly absorptive as the wavelength decreases from the near IR to the UV. However, the absorptive effect of optically thick oil films on the total detected radiance from the sea is most noticeable in the spectral range 450 - 500 nm, not in the UV. This is because the proportion of the total radiance that is volume reflected from the water is highest in the 450 - 550 nm range. If the oil is emulsified it adds its own volume reflected or scattered component. This latter effect is largest, relative to the other contributing components, in the near IR and decreases with decreasing wavelength into the UV.

The net result is that the highest and most consistent contrasts, for either thin or thick, emulsified or unemulsified, layers of oil are obtained in the UV. Oil thickness and emulsification state information can be obtained by making additional measurements at approximately 525 nm and 725 nm. Thick unemulsified oil gives a negative contrast at 525 nm; thick emulsified oil gives a very high contrast at 725 nm.

Oil on and mixed into the surface ice is made visible mainly by its light absorbing properties. As oil is much more absorptive in the UV than in the visible, this spectral range offers the highest oil to ice contrast. This is borne out by the UV line scanner imagery from the KURDISTAN spill. However, water also appears dark in the UV; this gives rise to ambiguities which can be resolved by comparing the UV with the thermal IR imagery.

4.5.2.2 **Polarization.** The use of a horizontally aligned polarizer and Brewster angle viewing improves, by a factor of two, the ratio of the surface reflected component to volume reflected component. As a result, a measurement in the near UV- region, which already yields excellent contrast, can be improved and, at the same time, made less sensitive to the contrast degrading effect of thicker oil layers. This is borne out by the LLLTV imagery where the thicker oil layers have only slightly reduced oil to water contrasts.

4.5.2.3 **Recommended sensors.** The following near UV-visible sensors are recommended for inclusion in an oil detection package; a LLLTV filtered and polarized as for this project; a nadir looking camera using natural colour film; a forward viewing UV camera; and a dual channel line scanner with a near UV detector.

LLLTV. The LLLTV (RCA TC1030H) filtered with both a spectral (Corning 7-51 or equivalent) and a polarizing filter (Polaroid HNP'B) is highly sensitive, gives excellent oil to water contrast and, with the addition of a gimbal mounting system, offers the potential for a powerful, wide swath mapping system. This system can distinguish oil slicks from slicks of other origins, e.g. boat wakes, internal waves, freshwater on seawater, etc., but has difficulty discriminating against foam, ice chunks, etc. Although not tested on oil-in-ice, it is expected to provide good contrast, where the oil is now dark against a bright background, but poor discrimination against leads in the ice.

Because the LLLTV is so sensitive, it is possible to detect oil under twilight conditions; however, the presence of even one light in the field of view, such as would be on a ship or in a harbour, causes the camera to reduce its sensitivity. It is recommended that for such applications an automatic iris/eclipser be added to the LLLTV to prevent this close down.

Photographic cameras. Photography cannot provide results in real time; however, for back up and documentation on an oil spill it can be quite useful. The natural colour nadir photography is recommended because it provides imagery that gives moderately good contrast with some spectral information and is easily interpreted by a non-professional. A high resolution camera, such as the 23 cm format Wild Heerbrugg RC-10, is recommended because it permits the detection from high altitudes of small targets, such as small areas of oil pollution along a beach. The forward looking UV photography is recommended because it provides higher contrast than the colour photography for both oil on water and oil on ice. While the 70 mm format provides adequate resolution, the Vinten cameras used in this project are not recommended for use at ambient temperatures below 15°C.

DCLS. The dual channel line scanner with UV and thermal IR channels provides data in a form that allows processing and precise registration of the image from the two channels in real time. The UV channel, at relatively low altitudes, gives excellent contrast for the very thin regions of an oil slick on water, thereby delineating the slick's extent. It also provides very good contrast for oil on ice; however, if used alone, it will have difficulty in distinguishing oil in open pack ice conditions. The contrast in the UV will suffer from increased path radiance at the higher altitudes. At these altitudes it may be possible to improve the net contrast by moving the detected range from the present 300 - 370 nm, to 370 - 420 nm, or 420 - 450 nm where, although the oil to water contrast at the surface is less, the atmospheric path radiance is also less. Research should be directed towards this question; the conclusion may be that it should be possible to make an in flight choice of filter, depending on altitude and atmospheric condition.

4.5.3 Thermal IR.

4.5.3.1 Oil on water. The thermal IR imagery, coupled with coincident visible imagery, leads to the conclusion that an easily detectable emittance reduction, detected as an apparent temperature reduction, is produced by oil films as thin as 2 μm. This can be explained reasonably only by applying a coherent thin film emittance theory that takes into consideration thin film interference as it affects the transmitted IR radiation. Surface emittance reductions from 0.988 for water to 0.934 - 0.959 were measured. These values are consistent with bulk oil emissivities in the range 0.964 - 0.971.

Solar heating of optically thick layers of oil produces readily detectable warm areas in the oil. Apparent temperature increases of as much as 4.3 K, corresponding to a physical temperature increase of 5.5 K, were observed for a solar elevation of 33°.

Thin (<1 μm) films of oil produce a very slight warming of the surface because of reduced vaporization or reduced thermal conduction from a warm air layer to the cooler water.

4.5.3.2 Oil on ice. Measurements published in the literature (Poulin, 1973) indicate that the emissivity of ice is as high as water in the spectral range 8.5 - 10.5 μm. A sufficient thickness of oil, which has a lower emissivity, to be optically thick at these wavelengths, therefore, should appear cooler than the ice, provided solar heating is absent. This would be the expected effect for heavy overcast sky conditions or for night operations.

IR imagery of oil on ice obtained in this project was for solar elevations $\geq 30°$. Solar heating was evidenced by the fact that in this imagery the apparent temperatures for the oil were higher than for the surrounding ice. Under such conditions better signal-to-noise and possibly better contrasts can be obtained for the full 8.5 - 12.5 μm range.

4.5.3.3 Recommended sensor. The HgCdTe detector mounted in the Daedalus model 1230 dual channel line scanner performed well during the project, and is recommended as part of an oil detection package. The spectral range 8.5 - 12.5 μm should be used for oil on water and oil on ice with solar elevations >20°; the range 8.5 - 10.5 μm should be used for oil on ice with solar elevations <10°.

Apart from the fact that both the UV and thermal IR spectral ranges separately have high information content, the value of the DCLS is that it combines both, with the imagery precisely superimposed so that cross-correlation of the data can be performed in real time by an airborne computer. It is in this form that the DCLS is rated in Tables 4, 5 and 6 for daylight conditions.

It is noted that the oil on ice signature detected by the DCLS could be duplicated by any substance having high thermal emissivity and high visible/UV absorptivity; thus, certain types of soil on ice could not be distinguished from oil.

4.5.4 Fluorescence. The measurement of fluorescence emission is the only known operational, remote sensing technique that permits a positive identification of oil. As such, it is an extremely valuable method, especially for arctic and open pack ice conditions where no other method can provide even moderately good discrimination against other anomalous features.

An active method, in which a laser is used to induce fluorescence, is preferable to the passive, which relies on the sun for illumination. The active technique can be applied to night and arctic operations, and laboratory studies have indicated that, coupled with spectral analysis, a measurement of the fluorescence delay time can yield identification of the particular target oil (Rayner and Szabo, 1976).

TABLE 4 SENSOR PERFORMANCE: OIL ON WATER

Sensor	Contrast/ Detectability	Specificity	Minimum Thickness (nm)	Thickness Measure	Weather Capability	Illumination[d] Conditions	Imaging[b] Width
SLAR	good	nil	<100[a]	none	all[e]	all	20 km per side[a]
UV-IRLS	excellent	good	50[a]	good (relative)	clear	sun >10°	1.6 x altitude
IRLS[c]	excellent	fair	2000	poor	clear	all	1.6 x altitude
LLLTV (filtered)	excellent	fair	50[a]	none	clear	sun >-7.5°	1.7 x altitude
Photography							
23 cm-colour	very good	good	50[a]	fair	clear	sun >20°	2.6 x altitude
70 mm-UV	excellent	fair	50[a]	none	clear	sun >20°	1.0 x altitude
Fluorosensor	excellent	excellent	500	good (relative)	clear	all	profile only

a not measured during this project - taken from references.
b design dependent - numbers here are for sensors used during this project.
c for sun angles <10° the IR channel of the UV-IRLS may be used separately.
d sun elevation limits may be increased for overcast skies.
e very heavy precipitation (rain or snow) may degrade the performance of SLAR's operating at wavelengths shorter than or equal to X-band.

TABLE 5 SENSOR PERFORMANCE: OIL ON ICE

Sensor	Contrast/ Detectability	Specificity	Minimum Thickness (nm)	Thickness Measure	Weather Capability	Illumination[e] Conditions	Imaging[b] Width
SLAR	nil[d]	nil[d]			all[f]	all	20 km[a]
UV-IRLS	very good	fair	optically thick[d]	fair[d]	clear	sun >10°	1.6 x altitude
IRLS[c]	poor[d]	very poor[d]	200,000[d]	poor[d]	clear	all	1.6 x altitude
LLLTV	very good[d]	poor[d]	optically thick[d]	poor[d]	clear	sun >-7.5°	1.7 x altitude
Photography							
23 cm-colour	good	fair	optically thick[d]	poor[d]	clear	sun >20°	2.6 x altitude
70 mm - UV	very good[d]	poor	optically thick[d]	poor[d]	clear	sun >20°	1.0 x altitude
Fluorosensor	excellent[d]	excellent[d]	500[d]	fair (relative)[d]	clear	all	profile only

a not measured during this project - taken from references.
b design dependent - numbers here are for sensors used during this project.
c for sun angles <10° the IR channel of the UV-IRLS may be used separately.
d not tested in this project - estimated.
e sun elevation limits will be increased for overcast skies, decreased for higher ice reflectivity.
f very heavy precipitation (rain or snow) will degrade the performance of SLAR's operating at wavelengths shorter than or equal to X-band.

TABLE 6 SENSOR PERFORMANCE: OIL IN OPEN PACK ICE

Sensor	Contrast/Detectability[a]	Specificity[d]	Minimum Thickness (nm)[f]	Thickness Measure[f]	Weather Capability	Illumination Conditions[e]	Imaging[b] Width
SLAR	nil	nil			all[g]	all	20 km[a]
UV-IRLS	fair	poor			clear	sun >10°	1.6 x altitude
IRLS[c]	poor	very poor			clear	all	1.6 x altitude
LLLTV	poor	nil			clear	sun >-7.5°	1.7 x altitude
Photography							
23 cm-colour	fair	poor			clear	sun >20°	2.6 x altitude
70 mm-UV	fair	poor			clear	sun >20°	1.0 x altitude
Fluorosensor	excellent	excellent			clear	all	profile only

a not measured during this project - taken from references.
b design dependent - numbers here are for sensors used during this project.
c for sun angles <10° the IR channel of the UV-IRLS may be used separately.
d not tested during this project - estimated.
e sun elevation limits will be increased for overcast skies.
f see Table 7 for oil on water, Table 8 for oil on ice.
g heavy precipitation (snow or rain) may degrade the performance of SLAR's operating at wavelengths shorter than or equal to X-band.

4.5.4.1 Recommended sensor: CCRS MkIII fluorosensor. The CCRS MkIII fluorosensor at the present time measures the spectral fluorescence response but not the temporal response of the oil. Processing the spectral data by employing correlation techniques, however, enables the positive identification of oil and even permits the discrimination of oil types. Oil films as thin as 0.5 μm can be detected in this way. While the CCRS fluorosensor, the only known operational instrument of its kind, is a profiling sensor, it can be coupled with a UV-IR line scanner to identify features visible in the imagery. In this way the usefulness of the fluorosensor can be enhanced.

4.5.5 Oil Spill Detection from Satellites. An extensive study (Alvarado et al., 1979) has recently been completed in which the potential of space technology for monitoring oceanic pollution was assessed. The study examined: the requirement for an ocean pollution surveillance system and how well the current and foreseeable technology can be used to meet these requirements. It was recognized that further research would be required on the fundamentals of the pollution detection mechanism and that some advances would have to be made beyond the present technology before a pollution sensing satellite system could become operational; nonetheless, neither scientific nor technical difficulties could be foreseen. For an ocean surveillance satellite system to be truly operational in an oil pollution role, all data would have to be available in near real time. Automated algorithms for the detection of anomalies do not yet exist, and because of the vast regions of coastal waters which would be surveyed, the data reduction and interpretation system was seen to be one of the major development areas. It also appears that, in most operational situations, anomalies detected from the satellite borne sensors would have to be investigated using aircraft and surface vessels. Remote sensing in support of oil spill countermeasures would be carried out with a suitably equipped aircraft in order to obtain data of high spatial resolution in an acceptable time frame.

The following two sections summarize the experience to date on the detection of oil slicks with satellite borne sensors.

4.5.5.1 Optical sensors. Through the use of special enhancement techniques, oil slicks have been detected in Landsat imagery as areas of decreased brightness within the sun's glitter pattern (Deutsch et al., 1977). Clearly the sun-slick-satellite angles must be such that the slick is located within the glitter pattern, whose size depends on surface wind speed. For those instances in which this technique has been successful, the solar elevation has been greater than 39°.

There is one known instance in which an oil spill has been detected from satellite through the increased reflectance of the oil. The oil well blowout at Ixtoc 1 in the Gulf of Mexico resulted in a very large oil slick in which the oil was emulsified and hence highly reflective. The spill was detected by the Visible-Infrared Spin Scan Radiometer on GOES on June 6, 1979; by the Advanced Very High Resolution Radiometer on TIROS-N on June 6, 1979; and by the MSS on LANDSAT on July 20, 1979. However, even in these cases, undoubtedly because of the limited sensitivity of the sensors, the oil was visible only for certain sun angles.

Assuming that satellites carrying more sensitive detectors (e.g. the Coastal Zone Color Scanner (CZCS)) will be launched in the future, the cloud cover which frequently obscures Canada's coastal and arctic regions will still limit the effectiveness of optical surveillance from a space platform. An airborne sensor, on the other hand, can be flown beneath the clouds, even though the ceiling may be as low as 300 metres. Oil pollution surveillance demands that the imagery be processed and analyzed in real time. Although the present civilian satellite borne optical sensors and the associated ground systems cannot handle large volumes of data at an acceptable rate, a space system designed specifically to provide surveillance information on an operational basis could meet the requirement.

4.5.5.2 Microwave sensors. The answer to the cloud cover problem is the use of microwave sensors such as the L band SAR on SEASAT. The data obtained from this satellite, before its premature malfunction, indicate that its sensitivity was sufficient to detect surface slicks. The problem here is that the SAR imagery is non-specific as to the cause of the slick. Imagery from SEASAT showed numerous extensive slick areas on the oceans; presumably many of these were due to natural causes. Without corroborative data from some other source, this imagery would be of little value to an oil spill surveillance program because of the untenably high false alarm rate. Again, in ice-infested waters the satellite SAR would suffer from the same problems as the airborne SLAR and would be of little value for oil detection in the Arctic.

REFERENCES

Airborne Operation, Information Bulletin; 3rd. ed., Airborne Operations Section, Canada Centre for Remote Sensing, Ottawa, Ont. (July 1977).

Alvarado, U.R. et al., Assessment of the Use of Space Technology in the Monitoring of Oil Spills and Ocean Pollution; prepared by Space Division, General Electric for NASA Langley Research Centre, Contract No. NAS-1-15657 (December 1979).

Axelsson, S., Remote Sensing of Oil Slicks: Results from a Field Experiment in the Baltic Sea, Sept. 1974; SAAB-SCANIA AB, RL-0-3 R27, Linkoping, Sweden (May 1975).

Backlund, L., *Airborne Oil Spill Systems in Sweden*, Swedish Space Corp., Stockholm (March 1979).

Buettner, K.J.K. and C.D. Kern, "The Determination of Infrared Emissivities of Terrestrial Surfaces," *J. of Geophysical Research*, *70*, pp. 1329-1337 (1965).

Cox, C. and W. Munk, "Measurement of the Roughness of the Sea Surface from Photographs of the Sun's Glitter," *Journal of Optical Soc. of America*, *44*, pp. 838-850 (1954).

Croswell, W.A., NASA Langley Research Center, private communication (1979).

Deutsch, M., A.E. Strong and J.E. Estes, "Use of Landsat Data for the Detection of Marine Oil Slicks," *Proc., 9th Offshore Technology Conf.*, Houston, Texas (May 2-5, 1977).

de Villiers, J.N., "Airborne Detection and Mapping of Oil Spills, Grand Bahamas, Feb. 1973," CCRS Data Report 73-7, Canada Centre for Remote Sensing, Ottawa (September 1973).

Edgerton, A.T. and D.T. Trexler, "Oceanographic Applications of Remote Sensing with Passive Microwave Techniques," *Proc. 6th Symp. on Remote Sensing of Environment*, *2*, p. 767 (October 1969).

Edgerton, A.T. and P. Hinds, Microwave Radiometric Observations of Controlled Oil Spills, Southern California Oil Pollution Experiment: Remote Sensing; U.S. Coast Guard Hdqts., Office of Research and Development, Washington, D.C. (July 1971a).

Edgerton, A.T., D. Meeks and D. Williams, *Microwave Emission Characteristics of Oil Slicks; a Collection of Technical Papers-Land and Water*, Aerojet-General Corp., El Monte, Ca. (November 1971b).

Edgerton, A.T. and G. Poe, *Microwave Emission Characteristics of Sea Ice; Earth Resources Program Review*, 4, NOAA Programs and U.S. Naval Research Lab. Programs, L.B. Johnson Space Center (NASA), Houston, Texas (January 1972).

Edgerton, A.T., J.J. Bommarito, R.S. Schwantje and D.C. Meek, "Development of a Prototype Oil Surveillance System, Final Report," U.S. Coast Guard, Department of Transportation, Washington, D.C., Report No. CG-D-90-75 (May 1975).

Fingas, M.F., W.S. Duval and G.B. Stevenson, The Basics of Oil Spill Cleanup, Environmental Protection Service, Ottawa (1979).

Gray, A.L., R.K. Hawkins, C.E. Livingstone, R. Lowry, R. Larson and R. Rawson, "The Influence of Incidence Angle on Microwave Radar Returns on 'Targets' in an Ocean Background," Proc. 13th Symp. on Remote Sensing of Environment, Ann Arbor, Mich. (April 1979).

Henderson, S.T., Daylight and its Spectrum, Elsevier Scientific Pub. Co., N.Y. (1970).

Hoge, F.E. and R.N. Swift, "Oil Film Thickness Measurement Using Airborne Laser-Induced Water Raman Backscatter," Applied Optics, 19, pp. 3269-3281 (1980).

Hoge, Frank, NASA Wallops, private communication (1979).

Hollinger, J.P., "The Determination of Oil Slick Thickness by Means of Multifrequency Passive Microwave Techniques," NRL Memorandum Report 2953, U.S. Navy, Naval Research Lab., Washington, D.C. (June 1974).

Horstein, B., "The Appearance and Visibility of Thin Oil Films on Water," U.S. Environmental Protection Agency, Cincinnati, Ohio, EPA R2-72-039 (August 1972).

Horvath, R., W.L. Morgan and R. Spellicy, "Measurements Program for Oil-Slick Characteristics," Report No. 2766-7-F, Environmental Research Inst. of Michigan, Ann Arbor, Mich. (February 1970).

Horvath, R., W.L. Morgan and S.R. Stewart, "Optical Remote Sensing of Oil Slicks: Signature Analysis and Systems Evaluation," Willow Run Lab., Ann Arbor, Mich. (October 1971).

Johnson, J.C., JBF Scientific, private communication (1979).

Kirby, M.E. and R.T. Lowry, "Iceberg Detectability Problems Using SAR and SLAR Systems," American Water Resources Assoc. Satellite Hydrology Symp., Sioux Falls, S. Dakota (June 1979).

Krishen, K., "Correlation of Radar Back Scattering Cross Sections with Ocean Wave Height and Wind Velocity," Journal of Geophysical Research, 76, pp. 6528-6539 (1971).

Lapp, P.A., "An Investigation of Systems for the Surveillance and Monitoring of Oil Spills at Beaufort Sea," Canada Centre for Remote Sensing, Ottawa, Ont. (1975).

Levy, E.M., "Scott Inlet Slick: an Arctic Oil Seep?", Spill Technology Newsletter, pp. 21-27 (November-December 1977).

Lowry, R.T., D.R. Inkster and M.E. Kirby, "Ice and Iceberg Studies Using State of the Art Remote Sensing," 5th POAC Conference, Trondheim, Norway (August 14-18, 1979).

Macdonald, Dettwiler and Associates Ltd., "Fluorosensor Data Formatter Model FDF-80 for BRL Laser Fluorosensor," Macdonald, Dettwiler and Associates Ltd., Vancouver, B.C., p. 4-1 (May 1976).

MacLean, B. and R.K.H. Falconer, "Geological/Geophysical Studies in Baffin Bay and Scott Inlet-Buchan Gulf and Cape Dyer-Cumberland Sound Areas of the Baffin Island Shelf," Current Research, Part B, Geological Survey of Canada, Paper 79-1B, p. 231-244 (1979).

McMahon, H.O., "Thermal Radiation from Partially Transparent Reflecting Bodies," Journal of the Optical Society of America, 40, pp. 376-380 (1950).

Millard, J.P. and J.C. Arvesen, "Effects of Skylight Polarization, Cloudiness and View Angle on the Detection of Oil on Water; A Collection of Technical Papers," Paper No. 71-1075, Joint Conf. on Sensing of Environmental Pollutants, Palo Alto, CA. (November 1971).

Munday, J.C. et al., "Oil Slick Studies Using Photographic and Multispectral Scanner Data," Proc., 7th Symp. on Remote Sensing of Environment, 2, p. 1027 (May 1971).

Neville, R.A. and J.F. Gower, "Passive Remote Sensing of Phytoplankton via Chlorophyll 'a' Fluorescence," Journal of Geophysical Research, 82, p. 3487 (1977).

O'Neil, R., "Canadian Remote Sensing Systems of Use for the Control of Pollution of the Seas," Contribution to : NATO/CCMS Pilot Study - Teledetection for the Control of Pollution of the Seas, France (May 1977).

O'Neil, R.A., L. Buja-Bijunas and D. Rayner, "Field Performance of a Laser Fluorosensor for the Detection of Oil Spills," Applied Optics, 19, pp. 863-870 (1980).

O'Neil, R.A., V. Thomson and R.A. Neville, "Remote Sensing of Oil during the Kurdistan Spill," Impact Control Directorate, Manuscript Report, EE-25, 1982.

Parashar, S.K., B. Dawe and R.D. Worsfold, "Investigation of the Use of Microwave Systems in Detecting and Monitoring Oil Slicks over Ice and Ice-Infested Waters," Phase 1 Report C-Core Pub. 78-18, Phase 2,3 Report C-Core Pub. 79-4 (March 1979).

Poulin, A.O., "On the Thermal Nature and Sensing of Snow-Covered Arctic Terrain," U.S. Army Engineer Topographic Labs., Fort Belvoir, VA., Report No. ETL-RN-73-4 (May 1973).

Pronk, A.C., "Remote Sensing of Oil Pollution at the Sea Surface II: Damping of Water Waves by an Oil Layer as a Possible Indicator for SLAR Observations," Niwars Technical Pub. No. 22, Netherlands Interdepartmental Working Community for the Application of Remote Sensing Techniques, Delft, The Netherlands (July 1975).

Rayner, D., "Thin Film Detection Limits of Laser Fluorosensors," National Research Council of Canada, Report No. BY-79-1(RC), Ottawa, Ont. (June 1979).

Rayner, D.M. and A.G. Szabo, "A Laboratory Study of the Potential of Time-Resolved Laser Fluorosensors," National Research Council of Canada, Ottawa, Ont., Report No. BY-76-2 (November 1976).

Rosenegger, L.W., "Movement of Oil Under Sea Ice," Beaufort Sea Project Technical Report No. 28 (December 1975).

Skolnik, M.I., "A Review of Radar Sea Echo," U.S. Navy, Naval Research Lab., Radar Techniques Division, Washington, D.C., Report AD-693 452 (July 1969).

Thomson, K.P. and W.D. McColl, "A Remote Sensing Survey of the Chedabucto Bay Oil Spill," CCIW Scientific Ser. No. 26, Environment Canada, Canada Centre for Inland Waters, Burlington, Ont. (1972).

Thomson, K.P.B., S.L. Ross and H. Howard-Lock, "Remote Sensing of Oil Spills; Economic and Technical Review Report" Canada Centre for Inland Waters, Burlington, Ont., No. EPS-3-EE-74-2 (December 1974).

Troy, B.E. and J.P. Hollinger, "The Measurement of Oil Spill Volume by a Passive Microwave Imager," Naval Research Lab. Report 3515. DOT-USCG 2-21881, Dot U.S. Coast Guard, Washington, D.C. (May 1977).

van Kuilenburg, J., "Radar Observations of Controlled Oil Spills," Proc. 10th International Symp. on Remote Sensing of Environment, Ann Arbor, Mich., pp. 243-250 (October 1975).

Watson, R.D. and W.R. Hemphill, "Use of an Airborne Fraunhofer Line Discriminator for the Detection of Solar Stimulated Luminescence," U.S. Geological Survey Open File Report No. 76202, U.S. Geological Survey, Flagstaff, Arizona (1976).

Watson, R.D. et al., "Marine Monitoring of Natural Oil Slicks and Man Made Wastes Utilizing an Airborne Imaging Fraunhofer Line Discriminator," Proc. of 4th Joint Conf. on Sensing of Environmental Pollutants (Am. Chem. Society), New Orleans, Louisiana, p. 667 (November 1977).

White, J.R. and R.E. Schmidt, "Aireye-A New Generation Oil Pollution Sensing System for the 80's," Procs. of the First Workshop Sponsored by Working Group I of the Pilot Study for the NATO Committee on the Challenges of Modern Society, Washington, D.C. (April 18-20, 1979).

Wobber, F.J., "Imaging Techniques for Oil Pollution Survey Purposes; Photographic Applications in Science," Technology and Medicine, 6 (July 1971).

Wolfe, W.L., Handbook of Military Infrared Technology; Office of Naval Research, Washington, D.C. (1965).

BIBLIOGRAPHY

Buja-Bijunas, L., R.A. O'Neil and K. Dagg, "Oil Spill Detection and Identification Using a Laser Fluorosensor," *Talk presented at Vancouver, June 21, 1979*. Abstract: *Physics in Canada*, Vol. 35. No. 3 (1979).

Buja-Bijunas, L., R.A. O'Neil, V. Thomson, R.A. Neville, K. Dagg and D.M. Rayner, "Oil Spill Detection and Identification Using a Laser Fluorosensor," *Proceedings of the First Workshop Sponsored by Working Group I of the Pilot Study on the Use of Remote Sensing for the Control of Marine Pollution, sponsored by the NATO Committee on the Challenges of Modern Society, Washington, D.C.*, EPS Report (April 18-20, 1979).

Dagg, K., "Specification for Data Transfer from JSC Formatted CCT to CSFR," CCRS, Data Processing Memorandum (April 1978).

Dagg, K. "Airborne Fluorosensor Processing System," CCRS, DPD-TM79-087 (1979a).

Dagg, K. "Airborne Recorded New Sensor Non-Imagery CCT to Disk," CCRS, DPD-TM79-089 (1979b).

Dagg, K. "Airborne Non-Imagery Data to CSFR Overlay and Pseudo Imagery," CCRS, DPD-TM79-090 (1979c).

Dagg, K. "Airborne Non-Imagery Disk File Data Access Routines," CCRS, DPD-TM79-092 (1979d).

Dagg, K. and V. Thomson, "World Data Bank II General Users Guide," CCRS, DPD-TM79-98 (1979e).

Dagg, K. "A MSS-MEIS JSC Formatted Data Intensity Histogram Program," CCRS, DPD-TM79-99 (1979f).

Fingas, M.F., R.A. O'Neil, V. Thomson and R.A. Neville, "Preliminary Results of Remote Sensing Overflights during the KURDISTAN Operation," *Proceedings of the KURDISTAN Scientific Studies Workshop, BIO,* Dartmouth, N.S. (June 26-27, 1979).

Hawkins, R.K. and A.L. Gray, "Wallops Island Oil Spill: Scatterometer Results," CCRS DAD Report (1979).

Hawkins, R.K., L. Gray, V. Thomson and R.A. Neville, "Observation of Two Test Oil Spills with a Microwave Scatterometer and a Synthetic Aperture Radar," *Proceedings of the First Workshop Sponsored by Working Group I of the Pilot Study on the Use of Remote Sensing for the Control of Marine Pollution, sponsored by the NATO Commitee on the Challenges of Modern Society, Washington, D.C.*, EPS Report (April 18-20, 1979).

Kirby, M.E. and R.T. Lowry, "Iceberg Detectability Problems Using SAR and SLAR Systems. American Water Resources Association," Satellite Hydrology Symposium, Sioux Falls, S.D. (June 1979).

Neville, R.A., V. Thomson, K. Dagg and R.A. O'Neil, "An Analysis of Multispectral Line Scanner Imagery for Two Test Oil Spills," Proc. of the First Workshop Sponsored by Working Group I of the Pilot Study on the Use of Remote Sensing for the Control of Marine Pollution, sponsored by the NATO Committee on the Challenges of Modern Society, Washington, D.C., EPS Report (April 18-20, 1979).

Neville, R.A., V. Thomson, R.A. O'Neil, L. Buja-Bijunas, L. Gray, R. Hawkins and K. Dagg, "Remote Sensing of Oil Spills," Proceedings of the AMOP Seminar, Edmonton, Alta. March 1979. Spill Technology Newsletter, Vol. 4, p. 111 (March-April 1979).

Norcor Engineering and Research Ltd., "The Interaction of Crude Oil with Arctic Sea Ice," Beaufort Sea Project Technical Report No. 27 (December 1975).

O'Neil, R.A., "Research Required in the Remote Sensing of Oil in Ice-Infested Waters," Workshop on Oil, Gas and Ice; sponsored by APOA, University of Toronto Department of Chemical Engineering, and the Department of the Environment, Environmental Protection Service, AMOP; Toronto, Ontario (October 10-11, 1979).

O'Neil, R.A. "Remote Sensing Component of the Arctic Marine Oilspill Program," SURSAT Project Final Meeting, Ottawa, Ontario (January 22-24, 1980).

O'Neil, R.A., R.A. Neville and V. Thomson, "The Development of Techniques for the Detection and Tracking of Oil in Ice-Infested Waters," Proceedings of the Arctic Marine Oil Spill Program (AMOP) Seminar, Calgary, EPS Report (March 1978).

O'Neil, R.A., R.A. Neville and V. Thomson, "The Recommended System for the Remote Sensing of Oil Pollution in Canada," AMOP Technical Seminar, Edmonton, Alberta, EPS Report (June 3-5, 1980).

Parashar, S.K., B. Dawe and R.D. Worsfold, "Detection and Monitoring of Oil Pollution in the Ice Environment through Microwave Techniques," Proceedings of the 5th Canadian Symposium, Victoria, B.C., p. 348-355 (August 28-31, 1978).

Parashar, S., G. Stapleton, R. Worsfold, R.A. O'Neil and L. Gray, "Assessment of SAR for Oil Pollution Surveillance in the Ice Environment," 5th POAC Conference, Trondheim, Norway. (August 14-18, 1979).

Parashar, S., G. Stapleton, R. Worsfold and R.A. O'Neil, "Potential of SAR in Detecting and Monitoring Icebergs," Iceberg Dynamics Symposium, June 4, 1979, St. John's, Nfld. Also published in: pp. 195-210 Cold Regions Science & Technology (1980).

Rayner, D. "Effect of Surface Temperature on the Remote Sensing of Oil Using Laser Fluorosensors," EPS Report (April 1979).

Thomson, V. and K. Dagg, "AMOP Data Processing," CCRS, DPD-TM-79-105 (1979).

Thomson, V., R.A. Neville and R.A. O'Neil, "High Contrast Imaging of an Oil Slick by Means of a Low-Light-Level Television," Proceedings of the First Workshop Sponsored by working Group I of the Pilot Study on the Use of Remote Sensing for the Control of Marine Pollution, sponsored by the NATO Committee on the Challenges of Modern Society, Washington, D.C., EPS Report (April 18-20, 1979).

APPENDIX A

SPECIFICATIONS FOR THE SENSORS USED FOR THE AMOP REMOTE SENSING PROJECT

A.1 CCRS MK III LASER FLUOROSENSOR (FIGURES A.1 and A.2)

Description: A pulsed UV laser activated, range gated fluorescence detector. A medium resolution spectrometer allows the fluorescent return to be categorized.

Transmitter:

Laser:	nitrogen gas
Wavelength:	337 nm
Pulse length:	3 ns FWHM
Pulse energy:	1 mJ/pulse
Beam divergence:	3 mrad x 1 mrad
Repetition rate:	100 Hz

Receiver:

Telescope:	f/3.1 D all Kirkham
Clear aperture:	0.0232 m^2
Field of view:	3 x 1 mrad
Intensifier on-gate period:	70 ns
Spectral range:	377-689 nm
Nominal spectral bandpass:	20 nm/channel
Noise equivalent energy:	4.8×10^{-17} J
Lidar altimeter range:	75-750 m
Lidar resolution:	1.5 m
Recording medium:	computer compatible tape (see Section C.2 in Appendix C).
Real time analyzer and display:	FDF-80
Weight:	267 kg
Power:	28V DC, 20.5A 110V, 60Hz, 9A

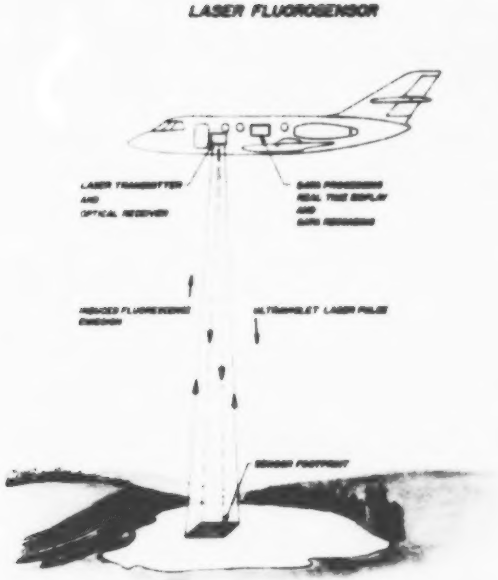
LASER FLUOROSENSOR
LASER TRANSMITTER AND OPTICAL RECEIVER
DATA PROCESSING REAL TIME DISPLAY AND DATA RECORDING
INDUCED FLUORESCENCE EMISSION
ULTRAVIOLET LASER PULSE
SENSOR FOOTPRINT

FIGURE A.1 SCHEMATIC DIAGRAM OF THE OPERATION OF THE FLUOROSENSOR.

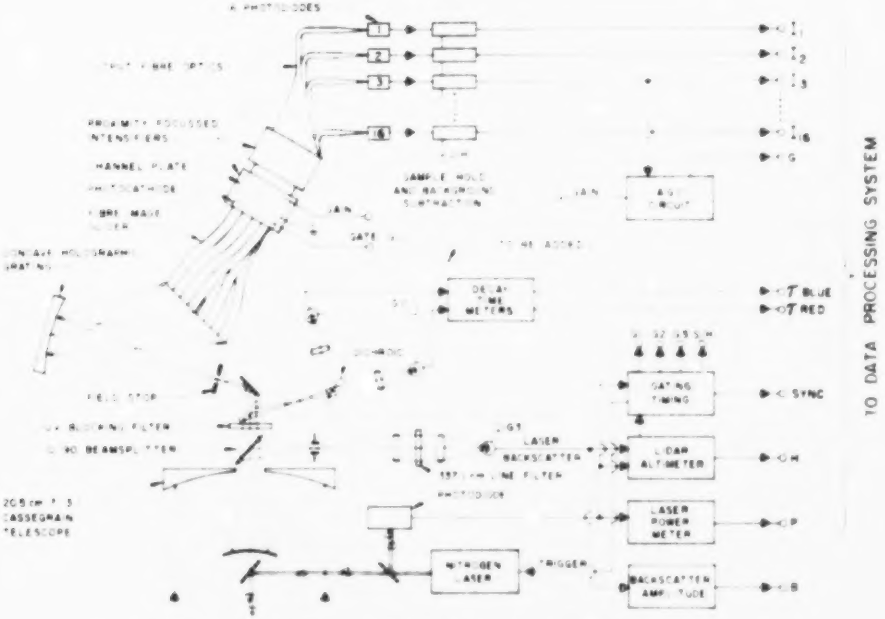
16 PHOTODIODES
OUTPUT FIBRE OPTICS
PROXIMITY FOCUSSED INTENSIFIERS
CHANNEL PLATE
PHOTOCATHODE
FIBRE IMAGE SLICER
CONCAVE HOLOGRAPHIC GRATING
FIELD STOP
UV BLOCKING FILTER
DICHROIC BEAMSPLITTER
20.5 cm f/3.5 CASSEGRAIN TELESCOPE
1
2
3
16
SAMPLE HOLD AND BACKGROUND SUBTRACTION
GAIN
GATE
AGC CIRCUIT
DELAY TIME METERS
DICHROIC
GATING TIMING
LASER BACKSCATTER
337 nm LINE FILTER
PHOTODIODE
LIDAR ALTIMETER
LASER POWER METER
NITROGEN LASER
TRIGGER
BACKSCATTER AMPLITUDE
I_1
I_2
I_3
I_{16}
G
T BLUE
T RED
SYNC
H
P
B
TO DATA PROCESSING SYSTEM

LASER FLUOROSENSOR – SENSOR HEAD

FIGURE A.2 SCHEMATIC DIAGRAM OF THE CCRS MKIII FLUOROSENSOR HEAD.

A.2 DUAL CHANNEL LINE SCANNER - Daedalus Model 1230

Description:	A dual channel optical mechanical line scanning radiometer that records energy reflected or emitted from the Earth's surface (see Figure A.3).	
Channel:	UV	IR
Spectral region:	0.30 - 0.37 µm FWHM	8.5 - 12.5 µm or 8.5 - 10.5 µm with filter
Spatial resolution:	5.5 mrad	2.5 mrad
Responsivity:	$2.56 \times 10^4 \dfrac{\text{counts}}{\text{Wm}^{-2}\cdot\text{sr}^{-1}\cdot\text{nm}^{-1}}$ for gain setting = 100	$2.10 \times 10^4 \dfrac{\text{counts}}{\text{Wm}^{-2}\cdot\text{sr}^{-1}\cdot\text{nm}^{-1}}$ for selected temperature range 0-10°C
NEN_λ/NET:	1×10^{-4} $\text{Wm}^{-2}\cdot\text{sr}^{-1}\cdot\text{nm}^{-1}$ (at approx. 20°C; temperature dependent)	0.04°C 0.2°C with filter

Field of view: 77.3°
Repetition rate: 60 scans per second
Recording medium: instrumentation tape recorder (analog)
Weight: 54.5 kg
Power: 28V DC, 20A

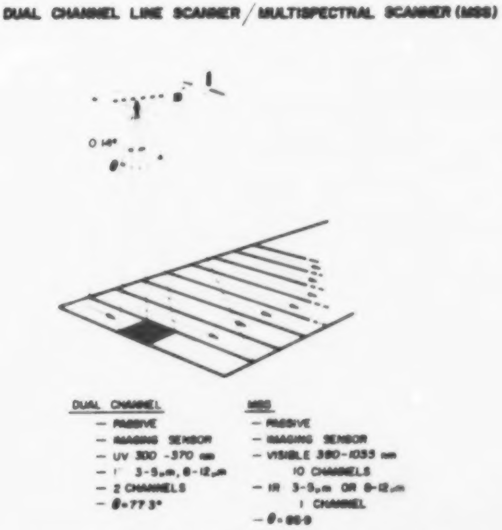
DUAL CHANNEL LINE SCANNER / MULTISPECTRAL SCANNER (MSS)
DUAL CHANNEL
— PASSIVE
— IMAGING SENSOR
— UV 300 -370 nm
— IR 3-5µm, 8-12µm
— 2 CHANNELS
— θ=77.3°
MSS
— PASSIVE
— IMAGING SENSOR
— VISIBLE 380-1055 nm
10 CHANNELS
— IR 3-5µm OR 8-12µm
1 CHANNEL
— θ=86.0

FIGURE A.3 SCHEMATIC DIAGRAM OF THE OPERATION OF THE DUAL CHANNEL LINE SCANNER AND THE MULTISPECTRAL SCANNER.

A.3 ERIM SYNTHETIC APERTURE RADAR

Description: The ERIM SAR provides simultaneous microwave imagery in the X and L bands (see Figure A.4).

		X band	L band
Frequency:		9.350 GHz (3.2 cm)	1.315 GHz (22.8 cm)
Transmitted peak power:		1 kW	5 kW
Antenna gain:		28 db	16.5 db
Along track beamwidth:		1.1°	7°
Depression angle:		0-90°	0-90°
Recorded swath width: (slant range)		5.6 km(1)	5.6 km
Maximum range:		24.1 km	24.1 km
Pulse width:		3 μs	2 μs
Resolution:	range:	1.5 m	2.3 m
	azimuth:	2.1 m	2.1 m
Sensitivity: (2) (SNR)		3 db for 6_o^{VV} = -40 db	12 db for 60_o^{VV} = -40 db
		-17 db for 6_o^{HH} = -60 db	-15 db for 60_o^{HH} = -67 db
Recording medium:		- film with subsequent optical processing	
		- a single channel real time processor is also available	
Weight:		- digital magnetic tape	
		1635 kg total	
		(501 kg real time processor)	
Power:		4.8 kVA	

(1) 20 km with wide swath antenna, X_{HH} mode only.

(2) for a depression angle of 8° and altitude of 600 m, and for normalized radar cross sections for the subsurface given in Edgerton (1975) and Skolnik (1969).

ERIM SYNTHETIC APERTURE RADAR (SAR)

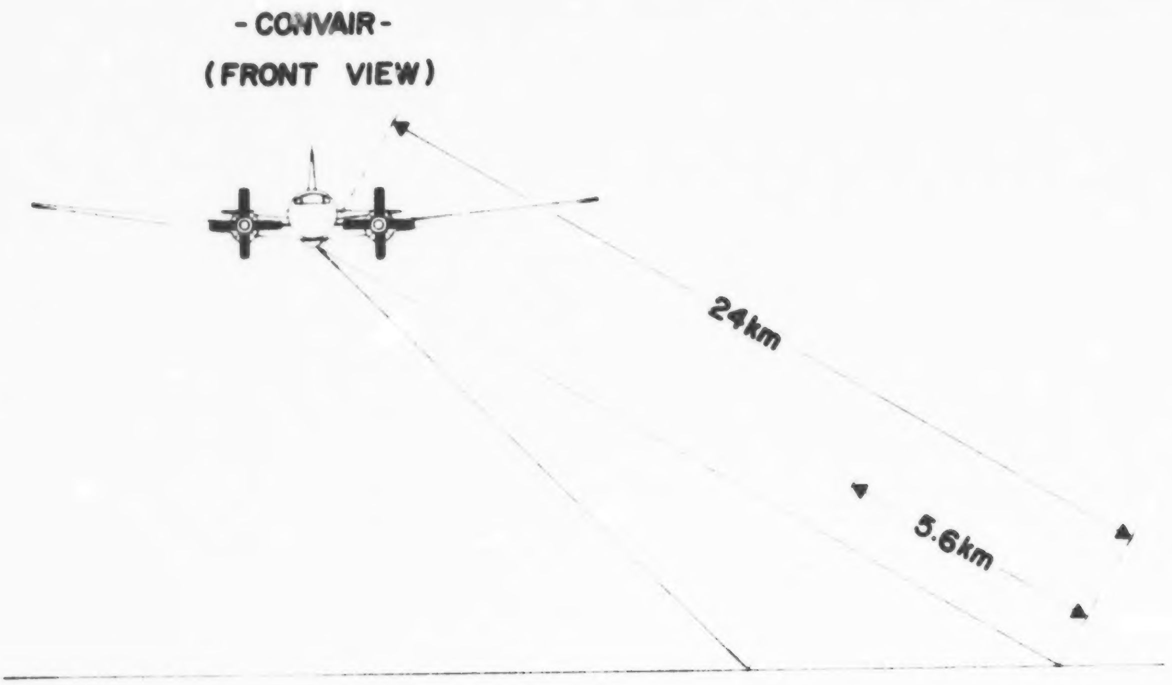
- CONVAIR -
(FRONT VIEW)
24km
5.6km

- — ACTIVE
- — IMAGING SENSOR
- — MICROWAVE : X, L BANDS
- — V, H POLARIZATIONS, TRANSMIT AND RECEIVE
- — ADJUSTABLE DEPRESSION ANGLE

FIGURE A.4 SCHEMATIC DIAGRAM OF THE OPERATION OF THE ERIM SYNTHETIC APERTURE RADAR.

A.4 LOW-LIGHT-LEVEL TELEVISION - RCA TC103OH

Description: A low bloom, high contrast, medium resolution, Silicon Intensified Target television camera.

Lens: Fujinon TV LH15A2 f/1.4, 12.5 mm focal length, 42.4° x 54.4° field of view.

Spectral response:	350-850 nm, full width
Polarizer:	Polaroid HNP'B horizontal (240-740)
Filter:	Corning 7-51. Transmission: 310-420, 700-1100 nm
Look angle:	53° off nadir, forward
Light range:	10^8
NEN:	10^{-9} $\mathrm{Wm^{-2} \cdot sr^{-1}}$; 5×10^{-12} $\mathrm{Wm^{-2} \cdot sr^{-1} \cdot nm^{-1}}$
NEN as outfitted:	1.1×10^{-7} $\mathrm{Wm^{-2} \cdot sr^{-1}}$ (370-420 nm, full width) 1.5×10^{-7} $\mathrm{Wm^{-2} \cdot sr^{-1}}$ (690-840 nm, full width)
Recording medium:	IVC model 815 X A video tape recorder (1" tape)
Weight:	69 kg (including tape recorder)
Power:	110V 60Hz, 4.2A

See Figure A.5 for spectral response of entire system when configured as above.

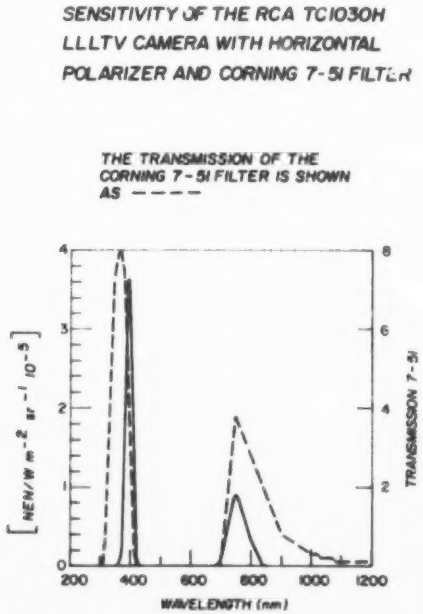

FIGURE A.5 SENSITIVITY OF THE RCA TC1030H CAMERA AS OUTFITTED FOR OIL DETECTION.

A.5 MICROWAVE SCATTEROMETER - Ryan Model 720

Description:	Measures absolute radar backscatter cross-section as a function of look angle from nadir (see Figure A.6).
Transmitter frequency:	13.3 GHz (2.25 cm)
Transmitter power:	2 watts
Antenna:	slotted guide phased array
Antenna gain:	38 db
Antenna beam width (broadside):	3°
Antenna beam width (fore-aft):	120°
Transmit polarization:	H or V
Receiver polarization:	like and crossed
Ground speed range:	120-180 knots
Recording medium:	instrumentation tape recorder (analog)
Accuracy:	Absolute HH 1 db HV 3 db VH 3 db VV 3 db Relative 0.5 db
Resolution;	0.26X (ground speed (m/s)) along track 0.052X (Altitude (m)) cross track
Sensitivity:	8 db SNR for σ_θHH =-35 db* at 600 m at 60° incidence angle.
Weight:	antenna 16 kg electronics 41 kg
Power:	110V 400Hz 2.8A 110V 60Hz 0.3A

*σ_θHH for sea clutter for wind speed of 2 m/s

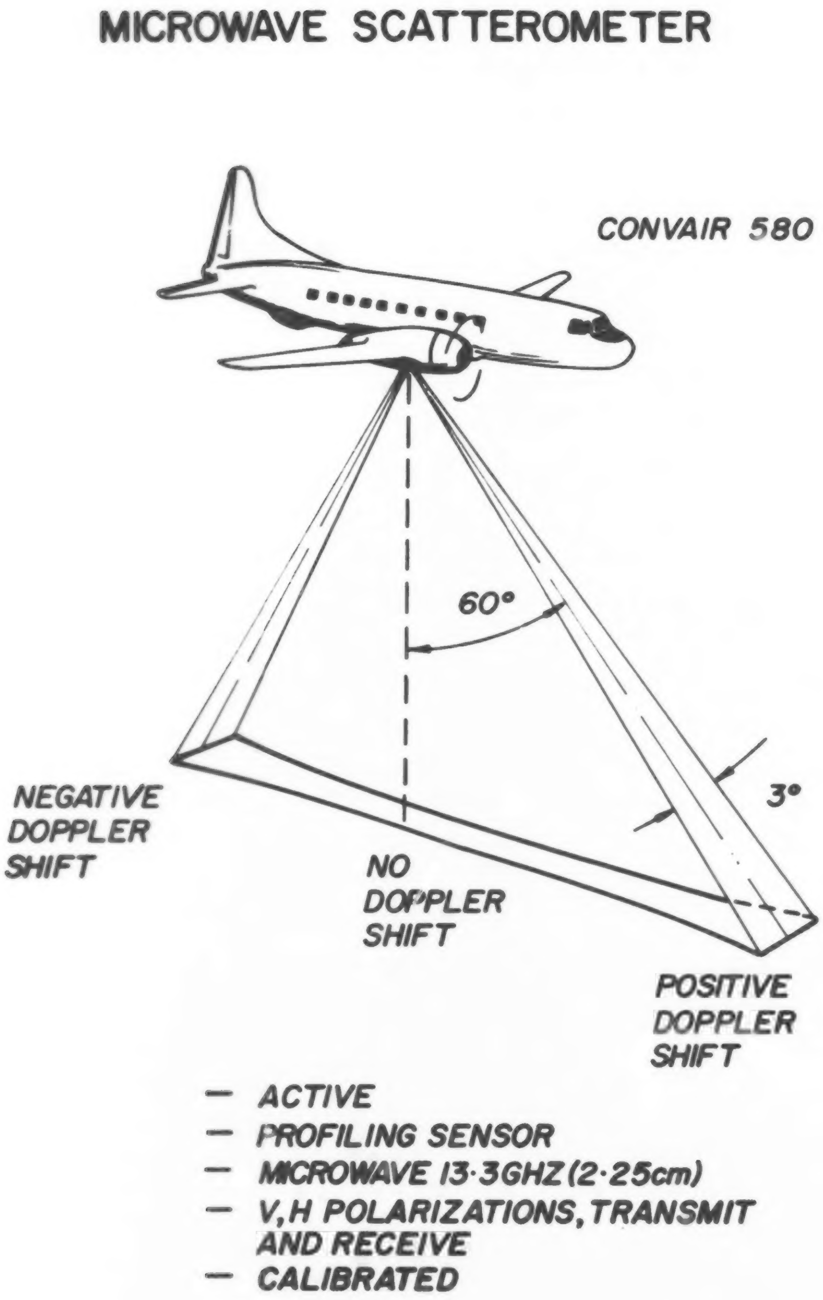
MICROWAVE SCATTEROMETER
CONVAIR 580
60°
3°
NEGATIVE DOPPLER SHIFT
NO DOPPLER SHIFT
POSITIVE DOPPLER SHIFT
— ACTIVE
— PROFILING SENSOR
— MICROWAVE 13·3GHZ (2·25cm)
— V,H POLARIZATIONS, TRANSMIT AND RECEIVE
— CALIBRATED

FIGURE A.6 SCHEMATIC DIAGRAM OF THE OPERATION OF THE MICROWAVE SCATTEROMETER.

A.6 MILLER-PIEAU PHOTOMETER

Description: A 4 barrel photometer - each barrel consisting of an interference filter, lens and silicon photodiode detector. Each detector views in turn upwelling and downwelling radiation.

Spectral characteristics:	Pass-band interference filter selectable between 300-800 nm. Spectral resolution is determined by filter. Filters used in this project; 445 nm, 560 nm, 710 nm, 960 nm.
Spatial characteristic:	10,20,50,100 mrad
Temporal characteristic:	selectable scene and solar reference viewing times - typically 20 seconds scene 2 seconds solar
Recording medium:	instrumentation tape recorder (analog or digital through ADAS)
NEN_λ:	3×10^{-6} $Wm^{-2}\cdot sr^{-1}\cdot nm^{-1}$ (700 nm)
Weight:	22 kg
Power:	28V DC, 15A

A.7 MULTIPLE DETECTOR ELECTRO-OPTICAL IMAGING SCANNER

Description: A prototype unit which consists of two 512 element linear photodiode arrays at the focal plane of two lenses. Spatial scanning is achieved by the forward motion of the aircraft platform in one dimension and by the electronic scanning of the array in the other dimension (see Figure A.7).

		Channel 1	Channel 2
		Corning	Corning
Spectral region:	filter:	7-54 or 2-64	7-54 or 7-54
	polarizer:	1 Nil	11 Nil
Spatial resolution: *		1 mrad IFOV swath width 24°	
Repetition rate:		12.5, 25, 50, 100 scans per second	
NEN$_\lambda$:		1.7×10^{-4} Wm^{-2}•sr^{-1}•nm^{-1} (731 nm)	
Recording medium:		instrumentation tape recorder	
Weight:		46 kg	
Power:		28V DC, 3.5A	

MEIS must be operated in conjunction with MSS since it uses some of MSS's electronic and recording system, as well as MSS's gyros for roll stabilization.

* with 28 mm focal length lenses.

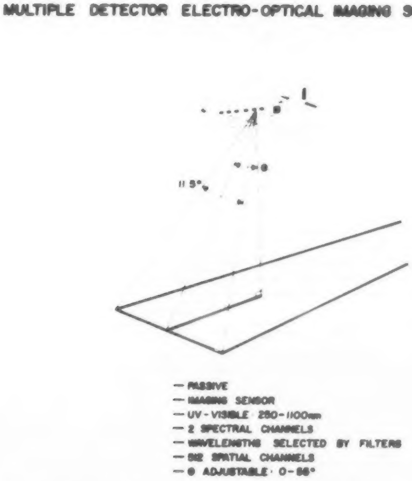
MULTIPLE DETECTOR ELECTRO-OPTICAL IMAGING SCANNER (MEIS)
11 5°
— PASSIVE
— IMAGING SENSOR
— UV-VISIBLE 250-1100nm
— 2 SPECTRAL CHANNELS
— WAVELENGTHS SELECTED BY FILTERS
— 512 SPATIAL CHANNELS
— θ ADJUSTABLE · 0-86°

FIGURE A.7 SCHEMATIC DIAGRAM OF THE OPERATION OF THE MULTIPLE DETECTOR ELECTRO-OPTICAL IMAGING SCANNER.

A.8 MULTISPECTRAL SCANNER - Daedalus Model 1260

Description: A multichannel optical mechanical line scan spectrometer that records energy reflected or emitted from the Earth's surface (see Figure A.3).

Channel	Spectral Range (μm)	Responsivity $\left(\frac{\text{counts} \times 10^3}{\text{Wm}^{-2} \cdot \text{sr}^{-1} \cdot \text{nm}^{-1}}\right)$ for gain 1	Noise Equivalent Spectral Radiance NEN_λ ($\text{Wm}^{-2} \cdot \text{sr}^{-1} \cdot \text{nm}^{-1} \times 10^{-3}$) for 50 scans/s	Noise Equivalent Temperature NET (C°)
1	0.390 - 0.415	5.7	4.2	
2	0.415 - 0.450	7.0	1.6	
3	0.445 - 0.495	2.6	0.72	
4	0.500 - 0.550	1.5	0.52	
5	0.550 - 0.595	1.1	0.45	
6	0.590 - 0.645	1.1	0.42	
7	0.625 - 0.695	1.3	0.40	
8	0.680 - 0.780	1.9	0.23	
9	0.765 - 0.895	1.5	0.31	
10	0.865 - 1.035	1.4	0.34	
IR	8.5 - 12.5	210*	0.005	0.04
w/filter	8.5 - 10.5		0.02	0.2

Digital range: 0.255 (8 bit)
Gains: 0.5, 1, 2, 4, 10
Spatial resolution: 2.5 mrad
Field of view: 85.9° (73.7° with S-bend correction)
Repetition rate: 12.5, 25, 50 100 scans/s
Recording medium: instrumentation tape recorder (digital)
Weight: 129 kg
Power: 28V DC, 50A

* IR responsivity is continuously adjustable for coverage of selected temperature range; value given is for coverage of range 0-10°C.

A.9 OPTICAL MULTICHANNEL ANALYZER

Description: A 500 channel spectrometer which uses a Silicon Intensified Target TV camera tube as a detector. It is capable of measuring upwelling and downwelling radiation simultaneously (see Figure A.8).

Acquisition rate:	64 ms for both upwelling and downwelling irradiance
Instantaneous field of view:	5 mrad
Viewing direction:	selectable from 60° forward to 40° aft of nadir

	Grating	1	2	3	prism
Selectable spectral resolution:	(nm)	0.07	0.14	1.1	1.2 (400 nm) 12.4 (800 nm)
spectral range:	(nm)	17.5	35	275	700

NEN_λ ($Wm^{-2} \cdot sr^{-1} \cdot nm^{-1}$)	Grating 1 (2360 grooves/nm)	Prism
400 nm	3.5×10^{-5}	2.0×10^{-6}
600 nm	1.5×10^{-4}	1.4×10^{-6}
800 nm	----	6.0×10^{-6}

Recording medium:	instrumentation tape recorder (digital)
Weight:	110 kg
Power:	110V 60 Hz, 2.2 A

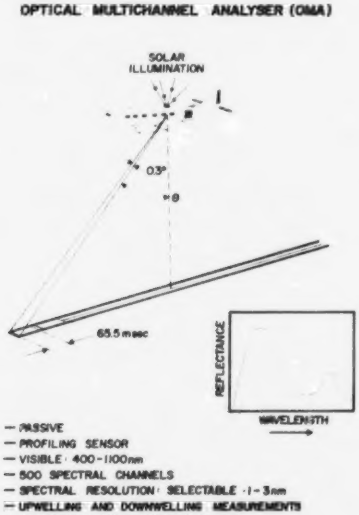
OPTICAL MULTICHANNEL ANALYSER (OMA)
SOLAR ILLUMINATION
0.3°
θ
65.5 msec
REFLECTANCE
WAVELENGTH
— PASSIVE
— PROFILING SENSOR
— VISIBLE · 400-1100nm
— 500 SPECTRAL CHANNELS
— SPECTRAL RESOLUTION · SELECTABLE · 1-3nm
— UPWELLING AND DOWNWELLING MEASUREMENTS
— ADJUSTABLE LOOK ANGLE θ · 0-60°

FIGURE A.8 SCHEMATIC DIAGRAM OF THE OPERATION OF THE OPTICAL MULTICHANNEL ANALYZER.

A.10 VINTEN 70mm CAMERA - Type 492

Description: A 5 by 5.5 cm format camera

AS FLOWN:	UV	VISIBLE
Filter:	Wratten 18A	NAV
Lens:	7.5 cm f/2.0	3.8 cm f/2.8
Film:	2405 (B & W neg)	2445 (colour neg)
Film capacity:	700 exposures	460 exposures
Position:	45° forward	Nadir
Shutter speed:	1/500 s	1/500 s
Cycle rate:	0.5 to 999 seconds - pulse mode	
Weight:	29.5 kg (2 cameras)	
Power:	28V DC, 15A (2 cameras)	

A.11 WILD HEERBRUGG - RC-10

Description: 23 x 23 cm format aerial survey camera

Lens:	88 mm SAG II
Shutter speed:	1/100 to 1/1000 second
Cycle rate:	1 per 1.8 second maximum
Film supply:	individual feed and take up cassettes with a separate vacuum platen
Film capacity:	280 exposures B & W, 225 exposures colour
Filter:	NAV 3.3
Film types:	2445 (colour neg) 2443 (false colour IR)
Weight:	164 kg
Power:	28V DC, 25A

APPENDIX B

NAVIGATION TRACK RECOVERY

APPENDIX B

Navigation Track Recovery

Aircraft track can be recovered in two ways: first, direct reading of the latitude and longitude from an inertial navigation system (INS) or INS flight record, and the altitude from a barometric or radar altimeter; second, a track recovery model which combines the INS and altimeter flight records and aerial camera photograph location parameters.

Inertial Navigation System (INS) (Airborne, 1977)

Description:	The LTN-51 is a self-contained navigation system which operates by sensing aircraft acceleration with a gyrostabilized platform. The system conforms to ARINC 561 specifications.
Modifications:	High resolution resolvers with first order accuracy of 30 seconds of arc for pitch, roll and azimuth. Vertical quantizer to quantize outputs from a vertical accelerometer.
Accuracy:	Not more than 2 km/h drift in latitude and longitude values.
Reliability:	MTBF > 1000 hours.
Data output:	Recorded on ADAS through an INS ADAS interface. Pitch, roll, azimuth from high resolution resolvers. Vertical acceleration from the vertical quantizer. 25 selectable parameters, e.g. direction cosines, horizontal velocity.

Each CCRS aircraft is flown routinely with an INS. INS parameters are recorded using ADAS (Appendix C) onboard C-GRSA and C-GRSC for post flight track recovery. Sensor operators on all aircraft record the INS parameters which are relevant to the sensor data recorded on remote sensing flights.

CCRS Track Recovery System

Description:	A track recovery model which presently employs cubic spline fitting at post flight to INS flight records and photographic location parameters.	
Accuracy:	Latitude, Longitude	30 m
	Altitude	30 m
	Attitude	1 minute of arc
	(above accuracies are with position fix data every 15 minutes)	

Reliability: Errors quoted above are for 1 standard deviation.

Output: Corrected latitude, longitude, altitude, aircraft attitude, as well as other flight parameters. Information may be printed out or plotted on standard map projections.

CCRS is presently developing a Kalman filter model for track recovery which is expected to yield better accuracies.

APPENDIX C

AUTOMATIC DATA ACQUISITION SYSTEMS

APPENDIX C

Automatic Data Acquisition Systems

C.1 Airborne Data Acquisition System (ADAS) (Airborne, 1977)

ADAS is a mini-computer based airborne data acquisition system which is used to gather data from a wide variety of low-speed and high-speed sensors and records this data digitally on a 14 track Mincom tape recorder. One track is used for each of: reference, time code and multiplex track data (MTD). MSS and MEIS data are digitized and recorded on as many tracks as are required. The remaining tracks can be used for conventional analog or digital recording as required. The system is operated using a keyboard and video display, and provides extensive in-flight checks of recorded data.

The multiplex track contains data from a time code generator, up to 32 low speed sensors, and an LTN-51 inertial navigation system. These data are routed through the ADAS computer, and are recorded in "frames" of 150 - 16-bit words at a rate of 100 frames per second. Each frame includes the time to 1 ms. A multiple of two 16-bit words (e.g. 2 or 4 words) are recorded from each low speed sensor in each frame. The following low speed sensors are currently interfaced to the system: RC-10 camera, PRT-5 Precision Radiation Thermometer, Garrett AFTS-23 Digital Pressure Monitor, GSN-500 VLF navigation system, Marconi Doppler MC712, MSS-Hystogram, Honeywell Radar Altimeter, triple A/D converter units and others available through general purpose digital interfaces (DGI). The navigation data from the LTN-51 include longitude, latitude, heading, groundspeed, track angle, X and Y velocities, direction cosines and remainder terms, high accuracy roll, pitch and azimuth, and vertical quantizer. The navigation data are updated every 50 ms (except longitude, latitude, heading, groundspeed and track angle which are updated about one per second). The direction cosines can be processed later on a computer to obtain high accuracy position information. The MTD frames also contain camera firing information each time an RC-10 or Vinten camera takes a picture. A special "trailer" MTD frame at the end of each flight line contains a cumulative index of all the flight lines on the roll of tape.

An ADAS system is presently installed in the Convair 580, C-GRSC, and the DC 3, C-GRSA. These two systems are available for the recording of digital data from a complement of sensors and navigation equipment.

Weight: 295 kg including a Mincom instrumentation tape recorder ADAS occupies two 54 x 19 in standard equipment racks

Power:	28V DC	28A
	110V 60Hz	2.8A
	110V 400Hz	4.6A

C.2 Fluorosensor Data Formatter Model FDF-80 for the BRL Laser Fluorosensor (MacDonald, 1976)

The FDF-80 is a data processing system with the following basic functions:

a) receives the input signals from the laser fluorosensor, from navigational equipment on board the aircraft and from operator select switches;
b) digitizes the analog input channels;
c) performs certain computations on the raw data, including some signal averaging;
d) presents an on-line video display of the computed data;
e) records the raw data on the digital tape recorder; and
f) provides playback capability.

The electronics of the FDF-80 is divided between two units, the analog and the main chassis.

The analog chassis of the FDF-80 interfaces the laser fluorosensor and is located close to it. The analog input channels are digitized and then transmitted as digital data to the main chassis of the FDF-80. The main chassis of the FDF-80 contains the microprocessor and interfaces to the ARINC navigation data bus, IRIG-A time code bus, video monitor, front panel and computer compatible tape transport.

Weight: 21 kg
Power: 28V DC, 8.5A

APPENDIX D

PLATFORMS USED FOR THE AMOP REMOTE SENSING PROJECT (Airborne, 1977)

APPENDIX D

Platforms used for the AMOP Remote Sensing Project (Airborne, 1977)

D.1 Aircraft C-GRSA (Figures D.1 to D.5)

Type	DC.3 (Dakota)
Description:	Transport type aircraft having two Pratt and Whitney reciprocating engines. Two pilots are mandatory and an additional five or six sensor operators may be carried.
Performance:	Operational Ceiling: 3 000 m Flight Duration: 5 hours Range: 1 200 km True Airspeed: 220 - 280 km/h Basic Weight: 8 871 kg Fuel Load (vol; wt): 3 046 L; 2 188 kg Total all up Weight: 12 200 kg Fuel Consumption: 245 kg/h @ 260 km/h Electric Power Available: 7.2 kVA
Sensor Locations:	All sensors are located aft of the wing-root and are completely accessible during flight (see Figure D.1).
Sensor Control:	Three double equipment racks have been provided to mount all sensor controls.
Support Systems:	14 channel Mincom tape recorder; Closed circuit television and videotape recording system; ADAS Navigation: ADF, INS, VLF, provision for Doppler. Radar altimeter. Communication: VHF, HF; APU - Gas operated for ground power and internal engine starting.

Sensor Complement: see Appendix E.

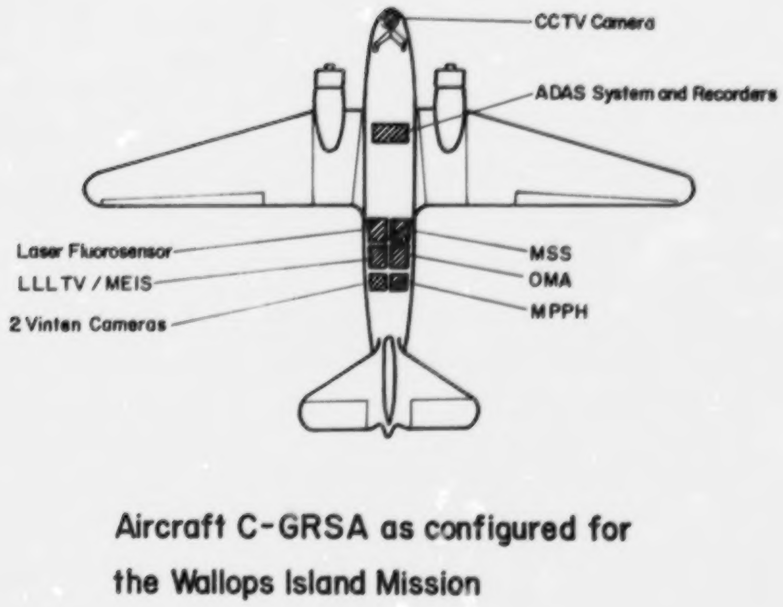
CCTV Camera
ADAS System and Recorders
Laser Fluorosensor
LLLTV / MEIS
2 Vinten Cameras
MSS
OMA
MPPH
Aircraft C-GRSA as configured for
the Wallops Island Mission

FIGURE D.1 LAYOUT OF CCRS DC-3 C-GRSA (as configured for the Wallops Island mission).

C - GRSA TAKING OFF AT CLYDE RIVER, BAFFIN ISLAND

FIGURE D.2 C-GRSA TAKING OFF AT CLYDE RIVER, BAFFIN ISLAND.

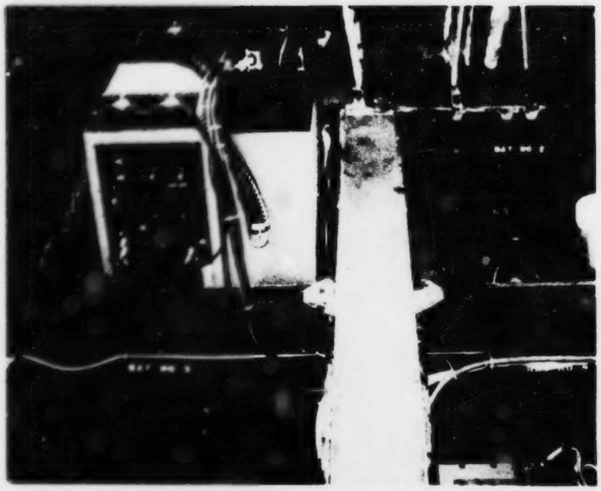

SENSOR BAYS ON C-GRSA SHOWING THE LASER FLUOROSENSOR (BAY1), MSS(BAY2), LLLTV AND MEIS(BAY3), MPPH(BAY 4)
THIS IS THE SENSOR LAYOUT USED FOR THE SCOTT INLET MISSION

FIGURE D.3 SENSOR BAY LAYOUT IN C-GRSA AS PREPARED FOR SCOTT INLET.

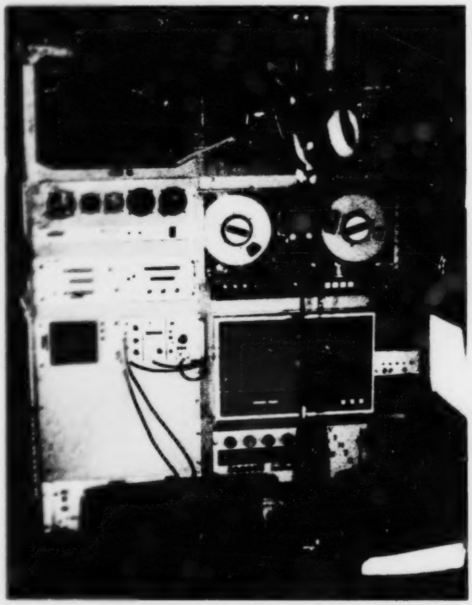

LASER FLUOROSENSOR, LLLTV, VINTEN CAMERA, MPPH CONTROL PANELS ON C-GRSA

FIGURE D.4 SENSOR CONTROL EQUIPMENT IN C-GRSA FOR THE FLUOROSENSOR, LOW-LIGHT-LEVEL TELEVISION, VINTEN CAMERAS AND MPPH.

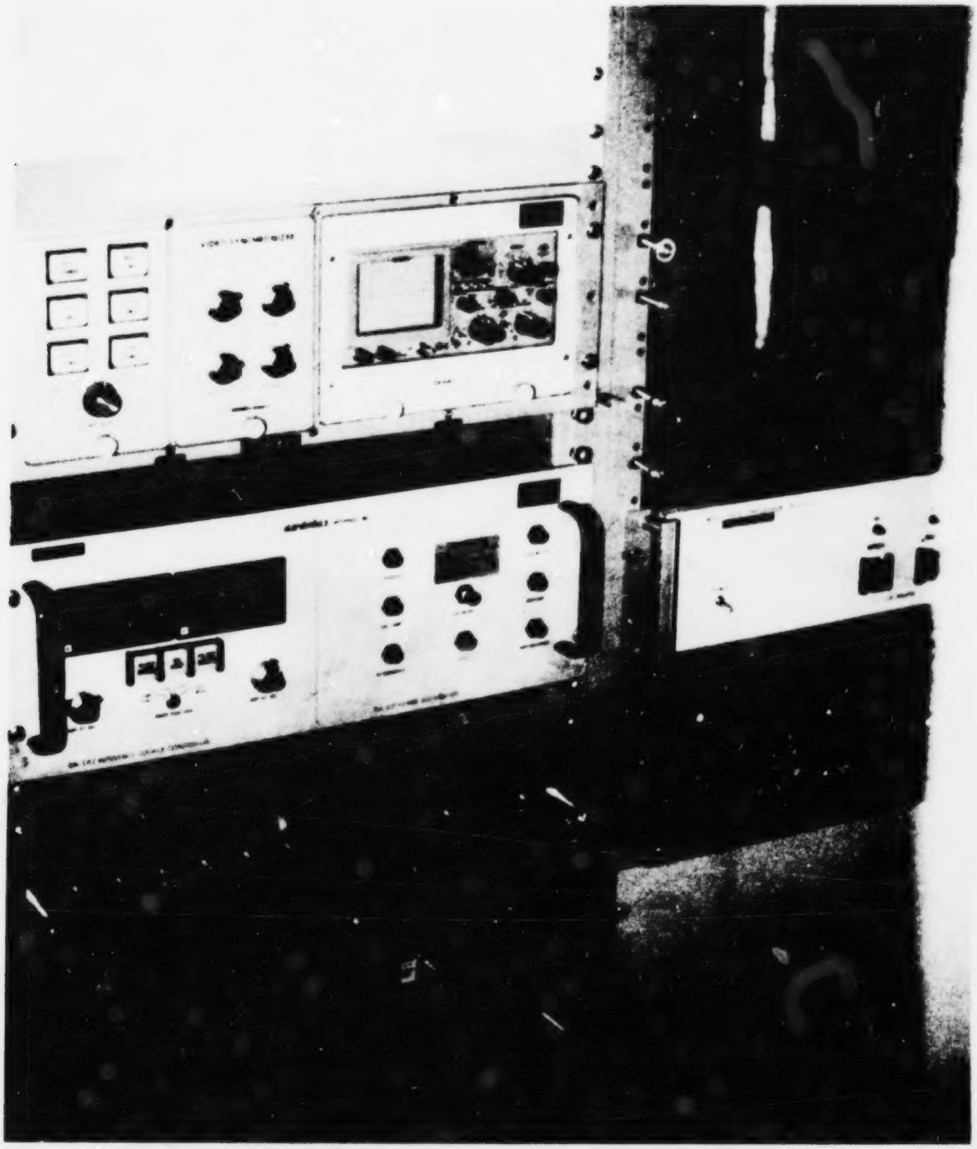

MSS— MEIS STATION ON C-GRSA

FIGURE D.5 MSS-MEIS STATION IN C-GRSA.

D.2 Aircraft C-GRSB (see Figure D.6)

Type:	DC-3 (Dakota)
Description:	Transport type aircraft having two Pratt and Whitney reciprocating engines. Two pilots are mandatory and an additional five or six sensor operators may be carried.
Performance:	Operational Ceiling: 3 000 m Flight Duration: 5 hours Range: 1 200 km True Airspeed: 220 - 280 km/h Basic Weight: 8 871 kg Fuel Load (vol; wt): 3 046 L; 2 188 kg Total all up Weight: 12 200 kg Fuel Consumption: 245 kg/h @ 260 km/h Electric Power Available: 5.5 kVA
Sensor Locations:	All sensors are located aft of the wing-root and are completely accessible during flight (see Figure D.2).
Sensor Control:	Sensor controls are mounted in two double equipment racks.
Support Systems:	14 channel Mincom Tape Recorder; Closed-circuit television and videotape recording system; Navigation: ADF, INS; Communication: VHF, HF; APU - Gas operated for ground power and internal engine starting.

Sensor Complement: see Appendix E.

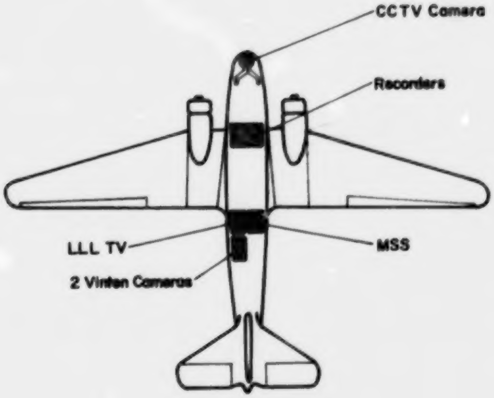

Aircraft C-GRSB as configured for the 'Kurdistan' Mission

FIGURE D.6 LAYOUT OF THE CCRS DC-3 C-GRSB (as configured for the KURDISTAN mission).

D.3 Aircraft C-GRSC (see Figures D.7 to D.11)

Type: Convair 580 (known as the SAR580 when equipped with SAR).

Description: The Convair 580 is a former passenger transport aircraft having two Allison 501-d13d propeller jet engines producing 8 000 hp. The aircraft crew consists of two pilots. It has positions for seven sensor operators.

Performance:
Operational Ceiling: 7 000 m
Flight Duration: 5 hours (with full sensor and operator complement aboard)
Range: 2 800 km
True Airspeed: 280 - 550 km/h
Basic Weight: 13 044 kg
Zero Fuel Weight: 20 408 kg
Fuel Load (vol; wt): 11 010 L; 8 941 kg
Total all up Weight: 26 375 kg
Fuel Consumption: 900 kg/h @ 550 km/h (5,500 m) @ 370 km/h (1 500 m)
Electric Power Available: 15 kVA

Sensor Location: Aft part of the fuselage completely accessible during flight (see Figure D.3).

Support Systems:
14 channel Mincom Tape Recorder;
Closed-circuit colour television and videotape recording system;
ADAS
Navigation: ADF, INS, VLF, provision for Doppler
APU: for ground power and internal engine starting

Sensor Complement: see Appendix E.

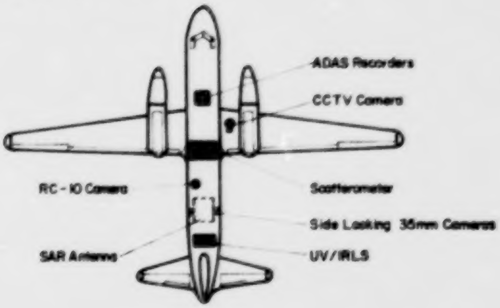

Aircraft C-GRSC as configured for the Scott Inlet and Wallops Island Mission

FIGURE D.7 LAYOUT OF THE CCRS CONVAIR 580 C-GRSC (as configured for the Scott Inlet and Wallops Island missions).

C – GRSC ON RUNWAY AT THULE, GREENLAND

FIGURE D.8 C-GRSC ON THE RUNWAY AT THULE, GREENLAND.

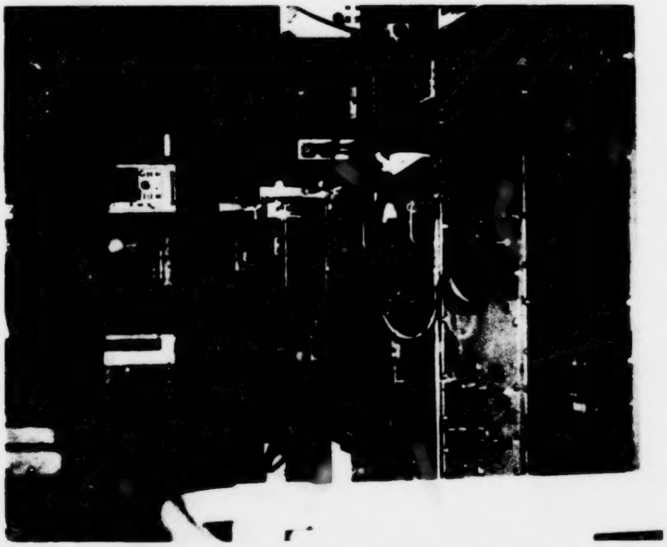

ERIM SAR CONTROL EQUIPMENT TO RIGHT AND OPERATOR
IN FRONT OF CCRS ADAS CONTROL PANEL IN C – GRSC

FIGURE D.9 ERIM SAR CONTROL EQUIPMENT IN C-GRSC.

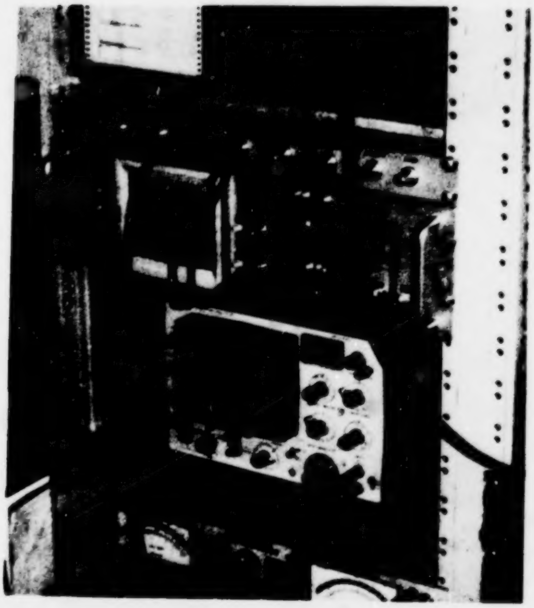

SCATTEROMETER STATION IN C-GRSC

FIGURE D.10 MICROWAVE SCATTEROMETER STATION IN C-GRSC.

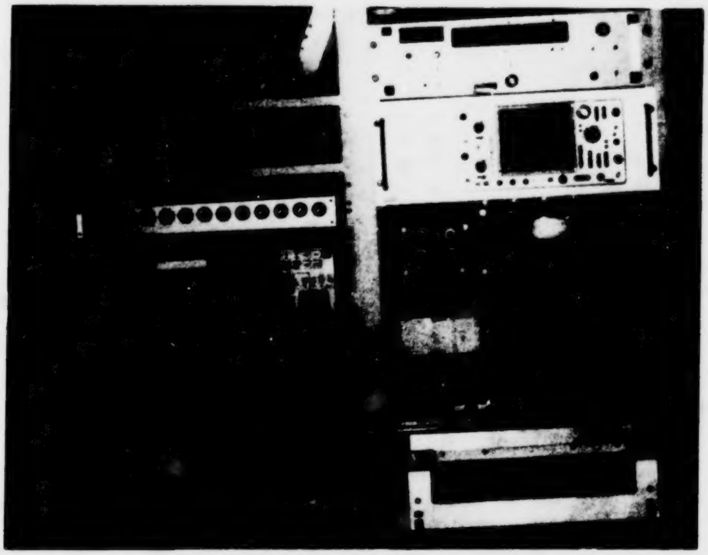

CCRS ADAS CONTROL PANEL IN C-GRSC

FIGURE D.11 ADAS CONTROL EQUIPMENT IN C-GRSC.

D.4 Aircraft C-GRSD (see Figure D.12)

Type:	Falcon 20 fan jet.
Description:	Executive transport type aircraft manufactured by Dassault (France). It has two fan-jet engines and carries two pilots and four or five sensor operators.
Performance:	Operational Ceiling: 11 000 m (stable platform) Flight Duration: 2.5 to 3 hours Range: 2 200 km True Airspeed: 460-740 km/h Basic Weight: 7 684 kg Zero Fuel Weight: 9 977 kg Fuel Load (vol; wt): 4 718 L; 3 772 kg Total all up Weight: 12 998 kg Fuel Consumption: 1360 kg/h @ 740 km/h (9 150 m) @ 460 km/h (1 500 m) Electric Power Available: 4.5 kVA
Sensor Locations:	The Daedalus Scanner is mounted in the nose outside the pressurized hull. Cameras are located inside the aircraft cabin behind special ports (see Figure D.4).
Sensor Control:	Sensor controls are grouped on a series of consoles in the cabin.
Support Systems:	14 channel Mincom Tape Recorder; Closed circuit television and video tape recording system; Navigation: INS, ADF, provision for VLF; APU: for ground power and internal engine starting.

Sensor Complement: see Appendix E.

NOTE: On CCRS Aircraft Weights

1. Basic Weight includes racks and seats only. No equipment.
2. Zero Fuel Weight (maximum weight without fuel) includes crew, operators, baggage and all installed equipment before fuel is added.
3. These figures do not take into account the centre of gravity constraints; it is assumed that the locations of the sensors and operators are such that the aircraft centre of gravity is within the allowed range.

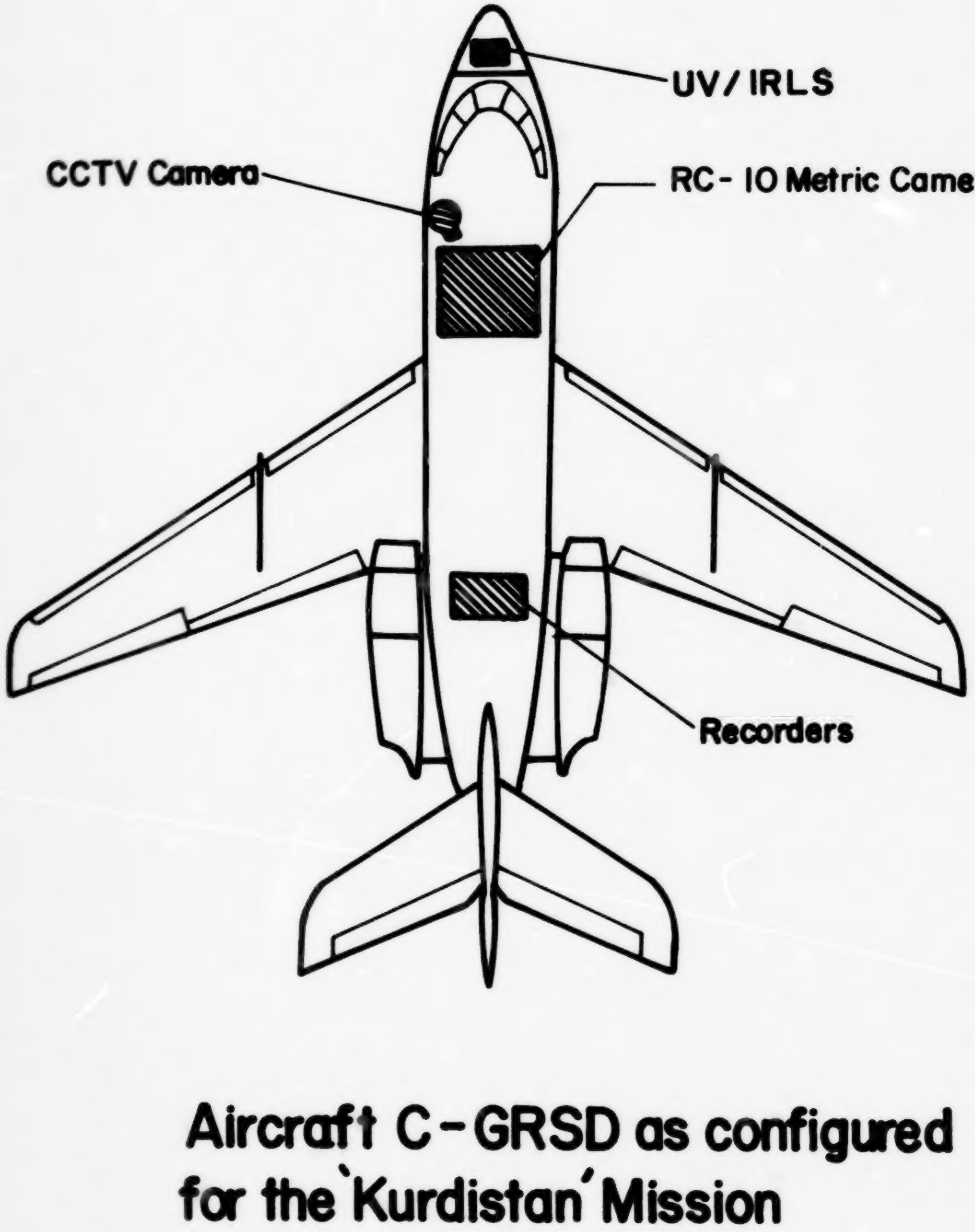
UV/IRLS
CCTV Camera
RC-10 Metric Camera
Recorders
Aircraft C-GRSD as configured for the 'Kurdistan' Mission

FIGURE D.12 LAYOUT OF CCRS FALCON FAN JET C-GRSD (as configured for the KURDISTAN mission).

APPENDIX E

FLIGHT OPERATIONS DURING THE AMOP REMOTE SENSING PROJECT

APPENDIX E

Flight Operations During the AMOP Remote Sensing Project

The AMOP remote sensing project operations consisted of four missions and test flights. The four missions were: Montreal Island, Scott Inlet, Wallops Island, and the KURDISTAN. Each mission was performed under a different set of operational circumstances; each provided for the remote detection of oil spills under a different set of environmental conditions.

All flight line information was recorded in a flight log at the time of the missions. Also, a data log was compiled at the time of data analysis which outlines the types of data recorded and gives other pertinent information necessary for interpretation. These two logs are not included in this report but may be obtained if desired (see Appendix I). What follows is a summary of the purpose, logistics and execution of the four missions. The sensor complement for each mission is listed in Table E.1 and a summary of all flight times and distances is found in Tables E.2 and 3. Photographs of the aircraft, C-GRSA and C-GRSC, and the sensor installations may be found in Appendix D.

E.1 Montreal Island

E.1.1 Purpose

The remote sensing of oil spills at Montreal Island was initiated in response to enquiries by the Quebec regional office of the Environmental Protection Service (EPS) into the possibility of using remote sensing for cleanup support surveillance of accidental or deliberate oil spills in the oil refinery depot region of Montreal Harbour. With some regularity, oil spills in the Montreal Harbour area had been appearing on holiday weekends; so, a mission was planned for the Canada Day weekend of 1978. Besides Montreal Harbour, the Sorel Harbour was also to be surveyed at the request of the EPS Quebec regional office.

In particular, this mission provided the opportunity to investigate the detection of oil under night as well as day conditions, and to evaluate the problems inherent in the remote sensing of oil in a harbour environment.

TABLE E.1 SUMMARY OF AIRCRAFT/SENSOR COMPLEMENTS USED IN THE PROJECT

Mission	Aircraft*	Sensors**
Montreal Island	C-GRSB	IR Line Scanner (IRLS) Low-light-level Television (LLLTV)
Scott Inlet	C-GRSA	CCRS MkIII Laser Fluorosensor Low-light-level Television (LLLTV) Multiple Detector Electro-optical Imaging Scanner (MEIS) Multispectral Scanner (MSS) Miller Pieau Photometer (MPPH) 2 Vinten 70 mm cameras
	C-GRSC	ERIM Synthetic Aperture Radar (SAR) Microwave Scatterometer UV/IR Line Scanner (UV/IRLS) Wild Heerbrugg RC-10 23 cm camera Side-looking 35 mm camera
Wallops Island	C-GRSA	CCRS MkIII Laser Fluorosensor Low-light-level Television (LLLTV) Multiple Detector Electro-optical Imaging Scanner (MEIS) Multispectral Scanner (MSS) Miller Pieau Photometer (MPPH) Optical Multichannel Analyser (OMA) 2 Vinten 70 mm cameras
	C-GRSC	ERIM Synthetic Aperture Radar (SAR) Microwave Scatterometer UV/IR Line Scanner (UV/IRLS) Wild Heerbrugg RC-10 23 cm camera
KURDISTAN	C-GRSD	UV/IR Line Scanner (UV/IRLS) Wild Heerbrugg RC-10 23 cm camera
	C-GRSB	Multispectral Scanner (MSS) Multiple Detector Electro-optical Imaging Scanner (MEIS) Low-light-level Television (LLLTV) 2 Vinten 70 mm cameras

* see Appendix D

** see Appendix A

TABLE E.2 SORTIE SUMMARIES

		Time (min)/Distance (km)		
Mission	Sortie	Sensors on	In Area	Transit
Montreal Island (C-GRSB)	1	18/71	51/173	43/166
	2	21/75	69/245	46/77
Scott Inlet (C-GRSA)	1	81/300	96/356	84/311
	2	73/270	78/289	117/433
	3	45/174	57/220	83/320
	4	69/260	74/279	59/222
	5	108/400	126/467	99/367
	6	20/77	63/243	88/340
	7	130/481	168/622	15/56
	8	46/170	57/211	15/56
	9	53/196	99/367	81/300
	10	7/26	34/126	87/322
	11	34/126	83/307	74/274
Scott Inlet (C-GRSC)	1	22/107	42/205	198/1833
	2	36/156*	95/411	170/1574
	3	34/178	78/409	152/1408
	4	32/158	121/598	164/1519
	5	43/397	98/900	317/2935
Wallops Island (C-GRSC)	1	8.5/31	50/185	145/560
	2	11/42	74/286	161/621
	3	22.5/83**	112/416	173/641
	4	-	-	55/212
Wallops Island (C-GRSC)	1	22/169	142/1114	138/1278
	2	42.5/304***	135/1020	135/1250
KURDISTAN (C-GRSB)	all	215/840	623/2450	1365/5822
KURDISTAN (C-GRSD)	all	92/836	320/2910	390/4592

* The microwave scatterometer and the ERIM SAR were operated separately and not on a continuous basis. The DCLS was operated continuously.

** Includes two passes over Wallops Flight Center.

*** Does not include times for the two SAR passes at the Wallops Flight Center.

TABLE E.3 TOTAL FLIGHT TIME AND DISTANCE COVERED IN THE PROJECT

	Time (h:min)	Distance (km)
Over Oil		
Montreal (E)	00:10	35
Scott Inlet (E)	00:14	52
Wallops (E)	00:14	67
KURDISTAN	01:03	427
Total	01:41	581
Sensors On		
Montreal	00:39	146
Scott Inlet	13:53	3477
Wallops	01:46	629
KURDISTAN	05:07	1676
Total	21:25	5928
In Target Area		
Montreal	02:00	418
Scott Inlet	22:49	6010
Wallops	8:33	3021
KURDISTAN	15:43	5360
Total	49:05	14809
In Transit		
Montreal	01:29	343
Scott Inlet*	30:03	12270
Wallops**	13:27	4562
KURDISTAN	29:15	10414
Total	74:14	27589
Total		
Montreal	03:29	761
Scott Inlet	52:52	18280
Wallops	22:00	7583
KURDISTAN	44:58	15774
Total	123:19	42398

(E) Estimate

* Does not include transits between Ottawa and Clyde River for C-GRSA and between Ottawa and Frobisher Bay for C-GRSC.

** Does not include transit from Ottawa to NASA Wallops Flight Center (C-GRSA, C-GRSC).

E.1.2 Logistics

On June 30, 1978, a CCRS DC-3 aircraft, C-GRSB, was outfitted with data recording equipment and two sensors; a single channel infrared line scanner; virtually identical to the DCLS without the UV channel; and an unfiltered low-light-level television. Two sensor operators, an observer and a mission manager were taken on the flights in addition to the air crew. Two sorties with a total of 13 flight lines were flown over Montreal and Sorel.

E.1.3 Sortie summaries for Montreal Island

Sortie 1: The DC-3 aircraft C-GRSB left Ottawa at 22:46 GMT 30/06/78 and arrived at Montreal on line at 23:29 GMT. Oil was present on the St. Lawrence, apparently flowing from Sewer 80-1 near Pointe aux Trembles Channel and flowing down the St. Lawrence past Ile Sainte Thérèse. EPS and the Coast Guard were monitoring the situation. Two lines were flown over the spill area; then, the mission proceeded to Sorel, recording imagery along the south shore of the St. Lawrence en route. Sorel Harbour was overflown; then C-GRSB proceeded back to Montreal and the spill area was again imaged. No oil spillage was observed at Sorel. The aircraft landed in Montreal at 00:20 GMT 01/07/78.

Sortie 2: C-GRSB took of at 03:05, 01/07/78 and imagery was taken over the spill area. Again the airplane proceeded to Sorel taking imagery along the south shore of the St. Lawrence. Sorel Harbour was overflown and the plane proceeded back to Montreal. The spill area was imaged again and C-GRSB transited back to Ottawa, landing at 05:00 GMT 01/07/78.

The oil spill in the Montreal harbour was dissipating and again no oil spillage was seen at Sorel.

E.2 Scott Inlet

E.2.1 Purpose

The objective of the AMOP remote sensing project was to determine the ability of remote sensing techniques to detect oil in ice-infested waters. The natural seep reported at Scott Inlet (Levy, 1977) provided an opportunity to detect oil in Arctic conditions. In the original proposal, three experiments were planned: the first, at Scott Inlet, was to test for oil detection in Arctic waters containing little ice; the second two were to test remote sensing techniques for oil detection on shore fast ice and in open pack ice conditions. The Scott Inlet mission was to prepare for future tests in ice, the oil-in-ice experiments were not performed. The Scott Inlet mission provided the only test in Arctic conditions for all the sensors. A photograph showing the rugged character of the Baffin Island coast in the Scott Inlet region is displayed in Figure E.1.

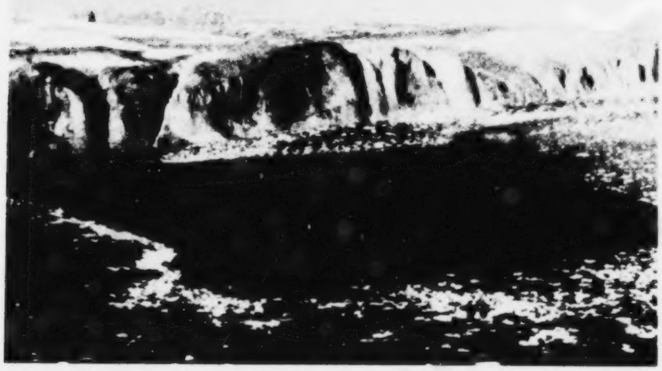

SCOTT ISLAND · 35mm PHOTOGRAPH TAKEN ON SEPTEMBER 11, 1978. 16:54 GMT

FIGURE E.1 SCOTT INLET: PHOTOGRAPH TAKEN AT 16:54 GMT, September 11, 1978.

E.2.2 Logistics

The planning of the Scott Inlet mission began in November 1977 and continued until September 1978 when the mission was flown. The mission consisted of a DC-3 (C-GRSA) with 10 crew, scientists and support personnel and a Convair 580 (C-GRSC) with 11 crew, scientists and support personnel, with a total complement of 12 sensors.

Planned for a two week period beginning September 1, 1978; the Scott Inlet seep was reported at 71° 24' N, 70° 10' W (Levy, 1977). The closest community with an airstrip was Clyde River (110 km southeast). The airstrip at Clyde River was gravel and only 900 m long; this was suitable for the DC-3, but not for the Convair 580. Two locations with paved runways near Scott Inlet from which to operate the Convair 580 were

Frobisher Bay and Thule. Of these, Thule was most suitable, since it was closer to the seep area.

The deployment of C-GRSC at Thule involved obtaining permission for airstrip rights from both the Danish and U.S. Governments. The personnel were billeted in the visiting air crew quarters at Thule and shared in the general facilities while staying there. Because of the amount of equipment and personnel taken on the mission and the lack of space on the Convair 580, three people and 350 kg of equipment were taken from Ottawa to Thule, by commercial air carrier to Resolute and, then, chartered aircraft to Thule.

The deployment of C-GRSA at Clyde River involved more preparation. Provision for lodging and other services had to be arranged with the Inuit at Clyde River. The service provided by the Qakigiaq Coop Association turned out to be very satisfactory; however, the lack of facilities at Clyde River at the beginning of planning and the difficulty of communications made for lengthy and time consuming preparation.

There was no aviation gasoline depot at Clyde River, so all the fuel to be used by C-GRSA had to be shipped in. Because of the expense of airlifting supplies in, the fuel (221 drums, 205 L per drum) and heavy equipment (emergency supplies, aircraft supplies, nitrogen gas for the fluorosensor, etc.) were brought in by the Ministry of Transport Sealift in early September. An emergency supply of 20 drums of fuel was placed at Pond Inlet by Sealift.

As with the Convair 580, the DC-3 (C-GRSA) was weight limited, so that all but the crew were flown into Clyde River by charter aircraft along with several hundred kilograms of equipment.

The schedule for the two aircraft was extremely tight because of delays in the completion of one major modification. In fact, C-GRSC was flown for only one week during the mission in the Arctic because of schedule pressure. Modifications, equipment procurement, and sensor testing proceeded from January through July prior to the mission; installation and testing of the equipment took place in July and August. Again, as a result of schedule pressure for use of the CCRS aircraft, inadequate time was obtained for installation and equipment testing, particularly in the case of C-GRSC. This led directly to equipment malfunctions and poorly recorded data from all the sensors on C-GRSC during the mission. For the most part, the sensors on C-GRSA worked properly, although additional time for fluorosensor testing would have resulted in improved performance.

Prior to departure, several possible means of communications were set up between the two parties so that information could be exchanged easily between Thule and Clyde River during the two week deployment.

The Scott Inlet mission was planned in conjunction with the Bedford Institute of Oceanography who had their ship, the C.S.S. HUDSON, in the Scott Inlet area from September 3 to September 6, 1978 and again for a few days after September 24. The CCRS aircraft were to survey the Scott Inlet area while the personnel on the HUDSON were taking surface measurements. However, fog cover at Clyde River prevented C-GRSA from landing there until September 8; in addition, necessary repairs to sensor equipment and the aircraft delayed departure of C-GRSC from Ottawa until September 7, 1978.

E.2.3 Sortie summaries for C-GRSA at Scott Inlet

A total of 11 sorties were flown by C-GRSA in the Scott Inlet region during the period from September 9 to September 20, 1978. In the sorties summaries, times and distances are listed for 'sensors on', 'in area', and 'transit'. The 'sensors on' time pertains to that part of the 'in area' time that is designated specifically as flight line time; however, most of the sensors were on for the greater part of the time and some, e.g. the LLLTV, were on for the 'transit' time as well. Maps indicating flight paths and oil sightings for Sorties 2-8 are displayed in Figures E.2 to E.7 respectively. Two maps at two different scales for each of Sorties 9-11 are shown in Figures E.9 to E.14. In addition, the flight paths for all the sorties are collected together in Figures E.15 and E.16, and the oil sightings in Figure E.17. Oil from the oil seep off Scott Inlet was observed on only two sorties, 9 and 10.

Sortie 1: C-GRSA departed Clyde River 15:45 GMT 09/09/78 and arrived at Scott Inlet at 16:32 GMT. The sky was clear and the wind was 50-60 knots. The sky was clear and the wind was 50-60 knots at 320° near the sea surface at Scott Inlet. The Scott Inlet area was searched for oil until 18:08; then, the aircraft returned to Clyde River and landed at 18:40. A number of equipment problems were encountered at the beginning of the sortie because of cold temperatures in the aircraft at startup.

Sortie 2 (Figure E.2): C-GRSA departed Clyde River at 15:03 GMT 11/09/78 and arrived on line at Scott Inlet at 15:50 GMT. The sky was clear and there was no perceptible wind. The area from Cape Hunter to Cape Eglinton was searched for oil; several possibilities were looked into but no oil sighting was confirmed. Fluorosensor malfunctions halted the search at 17:08 GMT, C-GRSA headed for Clyde River and landed at 18:18 GMT.

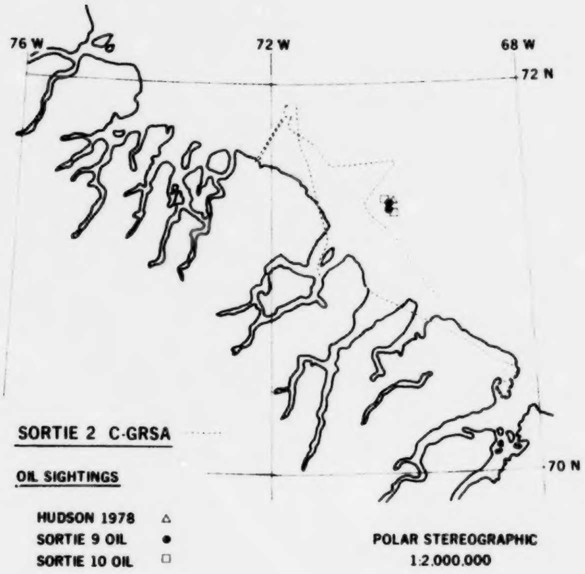
76 W
72 W
68 W
72 N
70 N
SORTIE 2 C-GRSA
OIL SIGHTINGS
HUDSON 1978 △
SORTIE 9 OIL ●
SORTIE 10 OIL □
POLAR STEREOGRAPHIC
1:2,000,000

FIGURE E.2 SCOTT INLET: NAVIGATION TRACK OF C-GRSA, SORTIE 2 (1:2 000 000).

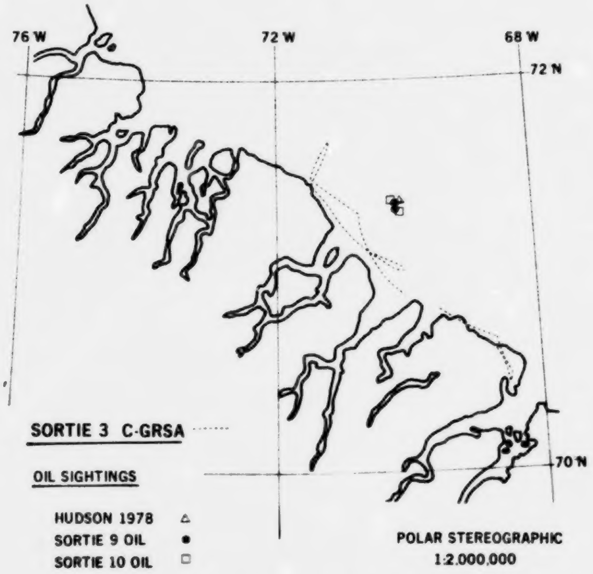
76 W
72 W
68 W
72 N
70 N
SORTIE 3 C-GRSA
OIL SIGHTINGS
HUDSON 1978 △
SORTIE 9 OIL ●
SORTIE 10 OIL □
POLAR STEREOGRAPHIC
1:2,000,000

FIGURE E.3 SCOTT INLET: NAVIGATION TRACK OF C-GRSA, SORTIE 3 (1:2 000 000).

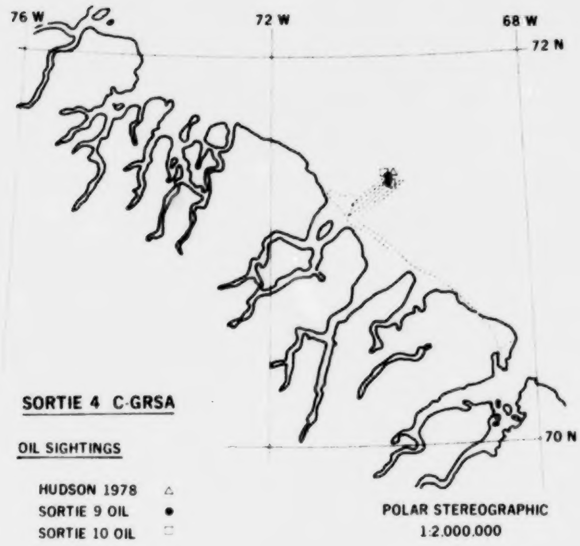
76 W
72 W
68 W
72 N
70 N
SORTIE 4 C-GRSA
OIL SIGHTINGS
HUDSON 1978 △
SORTIE 9 OIL ●
SORTIE 10 OIL □
POLAR STEREOGRAPHIC
1:2,000,000

FIGURE E.4 SCOTT INLET: NAVIGATION TRACK OF C-GRSA, SORTIE 4 (1:2 000 000).

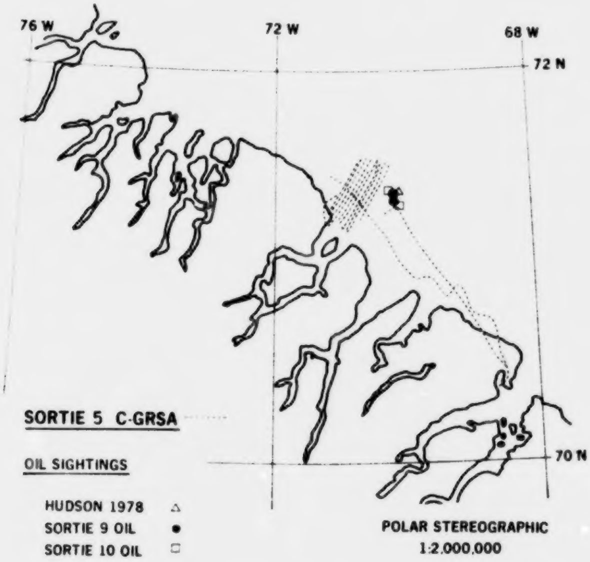
76 W
72 W
68 W
72 N
70 N
SORTIE 5 C-GRSA
OIL SIGHTINGS
HUDSON 1978 △
SORTIE 9 OIL ●
SORTIE 10 OIL □
POLAR STEREOGRAPHIC
1:2,000,000

FIGURE E.5 SCOTT INLET: NAVIGATION TRACK OF C-GRSA, SORTIE 5 (1:2 000 000).

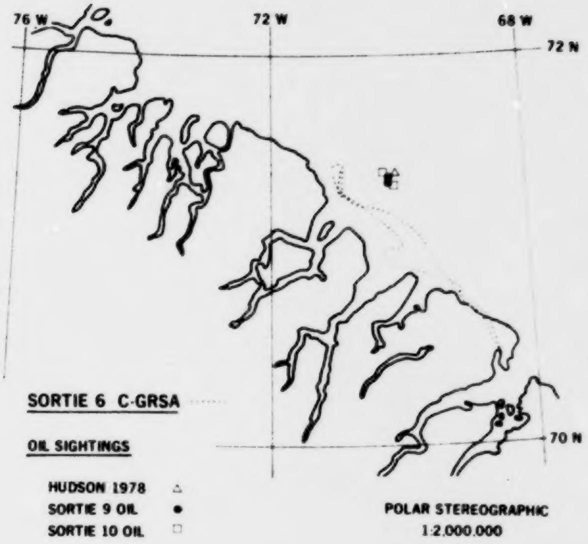
76 W
72 W
68 W
72 N
70 N
SORTIE 6 C-GRSA
OIL SIGHTINGS
HUDSON 1978 △
SORTIE 9 OIL ●
SORTIE 10 OIL □
POLAR STEREOGRAPHIC
1:2,000,000

FIGURE E.6 SCOTT INLET: NAVIGATION TRACK OF C-GRSA, SORTIE 6 (1:2 000 000).

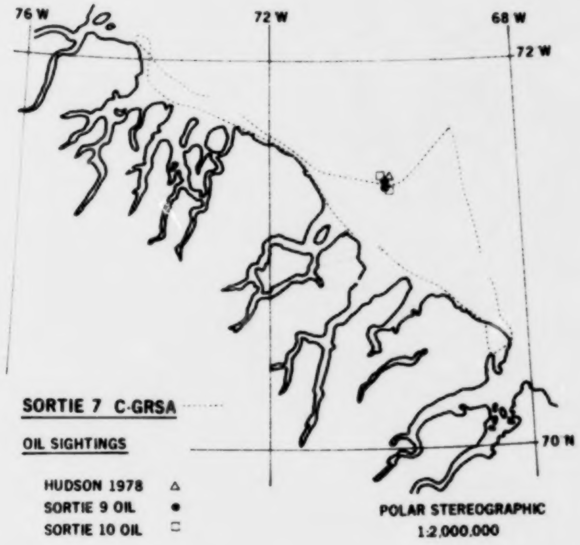
76 W
72 W
68 W
72 W
70 N
SORTIE 7 C-GRSA
OIL SIGHTINGS
HUDSON 1978 △
SORTIE 9 OIL ●
SORTIE 10 OIL □
POLAR STEREOGRAPHIC
1:2,000,000

FIGURE E.7 SCOTT INLET: NAVIGATION TRACK OF C-GRSA, SORTIE 7 (1:2 000 000).

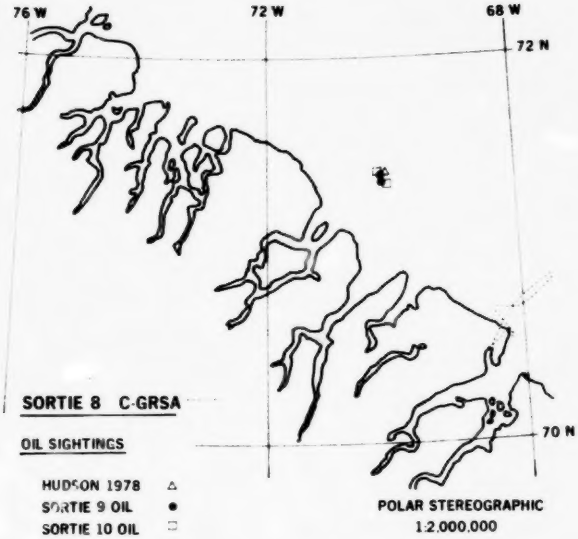
76 W
72 W
68 W
72 N
70 N
SORTIE 8 C-GRSA
OIL SIGHTINGS
HUDSON 1978 △
SORTIE 9 OIL ●
SORTIE 10 OIL □
POLAR STEREOGRAPHIC
1:2,000,000

FIGURE E.8 SCOTT INLET: NAVIGATION TRACK OF C-GRSA, SORTIE 8 (1:2 000 000).

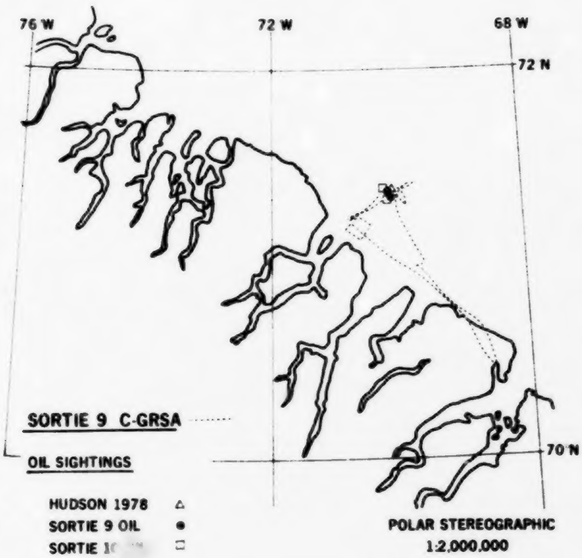
76 W
72 W
68 W
72 N
70 N
SORTIE 9 C-GRSA
OIL SIGHTINGS
HUDSON 1978 △
SORTIE 9 OIL ●
SORTIE 1 □
POLAR STEREOGRAPHIC
1:2,000,000

FIGURE E.9 SCOTT INLET: NAVIGATION TRACK OF C-GRSA, SORTIE 9 (1:2 000 000).

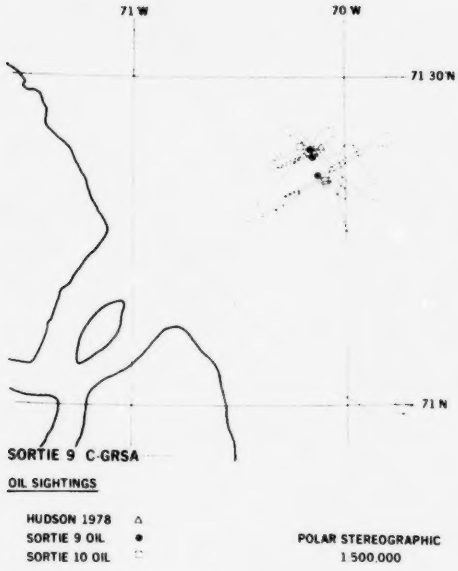
71 W
70 W
71 30 N
71 N
SORTIE 9 C-GRSA
OIL SIGHTINGS
HUDSON 1978 △
SORTIE 9 OIL ●
SORTIE 10 OIL □
POLAR STEREOGRAPHIC
1:500,000

FIGURE E.10 SCOTT INLET: NAVIGATION TRACK OF C-GRSA, SORTIE 9 (1:500 000).

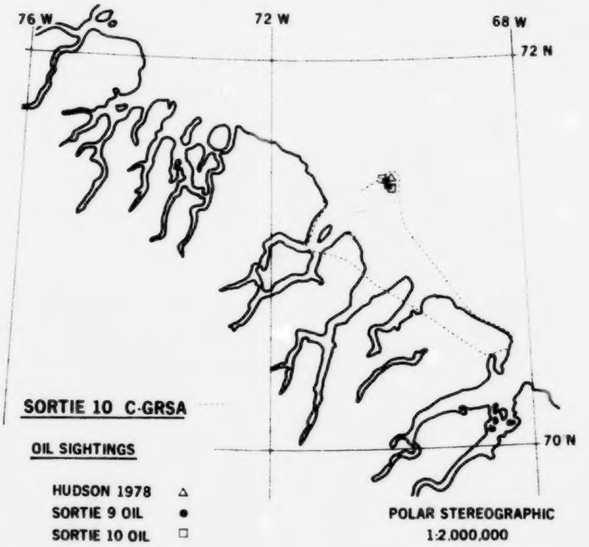
76 W
72 W
68 W
72 N
70 N
SORTIE 10 C-GRSA
OIL SIGHTINGS
HUDSON 1978 △
SORTIE 9 OIL ●
SORTIE 10 OIL □
POLAR STEREOGRAPHIC
1:2,000,000

FIGURE E.11 SCOTT INLET: NAVIGATION TRACK OF C-GRSA, SORTIE 10 (1:2 000 000).

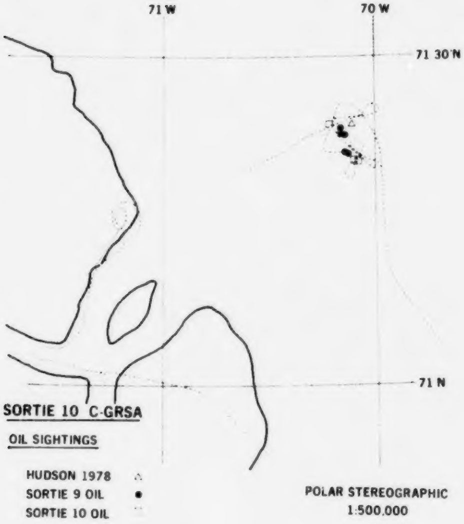
71 W
70 W
71 30 N
71 N
SORTIE 10 C-GRSA
OIL SIGHTINGS
HUDSON 1978 △
SORTIE 9 OIL ●
SORTIE 10 OIL
POLAR STEREOGRAPHIC
1:500,000

FIGURE E.12 SCOTT INLET: NAVIGATION TRACK OF C-GRSA, SORTIE 10 (1:500 000).

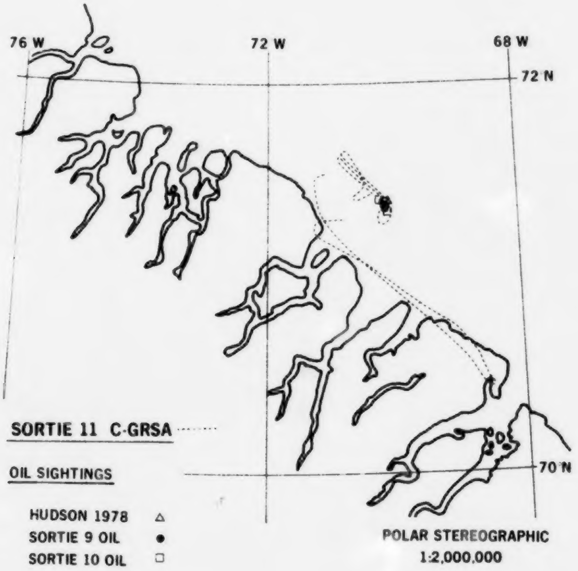
76 W
72 W
68 W
72 N
70 N
SORTIE 11 C-GRSA
OIL SIGHTINGS
HUDSON 1978 △
SORTIE 9 OIL ●
SORTIE 10 OIL □
POLAR STEREOGRAPHIC
1:2,000,000

FIGURE E.13 SCOTT INLET: NAVIGATION TRACK OF C-GRSA, SORTIE 11 (1:2 000 000).

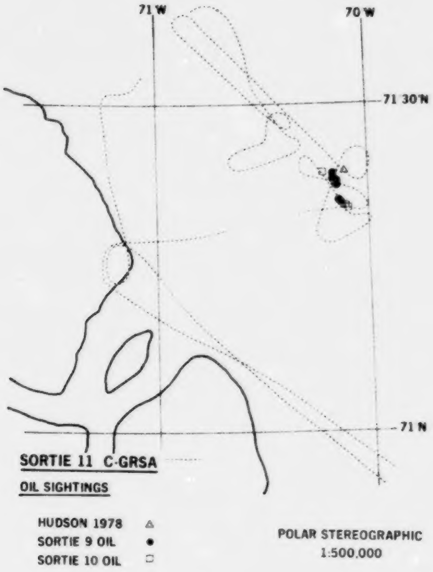
71°W
70°W
71°30'N
71°N
SORTIE 11 C-GRSA
OIL SIGHTINGS
HUDSON 1978 △
SORTIE 9 OIL ●
SORTIE 10 OIL □
POLAR STEREOGRAPHIC
1:500,000

FIGURE E.14 SCOTT INLET: NAVIGATION TRACK OF C-GRSA, SORTIE 11 (1:500 000).

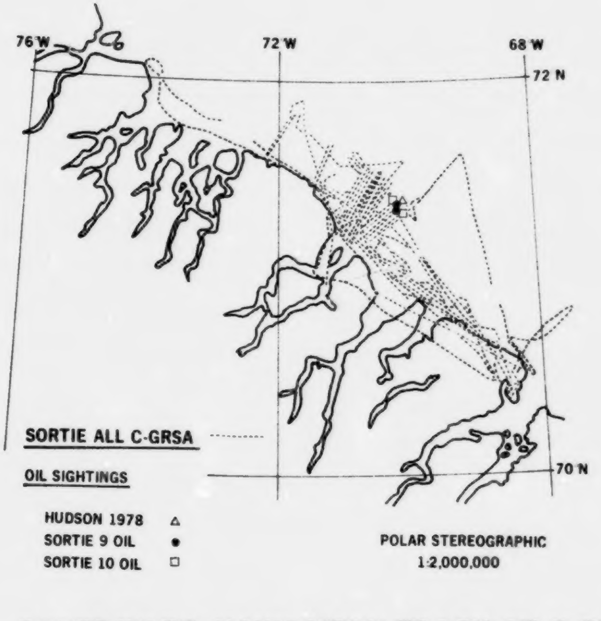
76°W
72°W
68°W
72°N
70°N
SORTIE ALL C-GRSA
OIL SIGHTINGS
HUDSON 1978 △
SORTIE 9 OIL ●
SORTIE 10 OIL □
POLAR STEREOGRAPHIC
1:2,000,000

FIGURE E.15 SCOTT INLET: NAVIGATION TRACK OF C-GRSA, ALL SORTIES (1:2 000 000).

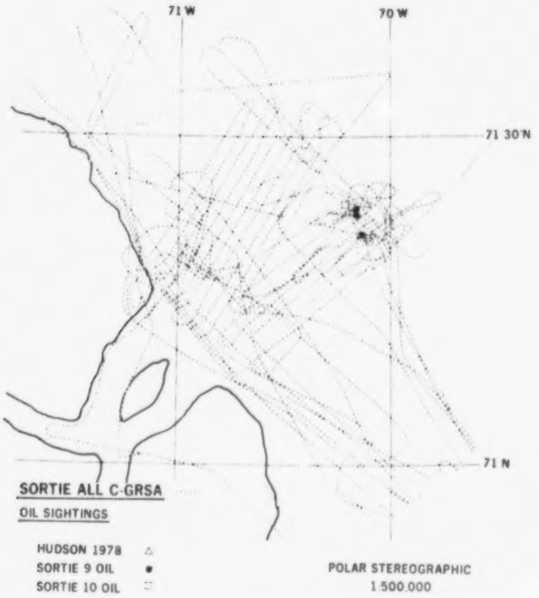
71 W
70 W
71 30'N
71 N
SORTIE ALL C-GRSA
OIL SIGHTINGS
HUDSON 1978 △
SORTIE 9 OIL ●
SORTIE 10 OIL ▫
POLAR STEREOGRAPHIC
1:500,000

FIGURE E.16 SCOTT INLET: NAVIGATION TRACK OF C-GRSA, ALL SORTIES (1:500 000).

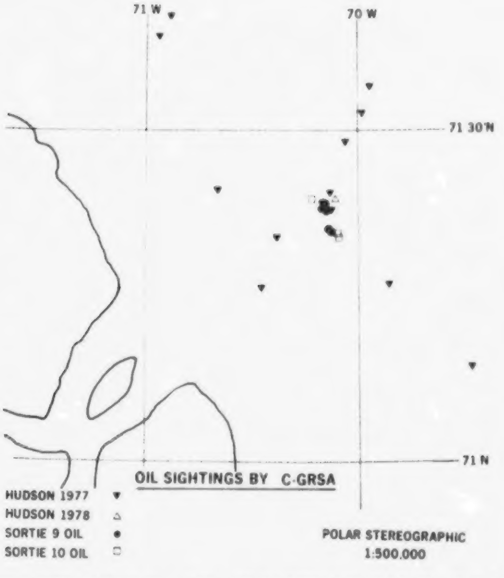
71 W
70 W
71 30'N
71 N
OIL SIGHTINGS BY C-GRSA
HUDSON 1977 ▼
HUDSON 1978 △
SORTIE 9 OIL ●
SORTIE 10 OIL ▫
POLAR STEREOGRAPHIC
1:500,000

FIGURE E.17 SCOTT INLET: OIL SIGHTING BY C-GRSA.

Sortie 3 (Figure E.3): C-GRSA left Clyde River at 20:09 GMT 11/09/78 after repairs to the fluorosensor. The coastline of Baffin Island from Sam Ford Fiord to Cape Adair on either side of Scott Inlet was searched for oil from 20:45 GMT until 21:42 GMT. Then the aircraft departed for Clyde River and landed at 22:29 GMT. On both Sorties 2 and 3 vast slick areas were observed visually, but could not be attributed to oil.

Sortie 4 (Figure E.4): C-GRSA departed Clyde River at 15:57 GMT 12/09/78 and arrived at Scott Inlet on line at 16:28 GMT. Clyde River had a 300 m ceiling; at the Scott Inlet there was variable cloud and 5-10 knots wind at 320°. Several flight lines were flown in a grid pattern over the area where oil had been reported previously (Levy, 1977) and where C-GRSA was to find oil a few days later. Oil was not sighted, and the search was terminated at 17:42 GMT. The aircraft then proceeded to Clyde River where it arrived at 18:10 GMT.

Sortie 5 (Figure E.5): Bad weather prohibited flight of the C-GRSA for several days. Sortie 5 was flown on 16/09/78, departing at 13:53 GMT. Upon start up the UV Vinten camera suffered a failure that could not be repaired in the field. The aircraft arrived north of the Scott Inlet area at 14:46 GMT and proceeded with a grid pattern searching for oil. At the end of the pattern, the search was carried to the location where oil had been previously reported by Levy (1977). No oil was observed. At 16:52 GMT C-GRSA left for Clyde River; a few lines were flown over an oil slick in Patricia Bay at Clyde River. The aircraft landed at 17:38 GMT.

Sortie 6 (Figure E.6): Later the same day, C-GRSA left Clyde River at 19:23 GMT. A few lines were flown over the oil in Clyde River harbour. The aircraft arrived near the same area searched in Sortie 5 at 20:09 GMT and checked out a few anomalies. An anomaly near Cape Eglinton was also observed. The aircraft returned to Clyde River, flew more flight lines over the oil in the harbour, and landed at 21:45 GMT.

Sortie 7 (Figure E.7): C-GRSA left Clyde River at 13:51 GMT 17/09/78 for a survey of the Baffin Island coast from Cape Christian past Scott Inlet and Buchan Gulf to Cape Jameson, where low altitude katabatic winds in excess of 80 knots where encountered. The aircraft arrived at Cape Jameson at 15:20 GMT and headed back for Clyde River. The area where oil had been sighted in previous years was overflown again but oil was not observed. It was noted on this sortie that the slick 'streamers' often observed were concentrated in the region of the grounded icebergs. The aircraft landed at Clyde River at 16:54 GMT.

Sortie 8 (Figure E.8): This sortie was an investigation of some anomalies noted off Cape Christian. The aircraft left Clyde River at 19:16 GMT 17/09/78. The area was searched for 30 minutes, but no oil was observed off Cape Christian; the anomalies were tide lines. C-GRSA returned to Patricia Bay and there flew several flight lines over another small oil spill in the harbour. C-GRSA landed at 20:28 GMT.

Sortie 9 (Figures E.9 and E.10): The decision was made to check out all points of interest; those where oil had been observed in past years, and those where anomalies had been sighted by the C-GRSA crew. C-GRSA took off from Clyde River and the anomaly was checked out at Cape Eglinton. The aircraft arrived at Scott Inlet at 14:05 GMT and flew a box pattern near the mount of Scott Inlet. The aircraft then proceeded to the site where oil had been reported in previous years. Oil was sighted at two locations 71°21'N, 70°08'W and 71°23'N, 70°10'W. Several flight lines were flown over each location. C-GRSA left the area at 15:44 GMT and landed at Clyde River at 16:27 GMT. It is noted that the region in which oil was observed on this sortie had been overflown on three previous Sorties, 4,5, and 7, at which times no oil was present.

Sortie 10 (Figures E.11 and E.12): Later on 19/09/78 C-GRSA took off at 18:18 GMT and proceeded back to the locations where oil was sighted earlier. The aircraft arrived in the Scott Inlet area at 19:07 GMT and again found oil at two locations: 71° 20.5' N, 70° 05.5'W and 71°24'N, 70°13'W.

The weather was deteriorating, with winds in excess of 30 knots and snow flurries in the search area. C-GRSA left the area at 19:41 GMT and landed in Clyde River at 20:19 GMT.

The personnel of the C.S.S. HUDSON observed upwelling of oil in the Scott Inlet area on September 24, 1978 at 71°23.7'N, 70°06.3'W (Figure 36). Surface samples were taken for subsequent laboratory analysis of the oil.

Sortie 11 (Figures E.13 and E.14): The last sortie of the mission was on 20/09/78; C-GRSA took off at 13:25 GMT and proceeded to points of interest off Cape Adair north of Scott Inlet, and then back to the same locations where oil was observed on the previous day. No oil was observed and C-GRSA flew back to Clyde River, landing at 16:02 GMT.

E.2.4 Sortie summaries for C-GRSC at Scott Inlet

C-GRSC flew a total of 5 sorties in the Scott Inlet region between 08/09/78 and 14/09/78. Maps indicating flight paths for Sorties 1 through 5 are displayed in Figures

E.18 to 22; a map including all flight paths for C-GRSC on this mission is shown in Figure E.23.

Sortie 1 (Figure E.18): C-GRSC left Frobisher Bay at 15:00 GMT 08/09/78 for Thule, Greenland. En route two flight lines were flown in the Scott Inlet area with all sensors operating. At Scott Inlet the wind was 10-15 knots at 320° and the clouds were variable. A survey was made of the area in which oil had been reported previously (Levy, 1977) and in which C-GRSA later found oil, but no oil was observed. The SAR was operated in a shallow depression angle mode and horizontal transmit polarization. C-GRSC arrived at Thule at 19:00 GMT.

Sortie 2 (Figure E.19): C-GRSC left Thule at 15:35 GMT 09/09/78 and arrived at the Baffin Island coast and started a survey line over the coast at 17:00 GMT. Two lines of SAR imagery and one line of microwave scatterometer data were taken. The SAR was operated at shallow depression angle and vertical transmit polarization. The sky was clear and the wind was 25-30 knots at 320°. The area of previously reported oil was surveyed and no oil observed. The aircraft left the area at 18:35 GMT and landed at Thule at 20:00 GMT.

Sortie 3 (Figure E.20): C-GRSC departed Thule at 14:50 GMT 11/09/78 and arrived at the Baffin Island coast at 16:00 GMT. Five flight lines were flown with the scatterometer operating, two with SAR recording imagery. The SAR was operated at shallow depression angle and vertical transmit polarization. The sky was clear and there was no perceptible wind. The microwave sensors showed very little scattering return. C-GRSC left the Scott Inlet area at 17:18 GMT and arrived at Thule at 18:40 GMT.

Sortie 4 (Figure E.21): C-GRSC departed Thule at 14:20 GMT 12/09/78 and arrived at the Baffin Island coast at 15:46 GMT near Clyde River. Two flight lines were flown in order to obtain imagery of targets at Clyde River airport. A line was also flown in order to photograph the airstrip at Clyde River. The sky conditions at Clyde River were quite overcast. At Scott Inlet there was variable cloud and light winds, 5-10 knots at 320°. The SAR was again operated at shallow depression angle and vertical transmit polarization. C-GRSC proceeded to Scott Inlet where six flight lines with the microwave scatterometer were flown. Another flight line of SAR imagery was taken while heading toward Thule. The aircraft arrived in Thule at 19:05 GMT.

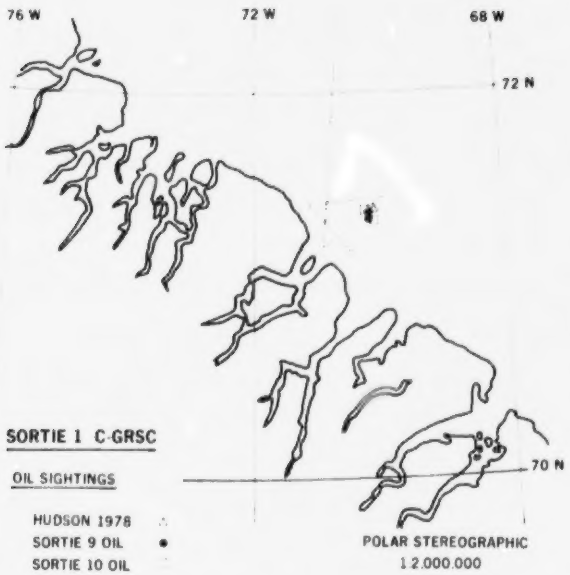
76 W
72 W
68 W
72 N
70 N
SORTIE 1 C-GRSC
OIL SIGHTINGS
HUDSON 1978 △
SORTIE 9 OIL ●
SORTIE 10 OIL □
POLAR STEREOGRAPHIC
1:2,000,000

FIGURE E.18 SCOTT INLET: NAVIGATION TRACK OF C-GRSC, SORTIE 1 (1:2 000 000).

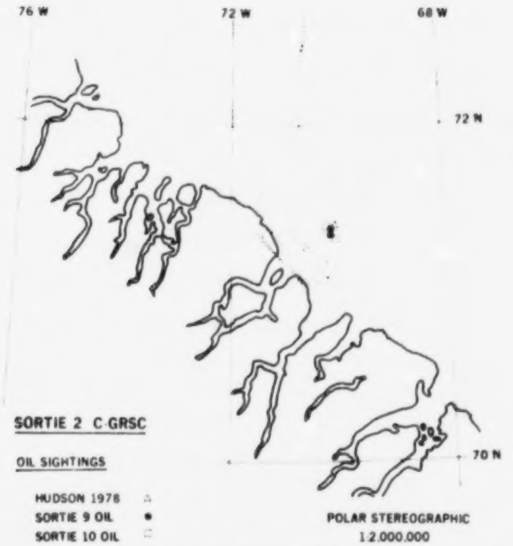
76 W
72 W
68 W
72 N
70 N
SORTIE 2 C-GRSC
OIL SIGHTINGS
HUDSON 1978 △
SORTIE 9 OIL ●
SORTIE 10 OIL □
POLAR STEREOGRAPHIC
1:2,000,000

FIGURE E.19 SCOTT INLET: NAVIGATION TRACK OF C-GRSC, SORTIE 2 (1:2 000 000).

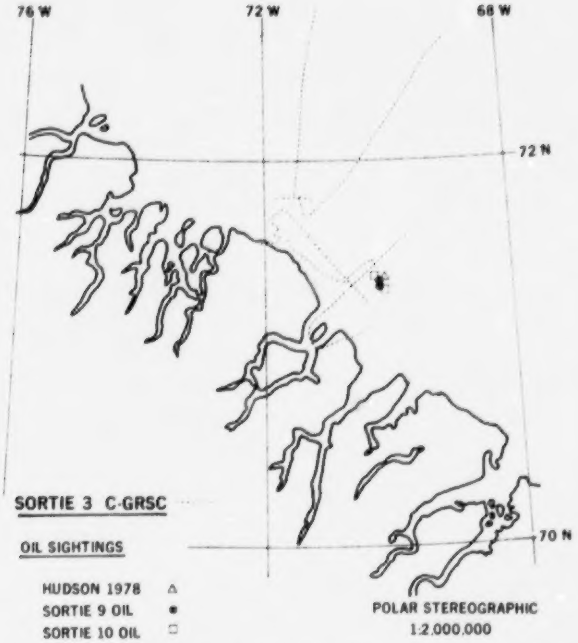
76 W
72 W
68 W
72 N
70 N
SORTIE 3 C-GRSC
OIL SIGHTINGS
HUDSON 1978 △
SORTIE 9 OIL ●
SORTIE 10 OIL □
POLAR STEREOGRAPHIC
1:2,000,000

FIGURE E.20 SCOTT INLET: NAVIGATION TRACK OF C-GRSC, SORTIE 3 (1:2 000 000).

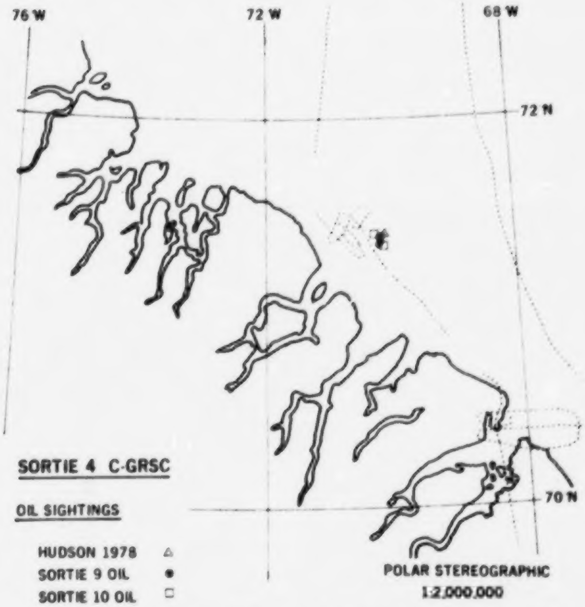
76 W
72 W
68 W
72 N
70 N
SORTIE 4 C-GRSC
OIL SIGHTINGS
HUDSON 1978 △
SORTIE 9 OIL ●
SORTIE 10 OIL □
POLAR STEREOGRAPHIC
1:2,000,000

FIGURE E.21 SCOTT INLET: NAVIGATION TRACK OF C-GRSC, SORTIE 4 (1:2 000 000).

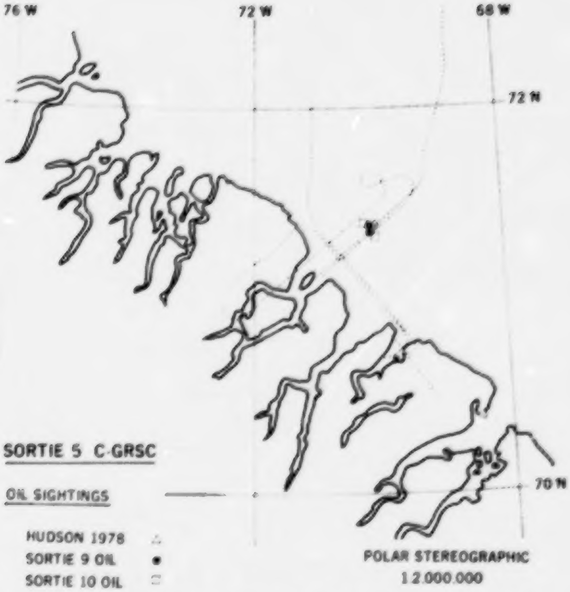
76 W
72 W
68 W
72 N
70 N
SORTIE 5 C-GRSC
OIL SIGHTINGS
HUDSON 1978 △
SORTIE 9 OIL ●
SORTIE 10 OIL □
POLAR STEREOGRAPHIC
1:2.000.000

FIGURE E.22 SCOTT INLET: NAVIGATION TRACK OF C-GRSC, SORTIE 5 (1:2 000 000).

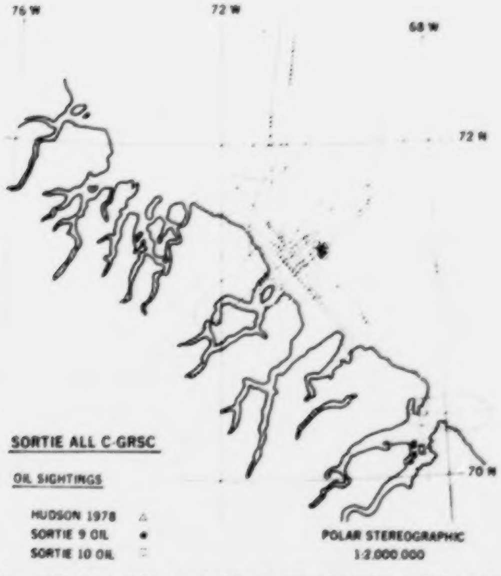
76 W
72 W
68 W
72 N
70 N
SORTIE ALL C-GRSC
OIL SIGHTINGS
HUDSON 1978 △
SORTIE 9 OIL ●
SORTIE 10 OIL □
POLAR STEREOGRAPHIC
1:2.000.000

FIGURE E.23 SCOTT INLET: NAVIGATION TRACK OF C-GRSC, ALL SORTIES (1:2 000 000).

Sortie 5 (Figure E.22): C-GRSC left Thule at 12:40 GMT 14/09/78 and arrived at the Baffin Island coast on line at 13:45 GMT. The SAR depression angle had been changed to the steep mode and the radar was operated in both the vertical and horizontal transmit polarizations. The Baffin Island coast was completely cloud covered with a low ceiling. Only the SAR was operated and the aircraft altitude was 5.5 km. Five flight lines of SAR imagery were obtained. C-GRSC arrived back in Thule at 16:30 GMT. Figure E.23 shows all the sorties from this mission.

The same day on the homeward transit journey from Thule to Frobisher an additional line of SAR imagery was obtained using the horizontal transmit polarization at an altitude of 6.7 km. The flight line was flown at 20:51 GMT; C-GRSC landed in Frobisher Bay at 22:35 GMT.

E.3 Wallops Island

E.3.1 Purpose

The AMOP remote sensing project team was asked to participate in the remote sensing of a set of controlled oil spills at Dump Site 106 off the New Jersey coast in the first week of November 1978. CCRS, in cooperation with remote sensing groups from NASA Wallops, U.S. Coast Guard and Environmental Research Institute of Michigan (ERIM), surveyed the test oil spills conducted by JBF Scientific Corp. for the American Petroleum Institute. The purpose of the test spills was to evaluate the effectiveness of the oil dispersant Corexit 9527.

Participation in this mission proved to be of considerable benefit to the AMOP effort for a number of reasons. Easy access to and precise location of the spill permitted the efficient collection of large quantities of excellent data with a minimum of logistical problems and search effort. Sensor improvements made as a result of the experience obtained at Scott Inlet were tested. Data collected with the CCRS sensors would be compared to and augmented by that from the other participants; in particular, as the CCRS sensor complement did not include a microwave radiometer, the NRL dual frequency imaging microwave radiometer data were of special interest. In addition, the visibility of the oil before and after the application of the dispersant could be tested by the various sensors.

E.3.2 Logistics

Two CCRS aircraft were used in the mission, C-GRSA and C-GRSC, the latter in cooperation with ERIM. C-GRSA was equipped and tested during the months of September and October. The preparation and testing schedule allowed for more time than was available for the Scott Inlet mission. Again because of schedule pressures the pre-mission testing of equipment mounted in C-GRSC was minimal; however, the sensors on this aircraft performed much better than on the Scott Inlet mission.

The base operations for the mission was NASA Wallops Flight Center, Wallops Island, Virginia. A planning session was held on October 31, 1978 to lay out the details of the spills, and the communications and protocol necessary to conduct the remote sensing part of the spill experiments. On November 1, there was a spill of Rhodamine WT dye; this was used as a 'dry run' for subsequent oil spills. C-GRSA and 427, the NASA C-54, went to the spill to obtain fluorescence spectra information. The two spills of 1666 litres each on November 2 and 3 were put down by the R/V ANNANDALE, a 27 m ship operated by the Marine Science Consortium Inc. Personnel on the NOAA vessel GEO. B. KELEZ placed buoys, dye markers and surface current cards about the oil spills in order to mark them after they were laid out.

The two CCRS aircraft C-GRSA, C-GRSC, the NASA C-54 and U.S. Coast Guard C-130 took remote sensing data over the spills, and the JBF Scientific Corp. Skymaster II overviewed the spill operations. A helicopter applied dispersant to the oil spills after 110 minutes from the beginning of the spills. Several spar buoys to which were tethered corner reflector buoys were deployed about the spill. Also, several hundred computer punch cards were released behind the spill. The punch cards lined up in 'streets' and revealed the wind driven surface currents present.

Both CCRS aircraft participated in the oil spills of November 2 and 3. Another two spills were planned for November 4 and 5 in which dispersant was to be applied immediately after spillage. C-GRSA was to participate at these spills; however, poor weather delayed the dates and other commitments forced the aircraft to abandon this part of the mission.

E.3.3 Sortie summaries for C-GRSA at Wallops Island

Sortie 1: The dye, consisting of 11.4 litres of Rhodamine WT (Dupont) in liquid concentrate form diluted in 151 litres of freshwater, was spilled at 15:00 GMT 01/11/78 at

Dump Site 106 off the New Jersey coast. C-GRSA departed Wallops Flight Center at 14:50 GMT and arrived on line at the spill at 16:07 GMT. Nineteen passes were made over the dye. The dye was observed with the MSS and fluorosensor. The maximum dye concentration observed was 13 ppb (measured by NASA). C-GRSA left the spill area at 16:57 GMT and landed at Wallops Flight Center at 18:05 GMT.

Sortie 2: Between 16:53 GMT and 16:55 GMT 02/11/78, 1666 litres of Murban crude oil (Abu Dahbi) were put out into a spill at 40°08.4'N, 73°32'W. C-GRSA departed Wallops Flight Center at 15:45 GMT and arrived on line in the spill area at 17:10 GMT. The sky was clear and the wind was 6-7 knots at 240°. The oil formed an emulsion during the spilling process or very shortly thereafter. C-GRSA made 25 passes over the oil before departing at 18:24 GMT. Besides the KELEZ and ANNANDALE, a 15 m sportsman fishing vessel was present in the spill area and may be observed in some of the imagery. A dispersant, Corexit 9527, was applied to the spill between 18:50 and 19:15 GMT. C-GRSA landed at Wallops Flight Center at 19:40 GMT.

Sortie 3: Between 15:14 and 15:18 GMT 03/11/78, 1666 litres of La Rosa crude oil (Venezuela) were spilled at 40°09.5'N, 73°35'W. C-GRSA departed Wallops Flight Center at 14:55 GMT and arrived in the spill area at 15:41 GMT. The sky was clear and the wind was 10 knots at 060°. The La Rosa crude oil appeared heavier and darker than the Murban crude spilled on November 2; the La Rosa crude did not form an emulsion. Between 16:55 and 17:10 GMT, the dispersant was applied to the oil. A total of 29 passes were made over the spill area. C-GRSA left the area at 18:20 GMT and arrived at Wallops Island at 19:30 GMT. Two passes were made along the Flight Center runway in order to establish sensor alignment. The aircraft landed at 19:40 GMT.

Sortie 4: C-GRSA joined in an attempted mission on 07/11/78; however, the mission was aborted as a result of poor weather. The aircraft did not remain at NASA Wallops for the two test spills which took place on November 9, 10.

E.3.4 Sortie summaries for C-GRSC at Wallops Island

Sortie 1: Between 16:53 and 16:55 GMT, 02/11/78, 1666 litres of Murban crude oil (Abu Dahbi) were put out into a spill at 40°08.4'N, 73°32'W. C-GRSC departed NASA Wallops Flight Center at 15:40 GMT and arrived in the spill area at 15:55 GMT. The sky was clear and the wind was 6-7 knots at 240°. There were 6 passes over the spill taken at an altitude of 250 m with the DCLS, RC10 and microwave scatterometer operating. Both transmit polarizations of the scatterometer were recorded over the spill. Water and oil samples were taken in the spill area by the technical crew on the ANNANDALE between 17:10 and 17:30 GMT. At 17:14 GMT, C-GRSC climbed to an altitude of 5.5 km and one pass of the area was made at 17:38 GMT while operating the DCLS. Between 17:53 and 19:17 GMT, SAR imagery was collected on 7 flight lines flown at an altitude of 5.5 km. Dispersant was applied to the spill between 18:50 and 19:15 GMT. C-GRSC landed at Wallops Flight Center at 20:20 GMT.

Sortie 2: Between 15:14 and 15:18 GMT 03/11/78, 1666 litres of La Rosa crude oil (Venezuela) were put out into a spill at 40°05.5'N, 73°35'W. C-GRSC departed NASA Wallops Flight Center at 14:20 GMT and arrived in the spill area at 15:17 GMT. The sky was clear and the wind was 10 knots at 060°. There were 6 passes over the spill taken at an altitude of 250 m using the DCLS, RC10 and microwave scatterometer. Water and oil samples were taken in the spill area by personnel on the ANNANDALE between 15:25 and 16:00 GMT. At 15:31 GMT, C-GRSC left low altitude and proceeded to an altitude of 5.5 km where one pass of the spill area was made with the DCLS and RC10 operating. SAR imagery was obtained on 9 flight lines flown at an altitude of 5.5 km. C-GRSC left the spill area at 17:32 GMT and arrived at Wallops Island at 18:21 GMT where 2 passes of the Flight Center were taken in order to obtain some imagery of calibrated reflectors. The aircraft landed at 18:50 GMT.

E.4 KURDISTAN

E.4.1 Purpose

CCRS was requested by EPS to search parts of the Gulf of St. Lawrence and the south coast of Cape Breton Island for the oil spill resulting from the breakup of the tanker KURDISTAN. The mission afforded the AMOP remote sensing project the first opportunity to test the sensors over oil-in-ice.

E.4.2 Logistics

The KURDISTAN was damaged by ice at 18:00 GMT 15/03/79, in the Laurentian Channel about 50 miles north of Glace Bay; then, at 01:19 GMT 16/03/79, it broke apart spilling 6400 tonnes of Bunker 'C' oil. At 20:00 GMT 16/03/79, CCRS was asked by EPS to respond to the KURDISTAN spill. A DC-3 aircraft (C-GRSB) was fitted with a sensor complement; operating crew and scientists departed Ottawa arriving in Halifax at 12:20 GMT 17/03/79. Four sorties were flown while operating out of

Summerside, P.E.I., between March 17 and March 21, 1979. The aircraft and crew returned to Ottawa 21/03/79.

On March 23, 1979 C-GRSB again departed for Cape Breton Island when oil had been reported in pack ice. One sortie was completed successfully before an aircraft failure prevented further flying on this occasion. Four sorties were flown by the CCRS Falcon Fan Jet (C-GRSD), two on March 29 and two on April 2.

A separate report of this mission has been prepared (O'Neil et al., 1979), and the reader is referred to it for additional details.

E.4.3 Sortie summary for the KURDISTAN mission

There were 9 sorties flown on the KURDISTAN mission; a complete record of the sorties is contained in the KURDISTAN Oil Spill Remote Sensing Report (O'Neil et al., 1979). Oil was first sighted in small patches on March 21, 1979. On March 23 an extensive oil slick covering approximately 7 000 square kilometres was detected southeast of Cape Breton Island with the slick centre at 45°00'N, 59°30'W.

Finally, on March 29 and April 2, large areas of ice along the Cape Breton Island Coast were observed to have trapped large quantities of oil.

APPENDIX F

PROCESSING OF THE AMOP
REMOTELY SENSED DATA

APPENDIX F

Processing of the AMOP Remotely Sensed Data

A three-tiered procedure was followed in order to reduce and process the necessary data. First, an overview of the data was taken with the aid of flight logs, photographs and video products; this delineated areas of interest and yielded flight line and time code information. Second, for the flight lines of interest, quick look products of imagery and profiling data were obtained from or viewed on a device appropriate for the data from a particular sensor. These output devices or products included: CCD display, CCRS Daedalus image processing system film, SAR survey prints, plotter or line printer output, CIAS, MAD and GRAMS. Third, final products were obtained for those examples which portrayed sensor capability. The sensor data chart in Table F.1 shows the sequence of data flow for each sensor from recording medium to final output products. The volume of AMOP data is outlined in Table F.2.

The in flight recording of the non-photographic data was accomplished via two automatic data acquisition systems, the CCRS airborne data acquisition system (ADAS) and the FDF-80, the latter used in conjunction with the fluorosensor. Descriptions of these systems are given in Appendix F. The processing of data from the various sensors and the production of the final results are discussed in the following sections. The CCRS ground based computers and display devices, and detailed procedures involved in processing the data from recording medium to final product are contained in the CCRS technical memorandum "AMOP Data Processing" (V. Thomson, K. Dagg, 1979).

F.1 MPPH, OMA

Sets of data from the Miller-Pieau photometer (MPPH) and Optical Multichannel Analyzer (OMA) were collected on the Scott Inlet and Wallops Island missions, but were analyzed only to the extent of determining that data were recorded. This was due to the fact that insufficient software was available for processing the OMA data, and that, in the case of the MPPH, insufficient time/manpower was available to perform any data reduction and analysis. The data are presently held by CCRS and could be analyzed in the future (Appendix I).

TABLE F.1 SENSOR DATA PRODUCTS

Sensor	Recording Medium	Quick Look Product/Facility	Final Product
DCLS	3 tracks ITR (analogue)	CCRS DIP CCD display CSFR imagery	CSFR imagery
Fluorosensor	CCT	FDF-80 display Plotter output CSFR false image	Plotter output CSFR false image
Television	Videotape with voice	Videotape replay Line scan image	Photograph of TV monitor Line scan image
MEIS	2 tracks ITR (digital)	CCD display CSFR image	CSFR image
MPPH	MUX ITR	Line printer output Plotter output	Line printer output Plotter output
MSS	up to 11 tracks ITR (digital)	CCD display CSFR image	CSFR image
OMA	1 track ITR (digital) Videotape	Line printer output CSFR false image Plotter output	CSFR false image Plotter output
RC10	Film	Processed Film	Film prints
SAR	Film	Survey prints	Film prints
Scatterometer	2 tracks ITR (analogue)	GRAMS-spectrum analyzer Line printer output	CSFR false image
Vinten	Film	Processed film	Film prints

CCD - charge coupled device
CCT - computer compatible tape
CSFR - continuous strip film recorder
GRAMS - ground recovery and monitoring system
MUX - multiplex track data formatted by ADAS
DIPS - Daedalus image processing system
ITR - instrumentation tape recorder

N.B. - in addition to the above quick look facilities, the Multispectral Analysis Display (MAD) and the CCRS Image Analysis System (CIAS) were used for image analysis.

TABLE F.2 QUALITY OF DATA HANDLED IN THE PROJECT

	Medium		Quantity	Content
Recorded Data				
	Mincom Tape		73 tapes	$8x10^{11}$ bits
	Photographic Film:	70 mm colour	318 m	5300 frames
		70 mm B&W	288 m	4800 frames
		23 cm colour	195 m	650 frames
	Sar Film: 70 mm image colour		100 m	
	Television Videotape :	1" tape	25 hours	
		1/2" tape	11 hours	
	Fluorosensor CCT		25 tapes	$6x10^{9}$ bits
Analysed Data				
	Digital Media:	CCT	505 tapes	$6x10^{10}$ bits
		DISK	6 packs	$2x10^{9}$ bits
	Analogue Imagery:	13cm film	125 m	
	CSFR:	quick look	1300 m	
		MAD prints	30 m	
		standard products	600 m	
Summary				
	Recorded Data		$8x10^{11}$ bits	
	Photographic Film		800 m	
	Sar Image Film		100 m	
	Television Videotape		36 hours	
	Processed Data (stored)		$6x10^{10}$ bits	
	Final Film Products		2055 m	

F.2 ERIM SAR

Data from the ERIM synthetic aperture radar were recorded as a hologram on 70 mm signal film at the time of radar operation; subsequently, it was processed by ERIM to produce an image film. It was this image film which was delivered to the project and analyzed. From the negative image film, positive strip transparancies or prints, or enlarged prints were produced for presentation or analysis.

F.3 Photographic Film

Photographic film was developed and printed at the National Air Photo Library (NAPL). Enlargements from 70 mm negative film were made at the Government Photo Centre.

Only visual analysis was performed on the photographs taken; this was because of a lack of time and the line scan imagery (MSS, DCLS) of most targets was recorded coincidently.

The Kodak type 2445 Aerocolour negative film used produced generally good photographs when illumination was sufficient (see Figures 47, 61, 62, 71, 68, 69).

Kodak type 2405 Double-x Aerographic film was used in conjunction with a Wratten 18A filter on the camera to produce ultraviolet photographs. The ultraviolet provided better contrast between oil and water than did the colour photography (see Figures F.1 to F.4), but little discrimination between thick and thin slick areas.

F.4 Television

Television data were replayed by means of a one inch videotape recorder. Images were produced either by taking a 35 mm photograph of a high resolution television monitor (see Figure F.5) or by printing a line scan image on a Honeywell model 1856A visicorder (see Figure 29).

The line scan image was created by: first, choosing a single video scan line by means of a time delayed sync separator; second, presenting the separated triggering pulse and video signal to the visicorder. The net effect of this operation was to reduce the video data to 30 scan lines per second. Choosing the correct time delay allowed the image recorded at any angle in the field of view of the television camera to be displayed.

F.5 Line Scan Imagery (MSS, MEIS, DCLS)

Data from the MSS, MEIS and DCLS line scanning sensors were recorded on the appropriate number (see Table F.1) of tracks of a MINCOM instrumentation tape recorder; the MSS and MEIS were recorded digitally and the DCLS analogue. The line scanner data were transferred to JSC formatted computer compatible tapes for later analysis.

In order to view the data from these sensors as an image, one of the following devices was used: CCD Display, Bendix Multispectral Analyzer Display (MAD), Continuous Strip Film Recorder (CSFR) or CCRS Daedalus Image Processing System (DIPS). The first three devices are described in CCRS-DPD-TM-79-105.

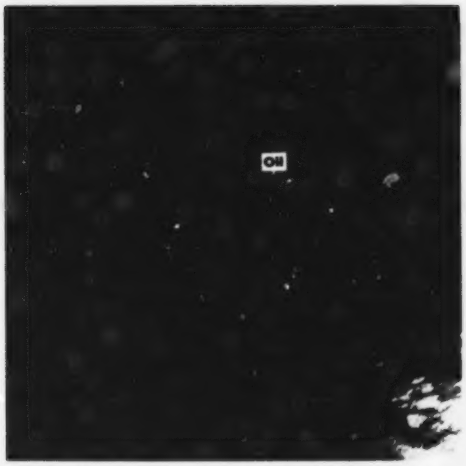

Vinten 70mm Camera with UV Filter
2405 Double-X Aerographic Film
Kurdistan Oil Spill
C-GRSB
Flight Line 2
March 23,1979
18:58:20 GMT

FIGURE F.1 VINTEN COLOUR PHOTOGRAPHY, KURDISTAN OIL SPILL. C-GRSB, Flight Line 2, March 23, 1979.

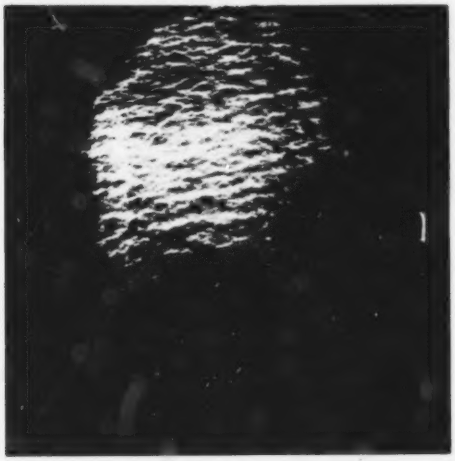

Vinten 70mm Camera with UV Filter
2405 Double-X Aerographic Film
Wallops Oil Spill
C-GRSA
Flight Line 17
November 2,1978
18:01:41 GMT

FIGURE F.2 VINTEN ULTRAVIOLET PHOTOGRAPHY, WALLOPS OIL SPILL. C-GRSA, Flight Line 17, November 2, 1978.

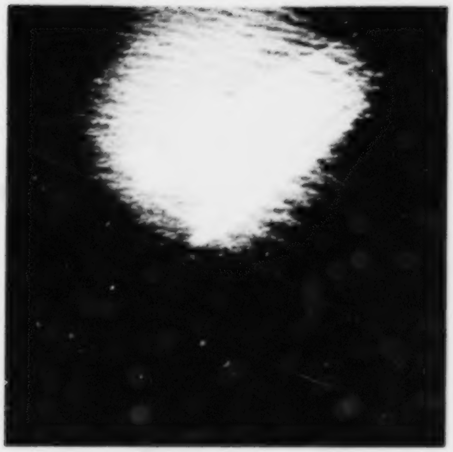

Vinten 70mm Camera with UV Filter
2405 Double-X Aerographic Film
Wallops Oil Spill
C-GRSA
Flight Line 22
November 3, 1978
17:50:17 GMT

FIGURE F.3 VINTEN ULTRAVIOLET PHOTOGRAPHY, WALLOPS OIL SPILL. C-GRSA. Flight Line 22, November 3, 1978.

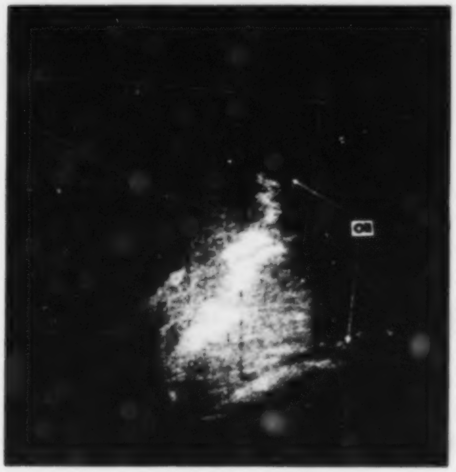

Vinten 70mm Camera
2445 Aerocolour Negative Film
Kurdistan Oil Spill
C-GRSB
Flight Line 2
March 23, 1979
18:58:20 GMT

FIGURE F.4 VINTEN ULTRAVIOLET PHOTOGRAPHY, KURDISTAN OIL SPILL. C-GRSB, Flight Line 2, March 23, 1979.

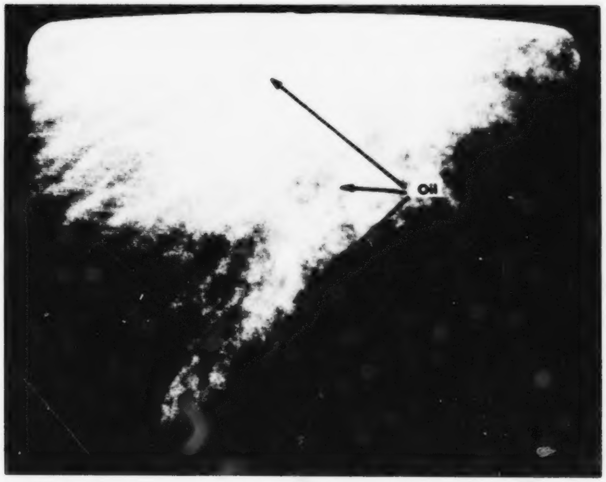

Low Light Level Television
Scott Inlet
C-GRSA
Sortie 9
Flight Line 16
September 19, 1978
15:27:08 GMT

FIGURE F.5 LOW-LIGHT-LEVEL TELEVISION, SCOTT INLET. Photography of TV monitor showing the oil seep. C-GRSA Sortie 9, Flight Line 16, September 19, 1978.

The Daedalus image processing system is an analogue scan printer which can produce a geometrically correct grey tone image from the DCLS analogue recorded data. Grey tone line scan imagery was viewed on the CCD and MAD monitors; quality hard copy reproduction of such imagery was produced on the CSFR and DIPS. It was also possible to transfer an image on the MAD display to the CSFR for printing. From these grey tone products a few flight lines of data were chosen as being representative of the capability of the line scan sensors.

Feature enhancement methods were employed on selected images to improve the oil-water contrast in the colour imaging products. As such methods can be implemented by means of a real time processor, this imagery can be taken as representative of the type of capability desirable in a real time display system. Feature enhancement was performed on the MAD or the CCRS Image Analysis System (CIAS) using the following methods: i) a grey level to colour translation; and ii) a thematic classification of the data presented in colour.

F.5.1 Grey level to colour translation

In a digitally recorded image each pixel (for each channel of a given sensor) has a digital intensity value associated with it. An image can be produced by using this digital value to modulate the display pixel intensity, i.e., in a positive image the lowest digital intensity appears black and the highest, white. On most imaging devices the translation of a recorded digital level to a displayed intensity is controlled by a look up table. For instance, a look up table may be chosen which allows the display of only a narrow range of digital intensity values as grey tones.

The use of a look up table permits flexibility in the assignment of a grey tone to a pixel in an image. For many images in this report, a look up table was devised which assigns a colour to a given digital intensity value. Colour assignments were chosen such that the oil-water contrast was enhanced. In those MSS and DCLS bands that contained oil film thickness information, colours were assigned which improved the visual differentiability and interpretability of the image.

F.5.2 Thematic classification

The thematic classification of data was performed on CIAS and printed on the CSFR. Various models exist for automatically classifying the imagery data; most of these models base their classifications on certain statistical criteria. Several models were tested on AMOP project data and a clustering model was chosen. As an example of the application of this method the classified DCLS imagery appearing in Figures 73, 74, and 51 will be discussed.

For the DCLS two channels of data are recorded, a UV and an IR channel. The image of a scene for these two channels is read into CIAS memory. Then, a two dimensional vector space of UV-IR intensities is formed in which there is a vector (a,b) for each pair of (UV, IR) intensities; the vector (a,b) is the UV-IR vector space representation of an image pixel having UV intensity 'a' and IR intensity 'b'. Vectors corresponding to each pixel in an operator specified portion of the total image are determined. The operator chooses the number of desired themes (8 in the present case); the computer then attempts to locate in UV-IR space an equal number (8) of regions of maximum density, or clusters, by a migrating means model. When this is completed, the pixel vectors are all classified according to which of the clusters includes them. Colours are assigned to each cluster; the image pixels corresponding to vectors in a given cluster then are depicted in the cluster colour. In this way the image is classified into a chosen number (8) of themes according to the UV and IR intensities. The clustering or migrating means model was also used to produce thematic images of MSS data where 2 or 4 channels of data were used (see Figures 79 and 80).

F.6 Fluorosensor

Fluorosensor data were recorded by the FDF-80 onto computer compatible tape. Fluorosensor data are presented in three different formats: first, a graph of spectral channel intensity plotted versus time; second, a graph of correlation coefficient plotted versus time; and third, a CSFR product displaying all spectral channels as a time history in the form of a false image.

F.6.1 Spectral channel intensity graphs

The fluorosensor data are output to a digital plotter in a format of intensity versus laser shot number or time (see Figures 85) for each of the 16 spectral channels. Oil detection is seen as an increased fluorescence intensity in one or more of the spectral channels depending on the fluorescence response of the particular oil to UV excitation.

F.6.2 Correlation plots

A more sensitive and comprehensive way of presenting fluorosensor data is by means of the linear or Pearson correlation coefficient. A correlation of a sample oil fluorescence spectrum against the gathered data is performed and plotted as a function of laser shot number or time history (see Figure 86). While noting that the increase in fluorescence in the spectral channel intensity graph indicates the presence of an anomalous substance (in this case, compared to the return from water), it does not help to identify the substance. The presentation of a time history of correlation coefficients not only indicates the anomaly but also gives an indication as to the identity of the substance causing it.

The Pearson correlation coefficient, σ, is given as:

$$\sigma = \frac{N \sum_{i}^{N} x_i y_i - \sum_{i}^{N} x_i \sum_{j}^{N} y_j}{\left| N \sum_{i}^{N} x_i^2 - \left(\sum_{i}^{N} x_i \right)^2 \right|^{1/2} \cdot \left| N \sum_{i}^{N} y_i^2 - \left(\sum_{i}^{N} y_i \right)^2 \right|^{1/2}} \qquad (16)$$

where: $\{x_i\ ; i=1, N\}$ and $\{y_i\ ; i=1, N\}$

are the two arrays of N numbers (N = 16 for the fluorosensor) that are being compared.

The coefficient will tend towards a value of +1 to indicate a correlation in the two sets of data, to a value of 0 to indicate no correlation, and to -1 to indicate an anticorrelation.

For fluorosensor data, a 16 channel sample spectrum of a suspected oil type is compared to the return data from the fluorosensor via the correlation calculation and the result is plotted. Any significant variation from a 'background' level is noted and interpreted as indicating the presence of oil having a spectrum similar to that of the sample. In the calculation of correlation coefficients, ordinarily 5 to 10 data samples were averaged and then correlated.

F.6.3 CSFR false image diagrams

In this presentation the 16 channel fluorescence return is displayed as a time history (see Figure 98). Fluorescence intensity is indicated as a colour change starting as a grey background and increasing to dark blue, light blue, orange, yellow, red, white. Thus, as in the spectral channel diagrams, anomalies may be noted. However, the coloured false image presentation is more readily interpreted.

F.7 Microwave Scatterometer

Microwave scatterometer data are recorded on an instrumentation tape recorder and later reformatted into computer disk files. The scatterometer data are displayed in three formats: i) a backscatter cross section as a function of look angle; ii) a density plot (densigram) of relative backscatter cross section as a function of look angle; iii) a CSFR false image of relative backscatter cross section as a function of look angle in a colour density format.

F.7.1 Backscatter vs look angle diagrams

This is a Cartesian plot of normalized backscatter cross section versus time for a selected set of look angles in both the fore and aft radar beams (see Figure 16).

F.7.2 Densigrams

A densigram or density plot is a diagram of a time history of relative normalized backscatter cross section as a function of look angle. The average sea backscatter cross section at each angle has been removed from the representation so that a relative backscatter is shown. The grey level in the diagram shows the excursion of the target's scattering cross section from the average sea background. The vertical axis of the plots is the along track direction and the look angle varies along the horizontal axis. Negative and positive look angles are the aft and fore directions respectively. The data have been suitably shifted so that each section of angular data is given at the same time as the target area was overflown. A stationary target should be represented as a straight horizontal line. (Ordinarily this is not the case since the aircraft heading and track angle are different; this means that the sensor look direction deviates from the aircraft direction of travel.) Examples of densigrams are shown in Figures 17, 20, 23.

F.7.3 CSFR false image diagrams

The CSFR diagrams of coloured false images of relative normalized backscatter cross section time histories are similar to scatterometer densigrams except that cross section is coded by colour on the CSFR diagram; examples are shown in Figure 103.

F.8 Navigation

A brief description of CCRS navigation track recovery is given in Appendix B. In the AMOP remote sensing project, aircraft track plots were made from recorded navigation parameters of the Scott Inlet and KURDISTAN missions. For the Scott Inlet mission all navigation parameters were recorded by ADAS on the multiplex track on an instrumentation tape recorder. These navigation parameters were processed, stored in a disk file, and later presented as a plot on a map format with the use of a World Data Bank Program (CCRS-DPD-TM-79-98; K. Dagg, V. Thomson) (see Figures E.2 to E.23).

APPENDIX G

SCOTT INLET/CLYDE RIVER OIL SIGHTINGS

APPENDIX G

Scott Inlet/Clyde River Oil Sightings

Date	Sortie	Flight Line	Location Lat, Long (dm)	LLLTV Time (GMT)	MSS Time (GMT)
16 Sept 78	5		Patricia Bay off Clyde River townsite		
		17a		17:26:12-:48	17:26:26
		17b		17:28:41	
		17c		17:34:00-:08	
17 Sept 78	8		Patricia Bay off Clyde River townsite		
		3		20:18:00-:07	
		4		20:20:25-:33	
		5		20:23:11-:18	
		6		20:25:38-:46	
19 Sept 78	9		Baffin Bay off Scott Inlet		
		7	71:23N 70:10W	14:25:57-:26:03	14:26:05:86
		7	71:23N 70:08W	14:26:17.6	
		16	71:23N 70:09.5W	15:27:07.8-:19.2	15:27:14.6
		18	71:23.5N 70:09.5W	15:35:27.5-:30.3	
		20	71:23N 70:10W	15:43:21-:22	15:43:22.28
			71:23N 70:09W	15:43:33.2-36.2	
	10		Baffin Bay off Scott Inlet		
		9	71:20.5N 70:05W	19:31:21	
		10	71:20.5N 70:05.5W	19:32:45-:46	
		11	71:20.5N 70:05.5W	19:34:15	
		12	71:20.5N 70:06W	19:36:17	
		13	71:23.5N 70:13W	19:39:54-:57	

APPENDIX H

FIRMS AND AGENCIES WITH OPERATIONAL SYSTEMS APPLICABLE TO THE REMOTE SENSING OF OIL SPILLS

APPENDIX H

Firms and Agencies with Operational Systems Applicable to the Remote Sensing of Oil Spills (1,2)

Canada Centre for Remote Sensing
Data Acquisition Division
Energy Mines and Resources
2464 Sheffield Road
Ottawa, Ontario
K1A 0Y7

Telephone: (613) 998-9060

The Canada Centre for Remote Sensing is a federal government agency with the facilities for developing and demonstrating remote sensing equipment. The various sensors and platforms described in this report are owned by CCRS.

Ice Branch
Atmospheric Environment Service
Department of the Environment
4905 Dufferin Street
Downsview, (Toronto) Ontario
M3H 5T4

Telephone: (416) 667-4724

The Atmospheric Environment Service performs routine ice reconnaissance flights in addition to their meteorological activities. AES has Electra aircraft equipped with a Motorola AN/APS-94D radar (X_{HH}), a Bendix thermal mapper and a 70 mm photographic camera.

Department of National Defence
National Defence Headquarters
Ottawa, Ontario
K1A 0K2

Telephone: (613) 993-1502

The Canadian Armed Forces have aircraft which can be equipped with remote sensing equipment. They have two Reconafax XIIIA line scanners. The research carried out by the military is largely classified. The oil spill searches in which they have been involved have employed only visual observations.

Intertech Remote Sensing Ltd.
202 - 2841 Riverside Drive
Ottawa, Ontario
K1V 8N4

Telephone: (613) 521-1811

Intertech operates a Cessna 411 aircraft equipped with a Daedalus infrared line scanner and a 70 mm photographic camera.

Les Relèves Géophysiques Inc.
1975 boul. Charest ouest
Ste-Foy, Québec
G1N 2E6

Telephone: (418) 687-4055

Les Relèves Géophysiques owns a Bendix thermal mapper and 70 mm photographic camera which are flown by Aero Photo Inc.

MARS Ltd.
640 11th Avenue SW
Calgary, Alberta
T2R 0E2

Telephone: (403) 262-8482

MARS Ltd. operates a Grumman GI aircraft equipped with a Motorola APS-94D side looking radar (X_{HH}), two Wild Heerbrugg RC-8 mapping cameras, and a Daedalus DEI-100 thermal IR line scanner.

Norcor Engineering and Research Ltd.
P.O. Box 277
Yellowknife, NWT

Telephone: (403) 873-5845

Norcor operates a Britten-Norman Islander aircraft equipped with a Bendix RDR1400 ground search radar (X_{HH}), a RCA 1040 ISIT Television system and 70 mm photographic camera. The sensors and VLF Omega navigational system are integrated into a real time processor.

1 Excluded from the list are aerial survey companies with only photographic cameras.

2 (O'Neil, 1977).

APPENDIX I

INFORMATION ON DATA AVAILABLE FROM THE AMOP REMOTE SENSING PROJECT

APPENDIX I

Information on Data Available from the AMOP Remote Sensing Project

The AMOP remote sensing project consisted of four missions and several test flights. The four missions were: Montreal Island, Scott Inlet, Wallops Island, KURDISTAN. The data from these missions and other test flights are presently stored at:

Canada Centre for Remote Sensing
Data Acquisition Division
2464 Sheffield Rd.
Ottawa, Ontario
K1A 0Y7

Telephone: (613) 998-9060

Inquiries should be directed to R.A. O'Neil.

The data from the flights are stored on several magnetic media and photographic film; also, there are several analysis products which have been generated from the flight data. Below is a list of the type of information available.

Recorded Data

Instrumentation tape	MSS, MEIS, NAV, OMA, MPPH, CAM, MS
Photographic film	RC10, VINTEN
Signal and image film	SAR
JSC formatted tapes	FS
Videotape	LLLTV
Flight log sheets	flight line and sortie parameters for all missions

Analyzed Data

Data log sheets	flight line parameters sensor performance observations
Vinten log sheets	frame number to film number translation tables
Computer media list	data reformatted from instrumentation tape to computer compatible tape; CIAS images; and World data bank programs and maps MSS calibration

CSFR production list	all images produced on CSFR with film record numbers
MSS	multispectral scanner
MEIS	multiple detector electro-optical imaging scanner
FS	fluorosensor
NAV	navigation parameters
OMA	optical multichannel analyzer
MPPH	Miller-Pieau photometer
CAM	camera firings
MS	microwave scatterometer
LLLTV	low-light-level television
SAR	ERIM synthetic aperature radar
RC10	Wild Heerbrugg camera
Vinten	70 mm format camera

APPENDIX J

ACRONYMS

APPENDIX J

Acronyms

ADAS	Airborne Data Acquisition System
ADF	Automatic Direction Finder
AES	Atmospheric Environment Service (of DOE)
AGTV	Active Gated Television (Range gated, Laser Illuminated television)
AMOP	Arctic Marine Oilspill Program
AOSS	Airborne Oil Surveillance System (USCG)
API	American Petroleum Institute
APOA	Arctic Petroleum Operators Association
APU	Auxillary Power Unit
ARINC	Aeronautical Radio Incorporated (aviation standards)
CCD	Change Coupled Device
CCG	Canadian Coast Guard (of DOT)
C-CORE	Centre for Cold Oceans Research and Engineering
CCRS	Canada Centre for Remote Sensing
CCT	Computer Compatible Tape
CFSR	Continuous Film Strip Recorder
CIAS	CCRS Image Analysis System (formerly the Image 100)
CZCS	Coastal Zone Colour Scanner
DAD	Data Acquisition Division (of CCRS)
DCLS	Dual Channel Line Scanner (as in UV/IRLS)
DIPS	Daedalus Image Processing System
DND	Department of National Defence
DOE	Department of the Environment
DOT	Department of Transport
DPD	Data Processing Division (of CCRS)
EPS	Environmental Protection Service (of DOE)
ERIM	Environmental Research Institute of Michigan
FDF-80	Fluorosensor Data Formatter
FS	Fluorosensor
GDI	General Digital Interfaces (part of ADAS)

GMT	Greenwich Mean Time
GNS	Global Navigation System
GRAMS	Ground Recovery and Monitoring System
HDDT	High Density Digital Tape (from 14 track Mincom recorders)
HF	High Frequency (communication system)
HH	Horizontal transmit, Horizontal receive polarization
HV	Horizontal transmit, Vertical receive polarization (cross polarized)
INS	Inertial Navigation System (often used interchangeably with INU)
INU	Inertial Navigation Unit (often used interchangeably with INS)
IR	Infrared
IRIG	Inter Range Instrumentation Group (standard)
IRLS	Infrared Line Scanner (subsystem of DCLS or UV/IRLS)
ITR	Instrumentation Tape Recorder
JSC	Johnson Space Centre (in reference to a standard magnetic tape format)
LLLTV	Low-light-level Television
L^3TV	Low-light-level Television
MAD	Multispectral Analysis Display
MDA	Macdonald Dettwiler and Associates
MEIS	Multi-Detector Electro-optical Imaging Scanner (a push broom imager)
MPPH	Miller-Pieau Photometer
MSS	Multispectral Scanner
MTD	Multiplex Track Data
NAPL	National Airphoto Library
NASA	National Aeronautics and Space Administration
NOAA	National Oceans and Atmospheric Administration
OMA	Optical Multichannel Analyzer
RC10	Wild Heerbrugg RC10 aerial camera
SAR	Synthetic Aperture Radar (a type of SLR)
SCG	Swedish Coast Guard
SIT	Silcon Intensified Target
SLAR	Side-looking Airborne Radar (often used to designated the Real Aperture type of SLR)
SLR	Side-looking Radar
SURSAT	Surveillance Satellite Project

TSS	Time Sharing System
TV	Television
USCG	United States Coast Guard
UV	Ultraviolet
UV/IRLS	Ultraviolet/Infrared Line Scanner
UVLS	Ultraviolet Line Scanner (subsystem of DCLS or UV/IRLS)
VH	Vertical transmit, Horizontal receive polarization (cross polarized)
VHF	Very High Frequency (communications system)
VLF	Very Low Frequency (navigation system)
VV	Vertical transmit, Vertical receive polarization

POOR

QUALITY

ORIGINAL